



**UNIVERSIDADE FEDERAL DE MINAS GERAIS**  
**INSTITUTO DE GEOCIÊNCIAS**  
**PROGRAMA DE PÓS-GRADUAÇÃO EM GEOLOGIA**



**TESE DE**  
**DOUTORADO**

**EVOLUÇÃO DE TURBIDITOS E SUA MINERALIZAÇÃO AURÍFERA NO  
LINEAMENTO CÓRREGO DO SÍTIO E ÁREA CUIABÁ-LAMEGO,  
SUPERGRUPO RIO DAS VELHAS: GEQUÍMICA, GEOCRONOLOGIA E *IN*  
*SITU* LA-ICP-MS EM SULFETOS**

**Jorge Geraldo Roncato Júnior**

**Orientadora: Profa. Dra. Lydia Maria Lobato**

**Co-orientadora: Profa. Dra. Rosaline Cristina Figueiredo e Silva**

**034**

**BELO HORIZONTE**

**17 de Junho de 2016**

UNIVERSIDADE FEDERAL DE MINAS GERAIS  
INSTITUTO DE GEOCIÊNCIAS  
PROGRAMA DE PÓS-GRADUAÇÃO EM GEOLOGIA

**EVOLUÇÃO DE TURBIDITOS E SUA MINERALIZAÇÃO AURÍFERA NO  
LINEAMENTO CÓRREGO DO SÍTIO E ÁREA CUIABÁ-LAMEGO,  
SUPERGRUPO RIO DAS VELHAS: GEQUÍMICA, GEOCRONOLOGIA E *IN  
SITU* LA-ICP-MS EM SULFETOS**

Tese apresentada ao Programa de Pós-Graduação em Geologia da Universidade Federal de Minas Gerais como requisito parcial à obtenção do título de doutor em geologia.

Área de concentração: Geologia Econômica e Aplicada.

Orientadora: Profa. Dra. Lydia Maria Lobato

Co-orientadora: Rosaline Cristina Figueiredo e Silva

*“Uma pessoa que se diz resiliente deve ser capaz de superar os obstáculos e lidar com os problemas, ambas situações que estão presentes sempre na vida do homem e não podem ser evitadas. É sempre hora de levantar-se, mesmo se houver medo de cair de novo”*

*(...)*

À Carolina Roncato, minha maior fonte de inspiração!

## AGRADECIMENTOS

À minha orientadora Lydia Lobato, por ser tão apaixonada pela ciência, e por fazer parecer ser tão fácil. Uma pessoa que não mede esforços para fazer geologia com ética e extremo cuidado, nos doando seu valioso tempo, sua casa, sua família e sua impressionante dedicação. Obrigado, Lydia, por me proporcionar o orgulho de poder dizer: “Fui aluno da Profa. Lydia Lobato! ”.

À AngloGold Ashanti pela oportunidade e financiamento para a realização deste trabalho. Obrigado, principalmente à Rodrigo Martins e Juliano Maciel, por sempre acreditar e apoiar o grupo de pesquisa de metalogenia da UFMG. À equipe das minas de Córrego do Sítio I e II, Cuiabá e Lamego: Marco Aurélio Sequetto, Tatiana Mascarenhas, Julia Teixeira, Rafael Chaves, Pedro Sales e Fred Lana, por tantas amostras cedidas e momentos de discussão.

Ao mestre, Orivaldo Baltazar, pelo apoio e incansável transmissão de sua enorme experiência sobre a geologia do Quadrilátero Ferrífero. Levarei para minha história o Brasil e Alemanha (7X1) que dividimos no trabalho de campo desta tese em Santa Bárbara/MG!

Ao colega de doutorado Breno Martins, pela ajuda nas análises de LA-ICP-MS na Austrália. Pelos ensinamentos no mapeamento subterrâneo, pelas discussões, sugestões, correções e aprendizados. Obrigado, também à co-orientadora Rosaline Silva, pelas tantas discussões e sugestões que foram de suma importância para entender “o mundo” das técnicas analíticas.

À Monica Mendes, pelos momentos de desespero, animação, dúvidas e alegrias. Pela eterna promessa de porre, ainda não cumprida! Pelas horas e horas de preparação de amostras, pelos quilos e quilos de amostras bateadas e pelos quilômetros e quilômetros no roteiro BH-Caeté-Ouro Preto. Terei sempre saudade de nossas ausências e risadas!

À Mahyra Tedeschi, por deixar minha vida mais leve e, nos momentos de maiores dúvidas, usar sua doçura para acalmar meu coração. Ao amigo e Geólogo Guilherme Prosdocimi, exemplo de ser humano e profissional; pela incalculável ajuda, nunca reclamando de minhas ausências profissionais, mesmo com todos os motivos do mundo.

Aos geólogos Milton Morales, Tiago Novo, Carlos Alberto Rosière, Cecília Porto, Luiz Claudio Lima, “Serjão” Martins, Yuri Ribeiro, Vassilly, Camila Gradim, João Orestes Santos, e tantos outros aqui não citados, que contribuíram com suas observações, discussões, correções e incalculáveis contribuições geológicas!

Ao *Applied Isotope Research Group* da Universidade Federal de Ouro Preto, pelos meses de trabalho e entendimento geocronológico do *Greenstone Belt* Rio das Velhas. Obrigado ao Prof. Cristiano Lana, a Hugo Moreira, Federico Farina e Ana Alkmim, pelas discussões e orientações. Não há como agradecer, ainda, à Janaína Veloso, pelas incontáveis horas divididas durante as estadias em Ouro Preto. Discussões, problemas, soluções, mapas astrais, pizzas, batatas recheadas e algumas ressacas. Ouro Preto sem você não teria graça!

À minha família, amigos, Maria Flor e Miguel, pela enorme ausência nestes últimos anos. Pelas tantas vezes que não viajei e não estive presente nas festas e reuniões. Meus agradecimentos também a Jaudemir Carvalho, que acreditou e me incentivou, quando eu mesmo já tinha desistido! Em vários momentos na vida, precisamos fazer escolhas. Para cada escolha, diversas consequências!

## SUMÁRIO

### PARTE I – INTRODUÇÃO, CONTEXTO GEOLÓGICO, EVOLUÇÃO DO CONHECIMENTO E APRESENTAÇÃO DA TESE

<b>1 INTRODUÇÃO</b>	1
<b>1.1 Objetivos</b>	2
<b>1.2 Trabalhos anteriores e evolução dos conhecimentos</b>	3
1.2.1 Depósitos auríferos	3
1.2.2 Mineralizações auríferas em rochas sedimentares	4
1.2.3 Exemplos de depósitos auríferos no <i>greenstone belt</i> Rio das Velhas	5
<b>1.3 Geologia da região do Quadrilátero Ferrífero</b>	6
1.3.1 Associações de Litofácies Sedimentares	9
1.3.1.1 Associação de litofácies ressedimentada (Zucchetti e Baltazar, 2000)	11
1.3.2 Lineamento Aurífero Córrego do Sítio – Setor Leste	13
1.3.3 Área Cuiabá-Lamego – Setor Norte	15
<b>1.4 Evolução geocronológica do Distrito Mineral Quadrilátero Ferrífero</b>	16
1.4.1 Eventos magmáticos no Cráton São Francisco	16
<b>1.5 Métodos</b>	17
1.5.1 Trabalhos de campo	17
1.5.2 Amostragem	18
1.5.2.1 Análises por (laser ablation induced coupled plasma mass spectrometry) - Amostragem no Setor Leste	19
1.5.3 Análises Petrográficas	20
1.5.4 Análises por Microscopia Eletrônica	20
1.5.4.1 Imageamento e microanálises em sulfetos	20
1.5.4.2 Imageamento de zircões detríticos	21
1.5.5 Geoquímica de Rocha Total	21
1.5.6 Análises Geocronológicas U-Pb em zircões por LA-ICP-MS	22
1.5.7 Análises de Isótopos Radioativos Lu/Hf em zircões por LA-ICP-MS	25
1.5.7.1 Procedimentos analíticos	27
<b>1.6 Apresentação da Tese</b>	27
<b><u>PARTE II – GEOLOGIA DOS DEPÓSITOS AURÍFEROS NO LINEAMENTO CÓRREGO DO SÍTIO</u></b>	
<b>2 METATURBIDITE-HOSTED GOLD DEPOSITS, CÓRREGO DO SÍTIO LINEAMENT, QUADRILÁTERO FERRÍFERO, BRAZIL</b>	28
<b>2.1 Introduction</b>	31
<b>2.2 Regional geological setting</b>	32
<b>2.3 Local Geology</b>	35
<b>2.4 Geology and mineralogy of the deposits</b>	40
2.4.1 Structures	42
2.4.2 Mineralization and hydrothermal alteration	44
2.4.3 Petrography of sulfides	51
<b>2.5 Discussion and Conclusions</b>	54
<b>2.6 Acknowledgments</b>	56

**PARTE III – ESTUDOS COMPARATIVOS DAS ASSOCIAÇÕES RESEDIMENTADAS DO LINEAMENTO  
CÓRREGO DO SÍTIO E DA ÁREA AURÍFERA CUIABÁ-LAMEGO**

<b>3</b>	<b>GEOCHEMISTRY, IN SITU LA-ICP-MS AND SEDIMENTARY SOURCE OF THE HOST TO GOLD CLASTIC ROCKS IN THE RIO DAS VELHAS GREENSTONE BELT, BRAZIL</b>	57
	<b>3.1 Introduction</b>	59
	<b>3.2 Regional setting of the Quadrilátero Ferrífero-QF District and surroundings</b>	62
	<b>3.3 Geology of the Córrego do Sítio lineament and Cuiabá-Lamego gold deposits</b>	65
	<b>3.4 Methods</b>	68
	<b>3.5 Analytical isotope methods</b>	68
	3.5.1 U-Pb Determinations	68
	3.5.2 Lu-Hf Measurements	70
	3.5.3 Analytical EPMA methods	71
	3.5.4 In situ LA-ICP-MS analyses on sulfide minerals	72
	<b>3.6 Turbidites of the Córrego do Sítio lineament</b>	73
	3.6.1 Petrography studies	73
	3.6.2 Hydrothermal alteration in gold deposits of the Córrego do Sítio lineament	75
	3.6.3 Textural features and paragenetic sequence of ore minerals	78
	3.6.4 In-situ LA-ICP-MS in Trace elements of eastern sector	81
	3.6.5 Composition of pyrites, pyrrhotites and arsenopyrites	81
	3.6.5.1 Porous pyrite (P-Py) composition	82
	3.6.5.2 Laranjeiras smooth pyrite (S-Py) composition	82
	3.6.5.3 Smooth pyrrhotite (S-Po) composition	82
	3.6.5.4 Porous arsenopyrite (P-Apy) composition	82
	3.6.5.5 Smooth arsenopyrite (S-Apy) composition	83
	3.6.5.6 Cachorro Bravo smooth pyrite (S-Py) composition	83
	3.6.5.7 Correlating sulfide textures and composition	83
	<b>3.7 Cuiabá-Lamego gold deposit area</b>	87
	<b>3.8 Whole-rock geochemistry</b>	87
	3.8.1 Major elements analyses	87
	3.8.2 Trace and rare earth element geochemistry	90
	<b>3.9 Zircon radiogenic isotope results</b>	91
	3.9.1 Cachorro Bravo deposit	92
	3.9.2 Laranjeiras deposit	93
	3.9.3 Carvoaria deposit	93
	3.9.4 Cuiabá deposit	96
	3.9.5 Lamego deposit	96
	<b>3.9 Lu-Hf analyses</b>	85
	3.10.1 Eastern sector	85
	3.10.2 Northern sector	86

<b>3.11 Discussion</b>	-----	<b>99</b>
3.11.1 Geochemical features, provenance and tectonic setting of the resedimented association of the eastern and northern sectors	-----	99
3.11.2 U-Pb geochronolog and Lu-Hf signature	-----	104
3.11.3 LA-ICP-MS and the host rock signature	-----	106
3.11.3.1 Sulfide trace element evolution in carbonaceous pelite	-----	106
3.11.3.2 Evolution of sulfide minerals and related host rocks	-----	107
<b>3.12 Implications for gold exploration</b>	-----	<b>109</b>
<b>3.13 Conclusions</b>	-----	<b>110</b>
<b>3.14 Acknowledgments</b>	-----	<b>115</b>

**PARTE IV - INTEGRAÇÃO, DISCUSSÃO E CONCLUSÕES DO TRABALHO**

<b>4 CONSIDERAÇÕES FINAIS</b>	-----	<b>116</b>
<b>5 BIBLIOGRAFIA</b>	-----	<b>120</b>

**ANEXO 1 - Dados Mapeamento Subterrâneo**

**ANEXO 2 - Tabelas Análises Químicas e LA-ICP-MS em sulfetos**

**ANEXO 3 - Dados análises Geocronológicas**

**ANEXO 4 - Tabela Evolução Tectônica da Associação Ressedimentada do Quadrilátero Ferrífero**

**INDICE DE FIGURAS**

Figura	1.1	Mapa de localização das áreas estudadas e principais vias de acesso	-----	2
Figura	1.2	Localização do Quadrilátero Ferrífero no extremo sul do Cráton do São Francisco.	-----	7
Figura	1.3	Mapa geológico do Quadrilátero Ferrífero.	-----	8
Figura	1.4	Ocorrência da associação ressedimentada na região do Quadrilátero Ferrífero	-----	12
Figura	1.5	Ambiência geotectônica dos setores leste e norte, da associação ressedimentada	-----	13
Figura	1.6	Coluna estratigráfica incluindo dados geocronológicos da região do QF	-----	18
Figura	1.7	Mapa geológico do QF, segundo compilação de idades U-Pb publicadas	-----	19
Figura	1.8	Intervalos de testemunhos de sondagem constituídos por rocha sedimentar, Depósito Laranjeiras.	-----	20
Figura	1.9	Coluna estratigráfica (Dorr, 1969) da região do Quadrilátero Ferrífero, com ênfase na associação ressedimentada do setor leste, lineamento Córrego do Sítio	-----	22
Figura	1.10	Coluna estratigráfica (Dorr, 1969) da região do Quadrilátero Ferrífero, com ênfase na associação ressedimentada do setor norte, área Cuiabá-Lamego .	-----	23
Figura	1.11	Colunas associando, nas mesmas posições estratigráficas, as posições amostradas da associação ressedimentada dos setores norte e leste.	-----	23
Figura	2.1	Geological map of the Quadrilátero Ferrífero region	-----	34
Figura	2.2	The NE-SW 16-km long Córrego do Sítio auriferous lineament	-----	37
Figura	2.3	Geological map of the Córrego do Sítio Lineament	-----	38
Figura	2.4	Rhythmic alternation of graded phyllites (ph) and metagraywackes (mg). (A) Macroscopic. (B) Microscopic transmitted light (TL). (C) Photomicrograph of carbonaceous phyllite, TL. Metamafic dikes and sills: (D) Metamafic dikes and sills incipiently alteration.	-----	39
Figura	2.5	Simplified 1:100 scale geological map of mine Gallery CB-658-200/211-south	-----	42
Figura	2.6	Simplified 1:100 scale geological map of mine Gallery CB-711-200/211-south	-----	43



Figura	2.7	<b>Structural data from the Córrego do Sítio auriferous lineament.</b>	46
Figura	2.8	<b>Hydrothermal alteration zones along the contact between metasedimentary and metamafic rocks</b>	49
Figura	2.9	<b>Hydrothermal paragenetic zoning, including the main sulfide, associated with gold</b>	50
Figura	2.10	<b>Hydrothermal paragenetic zoning, including the main sulfide minerals in metamafic rocks</b>	51
Figura	2.11	<b>Generations of sulfide minerals associated with the Cachorro Bravo gold deposit, Córrego do Sítio auriferous lineament.</b>	53
Figura	3.1	<b>Geological map of the Quadrilátero Ferrífero</b>	61
Figura	3.2	<b>Schematic drill core logs of the resedimented association in the Córrego do Sítio lineament</b>	69
Figura	3.3	<b>Schematic NW-SE geological cross section of the Córrego do Sítio lineament</b>	72
Figura	3.4	<b>Rocks of the clastic sedimentary association from the eastern (A) and northern (B) sectors of the Quadrilátero Ferrífero district</b>	75
Figura	3.5	<b>Hydrothermal Spatial zoning of hydrothermal minerals</b>	77
Figura	3.6	<b>Paragenetic sequence of ore minerals and their characteristics with the advance of hydrothermal alteration</b>	79
Figura	3.7	<b>Photomicrographs of generations of ore minerals associated with gold</b>	80
Figura	3.8	<b>Box plot of trace metal content in descending order of elemental abundance</b>	85
Figura	3.9	<b>Trace element contents (ppm) of sulfide minerals</b>	86
Figura	3.10	<b>Spider diagrams normalized to the NASC of major and trace elements</b>	87
Figura	3.11	<b>Geochemical classification of graywackes and pelites</b>	89
Figura	3.12	<b>Chondrite-normalized REE patterns for the clastic sedimentary association</b>	91
Figura	3.13	<b>SEM representative images of zircon grains from the graywackes and pelites</b>	92
Figura	3.14	<b>Probability density diagrams showing <math>^{207}\text{Pb}/^{206}\text{Pb}</math> age spectra of zircon grains from graywackes and pelites</b>	94
Figura	3.15	<b>Epsilon Hf versus <math>^{207}\text{Pb}/^{206}\text{Pb}</math> age diagram</b>	96
Figura	3.16	<b>Initial <math>^{176}\text{Hf}/^{177}\text{Hf}</math> versus <math>^{207}\text{Pb}/^{206}\text{Pb}</math> age diagram</b>	97
Figura	3.17	<b>Provenance discrimination diagram (after Roser and Korsch, 1988)</b>	102
Figura	3.18	<b>Tectonic setting discrimination diagrams based on major element composition.</b>	103
Figura	3.19	<b>Sketch of Archean tectonic environments</b>	115
<b>INDICE DE TABELAS</b>			
Tabela	1.1	<b>Coluna estratigráfica e geocronológica simplificada</b>	10
Tabela	2.1	<b>Micro and macroscopic aspects of the Córrego do Sítio lineament metamafic rocks</b>	40
Tabela	2.2	<b>Synthesis of vein characteristics</b>	45
Tabela	3.1	<b>Major, trace and REE values of the selected greywackes and pelites samples of eastern and northern sectors of Quadrilátero Ferrífero.</b>	Anexo 2
Tabela	3.2	<b>REE values of the selected pelites samples of eastern and northern sectors of Quadrilátero Ferrífero with their normalized data.</b>	Anexo 2
Tabela	3.3	<b>Trace Element Contents (ppm) of sulfide minerals.</b>	Anexo 2

## RESUMO

O *Greenstone belt* Rio das Velhas está localizado no distrito metalogenético do Quadrilátero Ferrífero, na extremidade sudeste do Cráton São Francisco, região centro-sul do estado de Minas Gerais. Sequências turbidíticas típicas de *greenstone belts* arqueanos possuem ampla abrangência regional, sendo representadas pela associação ressedimentada, dominada pela alternância de grauvacas e pelitos, e associadas a diques e *sills* metamáficos, paralelos a discordantes. O estudo da geologia e paragênese do lineamento aurífero Córrego do Sítio foi conduzido, contendo os depósitos Cachorro Bravo, Laranjeiras e Carvoaria como foco principal. Esses três importantes depósitos são descritos para ilustrar as características semelhantes, composição mineralógica e diferenças no tipo de minério ao longo do lineamento. Para o depósito de Cachorro Bravo, o mapeamento geológico inclui duas galerias subterrâneas. Diferentes tipos de veios, compostos por cristais de quartzo, tanto fumê quanto leitoso, carbonato e uma grande variedade de sulfetos e sulfossais, são reconhecidos, mas a geração mais importante volumetricamente é concordante à estrutura S<sub>1</sub>. Sulfetos e sulfossais são inter-relacionados nos veios e disseminados nas rochas encaixantes. Fontes ressedimentadas das grauvacas do setor oriental, de composições mista e félsica, gradam para rochas sedimentares pelágicas, já no setor norte, tendo rochas félsicas como fontes principais, transicionam para grauvacas da associação vulcanoclástica. Análises *in situ* de U-Pb e Lu-Hf realizadas em zircão detrítico sugerem que os eventos Rio das Velhas II e Mamona registram as principais épocas fonte de sedimento para ambos os setores. Zircões de idade proterozoica foram identificados intercalados nas sequências turbidíticas arqueanas. Variações nas análises isotópicas Lu-Hf suportam o modelo que a evolução do embasamento ocorreu envolvendo fontes crustais e mantélicas. Análises de LA-ICP-MS realizadas *in situ* em cristais de arsenopiritas, pirita e pirrotitas, nos níveis de pelitos carbonosos do lineamento Córrego do Sítio, mostram uma considerável variedade composicional dos elementos traços. Dois estágios hidrotermais são reconhecidos: Cedo hidrotermal, marcado pelo desenvolvimento de sulfetos porosos, durante o qual algum ouro foi precipitado; estágio principal-tardio, reconhecido pelo desenvolvimento de sulfetos lisos, onde ocorre o pico do ouro. A concentração dos elementos As, Co, Ni, Te, Pb e Sb nas arsenopiritas porosa e lisa, principal estágio da mineralização aurífera, possui importante implicação para a exploração de depósitos hospedados em turbiditos. A fonte mista para as rochas hospedeiras podem explicar o fato do ouro ter correlação com Se, As, Sb e Te, elementos de filiação sedimentar, assim como Co, Ni, e Pt de filiação máfica-ultramáfica. Arsênio, seguido por Ni e Co, é o elemento traço mais importante nos principais sulfetos auríferos, pirita porosa e lisa (P-Py and S-Py) e arsenopirita porosa e lisa (P-Apy and S-Apy), dos depósitos de Laranjeiras e Cachorro Bravo. Estes elementos provavelmente foram lixiviados durante a alteração hidrotermal, indicando uma fonte local para os metais e fluidos durante a mineralização aurífera.

**Palavras-chave:** Ouro orogênico, depósitos hospedados em rochas metaturbidíticas, geoquímica, geocronologia U-Pb, análises Lu-Hf, paragênese hidrotermal, associação ressedimentada, *Greenstone belt* Rio das Velhas.

## ABSTRACT

The Rio das Velhas greenstone belt is located in the Quadrilátero Ferrífero district, in the southern extremity of the São Francisco Craton, central-southern part of the State of Minas Gerais, SE Brazil. Turbidite sequences of the greenstone stratigraphy are largely distributed in region, and represent resedimented associations dominated by alternating graywackes and pelites, with parallel to discordant metamafic dikes and sills. The Córrego do Sítio lineament in the eastern sector hosts important turbidite gold deposits. On the other hand, similar rocks overlying the area of the Cuiabá-Lamego BIF-hosted gold deposits are loci only to historical diggings and occurrences, in the northern sector of the Quadrilátero region. A study of geology and rocks paragenesis has been conducted at the Córrego do Sítio auriferous lineament, focusing the Cachorro Bravo, Laranjeiras and Carvoaria turbidite-hosted gold deposits, described to illustrate the essentially similar general character of all the deposits of the eastern sector lineament, where, for the Cachorro Bravo deposit, a geological mapping included two underground mine galleries. Different vein types of veins and veinlets are recognized, but the most important volumetrically is a  $S_1$ -concordant type characterized by smoky and milky quartz-carbonate-sulfide  $\pm$  sulfosalts veins. The resedimented mixed and felsic sources of eastern greywackes grade into pelagic sedimentary rocks, while mainly felsic source of northern graywackes are transitional with the volcanoclastic association graywackes. The in situ U–Pb and Lu–Hf detrital zircon analyses suggest the Rio das Velhas II and Mamona events as main periods of sources for both sectors. Proterozoic ages are also identified as zircon sources for the turbidites sequences, intercalated with the Paleoproterozoic and Archean data. Variations in Lu–Hf isotope analyses support the idea that the evolution of the basement was made by crust-mantle mixing processes. In situ LA-ICP-MS analyses of arsenopyrites, pyrites and pyrrhotites from carbonaceous pelites on Córrego do Sítio lineament, display a considerable range of trace element compositions. Two hydrothermal stages are recognized: Early hydrothermal, marked by the development of porous sulphides, during which some gold precipitation took place; Main to late hydrothermal, recognized by the development of smooth sulphides, with gold peaking its values. The As, Co, Ni, Te, Pb and Sb concentration in porous and smooth arsenopyrite from the main stages of gold mineralization has important implications for the exploration of the deposits. The mixed source for the host rocks may explain why gold correlates to Se, As, Sb and Te of sedimentary affiliation, as well as to the mafic-ultramafic elements Co, Ni, and Pt. Arsenic is the most abundant trace element in Au-bearing porous and smooth pyrite (P-Py and S-Py) and porous and smooth arsenopyrite (P-Apy and S-Apy), of the Laranjeiras and Cachorro Bravo deposits, followed by Ni and Co. These elements were probably leached during hydrothermal alteration indicating a local metal and fluid source during gold mineralization.

**Keywords:** Orogenic gold, Metaturbidite-hosted gold deposit, geochemistry, U-Pb geochronology, Lu-Hf analyses, hydrothermal paragenesis, resedimented association, Rio das Velhas greenstone belt.

# **PARTE I – INTRODUÇÃO, CONTEXTO GEOLÓGICO, EVOLUÇÃO DO CONHECIMENTO E APRESENTAÇÃO DA TESE**

## **1 INTRODUÇÃO**

A região do Quadrilátero Ferrífero é um polígono irregular, localizado na porção centro-sul do estado de Minas Gerais, imediatamente a sul de Belo Horizonte. Em seu interior estão os complexos granito-gnáissicos arqueanos e proterozoicos, o *greenstone belt* Rio das Velhas (Arqueano), os Supergrupos Minas e Espinhaço, ambos do Proterozoico (Figs. 1.3, 2.1 e 3.1).

A produção de ouro na sequência *greenstone belt* arqueana, na região do Quadrilátero Ferrífero, é importante em nível mundial (e.g., Ribeiro-Rodrigues, 1998), sendo os depósitos hospedados em formações ferríferas bandadas (FFB), historicamente entre os mais importantes (Lobato et al., 2001). Estes autores estimaram que apenas 4% de toda a produção de ouro do Supergrupo Rio das Velhas não é relacionada à FFB e ao conjunto rochoso hidrotermal conhecido como lapa seca; essa produção de 4% advém de rochas máficas-ultramáficas, vulcanoclásticas e clásticas em geral.

O Supergrupo Rio das Velhas de idade arqueana, é historicamente dividido nos grupos Nova Lima (base) e Maquiné (topo), em rochas metamorfasadas na fácies xisto verde (e.g., Dorr, 1965, 1969; Ladeira, 1991; Baltazar e Silva, 1996; Zucchetti e Baltazar, 1998; Lobato et al., 2005; Zucchetti e Baltazar, 2000, Baltazar e Zucchetti, 2007). Para fins de facilitar a apresentação do texto, o prefixo meta é subtraído de uma forma geral dos nomes das rochas mencionadas.

A estratigrafia do Supergrupo Rio das Velhas ainda pode ser subdividida em sete associações de litofácies sedimentares, conforme proposta de Baltazar e Zucchetti (2007). Com base nestes autores, Martins et al. (2016) calculou uma espessura aproximada de 5.550 m de sedimentos clásticos, vulcanoclásticos e clasto-químicos, classificando o *greenstone belt* Rio das Velhas como predominantemente sedimentar, o que já fora apontado por Baars (1997).

O lineamento Córrego do Sítio (Ribeiro et al., 2015; Roncato et al., 2015; Lima, 2012), aqui denominado setor leste, representa uma estrutura regional de orientação NE-SW, onde ocorre uma sequência turbidítica com intercalações de grauvacas e pelitos que registram sequências de Bouma incompletas. Esta sequência localmente hospeda importantes depósitos (Figs. 2.2 e 3.1) auríferos com recursos estimados em cerca de 5,12 Moz (Sequetto-Pereira et al., 2013; Roncato et al., 2015) e uma produção média prevista em 140.000 onças por ano, explorados a céu aberto e no subterrâneo pela empresa Anglogold Ashanti Córrego do Sítio Mineração-AGABM.

A área dos depósitos auríferos Cuiabá e Lamego, com suas minas subterrâneas também exploradas pela AGABM, está localizada próxima à cidade de Sabará (Figs. 1.1, 2.1 e 3.1). Neste trabalho, essa

área é referida como setor norte.

O setor leste situa-se a aproximadamente 35 km sudoeste do município de Santa Bárbara e 120 km distante de Belo Horizonte, estado de Minas Gerais. O acesso principal ocorre pelas BR 381 e MG's 381 e 436, resultando em aproximadamente 90 km a partir da capital mineira. O acesso ao setor norte é realizado a partir de Belo Horizonte em direção à cidade de Sabará pela MG-262, distando aproximadamente trinta e cinco quilômetros (Figura 1.1).

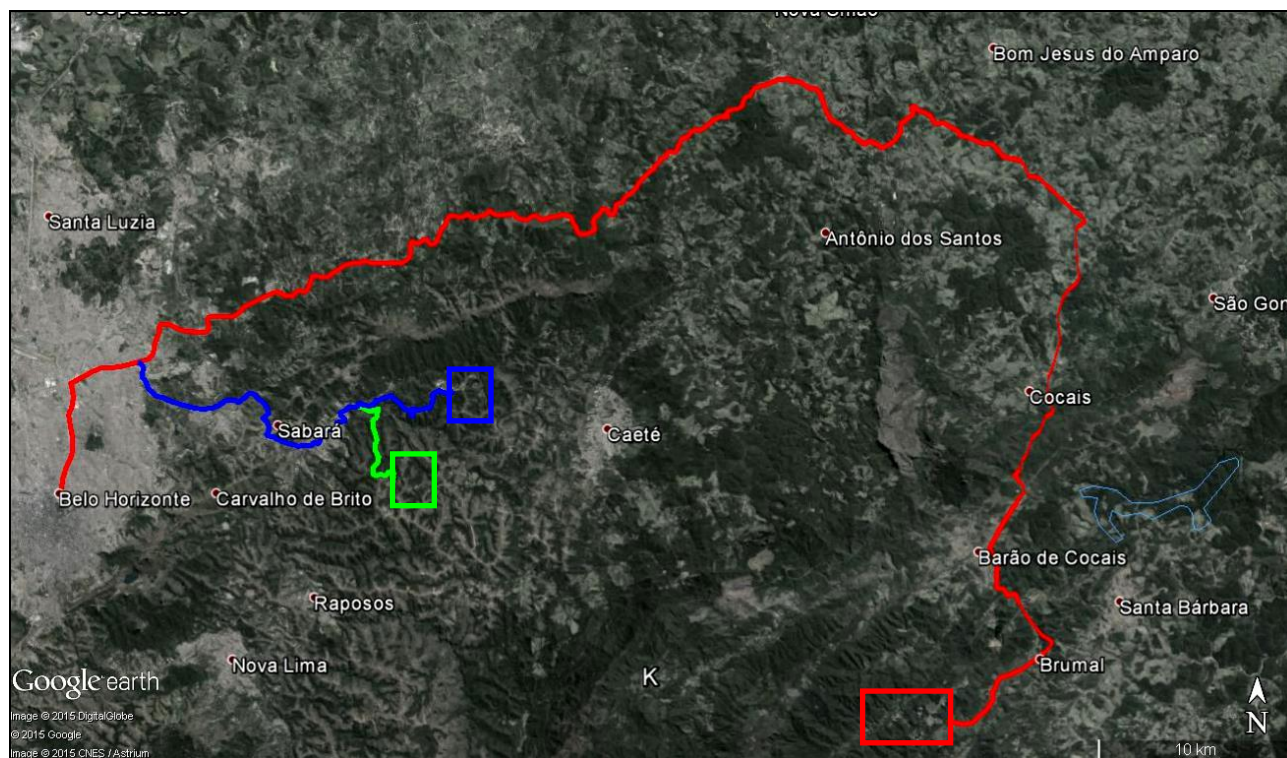


**Figura 1.1-** Mapa de localização das áreas estudadas e principais vias de acesso. Em vermelho, acesso ao setor leste (minas no lineamento Córrego do Sítio); o acesso ao setor norte é marcado pelas cores azul (Mina de Cuiabá) e verde (Mina de Lamego).

## 1.1 Objetivos

A linha condutora dessa tese de doutorado é o estudo de rochas da associação ressedimentada (Baltazar e Zucchetti, 2007) do Supergrupo - *greenstone belt* - Rio das Velhas do Quadrilátero Ferrífero, hospedeira de ouro nesse distrito mineral. Para tanto, seqüências rochosas turbidíticas foram selecionadas nos setores leste e norte (Fig. 1.1), com objetivo de construir um modelo de evolução para ambos setores, em especial no tocante às implicações para a mineralização aurífera.

No lineamento Córrego do Sítio, setor leste, foco principal deste estudo, fez-se um estudo detalhado da mineralização aurífera e paragênese mineral, associado a dados geológicos, estratigráficos,

estruturais, petrográficos, litoquímicos, geocronológicos, além de análises de ablação a *laser in situ ICP-MS* em sulfetos das jazidas Laranjeiras e Cachorro Bravo. Para o cumprimento desses objetivos, o mapeamento inicial visou esclarecer relações estratigráficas e estruturais, com foco em dois diferentes níveis da jazida Cachorro Bravo, além de um entendimento petrográfico e paragenético dos depósitos do lineamento aurífero.

Como parâmetro de comparação, no setor norte foram realizados estudos petrográficos, litoquímicos e geocronológicos nas rochas turbidíticas da associação ressedimentada. Com isso, caracterizam-se diferenças geoquímicas e isotópicas, bem como proveniência e a idade de suas diferentes áreas fonte, entre os setores leste e norte. Busca-se assim um melhor entendimento desse conjunto de rochas sedimentares arqueanas da associação ressedimentada na região do Quadrilátero Ferrífero, e seu possível impacto na exploração para depósitos auríferos, já que essa sequência clástica hospeda mineralizações no setor leste e registra ocorrências históricas no setor norte.

## **1.2 Trabalhos anteriores e evolução dos conhecimentos**

### **1.2.1 Depósitos auríferos**

Depósitos auríferos tipo *lode* são descritos por Groves e Foster (1993) como característicos do Arqueano, mais especificamente por volta de 2,65 Ga. São típicos de zonas metamórficas em orógenos compressionais. Estes depósitos foram classificados de diferentes formas ao longo da história, sendo a classificação adotada por Groves e Foster (1993) e utilizada neste trabalho, onde os depósitos são classificados pela profundidade e associados a diferentes fácies metamórficas. Groves et al. (1998) adotam o termo orogênico para depósitos auríferos em regime variando de compressional a transpressional, em profundidades que variam desde 15 km até aproximadamente 3 km sob a superfície (Poulsen et al., 2000; Goldfarb et al., 2005; Robert et al., 2005; Dubé e Gosselin, 2007; Groves e Santosh, 2015, Goldfarb e Groves, 2015).

A associação de grandes depósitos mundiais de ouro, responsáveis pela maioria da produção desse metal, vem de domínios de fácies xisto verde médio a superior, cuja transição rúptil-dúctil é característica (*e.g.*, Sibson et al., 1988). As profundidades relativas aos depósitos são classificadas como epizonal, quando rasos e (< 6 km), mesozonal (6 a 12 km) e hipozonal (> 12 km).

*Greenstone belts* com depósitos auríferos de variados potenciais são distribuídos de forma irregular por todo o mundo. Quando os depósitos são comparados através do tempo geológico, ocorre uma concentração de mineralizações conhecidas entre 2800-2550 Ma, 2100-1800 Ma e 600-50 Ma (Goldfarb et al., 2005). Torna-se evidente uma intensa mineralização aurífera no Neoarqueano, na

faixa de  $2.65 \pm 0.5$  Ga. Os depósitos mais jovens são menos comuns, pois ainda estão gradualmente sendo formados ou expostos (Goldfarb et al., 2005), não existindo depósitos gigantes mais jovens que 50 Ma (Goldfarb e Groves, 2015).

Mineralizações auríferas em ambiente orogênico são associadas comumente a zonas de cisalhamento, e são regidas por variações nos regimes de tensão regional e pela competência, e/ou, pelo contraste de competências, entre as diferentes rochas hospedeiras (Sibson et al., 1988). Esta característica pode ser facilmente notada pela intensa ocorrência de mineralizações em contatos entre rochas de diferentes reologias. Alguns depósitos podem apresentar canais preferenciais associados a zonas de cisalhamento e outras zonas planares (Sibson et al., 1988).

### **1.2.2 Mineralizações auríferas em rochas sedimentares**

Pouco conhecidos no Brasil, depósitos auríferos em rochas sedimentares arqueanas são conhecidos em orógenos paleozoicos, *e.g.* Lachlan *fold belt*, província de Vitória (Bierlein et al., 1998), Austrália; e arqueanos (*e.g.*, Quetico *metasedimentary belt*; *e.g.*, Li et al., 1998). Segundo dados da Goldo Australian (<https://www.goldo.com.au/>), o principal depósito desta província, Bendigo, ocupa o segundo lugar na produção de ouro do país. Porto (2008) e Bierlein et al. (1998, 2001) citam outros depósitos mesotermiais de ouro hospedados em rochas turbidíticas: Otago Goldfield (Nova Zelândia); Salsigne (França); Cariboo District e Meguma Terrane (Canadá); Sabie-Pilgrim's Rest Goldfield, Transval (África do Sul), Muruntau (Uzbequistão) e Clontibret (Irlanda).

Sucessões turbidíticas em sequências vulcanossedimentares tipo *greenstone* ocorrem nos crátons arqueanos Pilbara e Yilgarn (Austrália), Slave e Superior (Canadá) (Sawyer 1986, Fontaine et al., 2015, Beauchamp et al., 2015). Esses turbiditos estão seguidos localmente por vulcanismo félsico, e foram depositados anteriormente ou sincronicamente ao primeiro evento deformacional (Anhaeusser, 2014).

No cráton Slave, Canadá, as sequências sedimentares arqueanas hospedam pequenos prospectos, como os depósitos de ouro Randalls e Karnilbinia, hospedados em horizontes de FFB subordinados da formação Mount Belches (Sawyer, 1986). Turbiditos são importantes produtores de ouro, onde os depósitos do Quetico *metasedimentary belt* (Sawyer, 1986) e o depósito Roberto, de classe mundial (Fontaine et al., 2015), são exemplos. A descoberta do depósito Roberto em 2004 aumentou consideravelmente o interesse de empresas de mineração nessa província (Beauchamp et al., 2015).

No terreno granito-*greenstone* de Pilbara (Austrália), alguns dos mais importantes depósitos de ouro

aparecem nas sequências turbidíticas do grupo De Grey (idade ca 3000–2940 Ma), sendo os mais conhecidos os distritos auríferos das formações Mosquito Creek e Mallina (Huston et al., 2001). Os principais minérios associam-se com zonas de cisalhamento e contatos falhados entre unidades de rochas contrastantes. Idades modelo Pb-Pb entre  $2950\pm 5$  e  $2900\pm 10$  Ma foram obtidas para a mineralização do grupo De Grey, sugerindo dois eventos de mineralização (Huston et al., 2001). Segundo os mesmos autores, o depósito *lode gold* Withnell é o principal deste cráton, e o seu minério compreende quartzo, carbonato, sericita e feldspato com quantidades variáveis de pirita, clorita, arsenopirita, rutilo, calcopirita, galena e esfalerita. Esta paragênese é muito semelhante à das jazidas do lineamento Córrego do Sítio, setor leste.

No cráton Zimbábue, depósitos associados a turbiditos estão no grupo Shamvaim do *greenstone belt* Bindura Shamva. São parecidos em idade, composição e posição estratigráfica com os do *greenstone belt* da Província Superior do Canadá (Beauchamp et al., 2015).

As unidades litológicas supracitadas são similares às unidades que contêm a mineralização aurífera dos depósitos no lineamento Córrego do Sítio e às unidades que recobrem os depósitos Cuiabá e Lamego, nos setores leste e norte, respectivamente.

### **1.2.3 Exemplos de depósitos auríferos no *greenstone belt* Rio das Velhas**

Dentre as diferentes sete litofácies sedimentares de Baltazar e Zucchetti (2007), a associação ressedimentada é importante hospedeira de mineralização aurífera no lineamento Córrego do Sítio (Ribeiro et al., 2015, Roncato et al., 2015, Lima, 2012). Também registra ocorrências históricas na área de Cuiabá-Lamego (*e.g.*, Vial et al., 2007)

No setor leste do QF são reconhecidos lineamentos regionais NE-SW (Martins Pereira et al., 2007, Porto, 2008, Lima, 2012), contendo depósitos de ouro com recursos da ordem de 5,12 Moz (Sequetto-Pereira et al., 2013; Roncato et al., 2015). Estes representam os mais importantes depósitos de ouro hospedados em turbiditos no distrito do QF, com ou sem FFB associada. As ocorrências em turbiditos nesses lineamentos foram descobertas na década de 1980, e produziram ouro em operações a céu aberto entre 1990-2001. Em 2002, a extração subterrânea teve início, operada até o momento pela AngloGold Ashanti Córrego do Sítio Mineração (Porto, 2008, Sequetto Pereira et al., 2013). Os depósitos de ouro na sequência turbidítica do lineamento Córrego do Sítio representam os mais importantes em rochas clásticas do Arqueano do QF. São dezesseis escavações e depósitos, incluindo Cachorro Bravo, Laranjeiras e Carvoaria (Figs. 2.2, 3.1; Roncato et al., 2015). O depósito Cachorro Bravo é o mais produtivo, com teor de 7,65 g/t, seguido por Carvoaria



(6,69 g/t) e Laranjeiras (6,32 g/t), representando 25%, 18%, e 37% das reservas totais, respectivamente. O depósito São Bento hospedado em FFB está localizado no limite NE do lineamento, com uma produção histórica de 56,2 toneladas de 1986 a dezembro de 2006 (Martins Pereira et al., 2007).

O depósito aurífero *world-class* Cuiabá (e.g. Ribeiro-Rodrigues et al., 2007, Lobato et al., 2005) contém 150 toneladas de ouro (5 Moz produzido até 2015 e mais 7 Moz em recursos minerais; AGA, comunicação pessoal). O depósito de ouro orogênico Lamego (reservas aproximadas de 1,3 milhões de onças contidos em 7,26 g/t Au; Martins et al., 2016) está localizado na extremidade sudoeste da área Cuiabá-Lamego (Fig. 1.1).

Os depósitos do setor norte são hospedados em rochas das associações vulcano-química e clasto-química, com vulcânica máfica, *chert* e FFB, pelitos carbonoso e micáceo (e.g., Martins et al., 2016). No caso de Cuiabá-Lamego, rochas da associação ressedimentada recobrem toda a área dessas duas minas. Embora nenhum depósito importante de ouro tenha operado em rochas dessa associação do setor norte, uma série de escavações antigas é historicamente conhecida, como as minas Descoberto de Cuiabá e Biquinha (Vial et al., 2007). Pode-se também mencionar outras ocorrências importantes como Viana, São José, Cristais, Herberth Martins, Capão, Brumado, Enforcado e Galinha.

Outras ocorrências de ouro hospedadas em turbiditos são também descritas, incluindo Engenho de Baixo, Sobradinho, Engenho Velho e Serra do Paraíso. O lineamento estrutural Paciência ainda hospeda as ocorrências de Olhos d'água e Crista (Figs. 2.1 e 3.1).

### **1.3 Geologia da região do Quadrilátero Ferrífero**

O QF localiza-se no extremo sudeste do Cráton São Francisco (Figs. 1.2; tabela 1.1), e compreende três grandes domínios tectono-estratigráficos: terrenos granito-gnaissicos-TTG; seqüência do tipo *greenstone belt*-Supergrupo Rio das Velhas (Fig. 1.3; tabela 1.1); e seqüências supracrustais, sedimentares clásticas e químicas, englobando o Supergrupo Minas, o Grupo Sabará, o Grupo Itacolomi e o Supergrupo Espinhaço (Eschwege, 1922; Dorr, 1965, 1969; Ladeira, 1991; Baltazar e Silva, 1996; Zucchetti e Baltazar, 1998; Lobato et al., 2001, 2005; Zucchetti e Baltazar, 2000, Baltazar e Zucchetti, 2007).

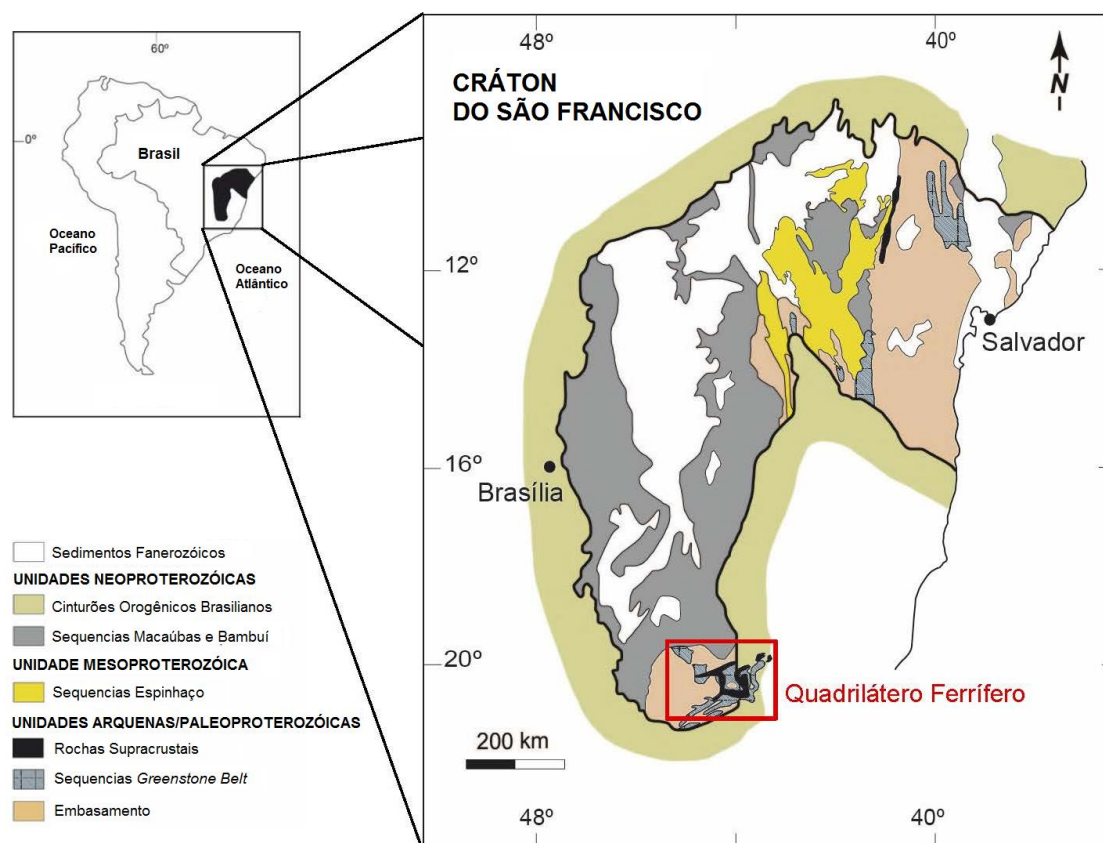


**Figura 1.2. Localização do Quadrilátero Ferrífero no extremo sul do Cráton do São Francisco. Modificado de Alkmin e Martins-Neto, 2012.**

Dorr et al. (1969) realizaram mapeamento em escala 1:25.000 da região do QF. Estes dados foram posteriormente compilados em escala 1:150.000 pelos mesmos autores, no âmbito do convênio DNPM / USGS. Recentemente, alguns trabalhos sintetizaram e apresentaram novas propostas de entendimentos sobre a região, onde um mapa de compilação foi publicado por Lobato et al. (2005).

O Supergrupo Rio das Velhas (Fig. 1.3; tabela 1.1), unidade focalizada neste trabalho, representa a sequência metavulcanossedimentar hospedeira das principais jazidas de ouro de Minas Gerais (Lobato et al., 2001; 2005).

Zucchetti e Baltazar (2000) dissertam sobre o Grupo Nova Lima, o qual é representado em sua unidade basal por um magmatismo máfico-ultramáfico (*e.g.*, Schorscher, 1982), quimicamente compatível com basaltos modernos tipo NMORB (*normal mid-ocean ridge basalt*); basaltos komatiíticos; e ultramáficas com texturas *spinifex* e cumuláticas. Rochas sedimentares químicas, espessas ocorrências de pelitos carbonosos e rochas sedimentares clásticas compõem as unidades intermediária e superior, ocorrendo de forma ampla nas áreas amostradas neste estudo.

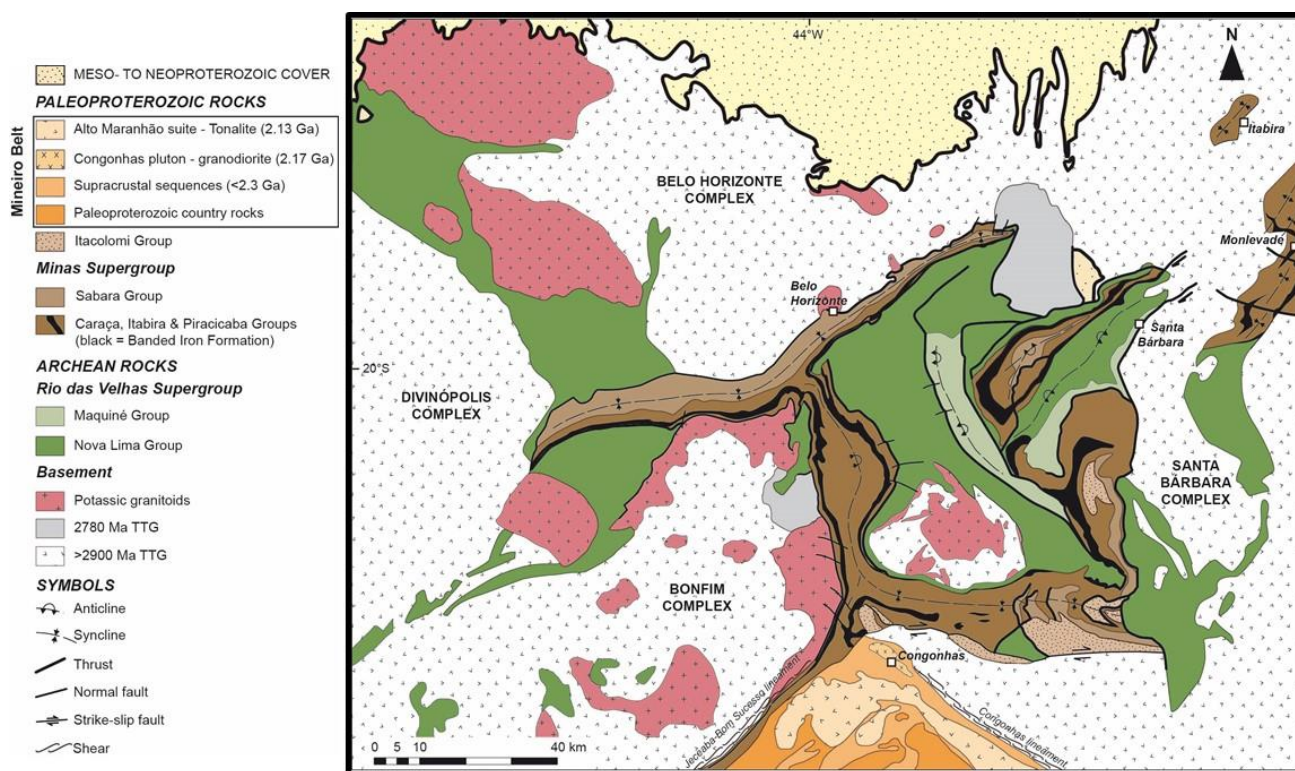


**Figura 1.1.** Mapa geológico do Quadrilátero Ferrífero. Modificado de Alkmim and Marshak (1998) e Farina (2015).

As seqüências sedimentares discutidas por Zucchetti e Baltazar (2000) registram rochas vulcanoclásticas representadas por tufos e aglomerados dacíticos, além de lavas cálcio-alcalinas. Rochas sedimentares vulcanogênicas, piroclásticas e epiclásticas possuem ocorrência restrita. Localmente ocorrem rochas sedimentares de fonte mista, representadas por pelitos, psamitos, grauvacas e raros registros de paraconglomerado, em seqüência turbidítica (Ladeira, 1991). Detalhamentos sobre a geologia regional do QF e, principalmente do Supergrupo Rio das Velhas, foco desta tese, são discriminados nos itens 2.2, 2.3, 3.2 e 3.3.

O embasamento cristalino é constituído por gnaisses de idade entre 3,0 e 2,6 Ga, retrabalhado entre 2,22 e 2,05 Ga pela orogênese Riacciana (Brito Neves, 2011). Este evento formou os domos que interceptaram as seqüências supracrustais mais recentes (Machado et al., 1989; Alkmim e Marshak, 1998). As rochas do Supergrupo Rio das Velhas são englobadas nos Grupos Nova Lima e Maquiné. O Grupo Nova Lima é composto por rochas com idade de 2,77 Ga (Tabela 1.1; Machado et al., 1989).

A seqüência paleoproterozoica é representada pelo Supergrupo Minas, composto por rochas sedimentares de plataforma, sobrepondo em contato discordante o Supergrupo Rio das Velhas

(Dorr, 1969). Os grupos Caraça, Itabira, Piracicaba e Sabará subdividem o Supergrupo Minas (Dorr, 1969; Tabela 1.1). Em discordância erosiva com o Grupo Piracicaba, o Grupo Sabará possui idade Riachiana (zircão detrítico; Machado et al., 1989) de 2,13 Ga, aproximadamente. Os sedimentos Sabará são representados por uma sequência *flysch* (graувacas, pelitos, diamictitos, conglomerados e rochas vulcânicas félsicas a intermediárias (Tabela 1.1; Dorr, 1969).

### 1.3.1 Associações de Litofácies Sedimentares

O estudo integrado das rochas vulcânicas e sedimentares do Supergrupo Rio das Velhas possibilitou o agrupamento de diversas litofácies identificadas em associações, características de ambientes de deposição típicos de terrenos *greenstone belts* por Zucchetti e Baltazar (2000).

Os autores, além de Baltazar e Zucchetti (2007), sugerem a subdivisão das rochas do Supergrupo Rio das Velhas em sete associações de litofácies, separadas pela sucessão estratigráfica e geneticamente relacionadas, conforme aqui descritas da base para o topo:

- Associação de rochas vulcânicas máficas a ultramáficas;
- Associação sedimentar vulcânica e química;
- Associação sedimentar clástica química;
- Associação vulcanoclástica com quatro litofácies (monomítica e polimítica, brechas e conglomerados, graувacas, graувacas-arenitos, graувacas-argilitos);
- Associação ressedimentada (detalhada no item 1.3.1.1) incluindo três sequências de graувacas a argilitos (na porção norte do QF as rochas predominam na fácies metamórfica xisto verde, enquanto ao sul na fácies anfíbolito);
- Associação costeira com quatro litofácies (arenitos com estratificação de média a grande escala, arenitos com *ripple-marks*, arenitos com estratificação cruzada acanalada, arenitos e siltitos);
- Associação não-marinha com litofácies de conglomerados e arenitos, arenitos de granulação grossa, arenitos de granulação fina a média.

Tabela 1.1. Coluna estratigráfica e geocronológica simplificada e modificada de Ladeira (1980), Machado et al. (1996) e Lima (2012).

Idade	Supergrupo	Grupo	Formação	Litotipos
	Espinhaço			Rochas sedimentares clásticas marinhas.
2,06 Ga		Itacolomi		Orto e protoarenitos, conglomerados. Fácies Santo Antônio: pelitos, arenito, conglomerado.
Discordância erosiva e angular profunda				
2,12 Ga		Sabará	Indiviso	Grauvacas, xistos cloríticos, pelito, rochas vulcânicas, conglomerados, arenitos e subordinadas lentes de formação ferrífera.
Discordância erosiva local				
	Supergrupo Minas		Barreiro	Pelitos e pelitos grafitosos.
			Taboões	Ortoarenitos
			Fecho do Funil	Pelito dolomítico e quartzoso, dolomitos silicosos.
		Piracicaba	Cercadinho	Arenito ferruginoso, arenito, pelitos, pelito ferruginoso, subordinadas lentes de conglomerados e dolomitos.
2,42 Ga		Itabira	Gandarela	Dolomito e subordinadas lentes de calcários, itabirito dolomítico, pelito dolomítico.
2,50 Ga			Cauê	Itabiritos quartzosos, dolomíticos e anfibolíticos; subordinadas lentes de pelitos e dolomitos.
2,66 Ga		Caraça	Batatal	Pelitos, pelito grafitoso, subordinadas lentes de chert, e FFB rica em óxidos de Fe.
			Moeda	Ortoarenitos, <i>grit</i> , conglomerados, pelitos, arenitos sericíticos, pelitos, protoarenitos.
Discordância erosiva e angular				
	Supergrupo Rio das Velhas	Maquiné	Casa Forte	Protoarenitos, conglomerado, subordinadas lentes de pelitos e subgrauvacas.
			Palmital	Pelitos, pelito quartzoso, protoarenito, grauvaca, subordinadas lentes de conglomerado na base.
2,77 Ga		Nova Lima	Sub-unidade Superior	Grauvacas e pelitos carbonosos, arenitos imaturos, quartzo pelitos e subordinadas lentes de conglomerados.
			Sub-unidade Intermediária	Pelitos carbonosos, cloríticos e tufáceos com inúmeras lentes de FFB.
2,78 Ga			Sub-unidade Inferior	Xistos verdes, basaltos espilitizados, xistos tufáceos, rochas ultramáficas.
	Quebra Ossos	Indiviso	Lavas komatiíticas e toleíticas, sedimentos clásticos, químicos, vulcânicos e vulcanoclásticos	
3,2 Ga	Complexo TTG – domos granito-gnaiss-migmatíticos			

#### 1.3.1.1 Associação de litofácies ressedimentada (Zucchetti e Baltazar, 2000)

A associação ressedimentada, detalhada neste item, possui a maior área de ocorrência dentro no *greenstone belt* Rio das Velhas, dentre todas as demais associações (Fig. 1.4), sendo representada pelas unidades mapeadas até então como: Córrego do Sítio, Mindá, Catarina Mendes, Fazenda Velha e Córrego da Paina. Esta associação será também particularizada nos itens 2.2, 2.3, 3.2 e 3.3.

A associação ressedimentada contém camadas com espessuras variando de subcentimétricas até 50 cm, gradação granodecrescente dentro de cada ciclo, com granulometria de areia grossa com grânulos, na base, até argila carbonosa, no topo, sendo os contatos bruscos entre os ciclos. As estruturas primárias são estratificação horizontal plano-paralela e cruzada tabular, de pequeno porte, sendo essas características bem expostas no setor leste da área de estudo.

Também se caracteriza por apresentar ciclicidade, gradação interna dos ciclos e contatos abruptos entre si. É interpretada como resultante de deposição por correntes de turbidez, com identificação inclusive de divisões incompletas do ciclo de Bouma (1962). Resulta de deposição por correntes de turbidez de alta e baixa densidades, sendo que os conglomerados da região sul teriam se depositado em águas profundas, podendo se originar da erosão de conglomerados depositados previamente por fluxos hiperconcentrados.

Na porção sul do QF (unidades Catarina Mendes, Córrego da Paina e Fazenda Velha), a associação ressedimentada difere das demais áreas, sendo composta essencialmente por grauvacas carbonáticas, com intercalações comuns de rochas cálcio-silicáticas e corpos expressivos de marga. São verificados, também, níveis espessos de conglomerado polimítico, com clastos estirados, em sua maioria de rochas vulcânicas ácidas.

Baltazar e Zucchetti (2007) propõem uma evolução para o *greenstone belt* Rio das Velhas, sugerindo ciclos tectono-estratigráficos em suas associações de litofácies:

(i) 2,8 – 2,78 Ba: Fase distensional com derrame de lava basáltica durante o desenvolvimento do assoalho oceânico;

(ii) 2,78 – 2,76 Ba. Início da fase de subducção. Complexos Caeté e Bonfim;

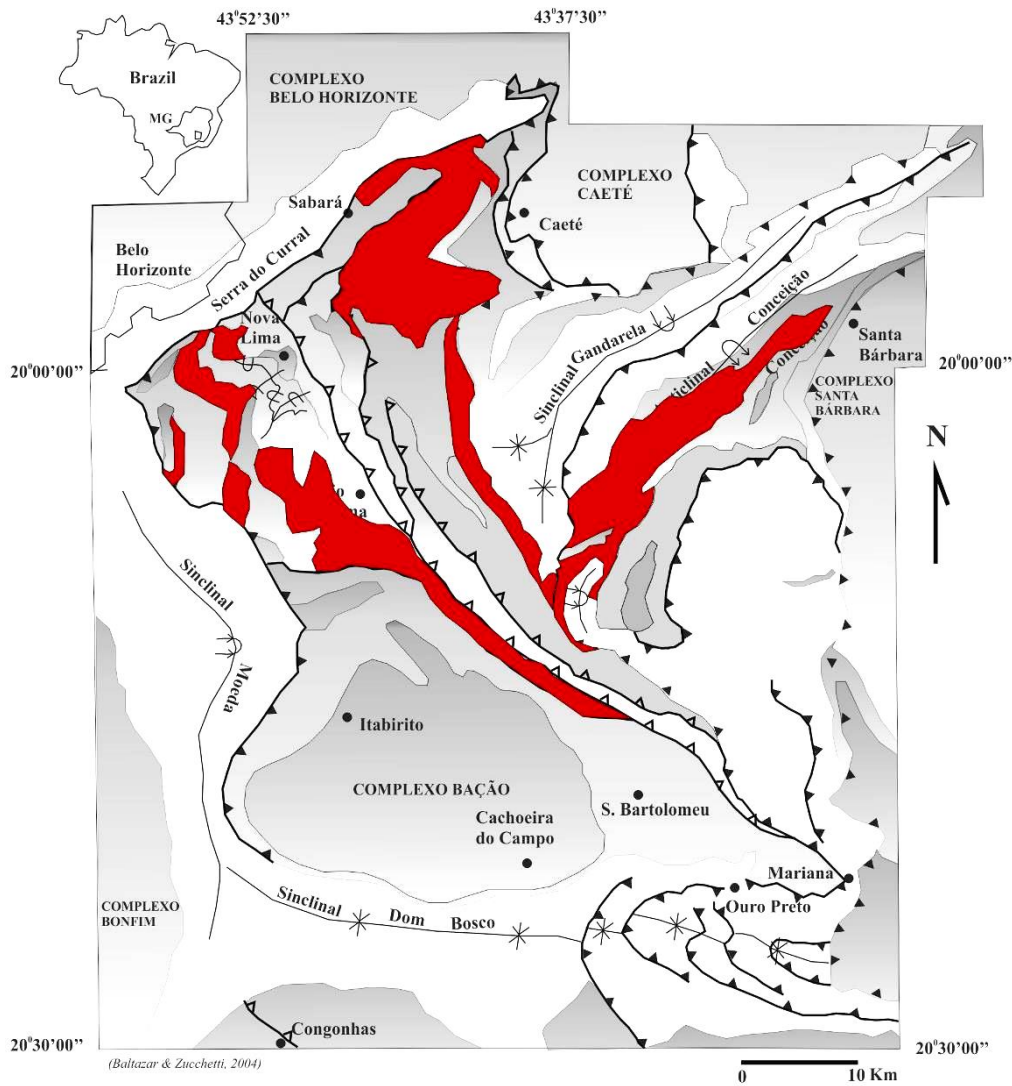


**Figura 1.4. Ocorrência da associação ressedimentada, em vermelho, na região do Quadrilátero Ferrífero, segundo Zucchetti e Baltazar (2000) e Baltazar e Zucchetti (2007).**

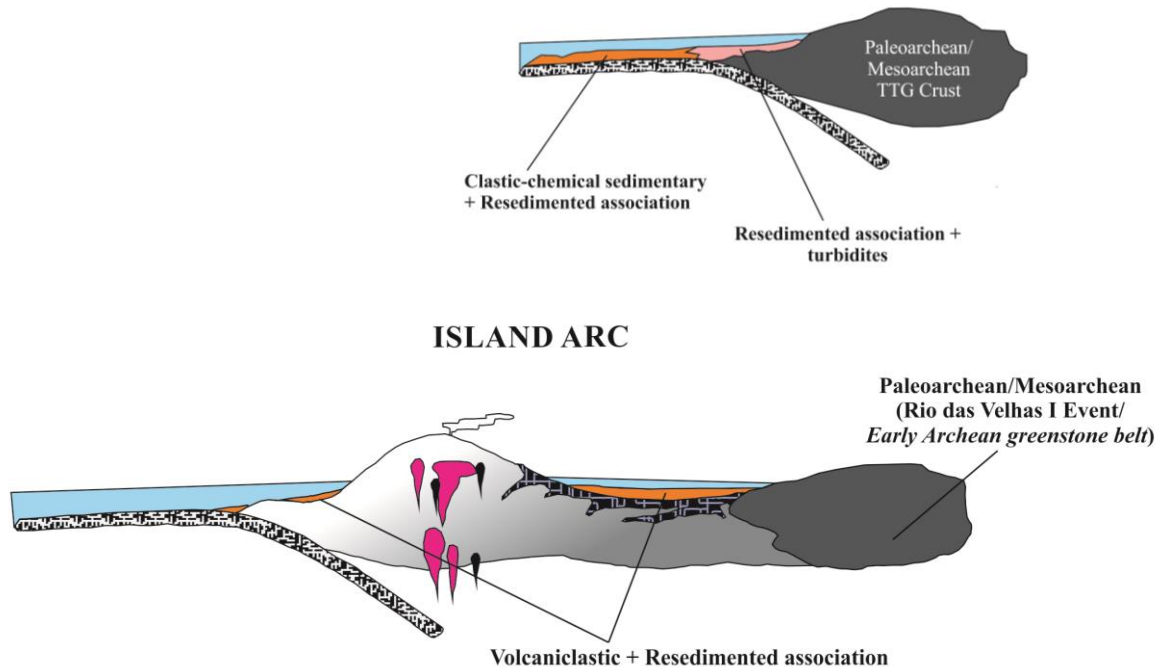
(iii) 2,76 – 2,75 Ba. Continuação da fase de subducção com vulcanismo félsico e deposição sedimentar de arenitos em margem continental estável distal e deposição de turbiditos próximos às zonas de subducção (Fig. 1.5);

(iv) 2,75 – 2,67 Ba. Fase de subducção avançada e colisão. Deposição de turbiditos em trincheiras e bacias de retro-arco. Deposição de sedimentos aluvio-fluviais em bacias de antepaís; mineralização aurífera. Posicionamento do Complexo Belo Horizonte.

(v) 2.60 – 2,67 Ba. Posicionamento dos corpos graníticos e granodioríticos em torno do QF, representando o último episódio de magmatismo no Neoarqueano;

**MAGMATIC ARC**  
*Late Archean greenstone belt*  
(Baltazar and Zucchetti, 2007)

## Córrego do Sítio lineament



## Cuiabá-Lamego area

Figura 1.5. Ambiência geotectônica dos setores leste e norte, da associação ressedimentada (Roncato et al., submetido, item 3.10 dessa tese).

### 1.3.2 Lineamento Aurífero Córrego do Sítio – Setor Leste

A porção leste do QF (Figs. 1.3, 2.1 e 3.1) caracteriza-se pelo predomínio de unidades sedimentares, principalmente clásticas, químicas e vulcanoclásticas definidas pelas unidades Santa Quitéria, Córrego do Sítio e Mindá (Zucchetti et al., 1998; Zucchetti e Baltazar, 2000) do Grupo Nova Lima, essencialmente clásticas, além das rochas TTG migmatíticas do Complexo Santa Bárbara.

O Complexo Santa Bárbara encontra-se em contato tectônico com rochas do Supergrupo Rio das Velhas e do Supergrupo Minas (Figs. 1.3, 2.1 e 3.1), sendo interpretado como uma falha de empurrão de leste para oeste, cavalgando sobre os supergrupos Rio das Velhas e Minas (Alkmim et al., 1998; Ladeira, 1991; Noce et al., 1998).



Segundo Dorr (1969), a Unidade Quebra Ossos (*e.g.* Schorscher, 1982) ocorre numa faixa de direção NE-SW no segmento leste do lineamento, em contato tectônico a leste com o Complexo Santa Bárbara e a oeste com as outras unidades mais novas do Grupo Nova Lima. Na parte, sua direção inflete para NNW-SSE e aparece em contato tectônico também com arenitos do Grupo Maquiné, Supergrupos Rio das Velhas e Minas (Figs. 1.3, 2.1 e 3.1; Tabela 1.1).

A Unidade Santa Quitéria contém pelitos carbonosos e serícíticos, associados a faixas contínuas de FFB onde situam-se as minas Pilar, São Bento e Santa Quitéria (Lima, 2012, Roncato et al., 2015). Os contatos da unidade Santa Quitéria com as outras unidades do Supergrupo Rio das Velhas são predominantemente tectônicos, por falhas de empurrão.

Regionalmente observa-se a diminuição dos níveis de FFB e um predomínio de sequências turbidíticas com pelitos e grauvas preservadas na Unidade Córrego do Sítio (Zucchetti e Baltazar, 2000), em contato transicional, que se posiciona estratigraficamente acima dessa unidade. Essa é a unidade com maior distribuição do Grupo Nova Lima em todo QF, constituída por espessa sequência turbidítica com acamamento gradacional de pelitos e grauvas (Baltazar e Zucchetti, 2007).

Nesta porção leste do QF, os supergrupos Rio das Velhas e Minas são estruturalmente controlados pelas megaestruturas denominadas Sinclinal Gandarela e Anticlinal Conceição, e são cortados pelos sistemas de falha do Fundão e da Água Quente (Dorr, 1969; Lima, 2012; Sequetto-Pereira, 2013).

Lima (2012) propôs a denominação “lineamento aurífero Córrego do Sítio” para agregar ocorrências e depósitos que no mesmo alinhamento NE-SW e possuem mineralização aurífera com características litoestratigráficas semelhantes. O lineamento aurífero engloba as escavações Sangue de Boi, Descoberta, Santana, Barra Feliz, Anomalia 1 e Santa Quitéria; no sudoeste estão as anomalias geoquímicas Saracura e Serra Redonda, além dos depósitos Cachorro Bravo, explotado a céu aberto e no subterrâneo, Laranjeiras e Carvoaria, explotados somente no subterrâneo (Figs. 2.2 e 3.1).

O lineamento proposto por (Lima, 2012) engloba as zonas de cisalhamento Córrego do Sítio, Cristina e São Bento-Donana. Estes três grandes lineamentos regionais registram as mais importantes ocorrências auríferas hospedadas em turbiditos do distrito do QF. A mineralização desta região se caracteriza por veios de quartzo-carbonato-sulfeto com ouro livre, bertierita ( $\text{FeSb}_2\text{S}_4$ ), arsenopirita ( $\text{FeAsS}$ ), estibnita ( $\text{Sb}_2\text{S}_3$ ), pirrotita ( $\text{Fe}_{1-x}\text{S}$ ), pirita ( $\text{Fe}_2\text{S}$ ), calcopirita ( $\text{CuFeS}_2$ ), esfalerita ( $\text{ZnS}$ ), além de traços de outros sulfetos e sulfossais, hospedados em sequências

de grauvacas e pelitos carbonosos (Porto, 2008; Lima, 2012; Sequetto-Pereira et al., 2015; Roncato et al., 2015; Ribeiro et al., 2015).

Lima (2012) propôs a subdivisão da Unidade Córrego do Sítio (Zucchetti e Baltazar, 1998), para suas rochas no lineamento aurífero Córrego do Sítio. São três subunidades, classificadas de oeste para leste, nomeadas Superior, Intermediária e Inferior, detalhadas no item 2.3.

Todos os litotipos do Grupo Nova Lima no setor leste são cortados obliquamente por enxames de diques e *sills* intrusivos máficos, com orientação geral NNE-SSW e mergulho para SE. São denominados por Lima (2012), sem relação cronológica, em três tipos diferentes: máfica incipientemente alterada com piroxênio relicto (MBpx); máfica com alteração clorítica e carbonática (MBcl) e máfica com alteração carbonática e muscovítica (MBcb). As subdivisões sugeridas por Lima (2012) para a unidade Córrego do Sítio e para as rochas máficas são descritas e caracterizadas no Item 3.3 desta tese. Em trabalho recente, David (2006) obteve uma idade U-Pb (SHRIMP) de  $2694 \pm 34$  Ma em zircões extraídos de rocha máfica.

### 1.3.3 Área Cuiabá-Lamego – Setor Norte

Importantes mineralizações auríferas do QF se encontram entre os municípios de Sabará, Nova Lima e Caeté, na área Cuiabá-Lamego (Figs. 1.1; 1.3). Ambos depósitos são hospedados em rochas das associações vulcano-química e clasto-química de Baltazar e Zucchetti (2007).

O depósito *world-class* Cuiabá está encaixado em sequência de rochas vulcânicas e sedimentares que compõem a base do *greenstone belt* Rio das Velhas. A estratigrafia foi definida por Vial (1980), sendo composta na base por rochas vulcânicas, de composição máfica a intermediária, envoltas por uma camada de pelito carbonoso, sobrepostas por um nível de tufos félsicos com intercalações de pelito carbonoso. Os corpos mineralizados são associados à FFB e podem ser maciços ou bandados, tendo pirita como principal sulfeto constituinte do minério, seguido de arsenopirita e pirrotita (Toledo, 1997; Vial et al., 2007).

O depósito Lamego é definido por um pacote concordante, da base para o topo, de basalto, FFB, pelito carbonoso e micáceo, hospedando intensa silicificação que ocorre tanto como massas dispersas, como na forma de veios de quartzo fumê e leitoso. O minério aurífero ocorre em corpos grosseiramente lineares, distribuídos de forma irregular, variando tanto segundo a direção como ao longo do caimento da lineação (Martins et al., 2016)

A associação ressedimentada no setor norte do *greenstone belt* Rio das Velhas ficou conhecida historicamente como unidade Morro Vermelho (Zucchetti et al., 1998; Zucchetti e Baltazar, 2000),

sendo caracterizada pelo domínio de rochas vulcânicas máficas a intermediárias, localmente com estruturas *pillow* preservadas, e com grande ocorrência de rochas sedimentares químicas e detríticas intercaladas, representadas por FFB, *chert* e pelitos carbonosos.

As rochas dessa associação, na área Cuiabá-Lamego, são piroclásticas representadas por tufo e rochas epiclásticas representadas por tufo félsicos, com composição variando de dacítica a riolítica. Os tufo estão comumente retrabalhados, observando-se o arredondamento dos grãos de quartzo e o desaparecimento de feldspatos, em relação a variedades de tufo mais proximais, passando a grauvacas com níveis de xisto carbonoso. Os tufo bandados se associam e transicionam para litofácies ressedimentadas, com estratificação gradacional cíclica, centimétrica, granodecrescente de areia a argila, com contatos bruscos entre ciclos, e preservando ainda características de sua derivação vulcanogênica. Fragmentos de derivação juvenil são restritos mostrando-se com mesma composição, porém com texturas devitrificadas (Zucchetti e Baltazar, 2000).

#### **1.4 Evolução geológica e geocronológica do Distrito Mineral Quadrilátero Ferrífero**

Dados geocronológicos foram compilados por Lana et al. (2013) a partir de diversos trabalhos na região do QF (Machado et al., 1992, Machado e Carneiro 1992; Romano, 1989; Noce et al., 1998; Romano et al., 2013; Figs. 1.6 e 1.7). Baltazar e Zucchetti (2007) já registravam estes eventos arqueanos como evento Rio das Velhas (2780-2760 Ma). De posse destes dados, Lana et al. (2013) sugerem a divisão do embasamento arqueano em dois estágios distintos:

- Entre 3220 e Ma a 2770 Ma → formação dos complexos TTG, resultando em uma crosta siálica que abrigou diversas ocorrências de *greenstone belt* (Teixeira et al., 1996; Lana et al., 2013);
- Formação de granitoides potássicos entre 2750 Ma e 2600 Ma (Lana et al., 2013; Farina et al., 2015).

##### **1.4.1 Eventos magmáticos no Cráton São Francisco**

De acordo com Lana et al., (2013; Fig. 1.7), a crosta TTG preservada consolidou-se em três fases, definidas a partir dos dados geocronológicos U-Pb nos vários complexos cristalinos do entorno do QF:

- **Evento Santa Bárbara (3220-3200 Ma)** – TTGs do Complexo Santa Bárbara, setor leste, cujas rochas são interpretadas como um núcleo paleoarqueano preservado (formado por injeções de magma juvenil TTG em uma crosta máfica-ultramáfica tipo *greenstone belt*).

- **Evento Rio das Velhas I (2930-2900 Ma)** – Edificação da maior parte do embasamento do QF, com sucessivas acreções de arcos de ilha. Presente em quase todos os complexos granito-gnáissicos.
- **Evento Rio das Velhas II (2800-2770 Ma)** – Implantação de arco magmático nas margens do bloco continental formado durante as fases anteriores. Está associada com a extrusão de lavas félsicas datadas em  $2792\pm 11$ ,  $2773\pm 7$  e  $2751\pm 9$  Ma por Noce et al. (2005; Lana et al., 2013) que, intercaladas com depósitos fluviais e turbidíticos, constituem as unidades superiores do Grupo Nova Lima no Supergrupo Rio das Velhas. Este evento representa terceira e última fase de formação de TTGs definida por Lana et al., (2013).

**Evento Mamona (2760-2680 Ma)** – Formação de granitoides potássicos que representam cerca de 30% do embasamento arqueano no QF (Romano et al., 2013). São dois pulsos de formação: entre 2760-2700 Ma em maior abundância, e em torno de 2612 Ma com poucos registros (Moreira et al., 2015; Farina et al., 2015).

As ocorrências de rochas vulcanoclásticas félsicas do Grupo Nova Lima foram datadas por Noce et al. (2005) em  $2792\pm 11$ ,  $2773\pm 7$  e  $2751\pm 9$ . Hartmann et al. (2006) analisaram pelo método U-Pb SHRIMP duas amostras de grauvacas da associação ressedimentada da Formação Palmital (Tabela 1.1). Os zircões detríticos indicaram duas populações de zircões de idade em torno de  $2953\pm 3$  e  $2759\pm 10$  Ma; o zircão mais novo foi datado em  $2749\pm 7$  Ma e indica a idade máxima de deposição da unidade. Foram também reconhecidos picos de idades em  $2774\pm 13$ ,  $2852\pm 9$  e  $2935\pm 12$  Ma, com alguns grãos isolados mais antigos entre 3050 e 3307 Ma.

## 1.5 Métodos

### 1.5.1 Trabalhos de campo

O trabalho de campo foi executado em um período de oito meses, em dias não consecutivos, totalizando aproximadamente 80 dias, entre janeiro a outubro/2012, em que foram levantados 155 pontos e 843 medidas estruturais. Os resultados do mapeamento geológico-estrutural de duas galerias do depósito Cachorro Bravo são apresentados no capítulo dois desta tese, no artigo denominado “*Metaturbidite-hosted gold deposits, Córrego do Sítio lineament, Quadrilátero Ferrífero, Brazil*”. As descrições de 20 furos de sondagem totalizaram 1600 metros. A amostragem teve apoio dos geólogos e técnicos da empresa AngloGold Ashanti Brasil Mineração e os estudos visaram rochas hospedeiras e mineralizadas em ouro nos diferentes graus de alteração hidrotermal.

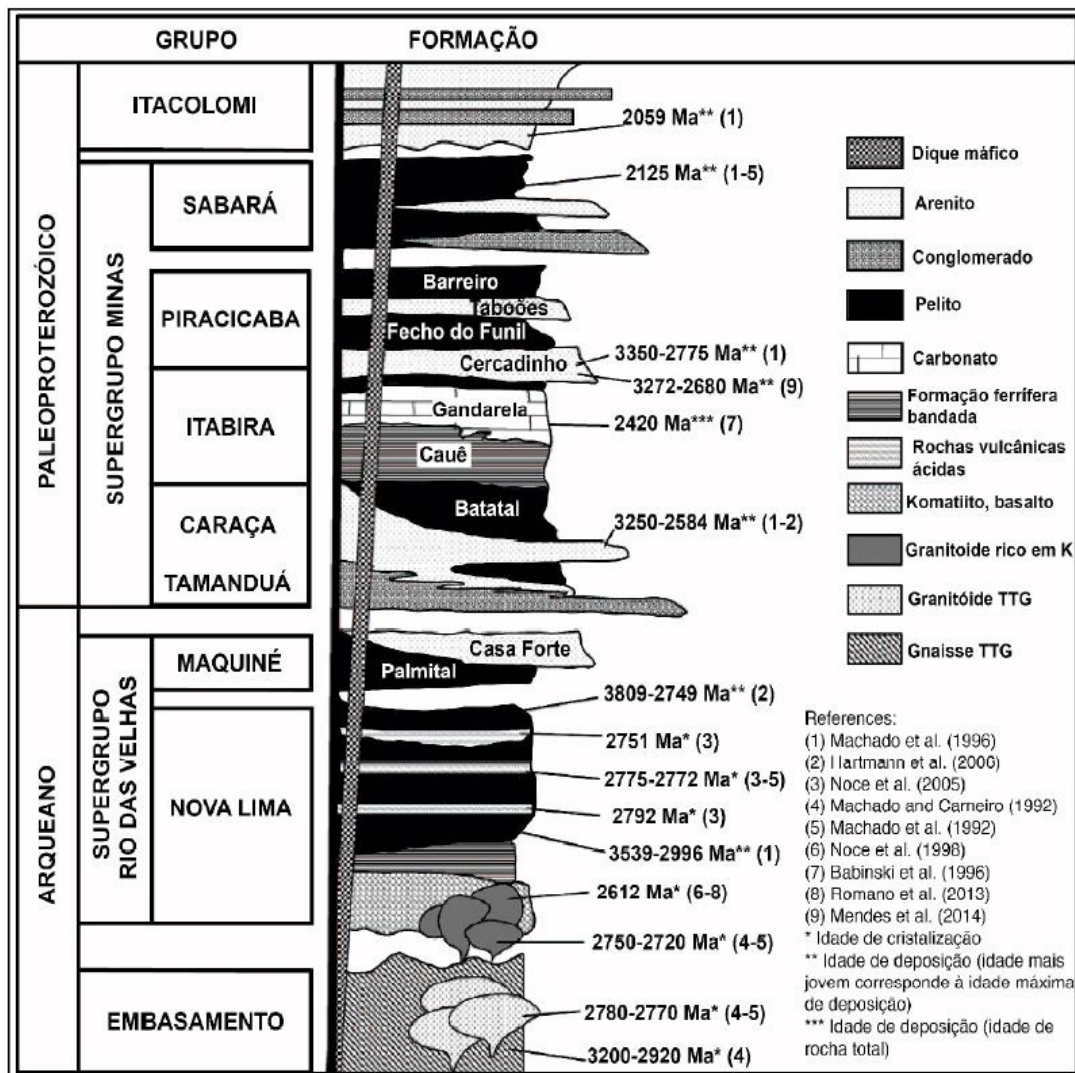


Figura 1.6 Coluna estratigráfica incluindo dados geocronológicos da região do QF (baseada em Dorr, 1969; Alkmim e Marshak, 1998; Romano et al., 2013). As referências para as idades estão indicadas na figura.

### 1.5.2 Amostragem

Realizada objetivando análises de ablação a *laser in situ* ICP-MS, geoquímicas e geocronológicas. A amostragem de rochas sedimentares foi realizada nas seguintes etapas:

- 1- Setor leste. Minério de alto teor, nos depósitos Cachorro Bravo, Laranjeiras e Carvoaria, para análises de ablação a *laser in situ* ICP-MS, de forma a realizar caracterização paragenética e geoquímica dos sulfetos;
- 2- Setores leste e norte. Coleta de amostras para análises geoquímicas de rocha, U-Pb e Lu-Hf em zircão.

As amostras foram coletadas dentro das áreas das jazidas (Anexo 1), em intervalos determinados de testemunhos de sondagem pré-selecionados, sugeridos e discutidos pela equipe das minas. As amostras selecionadas encontram-se preservadas de alteração intempérica, de forma que a assinatura geoquímica dos exemplares reflita as características primárias dessas rochas.

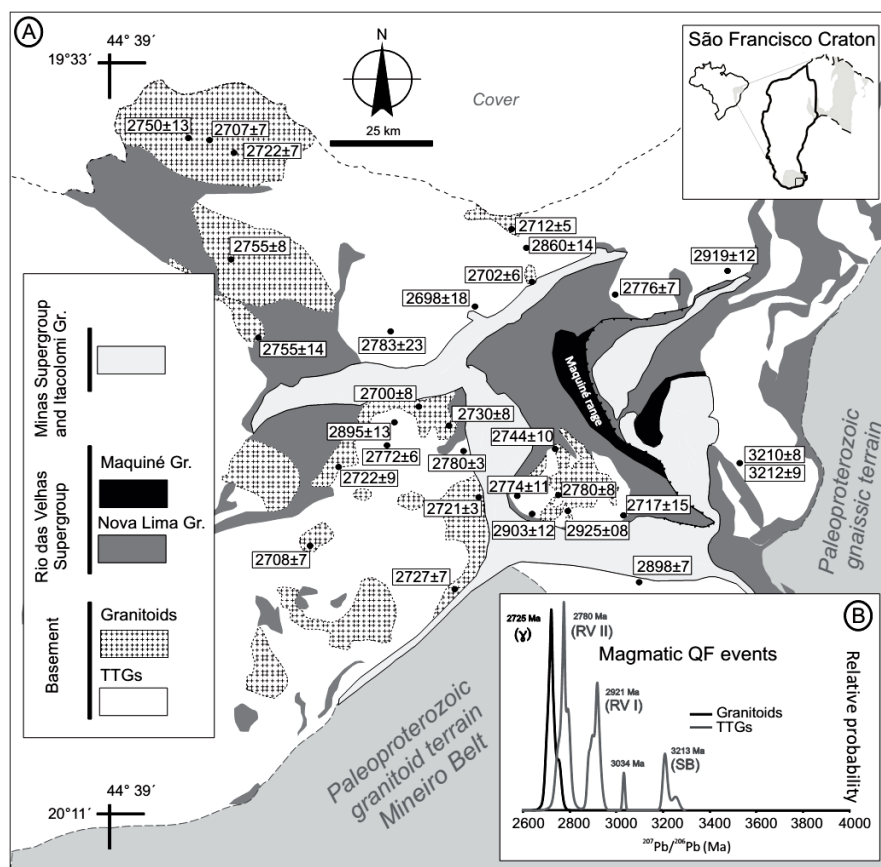
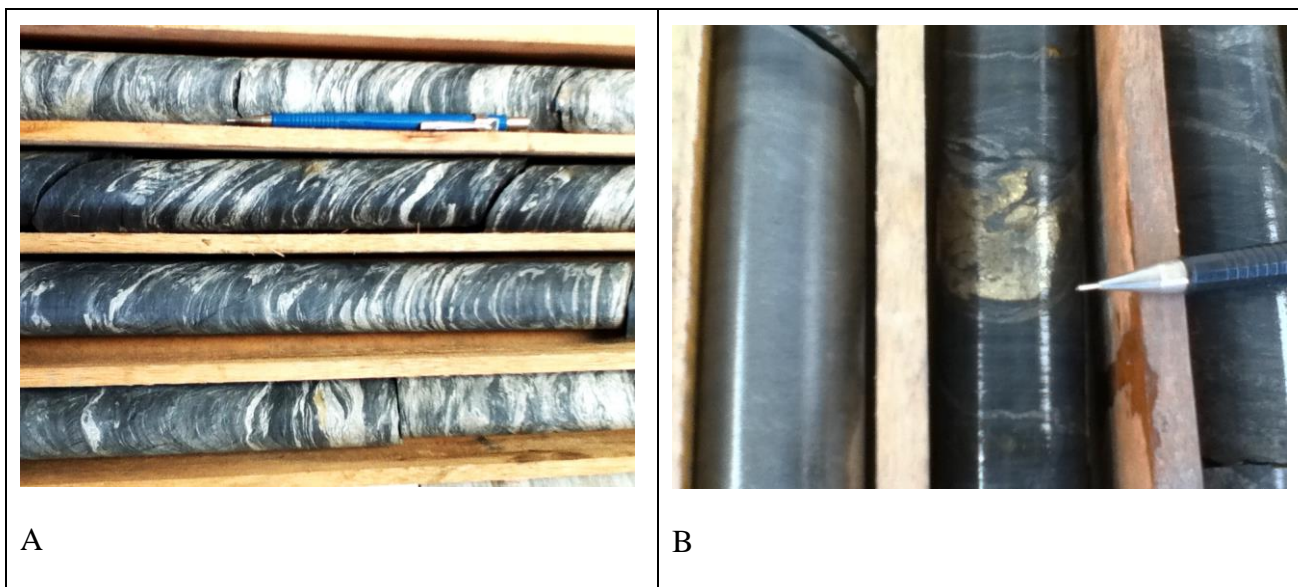


Figura 1.7. A) Mapa geológico do QF, segundo compilação de idades U-Pb publicadas por Lana et al. (2013). B) Diagrama de probabilidade que mostra os principais eventos magmáticos no cráton São Francisco: Rio das Velhas I (RV I); Rio das Velhas II (RV II), Santa Bárbara (SB) e Granitogênese ( $\gamma$ ) (retirado de Moreira et al., 2015).

#### 1.5.2.1 Análises por (*laser ablation induced coupled plasma mass spectrometry*) - Amostragem no Setor Leste

Rochas sedimentares (grauvacas e pelitos; Fig. 1.8) da subunidade Córrego do Sítio Intermediária, com alto teor de ouro, foram amostradas em testemunhos de sondagem nos depósitos Cachorro Bravo (FCS718) e Laranjeiras (FCS865, FCS910, FCS971), pertencentes à empresa AngloGold Asahnti Brasil Mineração. As descrições dessas amostras e critérios de amostragem encontram-se no artigo apresentado no Capítulo 3.



**Figura 1.8. Intervalos de testemunhos de sondagem constituídos por rocha sedimentar, Depósito Laranjeiras,**

As amostras de rochas sedimentares caracterizam-se pela intercalação entre níveis constituídos por grauvacas, pelitos e principalmente pelitos carbonosos, contendo sulfetos em veios e vênulas quartzo-carbonáticas (Fig. 1.8A). Amostras de arsenopirita, pirita e pirrotita (Fig. 1.8B) foram selecionadas em diferentes partes dos depósitos. As amostras selecionadas em testemunho de sondagem têm granulação muito fina a fina, com conteúdo variável de sulfetos e eventuais sulfossais (não analisados neste estudo).

### **1.5.3 Análises Petrográficas**

As análises petrográficas em microscópio óptico de luz transmitida e refletida e captura de fotomicrografias foram realizadas no Laboratório de Metalogenia do CPMTC/UFMG. As análises petrográficas das rochas sedimentares e metamáficas tiveram por objetivo identificar e caracterizar as diferentes fases de sulfetos existentes e suas características morfológicas, bem como toda a paragênese mineralógica, além de se fazer um levantamento da diferenciação entre as grauvacas e pelitos, permitindo, dessa forma, sua classificação mais precisa.

### **1.5.4 Análises por Microscopia Eletrônica**

#### **1.5.4.1 Imageamento e microanálises em sulfetos**

Análises de detalhe por microscópio eletrônico de varredura (MEV) foram realizadas em amostras de sulfetos de rochas sedimentares de alto teor de ouro. O microscópio eletrônico de varredura utilizado localiza-se no Centro de Microscopia da Universidade Federal de Minas Gerais, utilizando um Microscópio Eletrônico de Varredura com canhão de emissão por efeito de campo, Quanta 200 -

FEG - FEI – 2006. As condições de trabalho foram: voltagem 200 V a 30 kV; corrente do feixe >100 nA; resolução: 1.6 nm a 30 kV em alto vácuo e modo ESEM™; resolução: 3.5 nm -3 kV em baixo vácuo; distância focal: 3 - 99 mm; aumento 12x (na distância de trabalho mais longa) a 1,000,000x; detector de elétrons secundários; detector de elétrons retro espalhados; detector STEM; detector integrado sistema Pegasus: EDS e EBSD. Antes de serem levadas ao microscópio, as amostras foram recobertas por carbono, para evitar carregamento em sua superfície durante a análise.

Essas análises foram realizadas com o objetivo de observar as feições texturais, identificar poros, fraturas, vazios e inclusões, identificar as fases minerais silicáticas e carbonáticas existentes, com o auxílio de microanálises por EDS e realizar uma varredura de detalhe, de forma a procurar por fases minerais raras e não visíveis ao microscópio óptico. As imagens de elétrons retro-espalhados (*electron backscatter* – BSE) foram utilizadas para preparação das amostras para análise por ablação a *laser in situ* ICP-MS.

#### 1.5.4.2 Imageamento de zircões detríticos

O imageamento de zircões detríticos, extraídos das amostras de rochas sedimentares dos setores norte e leste, são descritos no item *Methods* do artigo “*Geochemistry and U-Pb depositional age of the resedimented association host to gold in the Rio das Velhas greenstone belt, with their sedimentary source constrained by zircon Hf isotopes and in situ LA-ICP-MS on sulfide minerals*”, apresentados no capítulo 3.

As seções embutidas contendo os zircões foram recobertas por grafite e analisadas ao MEV, a qual permite um imageamento da estrutura interna dos cristais de zircão. Esse imageamento é essencial para a identificação de inclusões, descontinuidades e zonas de sobrecrecimento, de forma a orientar, durante as análises geocronológicas (U-Pb e Lu-Hf), os pontos mais propícios para a obtenção dos dados. O imageamento dos zircões detríticos foi realizado no Laboratório de Microscopia Eletrônica do Departamento de Geologia da Universidade Federal de Ouro Preto (DEGEO/UFOP), utilizando-se um MEV JEOL 6510. As imagens encontram-se no Anexo 3.

#### **1.5.5 Geoquímica de Rocha Total**

As amostras coletadas nos setores norte e leste foram analisadas de forma a determinar sua composição geoquímica e, dessa forma, obter-se um melhor entendimento sobre os processos envolvidos em suas gêneses e deposição. Um total de vinte amostras foram analisadas para obtenção da composição em elementos maiores, traços e terras raras. São apresentados dados litoquímicos de 20 amostras (Anexo 2).



Os teores de elementos maiores, traços e terras raras foram determinados pela ACME Analytical Laboratories Ltda., em Vancouver, Canadá, via ICP-MS após fusão com metaborato / tetraborato de lítio e digestão com ácido nítrico diluído. A precisão é de 0,01% para a maioria dos óxidos de elementos maiores, de 0,1 ppb para Au e de 0,1 ppm para a maioria dos elementos traços e terras raras. Os teores de metais-base e preciosos foram determinados por digestão em Aqua Regia seguida de análise por ICP-MS. A perda ao fogo (PF ou LOI – *Lost On Ignition*) foi determinada pela diferença de peso após ignição a 1000 °C. Os diagramas litoquímicos foram confeccionados pelos programas MINPET 2.02, ioGAS e Microsoft Excel.

### 1.5.6 Análises Geocronológicas U-Pb em zircões por LA-ICP-MS

Análises geocronológicas U-Pb foram realizadas em zircões provenientes da associação ressedimentada de Zucchetti e Baltazar (2000) e Baltazar e Zucchetti (2007), nos setores leste e norte (Figs. 1.9, 1.10 e 1.11).

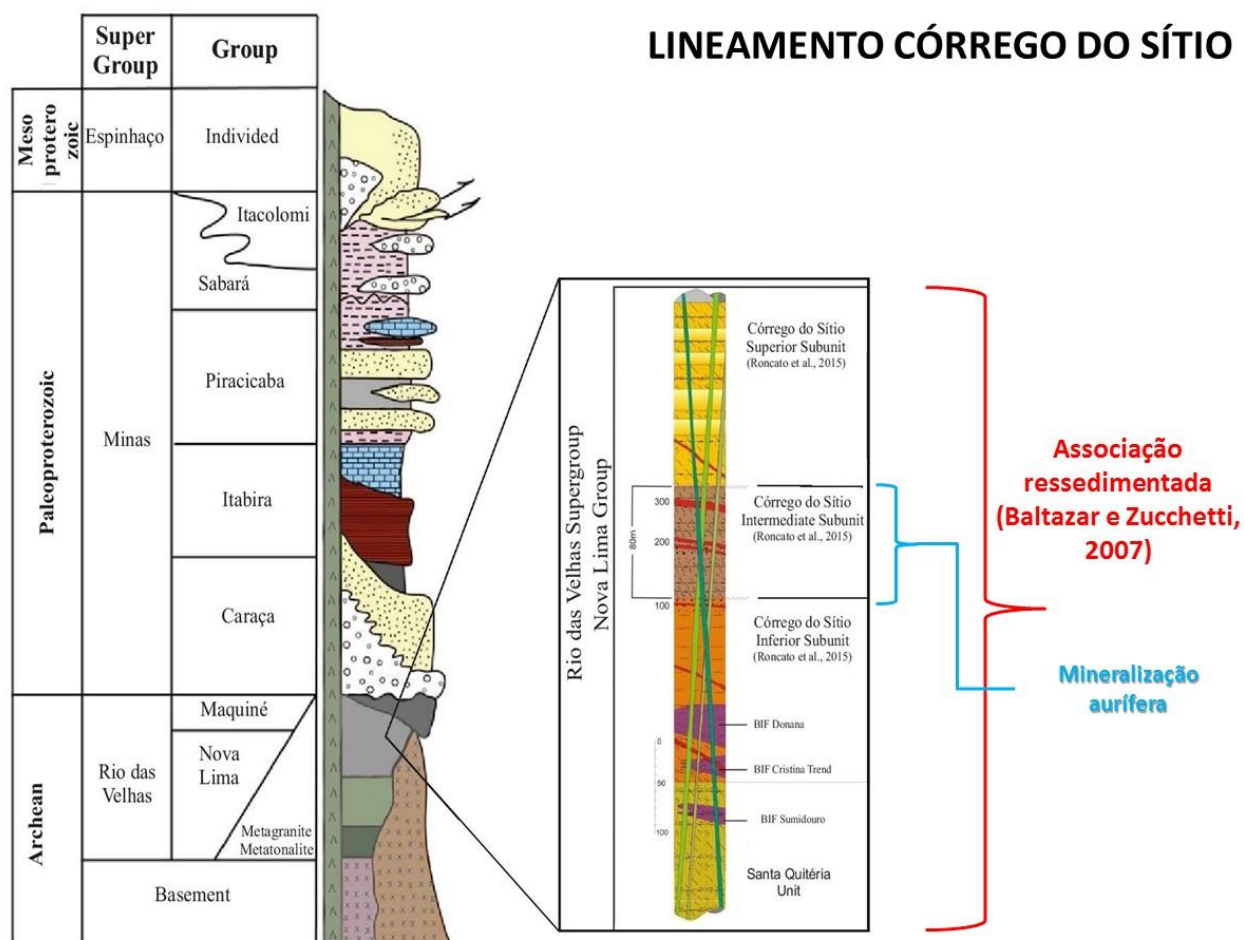


Figura 1.9. Coluna estratigráfica (Dorr, 1969) da região do Quadrilátero Ferrífero, com ênfase na associação ressedimentada do setor leste, lineamento Córrego do Sítio (modificado de Lima, 2012).

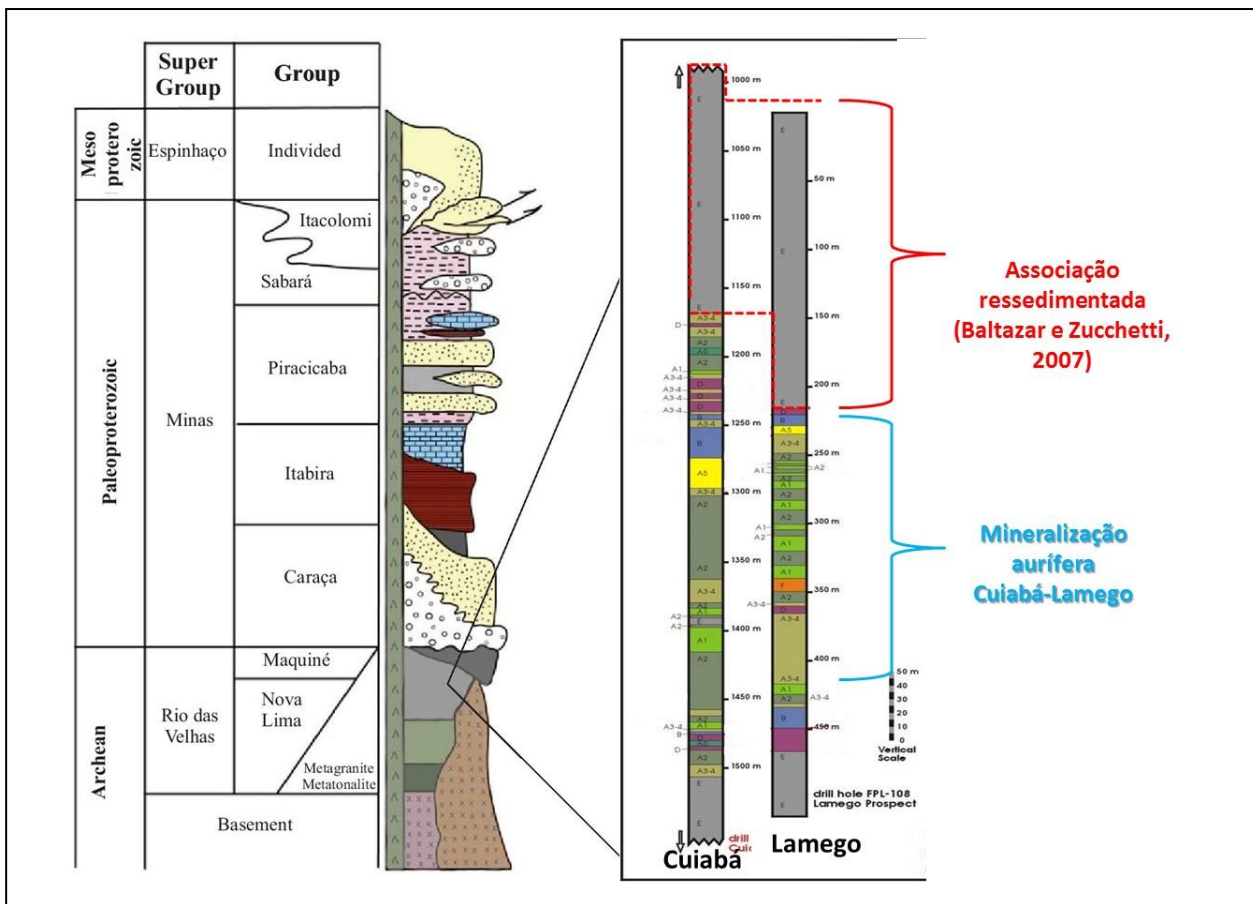


Figura 1.10. Coluna estratigráfica (Dorr, 1969) da região do Quadrilátero Ferrífero, com ênfase na associação ressedimentada do setor norte, área Cuiabá-Lamego .

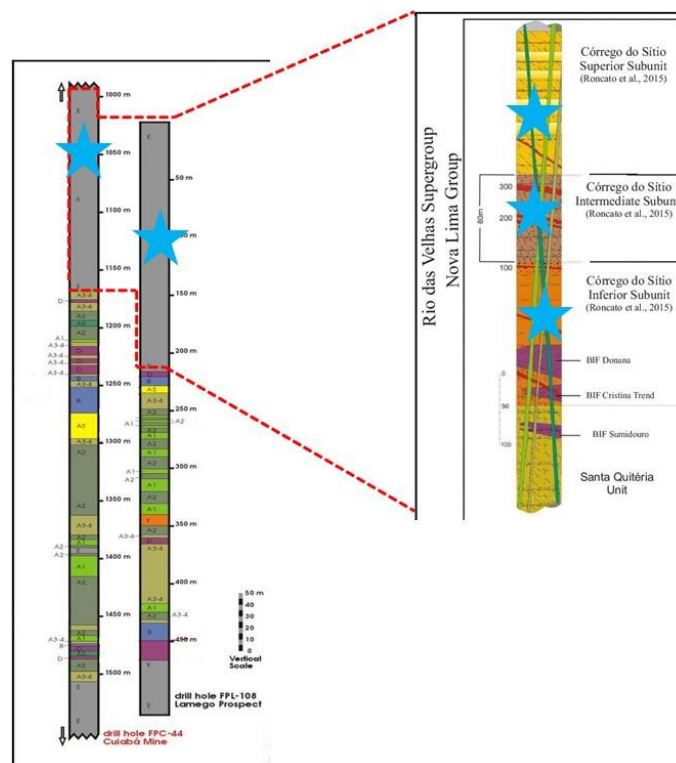


Figura 1.11. Colunas associando, nas mesmas posições estratigráficas, as posições amostradas da associação ressedimentada dos setores norte e leste.

O zircão é amplamente utilizado na geocronologia para o estudo da gênese de rochas magmáticas, metamórficas e sedimentares. Este mineral é portador de quantidades significativas de U, Th e Hf, elementos que formam sistemas isotópicos radiogênicos, e que permitem a determinação da idade de sua rocha hospedeira (Hoskin e Schaltegger, 2003). Estudos geocronológicos de zircões representam uma importante ferramenta para a compreensão dos processos de evolução crustal.

O zircão é utilizado como um geocronômetro baseado no decaimento do U e Th em Pb, sendo que os elevados tempos de meia-vida permitem a datação de rochas consideravelmente antigas no tempo geológico. O  $^{235}\text{U}$  decai para  $^{207}\text{Pb}$ , com um tempo de meia vida igual a 0,704 Ga; o  $^{238}\text{U}$  decai para  $^{206}\text{Pb}$ , apresentando um tempo de meia vida igual a 4,47 Ga; o  $^{232}\text{Th}$  decai para  $^{208}\text{Pb}$ , com um tempo de meia vida igual a 14,01 Ga (valores de Jeffrey et al., 1971, in Dickin, 2005).

As razões  $^{206}\text{Pb}/^{238}\text{U}$  e  $^{207}\text{Pb}/^{235}\text{U}$ , em um sistema fechado para a entrada de U e Pb, são plotados dentro de uma curva a qual se estende desde os tempos atuais até a idade de formação do sistema solar e da Terra, há aproximadamente 4,53 Ga, e fornecem valores concordantes de tempo  $t$ . Quando plotados em um gráfico, esses pontos definem uma curva, chamada de concórdia por Wetherill (1956a, in Dickin, 2005).

Quando essas razões são plotadas nesse diagrama, e o ponto correspondente é discordante à concórdia, indica que o zircão passou por uma perda episódica de Pb (Wetherill 1956a, in Dickin, 2005). Segundo esse autor, pontos discordantes apresentam uma tendência linear no diagrama da concórdia, sendo que o intercepto superior dessa reta com a curva da concórdia corresponde à idade de formação dos minerais ( $t_1$ ), e o intercepto inferior ( $t_2$ ) corresponde à idade de um evento termal que tenha causado a perda de Pb no mineral datado.

No caso das rochas sedimentares clásticas, análises geocronológicas de zircões detríticos representam uma importante ferramenta no estudo de proveniência dos sedimentos constituintes do protólito dessas rochas e a história deposicional das mesmas (Košler et al., 2002). Devido à sua elevada resistência aos processos físicos, os zircões detríticos ‘sobrevivem’ à múltiplos ciclos sedimentares (Košler et al., 2002). Para que um estudo de proveniência sedimentar seja bem embasado, com relação às várias áreas fontes que podem fornecer os sedimentos detríticos para uma bacia sedimentar, é necessária a utilização de um elevado número de zircões (ca. de 80 a 100 grãos, Košler et al., 2002).

A utilização da técnica analítica de ablação a laser, associada a um espectrômetro de massas com plasma indutivamente acoplado (LA-ICP-MS), constitui importante ferramenta para a geocronologia. O feixe de laser de alta potência é focado em uma área diminuta da amostra, resultando na ablação de uma pequena quantidade dessa amostra. O material vaporizado gerado é

transportado por gases carreadores (Ar ou He) até o equipamento de ICP-MS para a quantificação isotópica (Jackson et al., 2004). Esse método permite a datação de cristais individuais e de diferentes zoneamentos presentes no mesmo cristal, fornecendo as idades de diferentes zonas de crescimento em um mineral individual (Fedó et al., 2003).

Essa técnica apresenta várias vantagens, principalmente pelo seu baixo custo e por ser um método rápido para obtenção de dados, uma vez que o feixe incide diretamente em um ponto escolhido do cristal (Jackson et al., 2004). Dessa forma, o LA-ICP-MS representa importante ferramenta não somente para a determinação da idade de cristalização de uma rocha e identificação de eventos subsequentes que resultaram em um zoneamento em sua estrutura, mas também para o estudo de proveniência de sedimentos clásticos, uma vez que permite rápida análise do grande número de zircões requeridos para gerar informações de grande confiabilidade.

As amostras das grauvacas e pelitos foram preparadas e analisadas no LOPAG (Laboratório de Geocronologia e Geoquímica), na Universidade Federal de Ouro Preto (DEGEO/UFOP). A metodologia de preparação das amostras iniciais até a montagem dos embutimentos com os zircões e os parâmetros analíticos utilizados para a obtenção dos dados encontram-se no artigo, apresentados no capítulo 3.

### **1.5.7 Análises de Isótopos Radioativos Lu/Hf em zircões por LA-ICP-MS**

Além da determinação da idade de cristalização de uma rocha através da análise U-Pb em zircões, estudos isotópicos no sistema Lu-Hf fornecem informações complementares acerca da origem e evolução desse zircão, e conseqüentemente, da diferenciação ocorrida desde a formação do magma que gerou sua rocha hospedeira. Sendo assim, o sistema isotópico Lu-Hf é utilizado no estudo da diferenciação da crosta silicática (BSE – *Bulk Silicate Earth*), que levou à formação do sistema crosta-manto (Matteini et al., 2010). Como supracitado, o zircão apresenta quantidades significativas de Hf, com concentrações no nível de porcentagem (0,5-2,0 % Hf<sub>2</sub>O; Hoskin e Schaltegger 2002), e acomoda ainda os produtos do decaimento radioativo desse elemento (Kinny e Mass, 2002). O Lu também apresenta uma afinidade ao zircão, além de outros minerais portadores de ETR (Kinny e Mass, 2002).

O <sup>176</sup>Lu é um radionuclídeo instável que apresenta decaimento espontâneo para o isótopo estável <sup>176</sup>Hf, com emissão β<sup>-</sup> e meia-vida de aproximadamente 35 milhões de anos (Kinny e Mass, 2002). As variações na abundância do <sup>176</sup>Hf são expressas em relação ao <sup>177</sup>Hf, o qual apresenta concentração constante no sistema. Dessa forma, a equação máfica para o cálculo da idade pelo método Lu-Hf, para um sistema fechado, define-se como:

$$({}^{176}\text{Hf}/{}^{177}\text{Hf})_t = ({}^{176}\text{Hf}/{}^{177}\text{Hf})_{\text{inicial}} + ({}^{176}\text{Lu}/{}^{177}\text{Hf})_t * (e^{\lambda t} - 1),$$

Onde:

t = tempo decorrido desde o fechamento do sistema;

$\lambda$  = constante de decaimento do  ${}^{176}\text{Lu}$

O método se baseia na premissa de que a Terra apresentava, na sua origem, uma razão Lu/Hf inicial semelhante ao condrito. Esse reservatório inicial é referido como CHUR (*Chondritic Uniform Reservoir*), o qual foi modificado progressivamente com o tempo como resultado de fusão parcial do manto superior. Ao gerar magmas basálticos, resultou em depleção do manto residual em Hf em relação ao Lu, uma vez que o último é mais compatível do que o Hf. Consequentemente, durante um evento de geração de crosta juvenil, essa torna-se relativamente mais enriquecida em Hf, enquanto o manto residual torna-se depletado nesse elemento e enriquecido em Lu. Com o passar do tempo, a razão isotópica Lu/Hf do manto depletado em Hf torna-se maior do que a composição condritica ( $\text{Lu}/\text{Hf}_{\text{manto}} > \text{Lu}/\text{Hf}_{\text{CHUR}}$ ), enquanto que a crosta enriquecida em Hf resulta em uma razão Lu/Hf menor do que a do reservatório condritico ( $\text{Lu}/\text{Hf}_{\text{crosta}} < \text{Lu}/\text{Hf}_{\text{CHUR}}$ ). O manto residual não fracionado teria razão Lu/Hf igual à do condrito (Kinny e Mass 2002).

Em um tempo t, o desvio da composição isotópica em relação ao condrito é dada por:

$$\varepsilon_{\text{Hf}} = [ ({}^{176}\text{Hf}/{}^{177}\text{Hf})_t / ({}^{176}\text{Hf}/{}^{177}\text{Hf})_{\text{condritos}} - 1 ] \times 10^4,$$

sendo que o fator  $\varepsilon_{\text{Hf}}$  constitui um indicativo da fonte magmática formadora da rocha. Amostras que têm razão  ${}^{176}\text{Hf}/{}^{177}\text{Hf}$  maior do que o condrito em um tempo t apresentam valores positivos de  $\varepsilon_{\text{Hf}}$ , enquanto que amostras com  ${}^{176}\text{Hf}/{}^{177}\text{Hf}$  menor do que o condrito têm  $\varepsilon_{\text{Hf}}$  negativo. O condrito, por sua vez, apresenta  $\varepsilon_{\text{Hf}} = 0$ .

A idade modelo, a qual corresponde ao tempo decorrido desde a separação do magma da fonte mantélica, é dada por:

$$\text{Hf } T_{\text{DM}} = 1/\lambda \times \ln \{ ({}^{176}\text{Hf}/{}^{177}\text{Hf})_{\text{amostra}} - ({}^{176}\text{Hf}/{}^{177}\text{Hf})_{\text{DM}} / ({}^{176}\text{Lu}/{}^{177}\text{Hf})_{\text{amostra}} - ({}^{176}\text{Lu}/{}^{177}\text{Hf})_{\text{DM}} + 1 \}.$$

A idade TDM para um zircão é calculada a partir de sua composição inicial em Hf, usando uma média crustal da razão Lu/Hf, a qual representa o valor  ${}^{176}\text{Hf}/{}^{177}\text{Hf}$  calculado no momento em que o zircão cristalizou, sendo esse correspondente à idade U-Pb obtida no mesmo cristal. A idade modelo indica o tempo de residência crustal para a rocha hospedeira do zircão (Matteini et al. 2010).

Conforme assinalado por Matteini et al. (2010), é fundamental realizar as medições das razões isotópicas de Lu-Hf nas mesmas regiões dos cristais de zircão onde foram realizadas as medições das razões U-Pb, de forma a calcular valores de  $\varepsilon_{\text{Hf}}$  e  $\text{Hf}_{\text{TDM}}$  no momento da cristalização desse zircão. Sendo assim, a técnica LA-ICP-MS torna-se essencial para a realização de análises isotópicas no sistema Lu-Hf em diferentes zonas de intercrescimento em um mesmo grão, e em

porções próximas àquelas analisadas para o sistema isotópico U-Pb. Dessa forma, torna-se possível integrar as informações de idades de diferentes regiões de um mesmo cristal com os valores de  $\epsilon_{\text{Hf}}$  e  $\text{Hf}_{\text{TDM}}$  correspondentes.

#### 1.5.7.1 Procedimentos analíticos

As medições no sistema isotópico Lu-Hf em zircões foram realizadas no LOPAG (Laboratório de Geocronologia e Geoquímica), na Universidade Federal de Ouro Preto (DEGEO/UFOP) em um MC-ICP-MS Thermo-Finnigan Neptune acoplado a um sistema a laser Photon-Machines 193 nm. Os dados foram coletados no modo estático durante 60 s de ablação, com um feixe de diâmetro igual à 40  $\mu\text{m}$ . Os pontos foram amostrados com uma taxa de repetição igual a 8 Hz.

Nitrogênio foi introduzido ao gás argônio (carregador da amostra) por meio de um sistema de nebulização Aridus. A intensidade típica do sinal foi cerca de 10 V para o  $^{180}\text{Hf}$ . Os isótopos  $^{172}\text{Yb}$ ,  $^{173}\text{Yb}$  e  $^{175}\text{Lu}$  foram monitorados simultaneamente durante cada etapa analítica de forma a corrigir interferências isobáricas dos isótopos Lu e Yb na massa 176. Os isótopos  $^{176}\text{Yb}$  e  $^{176}\text{Lu}$  foram calculados utilizando-se a razão  $^{176}\text{Yb}/^{173}\text{Yb}$  igual a 0,796218 (Chu et al., 2002). O fracionamento instrumental de massa para as razões isotópicas de Hf foi corrigido por uma razão  $^{179}\text{Hf}/^{177}\text{Hf}$  igual a 0,7325 (Patchett e Tatsumoto 1980a). A acurácia e reprodutibilidade foram verificadas pelas análises dos zircões GJ-1 ( $^{176}\text{Hf}/^{177}\text{Hf}$  de  $0,282015 \pm 0,000019$ ; Jackson et al., 2004), Plešovice ( $^{176}\text{Hf}/^{177}\text{Hf}$   $0,282483 \pm 0,000017$ ; Sláma et al., 2008), Temora ( $^{176}\text{Hf}/^{177}\text{Hf}$   $0,282683 \pm 0,000019$ ; Black et al., 2003; Wu et al., 2006). Os parâmetros analíticos utilizados para a obtenção dos dados encontram-se no artigo apresentados no capítulo 3.

## 1.6 **Apresentação da Tese**

Esta tese está estruturada nas Partes I, II, III e IV. A Parte I é composta pelos capítulos introdutórios, onde são apresentados localização, os objetivos do trabalho, trabalhos anteriores e revisão do conhecimento, evolução e geologia regional e dos setores amostrados e os métodos utilizados.

A Parte II apresenta os resultados dos estudos estratigráficos, petrográficos e paragenéticos, além de mapeamento geológico do depósito Cachorro Bravo; realizados no setor leste do QF, lineamento Córrego do Sítio. Estes resultados são apresentados na forma de um artigo revisado após a publicação no Brazilian Journal of Geology (Roncato et al., 2015).

A Parte III compara a associação ressedimentada nos setores leste e norte, isto é, lineamento Córrego do Sítio e área Cuiabá-Lamego, apresentando análises litoquímicas, geocronológicas e de

ablação a *laser in situ ICP-MS* em sulfetos (exclusivas para o lineamento Córrego do Sítio), resultando em um modelo para a associação ressedimentada no âmbito da evolução arqueana do QF. Os dados são apresentados na forma de artigo já submetido ao periódico Precambrian Research. Na Parte IV da tese são apresentadas as considerações finais do trabalho, além das referências bibliográficas utilizadas e dos anexos, onde se encontram as tabelas com os resultados das análises geoquímicas e isotópicas.

## **PARTE II – GEOLOGIA DOS DEPÓSITOS AURÍFEROS NO LINEAMENTO CÓRREGO DO SÍTIO**

### **2 METATURBIDITE-HOSTED GOLD DEPOSITS, CÓRREGO DO SÍTIO LINEAMENT, QUADRILÁTERO FERRÍFERO, BRAZIL**

Jorge Geraldo Roncato Júnior<sup>1</sup>, Lydia Maria Lobato<sup>1</sup>, Luiz Claudio Lima<sup>2</sup>,

Cecília Germano Porto<sup>1</sup>, Rosaline Cristina Figueiredo e Silva<sup>1</sup>

<sup>1</sup>Department of Geology, Instituto de Geociências, Universidade Federal de Minas Gerais, Belo Horizonte (MG), Brazil.

*E-mail:* roncatojr@yahoo.com.br; lobato@netuno.lcc.ufmg.br; cericita@yahoo.com.br; rosalinecris@yahoo.com.br

<sup>2</sup>Luna Gold, Mineração Aurizona S.A., Godofredo Viana (MA), Brazil. E-mail: luiz.lima@lunagold.com

**Submetido em:** 09/11/2014. **Aceito em:** 21/01/2015. **Publicado em:** 03/2015

*Artigo publicado no Brazilian Journal of Geology*

**ABSTRACT:** A study of the geology and rock paragenesis has been conducted at the Córrego do Sítio auriferous lineament, containing the Cachorro Bravo, Laranjeiras and Carvoaria metaturbidite-hosted lode-gold deposits located in the Quadrilátero Ferrífero Region, Minas Gerais, Brazil. These representative deposits are described to illustrate the essentially similar general character of all the deposits of the lineament as well as the wide compositional and mineralogical differences in the ore of the different deposits, where for the Cachorro Bravo deposit a geological mapping included two underground mine galleries. The Córrego do Sítio unit is a metamorphosed turbidite in an alternating sequence of metagraywackes and phyllites, with parallel to discordant metamafic dikes and sills. The ore zone is predominantly hosted at the stratigraphic break between metasedimentary and metamafic rocks. Four deformation events affected the mine sequence. Mineralized veins and veinlets are considered to have formed within a brittle-ductile shear-zone environment and occurred in multiple episodes. Different vein types are recognized, but the most important volumetrically is a S<sub>1</sub>-concordant type characterized by smoky and milky quartz-carbonate-sulfide ± sulfosalts veins. Veins are dominated by quartz, but locally they are characterized by carbonate and a large variety of sulfide and sulfosalt minerals. Pyrite is the most common associated sulfide mineral, followed by arsenopyrite and pyrrhotite. An extensive mineralogical study of polished sections has confirmed different generations of sulfide minerals. The sulfides and sulfosalt minerals are interrelated in the veins and disseminated in the wall rocks. The data are consistent with a genetic models similar to other Archean greenstone belt, lode-gold deposits.

**KEYWORDS:** lode-gold deposits; orogenic gold; metasedimentary-hosted rocks.



**RESUMO:** *O estudo da geologia e paragênese do lineamento aurífero Córrego do Sítio foi conduzido, contendo os depósitos Cachorro Bravo, Laranjeiras e Carvoaria. Esses depósitos auríferos, do tipo lode, hospedados em sequência metaturbidítica, ocorrem na região do Quadrilátero Ferrífero, Minas Gerais, Brasil. Esses três importantes depósitos são descritos para ilustrar as características semelhantes, composição mineralógica e diferenças no tipo de minério ao longo desse lineamento. Para o depósito de Cachorro Bravo, o mapeamento geológico inclui duas galerias subterrâneas. A unidade Córrego do Sítio é composta por uma sequência turbidítica com alternância de grauvacas e filitos, associada a diques e sills metamáficos, paralelos a discordantes. A zona de minério é predominantemente relacionada ao intervalo estratigráfico localizado entre as rochas metassedimentares e as rochas metamáficas. Quatro eventos deformacionais afetaram a sequência estratigráfica do lineamento. Veios e venulações mineralizados formaram-se em vários episódios em ambiente de cisalhamento dúctil-rúptil. Diferentes tipos de veios são reconhecidos, mas a geração mais importante volumetricamente é concordante à estrutura S<sub>1</sub>. Os veios são compostos por cristais de quartzo, tanto fumê quanto leitoso, carbonato e uma grande variedade de sulfetos e sulfossais. A pirita é o sulfeto mais comum seguido por arsenopirita e pirrotita, confirmados por detalhamento mineralógico em seções polidas. Sulfetos e sulfossais são inter-relacionados nos veios e disseminados nas rochas encaixantes. Os dados apresentados são consistentes com modelos genéticos relacionados a outros depósitos lode-gold arqueanos.*

**PALAVRAS-CHAVE:** *ouro orogênico, depósito tipo lode-gold; depósito aurífero em turbidito.*

## 2.1 Introduction

The gold production in the Archean greenstone-hosted deposits of the Quadrilátero Ferrífero mining district, Brazil, is important worldwide (Ribeiro-Rodrigues 1998), with banded iron formations being the one of the most important host to gold mineralization (Lobato et al., 2001). These authors estimated that only 4% of all the gold production of the Rio das Velhas greenstone belt are hosted in rock types other than banded iron formation (BIF) and in the hydrothermal products generically referred to as *lapa seca*; these 4% encompass ultramafic, mafic, volcanoclastic, and clastic rocks in general.

In the focus area, a deformed sequence of schistose sediments of the Nova Lima Group (Fig. 2.1), Rio das Velhas greenstone belt, crops out in a series of NE-SW regional lineaments that host gold mineralization and are known as Córrego do Sítio, Cristina and São Bento-Donana shear zones, respectively from the SE to NW (Fig. 2.2; Lima, 2012). They contain gold deposits with resources of approximately 5.12 Moz (Sequetto-Pereira et al., 2013). The Córrego do Sítio shear zone, named Córrego do Sítio structural lineament (Lima, 2012), hosts the Cachorro Bravo, Laranjeiras and Carvoaria deposits, the most important in this area.

The main rock units comprise a repetitive succession of metamorphosed, carbonaceous turbiditic, graywacke-siltstone-shale and slates, which host lode-gold mineralization associated with quartz-carbonate-sulfide-sulfosalt veins (Lima, 2012, Ribeiro et al., 2013). As in other Archean greenstone-belt-hosted gold deposits, those at Córrego do Sítio are at the greenschist metamorphic facies (*e.g.* Condie 1981, Groves et al., 1998). A series of mafic dikes and sills have been emplaced and may have had an important control for the gold mineralization and sulfide paragenesis (*e.g.* Canale 1999, Porto, 2008, Lima, 2012, Sequetto-Pereira et al., 2013, Ribeiro et al., 2013).

This present study contributes for the unpublished existing data of the Córrego do Sítio gold deposits, describing the stratigraphic and structural aspects, as well as the petrographic

characteristics, particularly the hydrothermal alteration evolution and sulfide paragenesis. We also focus on the geology of the 200-211 orebody of the Cachorro Bravo deposit, the most important gold producer of the Córrego do Sítio lineament, where 1:100 scale geological mapping was undertaken.

## **2.2 Regional geological setting**

The Quadrilátero Ferrífero district (Figs. 1.2 e 2.1) is situated in the southern portion of the São Francisco craton (Almeida 1976) and is composed of the Archean Rio das Velhas greenstone belt (Schorscher et al. 1982), the paleoproterozoic Minas Supergroup and the Itacolomi Group. These supracrustal units are surrounded by granite-gneiss domes (Dorr 1969), which consist of poly-deformed unit. The regional basement metamorphic complexes crop out in several distinct domes and with metamorphic grades ranging from greenschist to granulite facies (Herz 1970).

The Rio das Velhas rocks comprise seven lithofacies associations (Fig. 2.1), according to Baltazar & Silva (1998a, 1998b), Zucchetti & Baltazar (2000), Lobato et al. (2005) and Baltazar & Zucchetti (2007), and these are, from base to top:

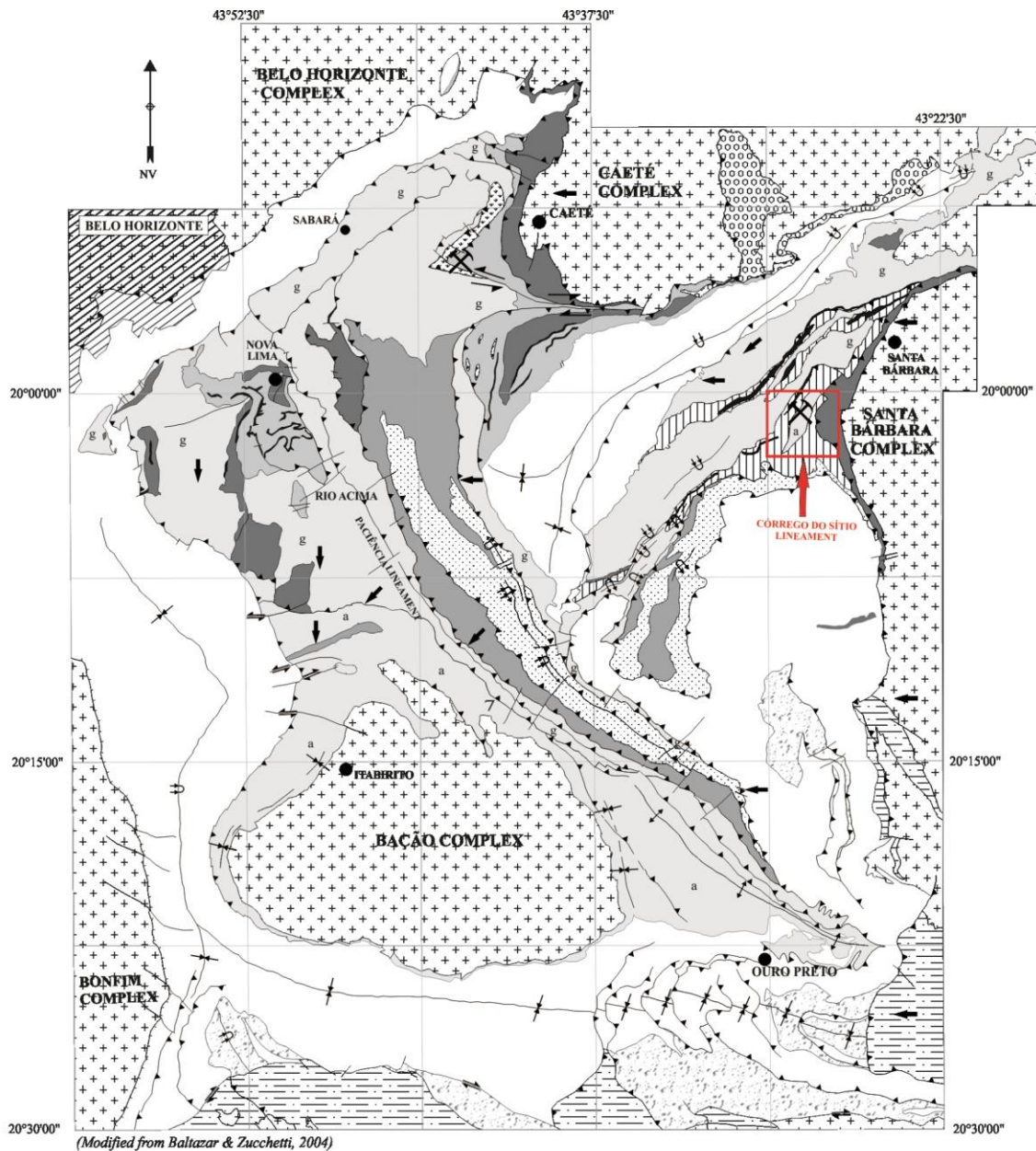
(1) Mafic-ultramafic: lavas with minor intrusions of gabbro, anorthosite and peridotite, as well as intercalations of BIF, ferruginous chert, carbonaceous pelite, turbidites, and rare felsic volcanoclastic rocks. It corresponds to the Quebra Ossos Group and Ouro Fino unit of the Nova Lima Group.

(2) Volcano-chemical-sedimentary: tholeiites intercalated with BIF and ferruginous chert and less fine-grained clastic sedimentary rocks, such as carbonaceous turbidites and pelites, intercalated with chemical sedimentary rocks.

(3) Clastic-chemical sedimentary: typified by alternating fine-grained, clastic and chemical rocks. Pelites (micaceous and chloritic schists) are intercalated with lesser BIF, subordinate chert and carbonaceous phyllites. It corresponds to the Santa Quitéria unit in the study area.

(4) Volcaniclastic: made up of volcaniclastic felsic and mafic rocks.

- (5) Resedimented: widely distributed in the Quadrilátero Ferrífero, it includes three different sequences of graywacke-argillite, two metamorphosed in the greenschist facies in the N and E sectors (they are composed mainly of graywackes, quartz graywackes, sandstones and siltstones, with cyclic layers and abrupt basal contacts between cycles) and one in the amphibolite facies in the south. In the E and N sectors, it includes the Córrego do Sítio unit outcropping in the study area.
- (6) Coastal: restricted to a small area, with sandstones exhibiting preserved sedimentary structures.
- (7) Non-marine: conglomerate-sandstone; coarse-grained sandstone, fine- to medium-grained sandstone; it includes the Casa Forte Formation of the Maquiné Group (Dorr et al., 1957).



**LEGEND**

<ul style="list-style-type: none"> <li> Espinhaço Supergroup</li> <li> Itacolomi Group</li> <li> Minas Supergroup</li> <li><b>RIO DAS VELHAS SUPERGROUP (2,78 ~ 2,66 Ga)</b></li> <li><b>MAQUINÉ GROUP</b></li> <li> Non-marine Association (Casa Forte Formation)</li> <li> Resedimented Association (Palmital Formation)</li> </ul>	<p><b>NOVA LIMA GROUP</b></p> <ul style="list-style-type: none"> <li> Resedimented Association</li> <li> Volcaniclastic Association</li> <li> Clastic-chemical Sedimentary Association (r/BIF)</li> <li> Volcano-chemical Sedimentary Association (r/BIF)</li> <li> Mafic-ultramafic Volcanic Association</li> <li> Undivided Rio das Velhas Supergroup</li> <li> Granite gneiss complex</li> </ul>	<ul style="list-style-type: none"> <li>Amphibolite facies (a)</li> <li>Greenschist facies (s)</li> <li> Gold deposit</li> <li> D1 thrust fault</li> <li> D2 thrust fault</li> <li> D4 thrust fault</li> <li> Normal fault</li> <li> Syncline, anticline</li> <li> Inverted syncline and anticline</li> <li> Tectonic transport direction</li> <li> Capital, town</li> </ul>
---	---	---

0 5 000 10 000 m

Figura 2.1. Geological map of the Quadrilátero Ferrífero region showing the study area in the Rio das Velhas Supergroup in detail (modified from Baltazar & Zucchetti 2007).

### 2.3 Local Geology

The term Córrego do Sítio auriferous structural lineament was initially proposed by Lima (2012) to include all gold occurrences that encompass those of the Córrego do Sítio, Cristina and São Bento-Donana shear zones (Fig. 2.2; Lima, 2012), since they all have the same NE-SW direction and mineralization in similar lithostratigraphic hosts. In its SW extension (Fig. 2.2), the Córrego do Sítio lineament comprises the Carvoaria, Laranjeiras, Cachorro Bravo, Cristina, Rosalino and Grota Funda deposits.

Porto (2008) and Lima (2012) consider the Córrego do Sítio lineament as a package of metasedimentary rocks consisting of alternating graywackes and phyllites in a turbidite sequence with incomplete Bouma cycles (Bouma 1983), metamorphosed to the greenschist facies. Metamafic dikes and sills are subparallel to discordant.

The Córrego do Sítio unit (Baltazar & Silva 1998b) is widely distributed in many parts of the Quadrilátero Ferrífero and includes sequences of graywacke and argillite. Graywackes, quartz graywackes, sandstones and siltstones display cyclic layers and abrupt basal contacts between cycles. The features of this association indicate that it was deposited by turbidity currents (Lima, 2012), and this unit is considered part of the re-sedimented association.

The contacts between the metasedimentary units are abrupt, oblique and marked by the development of hydrothermal alteration zones containing carbonate, sericite, quartz and sulfide minerals.

From E to W, Lima (2012) mapped the Córrego do Sítio unit based on the relative proportion of the different rock types and proposed an informal stratigraphic subdivision (Fig. 2.3):

- Lower subunit: thick carbonaceous phyllite and graywacke sequence. It contains subordinate metric-decimetric BIF layers, some of which are magnetic and intercalated with carbonaceous phyllites (Figs. 2.4A, 2.4B, and 2.4C).

- Intermediate subunit: carbonaceous phyllite with an anastomosing schistosity hosting millimetric to metric quartz-carbonate veins and microfolded layers, transposed locally in axial plans of asymmetric folds. This is where the auriferous mineralization is concentrated, with sulfide and sulfosalts in quartz-carbonate veins, representing an important zone of hydrothermal alteration. The upper and lower contacts are sharp.
- Upper subunit: intercalation of a thick graywacke sequence and subordinate carbonaceous phyllite in incomplete Bouma cycles. Bedding exhibits upward grain-size fining in normal and inverted sequence.

Metamafic dikes and sills have a NNE-SSW direction, dipping to the SE. Metamafic rocks with chlorite and muscovite alteration (MBcl) are epidote-rich dolerites (Fig. 2.4D, Table 2.1). Quartz-bearing, schistose chlorite-carbonate dominated metamafic rocks (MBcb) are the most hydrothermally altered; these are locally hydrothermally altered bearing gold (Fig. 2.4E, Table 2.1). The incipiently altered metamafic rocks (MBpx) (Fig. 2.4F, Table 2.1) represent a fine-grained dolerite with relict pyroxene, amphibole and plagioclase.

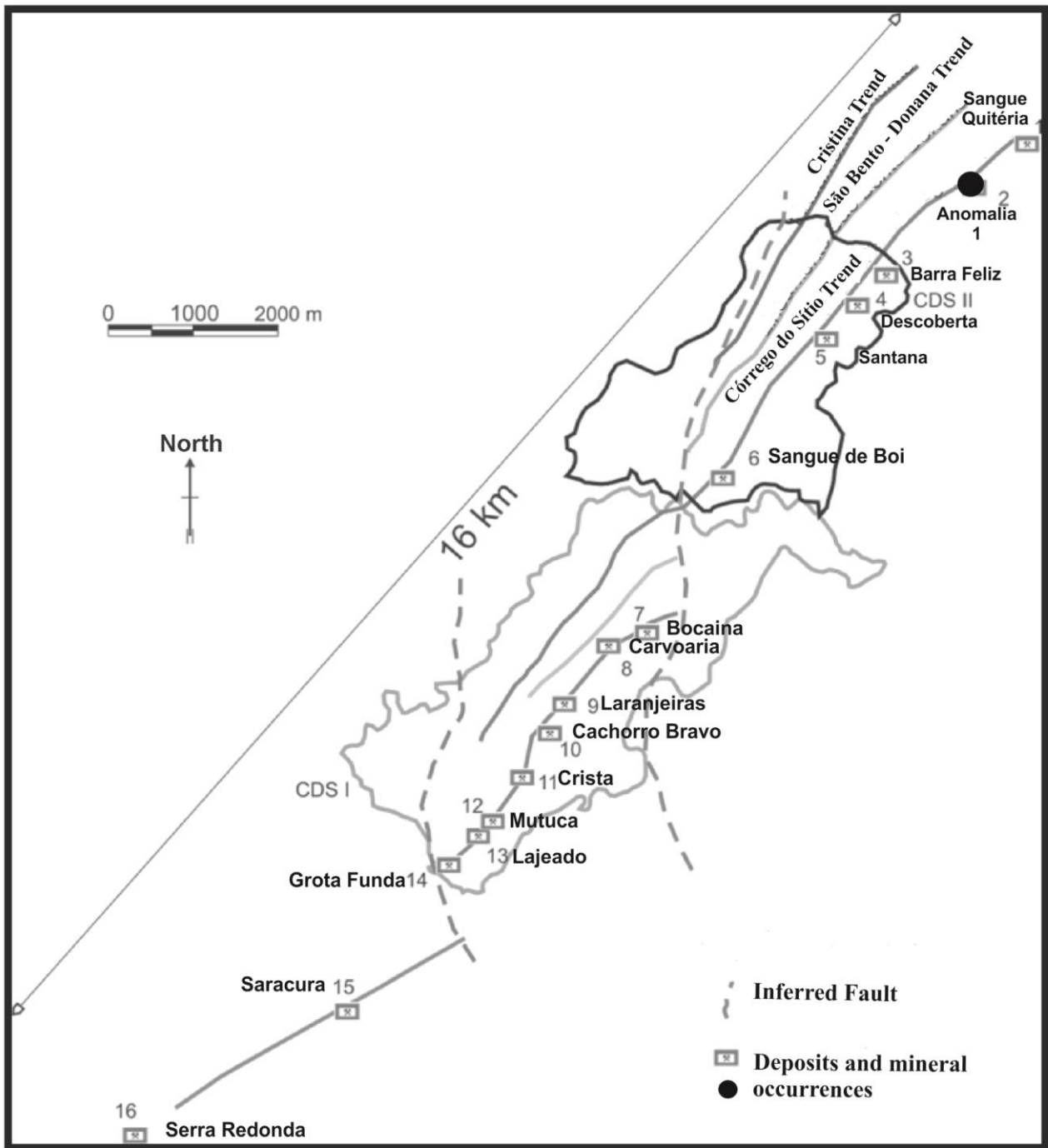


Figura 2.2. The NE-SW 16-km long Córrego do Sítio auriferous lineament, displaying the Cristina, São Bento-Donana and Córrego do Sítio structural trends (modified from Lima, 2012).



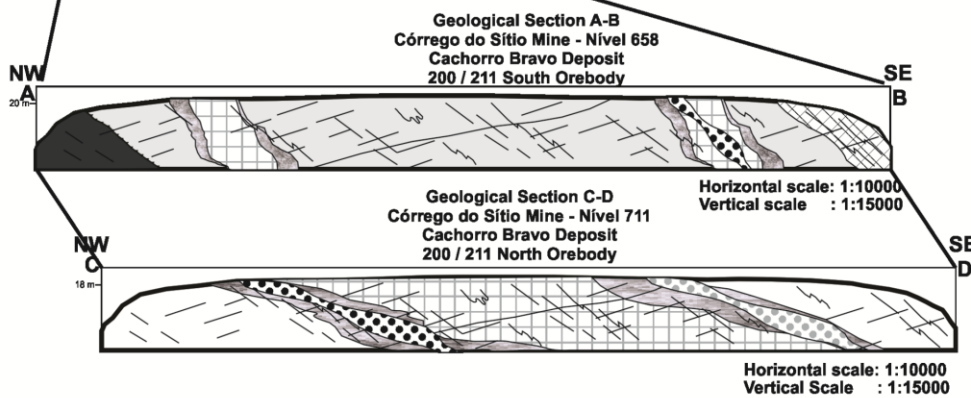
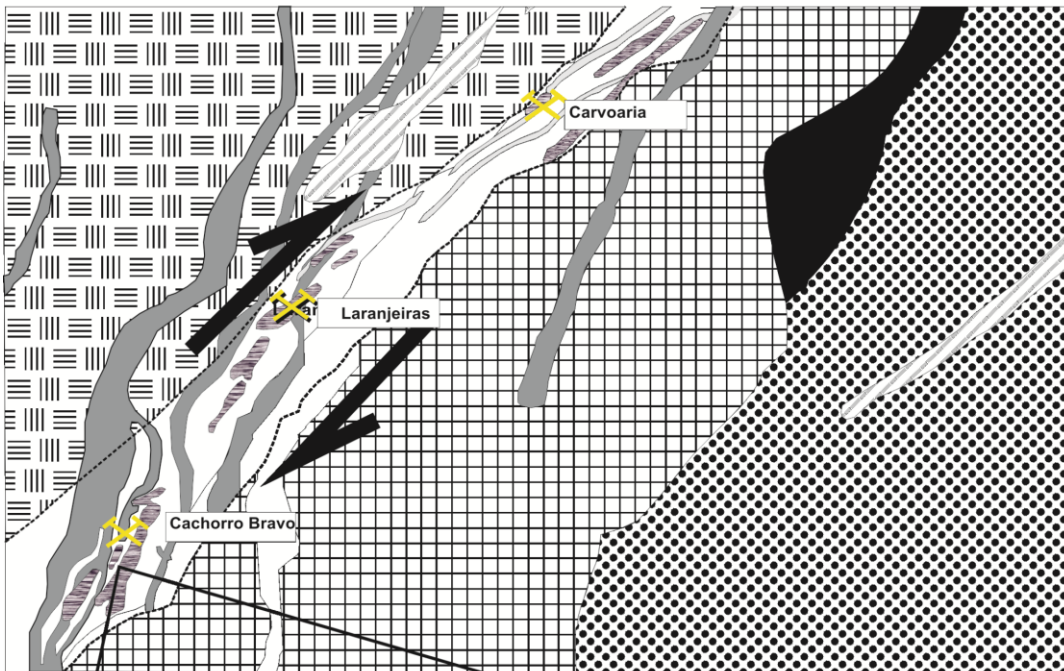
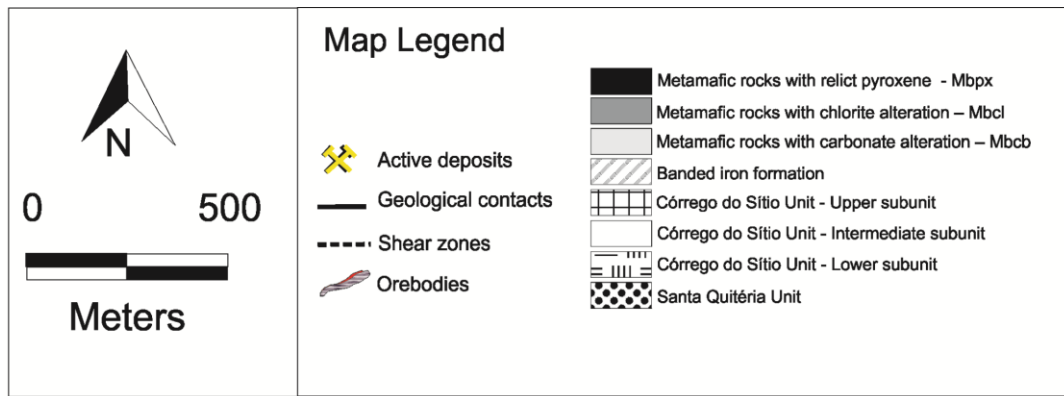
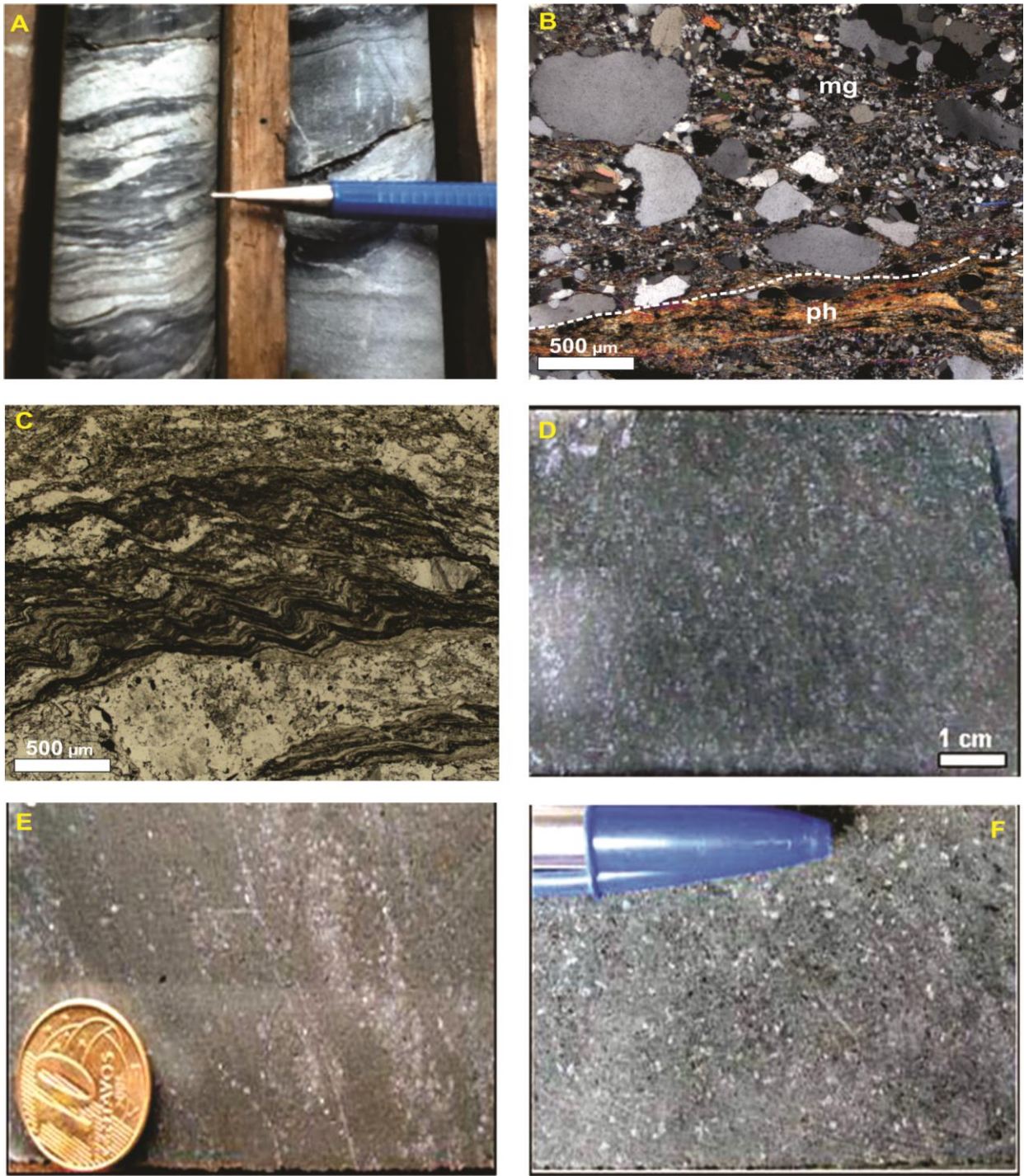


Figura 2.3. Geological map of the Córrego do Sítio Lineament, central portion (modified from Sequetto-Pereira et al. 2014)



**Figura 2.4. Rhythmic alternation of graded phyllites (ph) and metagraywackes (mg). (A) Macroscopic. (B) Microscopic transmitted light (TL). (C) Photomicrograph of carbonaceous phyllite, TL. Metamafic dikes and sills: (D) Metamafic dikes and sills incipiently alteration.**

**Tabela 2.1. Micro and macroscopic aspects of the Córrego do Sítio lineament metamafic rocks (modified from Lima, 2012)**

Geologic unit	Thickness (m)	Mineralogy	Macroscopic characteristics of rocks			
		Essential	Accessories	Center	Intermediate	Border
MBpx <sup>1</sup> - incipiently altered metamafic rocks with relict pyroxene (Fig. 4D)	60 to 100	Pyroxene Amphibole Biotite Plagioclase Chlorite Quartz Titanite Muscovite Carbonate	Magnetite Ilmenite Pyrite Pyrrhotite Chalcopyrite Sphalerite Apatite	Dark green Medium to coarse-grained Preserved ophitic to subophitic igneous texture Chlorite orientation in cleavage Rare quartz and carbonate veinlets	Light to dark green Medium to coarse-grained Chlorite, biotite and muscovite aligned along cleavage Stockwork with millimeter quartz-carbonate veinlets	Light to dark green Medium to coarse-grained Chlorite, biotite and muscovite aligned along cleavage Dense stockwork with centimetric to millimetric quartz-carbonate veinlets
MBcl <sup>2</sup> - metamafic rocks with chlorite and muscovite alteration (Fig. 4E)	10 to 40	Hornblende Tremolite-actinolite Plagioclase Chlorite Epidote Carbonate Quartz Muscovite Biotite	Magnetite Titanite Ilmenite Rutile Pyrrhotite Pyrite Chalcopyrite	Dark green Medium to coarse-grained Preserved ophitic to subophitic igneous texture Chlorite oriented in cleavage Rare quartz and carbonate veinlets	Light to dark green Medium to coarse-grained Chlorite and muscovite aligned along cleavage Stockwork with millimeter quartz and carbonate veinlets	Light green to grey Medium to coarse-grained Chlorite and muscovite orientated along penetrative cleavage Stockwork with millimeter quartz and carbonate veinlets
MBcb <sup>3</sup> - metamafic rocks with chlorite and carbonate alteration (Fig. 4F)	0.10 to 7	Muscovite Carbonate Chlorite Quartz Tremolite Actinolite	Pyrrhotite Pyrite Chalcopyrite	Grey to dark grey, massive rocks. Thinnest intrusion of all. In swarms and radial directions. Their contacts may be crosscut and displaced by E-W faults. Do not display hydrothermal zoning and exhibit incipient schistosity. Euhedral carbonate crystals are dispersed throughout the rocks. Quartz, carbonate, sulfide and sulfosalts may develop euhedral crystals in vugs. Local crenulation cleavage is present.		

Local mine names: (1) DB4; (2) DB2, DB5; (3) DB1.

## 2.4 Geology and mineralogy of the deposits

For the Cachorro Bravo deposit, the 1:100-scale geological mapping included the outcrops exposed in a 250-m section of the mine galleries. The host metaphyllites and metagraywackes of the 658 and 711 galleries are hydrothermally altered and deformed, showing no apparent significant geological depth variations. The mapped deposits are located exclusively in the Intermediate subunit, where the regional rocks and structural features are easily recognized and correlated (Figs. 2.5 and 2.6).

The gold-bearing ore veins take the form of narrow, mineralized lodes and elongated boudins that strike 20° – 30° to the NE and dip between 60° and 70° to the SE. Metamafic MBcl dikes and sills

are always located in the hanging wall; they only crop out in the 658 gallery (Fig. 2.5), although they occur to the west of the 711 gallery (Fig. 2.6),.

The galleries 658 and 711 (Figs. 2.5 and 2.6) have an N-S horizontal strike and a depth of 115 and 170 m below surface, respectively, with mineralized lenses that extend to 250 m along the length of each gallery. Each lens is about 6 m wide, covering an area of 1,500 m<sup>2</sup> (Figs. 2.5 and 2.6), with the orebody plunging on average 130/35. Together with graywacke lenses, carbonaceous phyllite locally dominates the mapped area along the eastern wall. In the SW portion of the 658 gallery, metamafic MBcl dikes and sills represent the hydrothermal alteration boundary, since these rocks are practically unaltered beyond the contact with the metasedimentary host rocks. Quartz-carbonate veins occur along the mine gallery. Fault zones are common in the carbonaceous phyllite layers. Silicification zones predominate in the southern part of the gallery.

From N to S in the mapped areas, the turbiditic sequence varies from a somewhat psammitic to more pelitic, although in general the pelitic component dominates and is mainly represented by carbonaceous phyllites; outcrops of metagraywacke are exposed on the E side (Figs. 2.5 and 2.6).

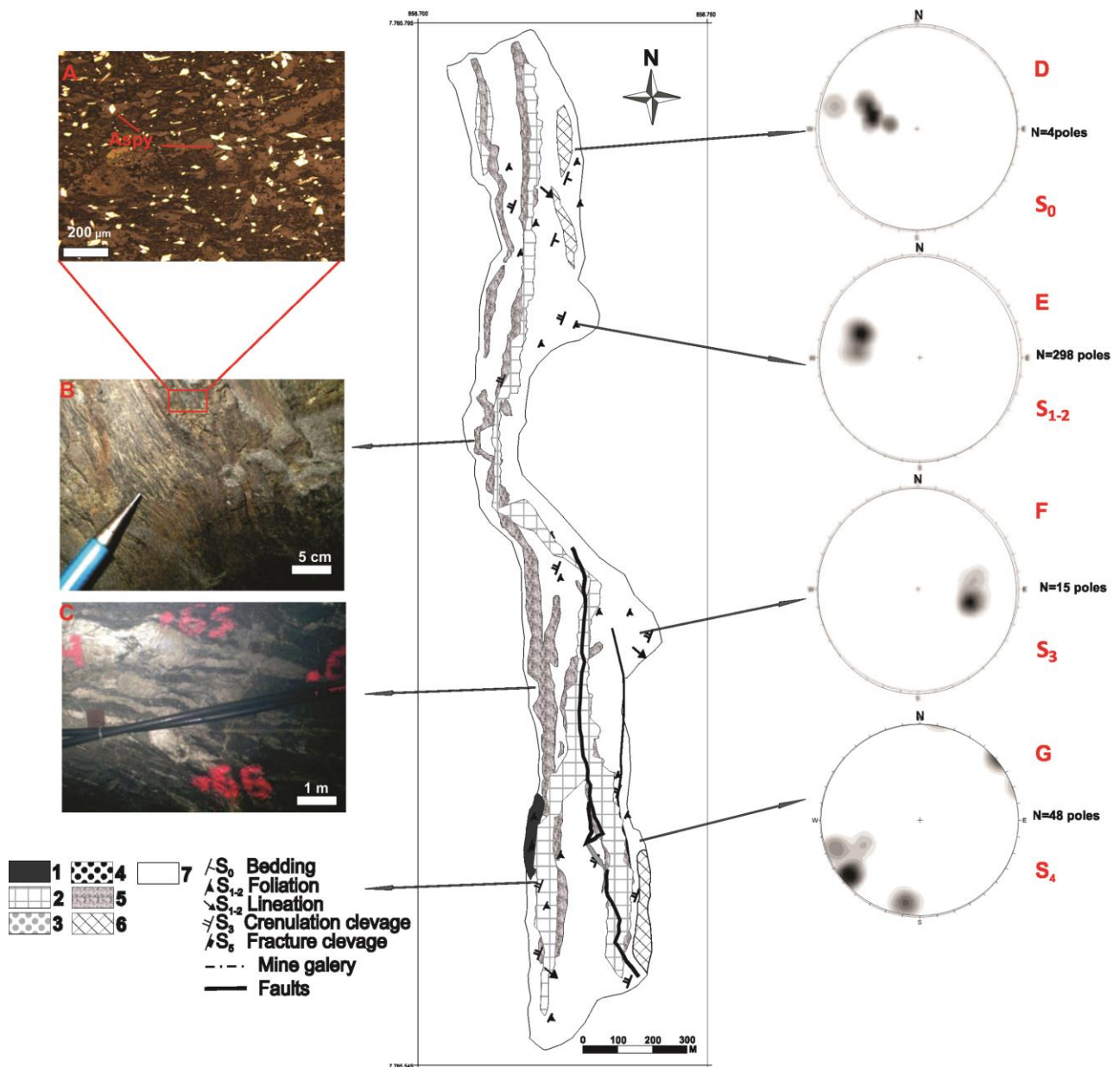


Figura 2.5. Simplified 1:100 scale geological map of mine Gallery CB-658-200/211-south with lithological types (A to C) and structural data (stereograms D to G), Córrego do Sítio intermediate unit, Cachorro Bravo gold deposit. (A) Photomicrograph of disseminated arsenopyrite (Aspy) in metasedimentary rocks (reflected light). (B) Intercalation of phyllite and metagraywacke along bedding ( $S_0$ ). (C) White/smoky-quartz-carbonate veins and veinlets in metasedimentary rocks. (D) Bedding ( $S_0$ ). (E) Mylonitic foliation ( $S_{1-2}$ ). (F) Crenulation cleavage ( $S_3$ ). (G) Fracture cleavage ( $S_5$ ).

### 2.4.1 Structures

The oldest planar structure,  $S_0$  is the compositional and gradational banding that trends to the SE and is concentrated in the phyllite layers as an upward grain-size coarsening, rarely perceptible in the metagraywacke lenses;  $S_0$  has a modal orientation of 114/59 (Figs. 2.5D, 2.6D, 2.7A, and 2.7E).

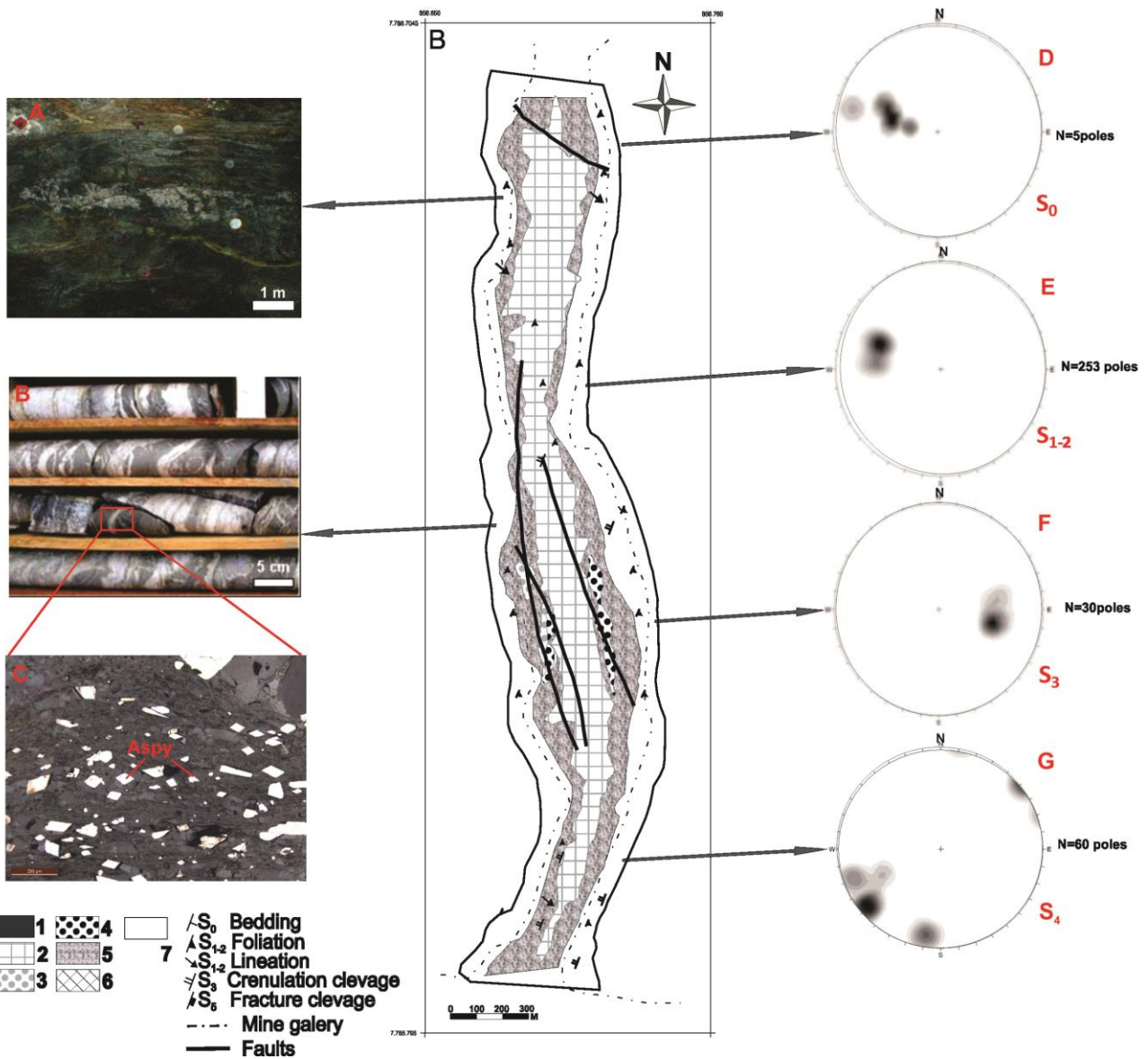


Figura 2.6. Simplified 1:100 scale geological map of mine Gallery CB-711-200/211-south (as in Fig. 5) with lithological types (A to C) and structural data (stereograms D to G), Córrego do Sítio intermediate unit, Cachorro Bravo gold deposit. (A) Intercalation of phyllite and metagraywacke along bedding (S<sub>0</sub>). (B) White/smoky-quartz carbonate veins and veinlets in metasedimentary rocks near the contact with metamafic dikes and sills with chlorite and muscovite alteration (MBcl). (C) Photomicrograph of disseminated arsenopyrite in metasedimentary rocks (reflected light). (D) Bedding (S<sub>0</sub>). (E) Mylonitic foliation (S<sub>1-2</sub>). (F) Crenulation cleavage (S<sub>3</sub>). (G) Fracture cleavage (S<sub>5</sub>).

The pervasive S<sub>1-2</sub> foliation is parallel or sub-parallel to the bedding planes. These structures are mainly present in the carbonaceous phyllite and the hydrothermally altered metamafic rocks, but are subordinate in the metagraywacke. The S<sub>1-2</sub> foliation is defined mainly by aligned sericite and has a strong dip to SE, with a modal orientation of 119/70 (Figs. 2.5E, 2.6E, 2.7B, and 2.7F), followed by a rarely observed down-dip L<sub>m1-2</sub> lineation with a 45/45 orientation. The dip of the foliation

increases both in the S direction and vertically (from the 658 to the 711 gallery) by roughly 1 – 2 degrees, and regionally it is more intense in the SW quarter. Folds are well visualized when structural data from various levels are compiled. They are well defined by the main foliation  $S_{1-2}$  in metasedimentary rocks.

The  $S_3$  crenulation cleavage is an important structural element characterized by having an opposing dip to  $S_{1-2}$ . Similarly to  $S_{1-2}$ , this structure is very well marked in the carbonaceous phyllite and is subordinate in graywackes (Figs. 2.5F, 3.6F, 2.7C, and 2.7G). The  $S_3$  crenulation cleavage data are concentrated in the SE quarter with orientations 280/60, 250/65, and 270/66 (Figs. 2.5F, 2.6F, and 2.7D).

The last structure recognized in the mapped areas is the  $S_4$  spaced fracture cleavage, with a N-NW direction and a modal orientation of 60/82. These fractures are centimetre-to-metre spaced and filled by quartz and carbonate (Figs. 2.5G and 2.6G).

Shear zones were mapped mainly in the carbonaceous phyllite layers, with the development of S-C structures parallel or sub-parallel to  $S_{1-2}$ . Faults are well displayed in the carbonaceous phyllite, showing a NW-SE strike.

#### **2.4.2 Mineralization and hydrothermal alteration**

The ore zone is predominantly hosted at the stratigraphic break between metasedimentary and metamafic rocks. Mineralization is associated with intense silicification and narrow, variably deformed, quartz-carbonate-bearing veins parallel to the  $S_{1-2}$  foliation (Figs. 2.7H and 2.7I). Lodes are generally located within structurally favorable  $S_{1-2}$  sites in shear zones and folds, while individual veins are 0.1 to 5 m thick, locally up to 10 m. The lode gold quartz-carbonate veins are discontinuous both along strike and down dip and are highly boudinaged (Ribeiro et al. 2013, Sequetto-Pereira et al., 2013; Table 2.2). Canale (1999), David (2006), Porto (2008), Lima (2012), Ribeiro et al. (2013) and Sequetto-Pereira et al., (2013) describe the structurally controlled

mineralization styles as disseminated, sulfide replacement and associated with quartz-carbonate-sulfide  $\pm$  sulfosalts veins.

Tabela 2.2. Synthesis of vein characteristics modified from Ribeiro et al. (2013) and Sequetto-Pereira et al. (2013).

Type	Reference		Mineralogy	Thickness (cm)	Host rock	Vein texture	Orientation	Associated structure
	Ribeiro et al. (2013)*	Sequetto-Pereira et al. (2013)						
Early-stage alteration, mineralized veins	V1	V1a	Smoky quartz-ankerite-arsenopyrite-pyrite-gold	1 - 600	Metagraywacke, schist and phyllite	Pinch-and-swell	120/70	Parallel to foliation $S_{1,2}$ Folded with axial- plane foliation Shear veins
		V1b	Milky quartz-ankerite-arsenopyrite-pyrite-pyrrhotite-free gold			Massive	120/70	
		V1c	Laminated smoky or milky quartz with pyrite gold			Granulated	120/70	
Later-stage veins (non-mineralized)	V2	V2a	Milky quartz-(subordinate) ankerite	Irregular	Metagraywacke, schist and phyllite	Massive	70/70 and 160/80	Diagonal to foliation $S_3$
		V2b	Quartz-ankerite-pyrite	2 - 300	Metagraywacke, schist and phyllite	Massive	295/40	Parallel to foliation $S_3$ Extensional veins
	V3	V3a	Milky quartz-(subordinate) ankerite	1 - 20	Metagraywacke, schist and phyllite	Fibrous	70 - 130/80	Parallel to foliation $S_4$ Fracture veins
		V3b	Milky quartz-ankerite veins and schist fragments			Breccia	60/70	
	-	V4	Varied mineralogy	Irregular	Metagraywacke, schist and phyllite	Massive	300/30	Parallel to foliation $S_3$
	V4	V5	Quartz-carbonate-calcite	1 - 15	Metamafic dikes and sills	Shear veins/stockwork	90/80	Varied structures Extensional veins

\*Chronological classification



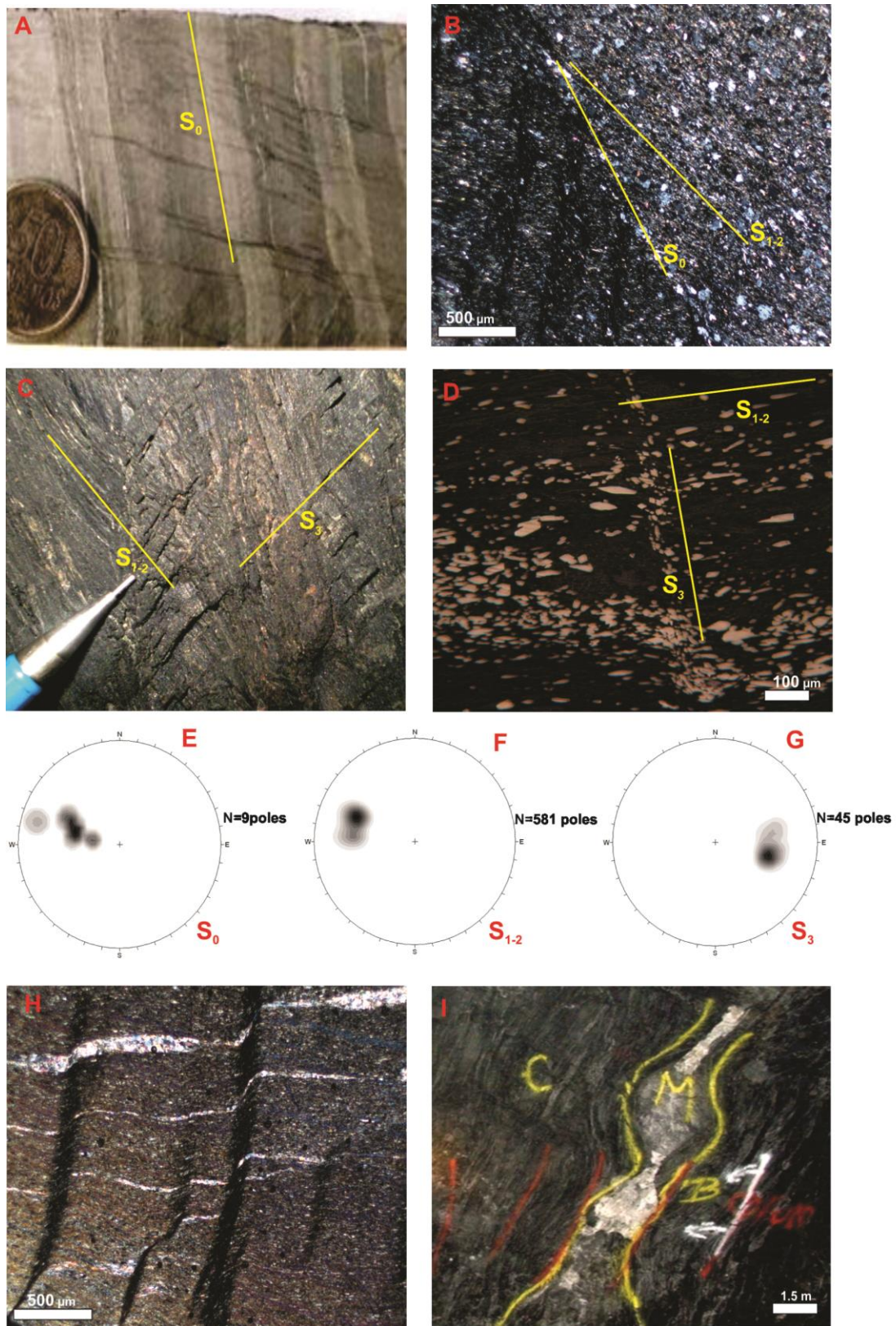


Figura 2.7. Structural data from the Córrego do Sítio auriferous lineament. (A, B, E) Bedding ( $S_0$ ). (B) With transmitted light. (C) With reflected light. (D, F) Mylonitic foliation ( $S_{1-2}$ ). (C, D, G) Crenulation cleavage ( $S_3$ ). (H) With transmitted light. (I) Pinch--and-swell mineralized flattened veins and veinlets (M) of Cachorro Bravo deposit (C and B in the picture).

Smoky quartz in veins containing carbonate-sulfide-sulfosalt is xenoblastic, very deformed, with lobate edges and wavy extinction. Subhedral and polygonal quartz crystals show straight to undulose extinction (Ribeiro et al., 2013). Fine-grained, anhedral carbonate is abundant. Milky quartz is granoblastic and represents a recrystallization product of the smoky quartz; it is commonly concentrated near metamafic dikes and sills. The milky recrystallized quartz forms mosaic textures of polygonal and subhedral crystals, with straight extinction. Fine-grained crystals are associated with fine, anhedral carbonate (Ribeiro et al., 2013).

Many descriptions of the relationship between gold and veins in the older literature of Archean deposits of the Quadrilátero Ferrífero indicate that gold is most commonly found in smoky quartz veins (e.g. Martins et al., 2016). However, in the Cachorro Bravo deposit, gold is consistently found in both milky and smoky quartz veins, and the same is true for the Laranjeiras deposit, in which gold is most commonly located in sulfide-bearing,  $S_1$ -concordant veins. However, this is not a typical feature of other metasedimentary-hosted vein gold deposits (e.g. Cox et al., 1991).

Mineralogical and textural transformations accompanying wall-rock alteration are observed surrounding the main mineralized vein systems (Fig. 2.8), although the limits of the alteration zones (Fig. 2.9) are not always sharp and regular. There are two main distinct hydrothermal alteration assemblages of the host metasedimentary rocks, which depend on the proximity to metamafic dikes. Whereas the Cachorro Bravo deposit is closely limited on both sides by dikes (specifically MBc1), these igneous intrusions are located farther away from the Laranjeiras and Carvoaria deposits (Fig. 2.2). In the former, chlorite and pyrrhotite are present, while at Laranjeiras and Carvoaria berthierite, stibnite and pyrite are part of the distinct mineral assemblage (Figs. 2.9A and 2.9B).

The main hydrothermal minerals in all deposits include quartz, carbonate, white mica, chlorite and accessory rutile, titanite, apatite ilmenite and sphalerite. Minerals in trace amounts include chalcopyrite, galena, sphalerite, sulfosalts and tetrahedrite.

The hydrothermal assemblage in metamafic rocks is chlorite, epidote, calcite, quartz, muscovite and rare biotite. The accessories are magnetite, ilmenite, rutile, pyrrhotite, pyrite, chalcopyrite, galena and sphalerite (Fig. 2.10). In transitional zones, the consumption of carbonaceous matter is almost complete (Porto et al., 2006, Porto, 2008) with bleaching of these carbon-rich phyllites.

Mineralization in the mapped area is composed of white/smoky-quartz-carbonate veins and veinlets in metasedimentary rocks near the contact with MBcl dikes, containing sericite, chlorite and carbonate and showing transitional zones with dikes. Arsenopyrite is the main sulfide mineral, but pyrrhotite is also significant in the proximity to dikes.

Based on the mineralogical composition and mineral textures, Lima (2012) identified gold in five associations: (i) free and disseminated electrum in quartz-carbonate veins; (ii) included in disseminated arsenopyrite, generally parallel to the main foliation and associated with phyllosilicates, chlorite, sericite or muscovite; submicroscopic gold observed in subhedral arsenopyrite crystals, suggesting the presence of invisible gold (Porto, 2008); (iii) included in berthierite; (iv) included in pyrite or pyrrhotite that are disseminated parallel to the main foliation in micaceous portions; (v) included in silicates, such as quartz or muscovite.

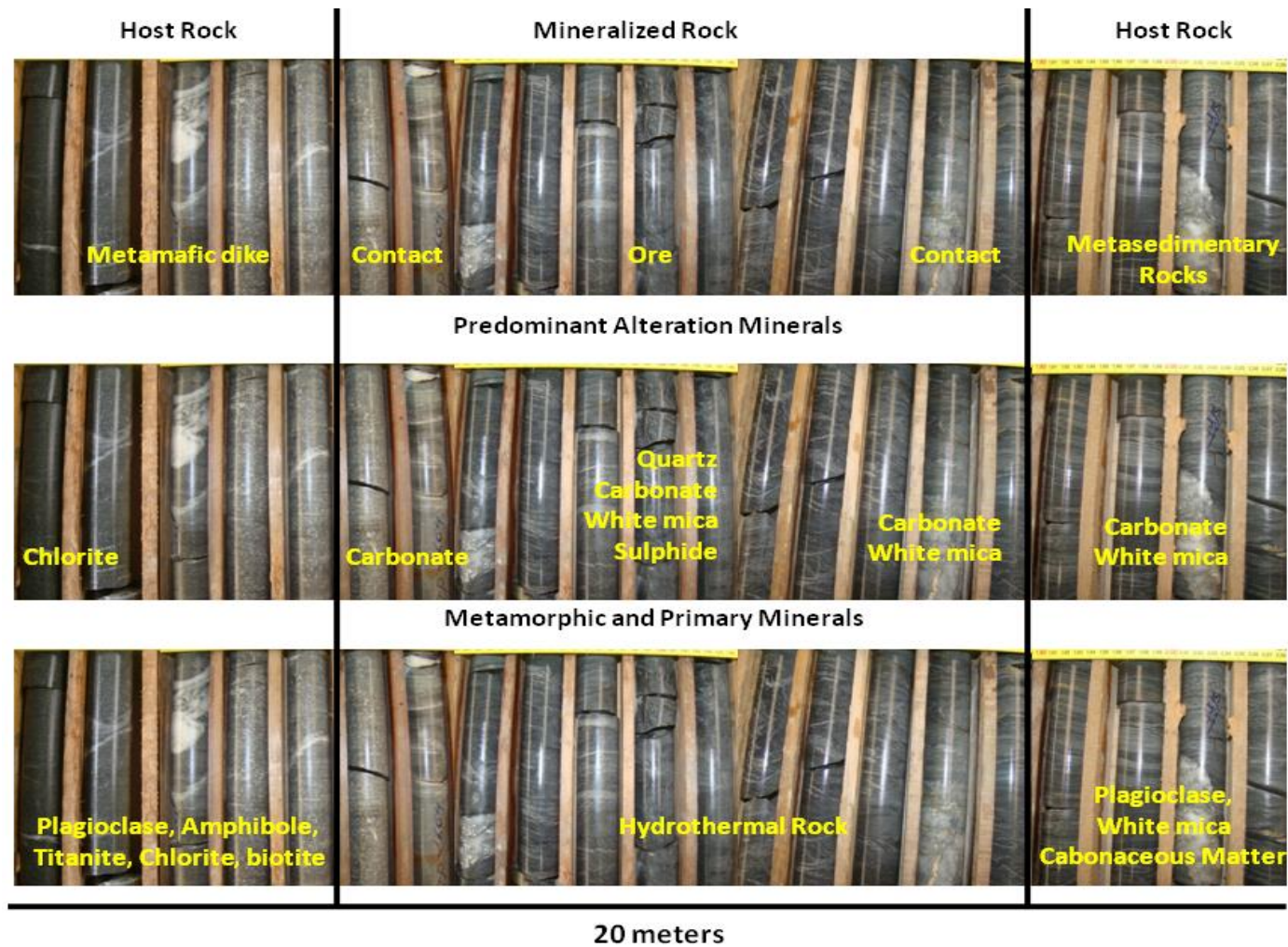


Figura 2.8. Hydrothermal alteration zones along the contact between metasedimentary and metamafic rocks (modified from Porto, 2008).

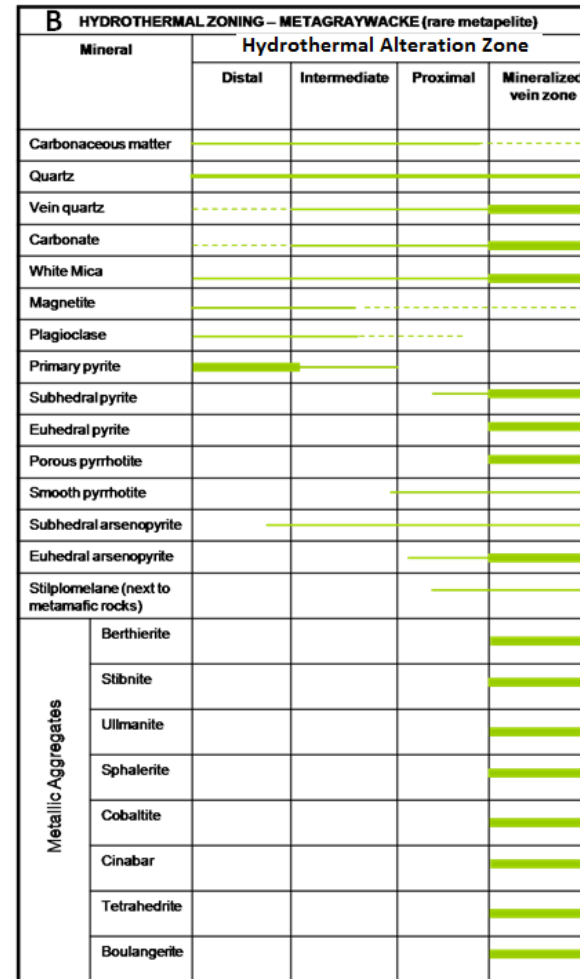
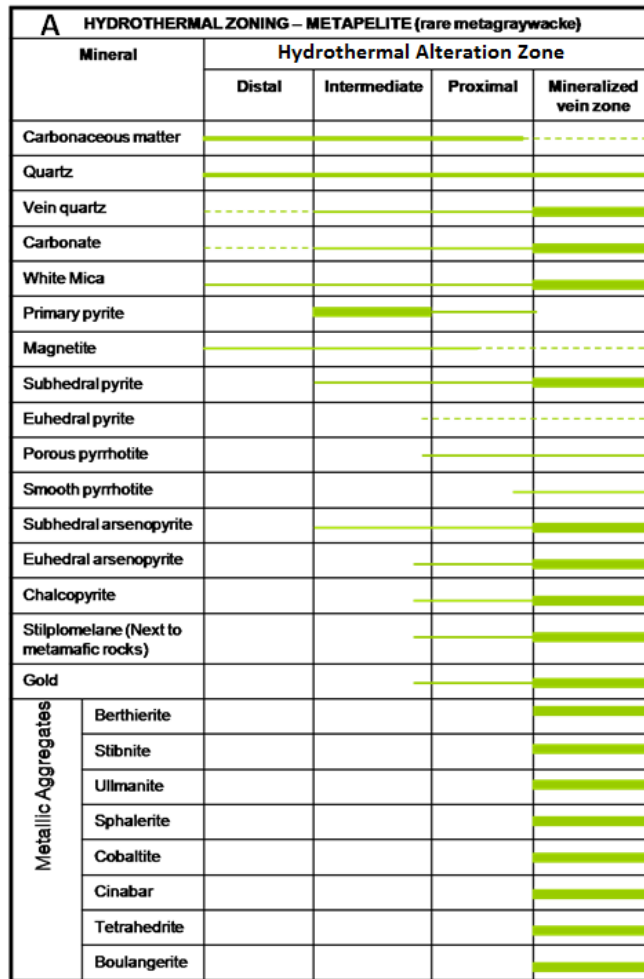


Figura 2.9. Hydrothermal paragenetic zoning, including the main sulfides, associated with gold in (A) Metapelite. (B) Metagraywackes, Córrego do Sítio auriferous lineament. Line thicknesses represent schematically the relative quantities of each mineral deposited (constructed also including data from Porto, 2008 and Lima, 2012).

HYDROTHERMAL ZONING			
Mineral	Edge	Intermediate	Center
Quartz	Thick line	Thin line	
Carbonate	Thick line	Thin line	
White Mica	Thick line		
Chlorite	Thick line	Thin line	Thin line
Titanite	Thick line	Thin line	Thin line
Primary pyrite	Thick line	Thin line	Thin line
Porous pyrrhotite	Thin line	Thick line	
Chalcopyrite	Thin line	Thick line	
Gold	Thin line		

Figura 2.10. Hydrothermal paragenetic zoning, including the main sulfide minerals in metamafic rocks of the Córrego do Sítio auriferous lineament. Line thicknesses represent schematically the relative quantities of each mineral deposited (constructed also including data from Porto, 2008 and Lima, 2012).

### 2.4.3 Petrography of sulfides

Sulfide minerals are present mainly along the edges of veins, with pyrite being the most common (Lima, 2012). Three generations of pyrite are recognized: (i) isolated and disseminated pyrite in carbonaceous layers, in non-mineralized zones, in circular or rounded aggregates that may be folded and partly disintegrated (Fig. 2.11A); (ii) ± porous pyrite crystals, which may contain gold, associated with a myriad of other sulfide minerals, commonly displaying irregular boundaries of smooth pyrite; porous pyrite may be replaced by arsenopyrite (Figs. 2.11B and 2.11C); (iii) late-stage, smooth euhedral pyrite in isolated crystals that apparently result from borders of the porous pyrite (Fig. 2.11D). Early-stage porous pyrrhotite is sometimes replaced by smooth pyrrhotite (Fig. 2.11D).

Arsenopyrite is the predominant gold-associated sulfide mineral in the Cachorro Bravo deposit, and is always present in the carbonaceous phyllites, where in veins it is also related to phyllite portions.

Arsenopyrite forms from pyrite in mineralized metasedimentary rock zones away from metamafic

dikes and sills, or from pyrrhotite in mineralized transitional zones between metasedimentary rock zones and metamafic dikes and sills. Two generations of arsenopyrite are identified: (i) euhedral and subhedral, smooth, very fine-grained crystals, in prisms or needles (Fig. 2.11E), or (ii) anhedral to subhedral crystals (Fig. 2.11F) associated with pyrite or pyrrhotite, preserving the original habit and porosity of the latter sulfides. Stibinite and berthierite are commonly associated with the main sulfide minerals in the mineralized metasedimentary rocks, mainly in smoky quartz-carbonate-sulfide-sulfosalt veins. As indicated by Lima (2012), both porous pyrrhotite and pyrite occur in the core of sulfide crystal aggregates (Fig. 2.11G), with berthierite being the most abundant. This opaque mineral is present mainly in millimetric, subhedral to euhedral crystals in vugs, with inclusions of anhedral pyrrhotite, porous pyrite, anhedral arsenopyrite, chalcopyrite, sphalerite and gold.

Microprobe studies undertaken by Lima (2012) and Ribeiro et al. (2013) detailed a series of phases that are not identified under the microscope, including sphalerite, cobaltite, cinnabar, tetrahedrite, boulangerite-group minerals and ullmanite.

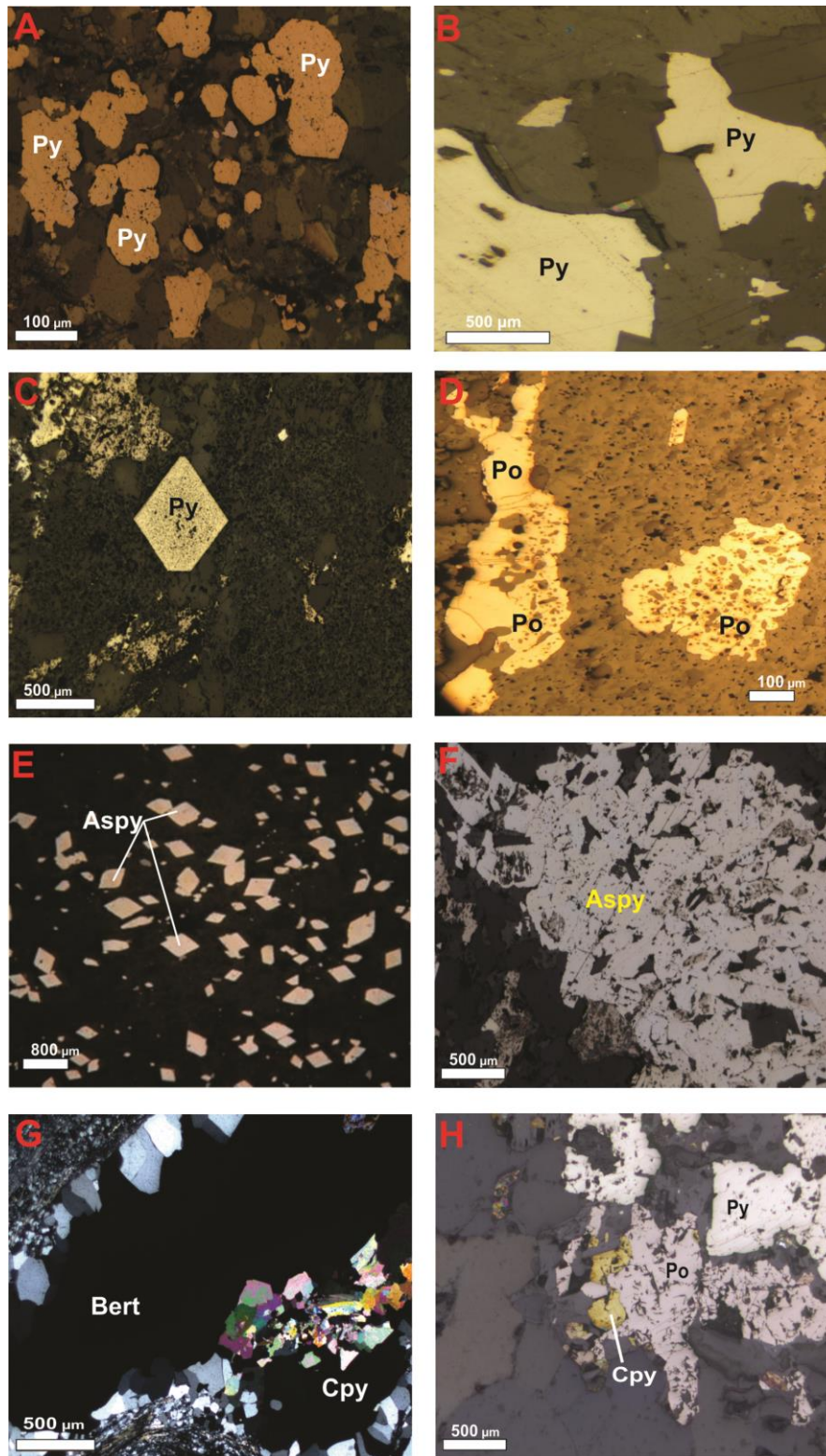


Figura 2.11 Generations of sulfide minerals associated with the Cachorro Bravo gold deposit, Córrego do Sítio auriferous lineament. (A) Primary rounded pyrite (Py) reflected light. (B) ± Porous pyrite (Py) reflected light. (C) Euhedral pyrite (Py) transmitted light. (D) Early stage, porous pyrrhotite (Po) replaced by smooth pyrrhotite (Po) reflected light. (E) Euhedral acicular arsenopyrite (Aspy) reflected light. (F) Anhedral-to-subhedral arsenopyrite (Aspy) reflected light. (G) Subhedral-to-euhedral berthierite (Bert) in vugs (transmitted light). (H) Sulfide crystals aggregates with chalcopyrite (Cpy) reflected light.



## 2.5 Discussion and Conclusions

The Archean Córrego do Sítio unit is the most abundant metasedimentary unit in the Rio das Velhas greenstone belt in Quadrilátero Ferrífero region (Baltazar and Zuchetti, 2007), occur as a sequence of metamorphosed turbidite sequence. Baltazar and Zuchetti (2007) included this unit in a resedimented association, which contains greywacke, phyllites, and banded iron-formation. These facies represent deposition within different submarine ambient. Depositional characteristics in the Rio das Velhas greenstone belt are similar to other Archean sedimentary dominated greenstone belts in the world (Padgham, 1992; Krapez, 1993; Jackson *et al.*, 1994; Ootes *et al.*, 2011).

The eastern portion of the Rio das Velhas greenstone belt is dominated by a package of metasedimentary rocks consisting of alternating metagraywackes and phyllites in a turbidite sequence, metamorphosed to the greenschist facies.

Metamafic dikes and sills have an NNE-SSW direction and are divided as incipiently altered metamafic rocks and hydrothermally altered type locally mineralized in gold. Clearly, the increased mineralization is combined with the proximity of metamafic dikes and sills. The Cachorro Bravo Deposit is, currently, the most important in production and records the largest amount of the metamafic rocks.

Four deformation events affected the mine sequence, and these are in part progressive. Event  $D_1$  is characterized by a progressive foliation  $S_{1-2}$ , striking NNE, and dipping to ESE, producing tight, asymmetric, isoclinal and disharmonic, kink folds;  $D_2$  is typified by a crenulation cleavage and a spaced crenulation cleavage  $S_3$ , which strikes NNE crosscutting the regional foliation  $S_{1-2}$  at a high angle to the NW;  $D_3$  is represented by large-scale, open folds, arching  $S_0$ ,  $S_{1-2}$  and  $S_3$ . These structures may represent more recent orogeny; and  $D_4$  has parallel fractures, spaced from centimetres to metres along with open folds or subordinate kink folds with high angle vertical axial plane, striking mainly towards NW.

Two different vein types are important to mineralization, smoky-quartz-carbonate-sulfide-sulfosalt veins, which are very deformed; and milky-quartz-carbonate veins that represent the recrystallization product of the smoky quartz-carbonate veins. Sequetto-Pereira (2013) and Ribeiro *et al.* (2013) classified the mineralized veins as associated with smoky and milky quartz veins, and at the non-mineralized veins, are observed only

milky quartz veins. They commonly occur close to dikes and sills that probably have influenced their recrystallization (Ribeiro *et al.*, 2013).

Four types of structurally controlled, gold mineralization are identified along the deposits. These include disseminated, sulfide replacement, and associated with quartz-carbonate-sulfide±sulfosalt veins each showing a representative mineralogy and paragenetic sequence.

The main deposits Cachorro Bravo, Laranjeiras and Carvoaria have a paragenesis similar in other turbidite-hosted deposits worldwide (e.g., Jaclyn Deposit, Newfoundland Appalachians, Sandeman *et al.*, 2010; Bendigo-Ballararat, Australia, Gao & Kwat, 1995; Wattle Gully Deposit, Australia, Cox *et al.* 1995; Lachlan Fold Belt, Australia, Bierlein, 1998), where gold occurs both as free grains and in association with arsenopyrite and pyrite; stibnite in some lodes. The most common sulphides in all vein types are arsenopyrite, pyrite, chalcopyrite and pyrrhotite, presenting diverse textures, and more than one generation.

In the hydrothermal zones, arsenopyrite forms after pyrite or pyrrhotite, both of which is locally seen originated from the consumption of magnetite. Near the metamafic dikes, especially in the Cachorro Bravo deposit, arsenopyrite develops after pyrrhotite in the mineralized veins and veinlets. The pyrrhotite/arsenopyrite association along dike zones may reflect local conditions of relatively higher temperature (Mikucki, 1993). Arsenopyrite after pyrite is typical of alteration zones far from metamafic dikes, where veins are dominated by smoky quartz-carbonate veins with berthierite, stibnite and pyrite, and gold. In the Sb-Au-quartz veins, berthierite and stibnite are the most abundant Sb-bearing minerals. This mineralization stage is mainly observed in carbonaceous phyllites and has a gold-dominated association with porous arsenopyrite, which is the predominant gold-associated sulfide in the Cachorro Bravo deposit. Historical data reveal a remarkable correspondence to variations of gold abundance, suggesting a genetic relationship of gold enrichment to hydrothermal alteration, and this are common to several other described Archean lode gold deposits.

A 1:100-scale geological mapping of the Cachorro Bravo deposit was undertaken at the mine galleries 658 and 711 in the CB-658-200/211-south and CB-711-200/211-north orebodies, composed of carbonaceous phyllite with graywacke lenses that host millimetric to metric smoky-milky quartz-carbonate-sulfide-

sulfosalt veins. Metamafic rocks with chloritic alteration sills are always located west of the mined 200 series orebodies in the hanging wall and only outcrop in the 658 gallery.

Nevertheless, the mapped galleries illustrates that detailed petrographic and structural studies are capable of detecting mineralization and wallrock alteration zones around this deposit. The increase in the intensity of the hydrothermal alteration with the proximity to quartz lodes is indicated by the bleaching of the wall rocks, and the abundance of disseminated pyrite, pyrrhotite and arsenopyrite, as well as stibnite and berthierite.

The data presented provide some structural and petrographic similarities on models for formation of these deposits, assuming that the Cachorro Bravo, Laranjeiras and Carvoaria are representative of the metaturbidite-hosted lode-gold deposits. Vein formation and mineralization occurred in multiple episodes, as suggested by Sequetto-Pereira et al. (2013). The fluid was most likely modified during ascent and later interaction with wallrocks. This is consistent with the conclusions of other studies directed at lode-gold deposits of Archean to Phanerozoic ages (*e.g.* Goldfarb et al., 1988, 1991).

## **2.6 Acknowledgments**

We thank all members of AngloGold Ashanti Córrego do Sítio Mineração (AGACSM) for their help, logistic and financial support, especially Rodrigo Martins, who has maintained his commitment to our research group. This research is fully financed by Conselho Nacional de Desenvolvimento Científico e Tecnológico (CNPq), Vale and AGABM. We acknowledge the support of Universidade Federal de Minas Gerais (UFMG), Coordenação de Aperfeiçoamento de Pessoal de Nível Superior (CAPES), Fundação de Amparo à Pesquisa do Estado de Minas Gerais (FAPEMIG) and Fundação de Desenvolvimento da Pesquisa (FUNDEP). We also thank Prof. C.A. Rosière for his valuable comments and corrections, as well as Robert Pankhurst and two anonymous referees for their important and constructive comments

**PARTE III – ESTUDOS COMPARATIVOS DAS ASSOCIAÇÕES RESSEDIMENTADAS DO  
LINEAMENTO CÓRREGO DO SÍTIO E DA ÁREA AURÍFERA CUIABÁ-LAMEGO**

**3 GEOCHEMISTRY, IN SITU LA-ICP-MS AND SEDIMENTARY SOURCE OF THE  
HOST TO GOLD CLASTIC ROCKS IN THE RIO DAS VELHAS GREENSTONE  
BELT, BRAZIL**

Jorge Roncato<sup>1</sup>, Lydia Maria Lobato<sup>1</sup>, Orivaldo Baltazar<sup>2</sup>, João Orestes Santos<sup>3</sup>, Rosaline Cristina  
Figueiredo e Silva<sup>1</sup>, Breno Souza Martins<sup>1</sup>, Cristiano Lana<sup>4</sup>

<sup>1</sup>Instituto de Geociências-Centro de Pesquisa Manoel Teixeira da Costa, Departamento de Geologia, Universidade Federal de Minas Gerais, Av. Antônio Carlos 6627, Campus Pampulha, 30130-009, Belo Horizonte, Minas Gerais, Brazil

Corresponding author: Jorge Roncato| Tel.: 55-31-997672937| fax: 55-31-34095410

E-mail address: [roncatojr@yahoo.com.br](mailto:roncatojr@yahoo.com.br)

<sup>2</sup>CPRM, Serviço Geológico do Brasil, Avenida Brasil 1731, Funcionários, Belo Horizonte, Minas Gerais, Brazil

<sup>3</sup>University of Western Australia, 35 Stirling Hwy, Crawley WA 6009, Austrália, +61 8 6488 6000

<sup>4</sup>Applied Isotope Research Group - Escola de Minas, Departamento de Geologia, Universidade Federal de Ouro Preto, Morro do Cruzeiro, Bauxita, 35400-000, Ouro Preto, Minas Gerais, Brazil

## ABSTRACT

The Rio das Velhas greenstone belt is located in the Quadrilátero Ferrífero district, in the southern extremity of the São Francisco Craton, State of Minas Gerais, SE Brazil. Turbidite sequences of the greenstone belt stratigraphy are largely distributed in the region, and represent clastic sedimentary associations dominated by alternating graywackes and pelites. Important turbidite-hosted gold deposits occur in the Córrego do Sítio lineament of the eastern sector of the Quadrilátero Ferrífero region. On the other hand, similar rocks overlying the area comprise the Cuiabá-Lamego BIF-hosted gold deposits which are loci to historical diggings and occurrences, in the northern sector. The geochemical data indicate that the clastic sedimentary rocks have a mixed and felsic sources for the eastern greywackes grade into pelagic sedimentary rocks. The in situ U-Pb and Lu-Hf detrital zircon analyses suggest that sedimentary rocks were sourced from granitoids belonging to the Rio das Velhas II and Mamona age magmatic events. Proterozoic ages, ranging between 2.0 and 2.45 Ga recorded by these isotope data reinforce the notion that Archean and Paleoproterozoic rocks are tectonically imbricated. Variations in Lu-Hf isotope analyses indicate that the source areas evolved via crust-mantle mixing processes. In situ LA-ICP-MS analyses on sulfide minerals of carbonaceous pelites from the Córrego do Sítio gold lineament, - pyrite, arsenopyrites and pyrrhotites grains from the Laranjeiras deposit, and pyrites grains from the Cachorro Bravo deposit which display a considerable range of trace element compositions. Two hydrothermal stages are recognized: (1) early hydrothermal, marked by the development of porous sulfides, during which some gold precipitation took place; and (2) main to late hydrothermal, recognized by the development of smooth sulphide minerals, containing peak gold in 135 ppm. The mixed source for the host rocks may explain why gold correlates to Se, As, Sb and Te of sedimentary affiliation, as well as to the mafic-ultramafic elements Co, Ni, and Pt. Arsenic is the most abundant trace element in Au-bearing porous and smooth pyrite (P-Py and S-Py), and porous and smooth arsenopyrite (P-Apy and S-Apy), of the Laranjeiras and Cachorro Bravo deposits, followed by Ni and Co. These elements were probably leached during hydrothermal alteration indicating a local metal and fluid source during gold mineralization. The As, Co, Ni, Te, Pb and Sb concentration in porous and smooth arsenopyrite from the main stages of gold mineralization has important implications for exploration of turbidite-hosted deposits in the Rio das Velhas greenstone belt, where Arsenopyrite and pyrite, which have the highest Au content, also record high concentration of these elements.

**Keywords:** Orogenic gold, geochemistry, U-Pb geochronology, Lu-Hf analyses, hydrothermal paragenesis, clastic sedimentary association, Rio das Velhas greenstone belt.

### 3.1 Introduction

Orogenic gold deposits (*e.g.*, Groves et al., 1998) are associated with a wide range of host rocks from from 2 to 15 km, and arguably 20 km in the crust. Most of them are typified by mineral parageneses of the greenschist metamorphic facies (Poulsen et al., 2000; Goldfarb et al., 2005; Robert et al., 2005; Dubé and Gosselin, 2007, and references therein; Groves and Santosh, 2015), as is the case in the Archean greenstone-hosted deposits of the Quadrilátero Ferrífero (QF) mining district, Brazil.

Gold production in the QF Archean Rio das Velhas greenstone belt is significant worldwide (Ribeiro Rodrigues, 1998), with banded iron formations (BIF) being one of the most important host to gold mineralization (*e.g.*, Lobato et al., 2001). These authors estimated that only 4% of all gold is produced from deposits hosted in rocks other than BIF, including ultramafic, mafic, volcanoclastic, and clastic rocks in general.

Based on these authors, Martins et al. (2016) calculated an approximate thickness of 5,550 m of clastic, clastic-chemical and volcanoclastic sedimentary rocks, making the Rio das Velhas a sedimentary-dominated greenstone belt.

The resedimented association, of Baltazar and Zucchetti (2007), hereinafter referred to as “clastic sedimentary association”, is locally an important host to gold. This is the case in the Córrego do Sítio lineament (*e.g.*, Ribeiro et al., 2015, Roncato et al., 2015, Lima, 2012), here referred to as the eastern sector, where three different sequences of graywacke-argillite outcrop. The lineament forms a series of NE-SW regional tracts known as Córrego do Sítio, Cristina and São Bento-Donana shear zones, containing gold deposits with resources of approximately 5.12 Moz (Sequetto Pereira et al., 2013; Roncato et al., 2015). They represent the most important metaturbidite-hosted gold deposits in the QF district, with sixteen diggings and deposits, including Cachorro Bravo, Laranjeiras and Carvoaria (Roncato et al., 2015), having an annual production planned to average 140,000 oz a year. The Cachorro Bravo deposit is the most productive of them all at 7.6 g/t of Au, followed by

Carvoaria (6.7 g/t) and Laranjeiras (6.3 g/t). They represent 25%, 18%, and 37% of the total reserves, respectively.

The Córrego do Sítio occurrences were discovered in the 1980's, produced gold in open-pit operations since 1990, and finally started underground mining in 2002 by AngloGold Ashanti Córrego do Sítio S/A-AGABM (Porto, 2008). The BIF-hosted São Bento deposit is located at the extreme NE limit of the lineament, with a historical production of 56.2 tonnes from 1986 to December 2006 (*e.g.*, Martins Pereira et al., 2007).

The Lamego and Cuiabá gold deposit area, with underground mines are also operated by AGABM, are here referred to as the northern sector, and located near the town of Sabará (Figs. 3.1). The BIF-hosted Lamego deposit (1.3 million ounces resource contained Au at 7.3 g/t Au; Martins et al., 2016) is located at the southwestern end of the area, where gold also associated with pervasive zones of silicification, similar to zones of silica flooding. The world-class BIF-hosted Cuiabá (*e.g.*, Ribeiro Rodrigues et al., 2007, Lobato et al., 2005) deposit contains 150 t of gold (5 Moz produced until 2015 and more 7 Moz in mineral resources; AGA, personal communication), where sulfide (mainly pyrite) replacement of BIF is the dominant gold mineralization style. Both deposits consist of mafic volcanic rock, chert and BIF, carbonaceous and micaceous pelites, which belong to the volcano-chemical and clastic-chemical lithofacies associations (Baltazar and Zucchetti, 2007).

Rocks belonging of the volcanoclastic-clastic sedimentary associations cover the whole area of the Cuiabá-Lamego gold deposit area, where metaturbidites prevail. Although no important gold deposit of this association have been mined until today, a series of old artisanal diggings have historically produced some gold, such as at the Descoberto de Cuiabá and Biquinha mines (Vial et al., 2007). Minor diggings also include Viana, São José, Cristais, Herbert Marins, Capão, Brumado, Enforcado and Galinha.

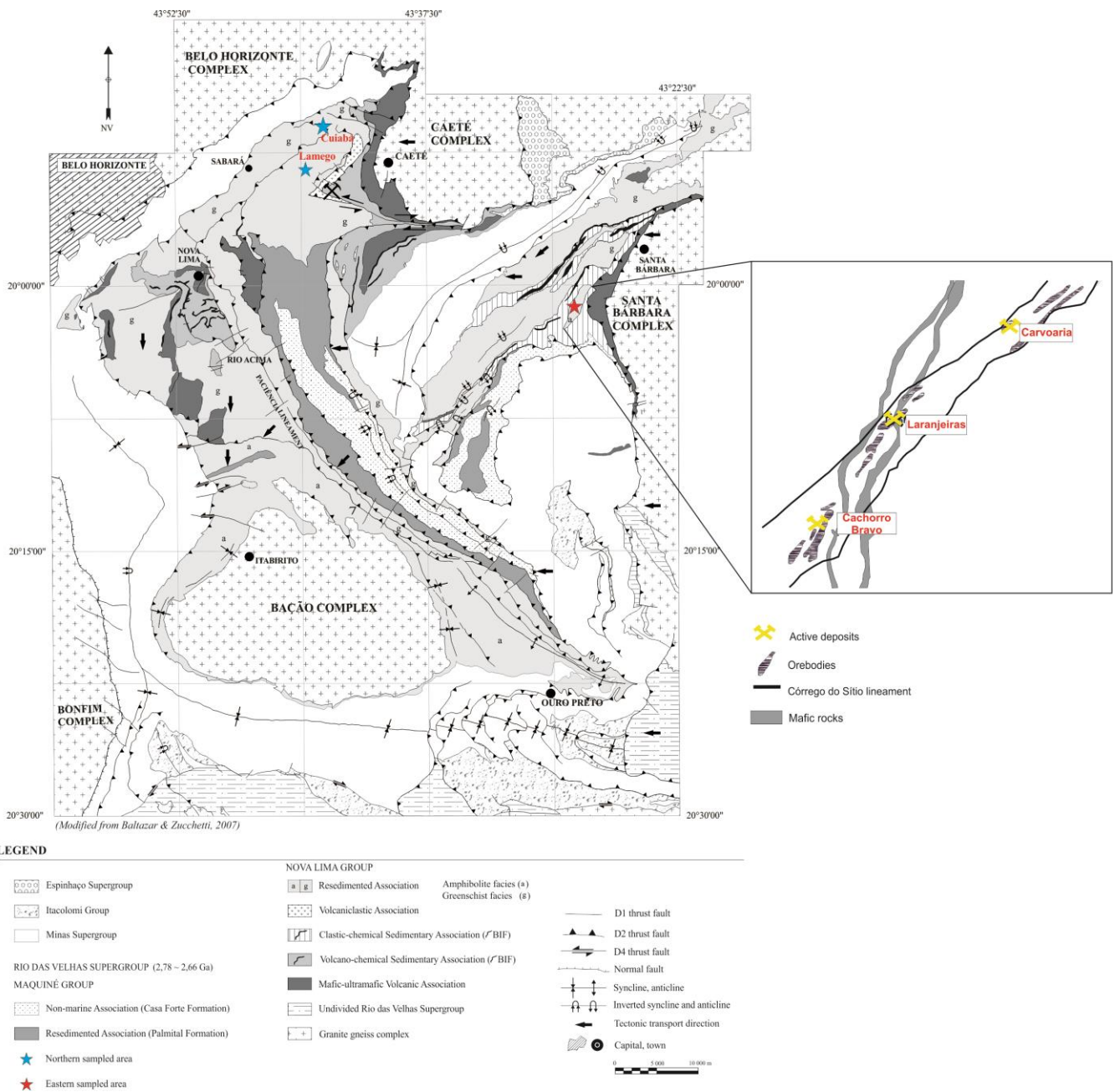


**Figure 3.1. Geological map of the Quadrilátero Ferrífero district showing location of sampled areas, i.e., the eastern Córrego do Sítio lineament (deposits indicated in inset; geology modified from Lima, 2012) and northern Cuiabá-Lamego gold deposit area in the Rio das Velhas Supergroup (modified from Baltazar and Zucchetti, 2007).**

Other metaturbidite-hosted gold diggings are described in the northern branch of the Paciência structural lineament (Fig. 3.1), including Engenho de Baixo and Velho. The lineament also hosts



Engenho d'Água (Beleque, 2015), which produced (2.91 tons of gold) mainly from 2007 to 2011, as well as the gold occurrences Olhos d'Água and Crista.

Archean metaturbidites are producers of gold especially in the Slave province of Canada, where deposits of the Quetico metasedimentary belt (Sawyer, 1986) and the world-class Roberto deposit (Fontaine et al., 2015) are examples. In fact, the discovery of the Roberto deposit in 2004 has greatly increased the interest of mining companies in the Archean sedimentary rock sequences such as of Superior Province, which became targets with high exploratory potential (Beauchamp et al., 2015).

As new exploration frontiers for gold in Archean greenstone belts are demanded, the characterization of their clastic sedimentary sequences become more critical in order to distinguish the most fertile host sediments. This is the case of the Rio das Velhas greenstone belt where sedimentary rocks dominate (Baars, 1997).

We have sampled (Fig. 3.1) turbiditic graywackes and pelites from the eastern, gold-producing Córrego do Sítio lineament, and the northern Cuiabá-Lamego gold deposit area, seeking to examine similarities and differences between them. The study intends to constrain the source of these sedimentary rocks, their tectonic setting and provenance, as well as possible exploration implications. To meet these purposes, whole-rock geochemistry, as well as U-Pb and Lu-Hf determinations on detrital zircon grains were applied. To further constrain the source of the Córrego do Sítio turbidites, in situ LA-ICP-MS analyses on the ore-sulfide minerals have also been undertaken, helping establish the hydrothermal stages experienced in selected deposits of this lineament.

### **3.2 Regional setting of the Quadrilátero Ferrífero-QF District and surroundings**

The Quadrilátero Ferrífero (QF) district is located in the southern part of the São Francisco Craton (Almeida, 1977; Teixeira and Figueiredo, 1994). The QF includes (Dorr et al., 1957; 1969): 1) granite-gneiss complexes, corresponding to the crystalline basement; 2) Archean greenstone belt

tracts belonging to the Rio das Velhas Supergroup; and 3) Proterozoic metasedimentary units, represented by the Minas Supergroup, the Itacolomi Group and the Espinhaço Supergroup (Fig. 3.1).

The Rio das Velhas greenstone belt corresponds to a metavolcanosedimentary sequence composed from the base to the top of the Nova Lima and Maquiné groups, respectively (Dorr et al., 1957; Almeida, 1977; Schorscher, 1978). The Nova Lima Group, shown on figure 3.2, comprises a basal unit formed by tholeiitic-komatiitic volcanic rocks, associated with chemical sedimentary rocks; a volcanoclastic intermediate unit, associated with felsic volcanism; and an upper unit with clastic sedimentary rocks (Ladeira 1980, 1991, Zucchetti and Baltazar 2000, Baltazar and Zucchetti 2007). Schorscher (1978) described komatiites at the base of the sequence, naming them the Quebra Osso Group. The largest gold deposits in the QF district, exemplified by Morro Velho, São Bento, Cuiabá, Lamego e Córrego do Sítio, are hosted in the Nova Lima Group (*e.g.*, Ladeira 1980, 1991; Lobato et al., 2001, 2016). The Maquiné Group, shown on figure 3.2, is composed (Gair, 1962) of sequences of graywacke and conglomerates deposited at ca. 2.73 Ga (Moreira et al., 2016).

The stratigraphic subdivision of the Rio das Velhas greenstone belt proposed by Zucchetti and Baltazar (2000) and Baltazar and Zucchetti (2007) is based on lithofacies associations that encompass, from the base to the top: (i) mafic-ultramafic volcanic rocks, with basalts, minor gabbro, anorthosite and peridotite, and intercalations of BIF, ferruginous chert, carbonaceous pelite, turbidites, and rare felsic volcanoclastic rocks. The ultramafic lavas are represented by peridotitic komatiites, in massive or pillowed flows, in places brecciated and with spinifex texture. Basalts dominate the association as massive and pillow flows, in places spilitized, with preserved primary textures such as varioles; (ii) volcano-chemical-sedimentary, with tholeiites intercalated with BIF-chert, and subordinate, fine-grained clastic sedimentary rocks, turbidites and pelites, intercalated with chemical rocks; (iii) clastic-chemical sedimentary, composed of alternating fine-grained micaceous and chloritic pelites with lesser BIF, and subordinate chert and carbonaceous pelite; (iv)

volcaniclastic, with felsic and mafic volcaniclastic rocks; (v) resedimented that is widely distributed in the QF, and comprises mainly graywackes, quartz graywackes, and siltstones. The features of this association indicate that it was deposited by turbidity currents of high and low densities; (vi) and (vii) coastal and non-marine associations corresponding to sandstone-siltstones and sandstones-conglomerates, respectively.

The U-Pb ages of detrital zircon from volcaniclastic rocks of the Nova Lima Group indicate felsic volcanism between 2.79-2.75 Ga (Machado and Carneiro, 1992; Noce 1998; Noce et al., 2007), and a minimum depositional age of 3.02 Ga (Machado et al., 1992).

The 2.60-2.10 Ga (Machado et al., 1996; Hartman et al., 2006) Minas Supergroup is subdivided into the Caraça, Itabira, Piracicaba and Sabará Groups (Dorr, 1969), all metamorphosed at low greenschist facies. The basal Caraça Group has metaconglomerate, quartzite and phyllite. The Itabira Group includes the Cauê Formation that hosts the great volume of Superior-lake BIF and iron orebodies in the region (Rosière et al., 2008). The Piracicaba Group is formed by phyllites and quartzites. The Sabará Group unconformably overlies the Piracicaba Group, and its deposition is considered about 2.12 Ga (Machado et al., 1996); it is a flysch sequence with metagraywacke, carbonaceous phyllite, metadiamicrites, metaconglomerates, and felsic to intermediate metavolcanic rocks (Dorr, 1969). The Itacolomi Group (Dorr, 1969) is the youngest unit in QF, resting unconformably on the Minas Supergroup, and contains quartzite, metarkose and metaconglomerate. The Paleo/Mesoproterozoic Espinhaço Supergroup covers a small area in the QF (Fig. 3.1). It is a rift sequence mainly with breccias, conglomerates and sandstone (*e.g.*, Brito-Neves et al., 1996).

The QF region has a geometry delineated by synform and antiform mega folds that, in its eastern portion, are truncated by north-south thrust faults (Baltazar and Zucchetti, 2007). Alkmin and Marshak (1998) describe in the QF a dome-and-keel structure, in which the basement occurs as domes (*e.g.* Bação, Bonfim, Santa Bárbara, etc.) that are circled by keels containing rocks of the Archean Rio das Velhas greenstone belt and the Minas Supergroup.

The structural evolution of the QF region took place in three main periods during the Rio das Velhas Orogeny (Baltazar and Zucchetti, 2007): between 2.8 and 2.67 Ga, which relates to the evolution of the Rio das Velhas greenstone belt; 2.10 to 1.90 Ga, the Transamazonian event; and the Brasiliano orogeny.

According to Alkmim and Marshak (1998), the Proterozoic tectonic evolution (Minas accretionary orogeny of Teixeira et al., 2015, from 2.35 to 2.00 Ga) took place in three main deformational phases. Fold and thrust belts shortly after 2.125 Ga; orogenic collapse with uplift of Archean granite-gneiss domes and formation of regional synclines at 2.09 Ga (Marshak and Alkmim, 1989); and the Brasiliano orogeny (0.7 – 0.45 Ga), with fold and thrust belts verging to the west.

South of the QF, the Mineiro belt (*e.g.*, Noce et al., 2000; Teixeira et al., 2000; Ávila et al., 2010) was created through successive accretion of oceanic and continental arcs during the Minas accretionary orogeny of Teixeira et al. (2015); it contains distinct granitoid suites dated between 2.36 and 2.12 Ga.

### **3.3 Geology of the Córrego do Sítio lineament and Cuiabá-Lamego gold deposits**

The description that follows refers to rocks that are metamorphosed; hence, the prefix “meta” applies to rock names but is hereafter omitted for brevity.

The sampled areas (Fig. 3.1) include turbidites belonging to the clastic sedimentary association (Baltazar and Zucchetti, 2007), which crops out at the Córrego do Sítio lineament (eastern sector; Fig. 3.1) and Cuiabá-Lamego gold deposit area (northern sector; Fig. 3.1). Turbidites host economic gold deposits at the eastern sector, whereas at the northern sector these rocks overlie the Cuiabá-Lamego lithostratigraphic mine sequences, and only locally are loci to gold occurrences (Vial et al., 2007).

Deposits of the Córrego do Sítio lineament (Lima, 2012; Roncato et al., 2015) are structurally controlled by the Gandarela Syncline and the Conceição Anticline, and are truncated by the Fundação and Água Quente fault systems (Martins Pereira, 2007; Lima, 2012).

The Córrego do Sítio Unit is dominated by rocks of the resedimented and clastic-chemical sedimentary lithofacies association. In the study area, these correspond to an alternation of pelites and psamites, with gradational layering, plane-parallel and cross-bedding stratification. Subordinate thin levels of carbonaceous pelite and BIF are present. These units are interpreted by Zucchetti et al. (1998) as a result of deposition by turbidity currents. The rocks from these units are classified as quartz-carbonate-mica-chlorite schists, and represent the greenschists facies metamorphism of graywackes, sandstones and pelites. Also present is a swarm of mafic dikes and sills, possessing various orientations, with the predominance of the NE-SW direction, dipping towards SE, and in general subparallel to the metasedimentary sequence (Porto, 2008; Lima, 2012; Roncato et al., 2015). These are mafic tabular bodies of metric and decametric thickness, and kilometric continuity, composed of fine-grained gabbros variably hydrothermally altered to carbonate, chlorite and sericite; near the orebodies, especially in the Cachorro Bravo deposit (Fig. 3.1), dikes are replaced by sulfides (Porto, 2008; Lima, 2012, Ribeiro et al., 2015, Roncato et al., 2015). Their age is still debatable, because these rocks lodge an enormous amount of inherited zircons from their host rocks, therefore not exhibit reliable geochronological data. David (2006) obtained  $2.69 \pm 0.034$  Ga by U-Pb SHRIMP on zircon.

Gold mineralization in the Córrego do Sítio lineament is structurally controlled and associated with hydrothermal alteration that gave place to the development of chlorite, carbonate, sericite, sulfide-sulfosalt minerals, and massive amounts of silica. Because of the nature of the sedimentary rocks, the contrast between pre-altered and altered sequences is very subtle, and has been dealt with in detail by Ribeiro et al. (2015) and Roncato et al. (2015). The sampled deposits for the present study are Cachorro Bravo, Laranjeiras and Carvoaria (Fig. 3.1).

The Cuiabá-Lamego gold deposit area (Fig. 3.1) is in the intermediate part of the Nova Lima Group, of the volcanoclastic and clastic sedimentary associations (Baltazar and Zucchetti, 2007). Both Cuiabá and Lamego represent tectonic windows in the area, exposing rocks that are

underneath these associations. Cuiabá (*e.g.*, Ribeiro Rodrigues et al., 2007, Lobato et al., 2005) and Lamego (Martins, 2011; Morales et al., 2016; Martins et al. 2016) are BIF-hosted gold deposits, marked by the contour of the large-scale Cuiabá and Lamego folds, respectively. For the case of Lamego, Martins et al. (2016) interpreted it as a rootless, reclined, isoclinal, cylindrical fold with an axial trace striking northeast-southwest, with a thickened hinge zone plunging parallel to the thinned limbs dipping 20° to 30° to the SE.

The lithological succession at Cuiabá includes volcanic, volcanoclastic and other sedimentary rocks (*e.g.*, Ribeiro Rodrigues et al., 2007). Rock types are described as lower and upper mafic volcanic rocks, the Cuiabá BIF, micaceous and carbonaceous pelites, volcanoclastic rocks and mafic dikes. The lower unit is characterized by a succession of mafic volcanics rocks interbedded with micaceous pelites and lenses of carbonaceous pelites. Mafic volcanics rocks are characterized by the presence of chlorite, epidote, plagioclase and actinolite and quartz as an alteration minerals. The BIF is characterized by alternating dark (rich in carbonaceous matter), carbonate-quartz ( $\pm$ magnetite) and light quartz-carbonate bands. The upper unit is constituted of pelites alternating with volcanoclastics rocks. Mafic dikes crosscut all rock types.

A concordant lithostratigraphic package of volcano-sedimentary rocks host the Lamego deposit (Sales, 1998; Martins et al., 2016). From bottom to top the lithostratigraphy at the Lamego deposit is defined by mafic volcanic rocks represented by basalt variably hydrothermally altered and schistose; banded chert with BIF that are both carbonaceous and/or ferruginous (the Lamego BIF); and carbonaceous and micaceous pelites (phyllites), which envelop the entire Lamego deposit (Martins et al., 2016). The Lamego BIF is composed of similar constituents as those of the Cuiabá mine, except that here the cherty component predominates. Diabase intrusions develop as dikes and sills.

The carbonaceous and micaceous pelites that overlie the Cuiabá and Lamego deposits, sampled for the present study (Fig. 3.1), are at the top of the stratigraphic succession. The carbonaceous pelite

(carbonaceous matter, quartz, chlorite, carbonate and minor sericite) is dark, finely laminated and thinly bedded. The micaceous pelite (sericite, muscovite, quartz, carbonate and minor carbonaceous matter) displays gradational and compositional stratification (Martins et al., 2016).

### **3.4 Methods**

Seventeen samples of graywackes and pelites were collected from fresh boreholes across the strike direction in different deposits of the Córrego do Sítio auriferous lineament and the Cuiabá-Lamego gold deposit area (Fig. 3.1). Geochemical and geochronological analyses were carried out on 17 samples. Whole-rock geochemical analyses were carried out at the Acme Labs/Bureau Veritas Commodities Canada Ltd., Vancouver, Canada. Major elements were analyzed by X-ray fluorescence spectrometry (XRF). Trace and REE elements concentrations were determined by ICP-ES/MS.

### **3.5 Analytical isotope methods**

A total of nine drill cores of the Nova Lima Group were sampled, alternating graywackes and pelites in a turbidite sequence of the clastic sedimentary association of Baltazar and Zucchetti (2007). Six are from the eastern (Cachorro Bravo – FCS0756-MG/PL, FCS1053-MG; Laranjeiras – FCS0831-MG/PL, FCS0929-MG/PL; and Carvoaria – FCS1196-MG, FCS1261-MG deposits), and three from the northern (Cuiabá – CBABSD04B-MG, CBABSD04B-PL and Lamego – CARBSD15-PL deposits) sectors of the QF district. Sampled areas are shown in Figure 3.1. Figure 3.2 shows the schematic drill core logs of the clastic sedimentary association (Baltazar and Zucchetti, 2007) and sampled locations of Córrego do Sítio lineament (A), Cuiabá (B) and Lamego (C) deposits.

#### **3.5.1 U-Pb Determinations**

The U-Pb isotopes were analyzed at the Department of Geology, Universidade Federal de Ouro Preto, Brazil. The technique of zircon separation uses a jaw crusher, milling and manual panning,

hand-picking under binocular microscope, with grains mounted on 25 mm epoxy (SpeciFix) mounts. Mounts were polished and imaged under SEM.

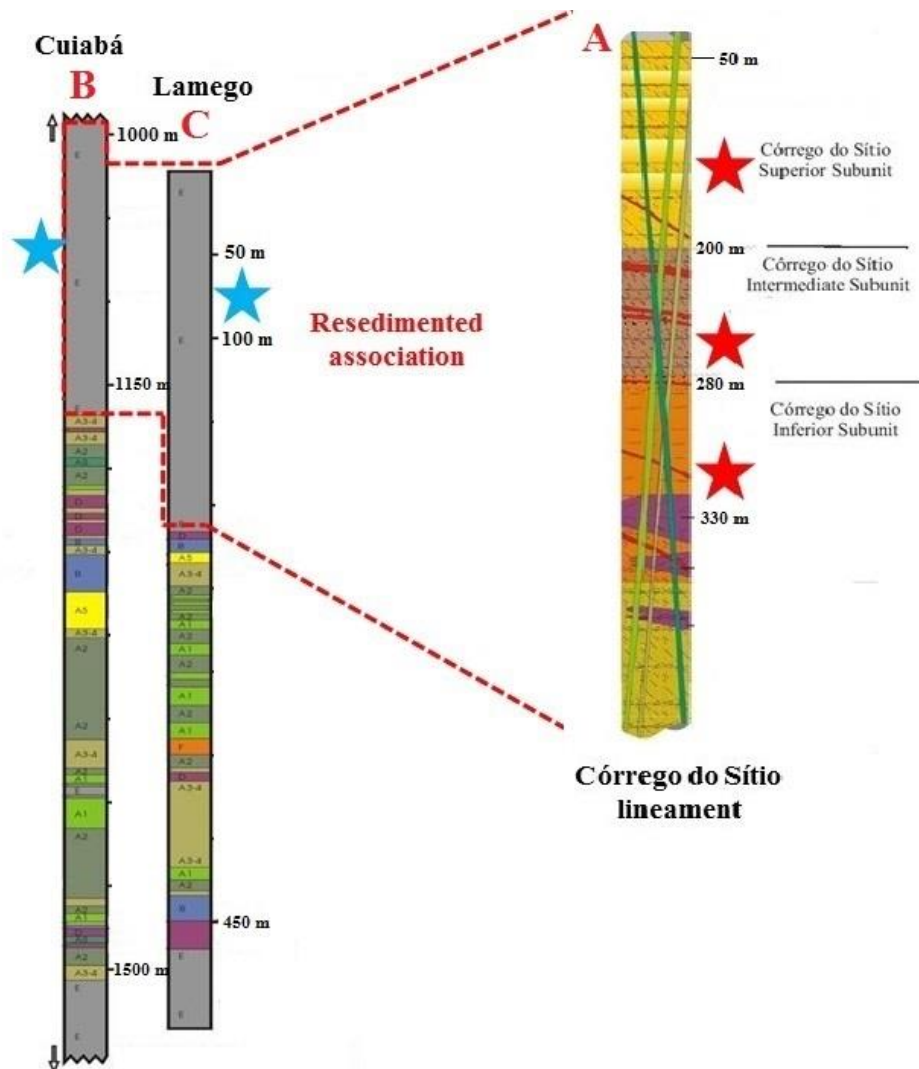


Figure 3.2. Schematic drill core logs of the clastic sedimentary association in the Córrego do Sítio lineament (A), Cuiabá (B) and Lamego (C) deposits. The stars indicate the sampled location for the eastern (red) and northern (blue) sectors. For detailed stratigraphic sequences of the Córrego do Sítio lineament (A) see Roncato et al. (2015) and the Cuiabá-Lamego gold deposit area (B and C) see Martins et al. (2016).

Seventeen different samples extracted from underground drill holes were used (Table 1). Zircons were analyzed using a Thermo-Finnigan Element 2 sector field ICP-MS coupled to a CETAC213 ultraviolet laser system. A laser spot size of 20  $\mu\text{m}$  was used (e.g., Farina et al., 2015). The typical depth of the ablation crater was 15-20  $\mu\text{m}$ . Data were acquired in peak jumping mode during 20 s



background measurement followed by 20 s sample ablation. Signal was tuned for maximum sensitivity for Pb and U while keeping oxide production well below 1%. Raw data were corrected for background signal, common Pb, laser-induced elemental fractionation, instrumental mass discrimination, and time-dependent elemental fractionation of Pb/U using an in-house MS Excel spreadsheet program. The common Pb correction was based on the Pb composition model (Stacey and Kramers, 1975). Laser-induced elemental fractionation and instrumental mass discrimination were corrected by normalization to the reference zircon GJ-1 (Jackson et al., 2004), which was analyzed during the analytical session under exactly the same conditions as the samples. Prior to this normalization, the drift in elemental fractionation was corrected by applying a linear regression through all measured ratios, excluding the outliers ( $N \pm 2$  S.D.), and using the intercept with the y-axis as the initial ratio. The total offset of the measured drift-corrected  $^{206}\text{Pb}/^{238}\text{U}$  ratio from the “true” IDTIMS value of the analyzed GJ-1 grain was typically around 1-3%. Reported uncertainties ( $2\sigma$ ) were propagated by quadratic addition of the external reproducibility (2 S.D.) obtained from the zircon reference material GJ-1 during the individual analytical session. Signal data were reduced using the software Glitter (Van Achterbergh et al., 2001); plotting and age were calculated using the Excel Isoplot program (Ludwig, 2012). The data reduction included the correction of fractionation problems and of errors in the masses counting. For both U-Pb methods, > 5% discordant zircons were not used to construct the distribution diagrams since they have no composition quality maintained and pinpoint unreliable ages.

### **3.5.2 Lu-Hf Measurements**

Lutetium and Hf isotope analyses were carried out at Universidade Federal de Ouro Preto using a Thermo-Finnigan Neptune multicollector ICP-MS coupled to a Photon- Machine 193 nm laser system. Data were collected in static mode during 60 s of ablation with a spot size of 40  $\mu\text{m}$ . The spots were drilled with a repetition rate of 6 Hz. Typical signal intensity was ca. 10 V for  $^{180}\text{Hf}$ . The  $^{172}\text{Yb}$ ,  $^{173}\text{Yb}$  and  $^{175}\text{Lu}$  isotopes were simultaneously monitored during each analysis step to allow

for correction of isobaric interferences of Lu and isotopes on mass 176. The accuracy and external reproducibility were verified by repeated analyses of the standard zircons Mud tank (Woodhead and Hergt, 2005), which yielded  $^{176}\text{Hf}/^{177}\text{Hf}$  of  $0.282504 \pm 0.000040$ , respectively.

### 3.5.3 Analytical EPMA methods

Electron microprobe analyses (EMPA) of arsenic in all sulfide minerals were performed at the Centre for Microscopy, Characterisation and Analysis (CMCA), at The University of Western Australia (UWA). The microprobe used was a Jeol 8530F, with an accelerating voltage of 20 kV, beam current of 50 nA and an electron beam with 1  $\mu\text{m}$  in diameter. The following elements were analyzed: Fe ( $\text{K}\alpha$ ), Au ( $\text{L}\alpha$ ), Te ( $\text{L}\alpha$ ), Ni( $\text{K}\alpha$ ), Hg ( $\text{L}\alpha$ ), Zn ( $\text{K}\alpha$ ), Cu ( $\text{K}\alpha$ ), Co ( $\text{K}\alpha$ ), V ( $\text{K}\alpha$ ), Ti ( $\text{K}\alpha$ ), on LiF crystal; Sb ( $\text{L}\alpha$ ), Pb ( $\text{M}\alpha$ ), and Bi ( $\text{M}\beta$ ) on PETH crystal; S ( $\text{K}\alpha$ ), Ag ( $\text{L}\alpha$ ) and Cd ( $\text{L}\alpha$ ) on PETJ crystal; and As ( $\text{L}\alpha$ ) and Se ( $\text{L}\alpha$ ) on TAP crystal. In order to improve count rate statistics, counting times were 20 s for Fe and S, 60 s for As, Cu, Ni, Se, Zn, and Co and 120 s for Pb, Ag, Sb, Te, Au, Hg, Cd, V, Ti and Bi.

Standards used for calibration were  $\text{Fe}_3\text{O}_4$  (magnetite for Fe),  $\text{FeS}_2$  (pyrite for S and Fe), FeAsS (arsenopyrite for As), PbS (galena for Pb),  $\text{Bi}_2\text{Se}_3$  (for Bi and Se), Ag (silver for Ag), HgS (cinnabar for Hg), ZnO (for Zn),  $\text{CuFeS}_2$  (chalcopyrite for Cu), NiS (millerite for Ni),  $\text{Sb}_2\text{Te}_3$  (for Sb and Te),  $\text{TiO}_2$  (rutile for Ti), cobalt (for Co), cadmium (for Cd), and vanadium (for V).

The analyses of Au used Au( $\text{L}\alpha$ ) on LIF to avoid interferences between Au( $\text{M}\alpha$ ,  $\text{M}\beta$ ) lines and Hg( $\text{M}\beta$ ) and Te( $\text{L}\alpha$ ), respectively, noted on PETH; Hg( $\text{L}\alpha$ ) on LIF crystal instead of PETH to avoid interference with Au( $\text{M}\beta$ ); Te( $\text{L}\alpha$ ) on LLIF to avoid contribution from Ni( $\text{K}\alpha$ ) on PETH. The Bi( $\text{M}\beta$ ) line was used instead of Bi( $\text{M}\alpha$ ), to avoid interference with Pb ( $\text{M}\beta$ ). The correction factor for Pb( $\text{M}\alpha$ ) for contribution from S( $\text{K}\alpha$ ) was applied

Electron probe maps were collected using accelerating voltage of 20 kV, beam current of 50 nA, and a counting time of 20 ms/step to Fe ( $\text{K}\alpha$ ) and S( $\text{K}\alpha$ ), and 60 ms/step to Ti( $\text{M}\alpha$ ), Hf( $\text{M}\alpha$ ), As( $\text{L}\alpha$ ), Au( $\text{L}\alpha$ ), Ag( $\text{L}\alpha$ ), Ni( $\text{K}\alpha$ ), Sb( $\text{L}\alpha$ ), Co( $\text{K}\alpha$ ) and Mn( $\text{K}\alpha$ ). For the specific case of the geochemical

distribution maps on sulfides, the standards used for Tl and Hf were TlBr/TlI and hafnium, respectively.

### 3.5.4 In situ LA-ICP-MS analyses on sulfide minerals

The study on the compositional data of sulfide minerals in the Córrego do Sítio lineament is an important part of the studies that focuses on the turbidite-hosted of the Laranjeiras (porous and smooth pyrite - P-Py and S-Py; smooth pyrrhotite - S-Po; porous and smooth arsenopyrite - P-Apy and S-Apy) and Cachorro Bravo (smooth pyrite - S-Py) gold deposits (Figs. 3.1 and 3.3), using analyses by in-situ LA-ICP-MS technique and electron microprobe for the determination of arsenic.

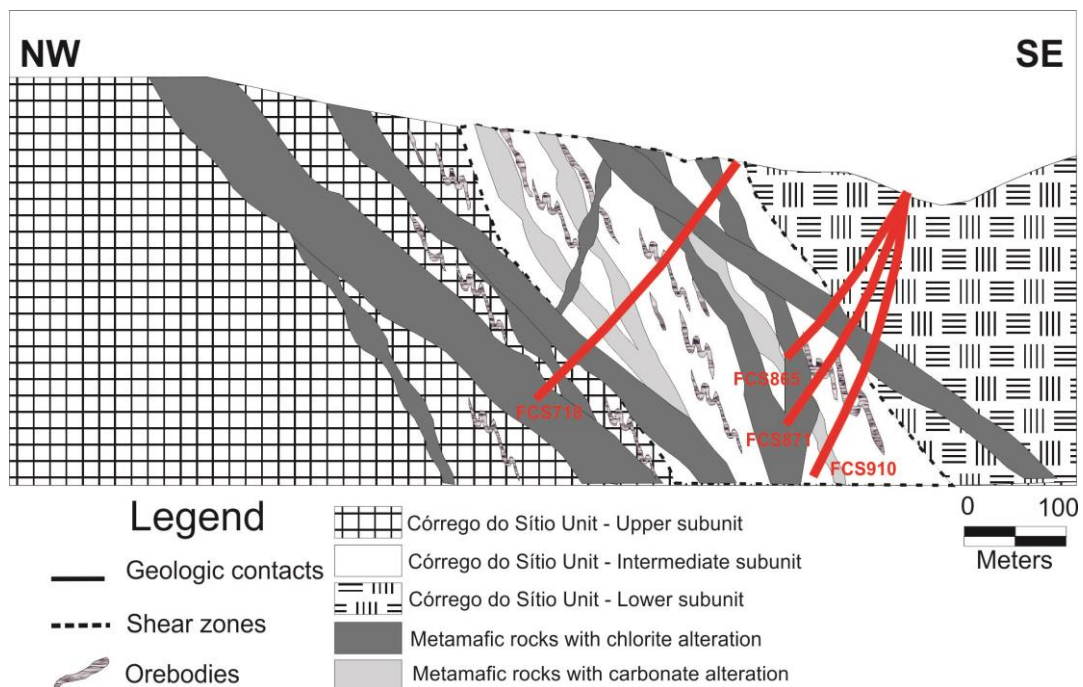


**Figure 3.3. Schematic NW-SE geological cross section of the Córrego do Sítio lineament, eastern sector, showing the extrapolated position of the drill holes of AngloGold Ashanti Brasil Mineração - AGA. Units and subunits according to Lima (2012).**

Trace elements contained in sulfide minerals were analyzed at CODES, University of Tasmania, using LA-ICP-MS. A total of 10 pyrite, 3 pyrrhotite and 4 arsenopyrite spots were analyzed. These are contained in six rock samples from the Cachorro Bravo, Laranjeiras and Carvoaria deposits, Córrego do Sítio lineament (Table 3). The study intends to understand the in situ LA-ICP-MS analyses on the ore-sulfide minerals of the lineament, helping establish the hydrothermal stages

experienced in selected deposits of this lineament and compare with the future results in the Cuiabá-Lamego area.

The minerals and matrix were analyzed *in situ* via polished laser mounts. For details of the preparation of laser mounts see Gregory (2014). These samples were selected for sulfide trace element analyses using the LA-ICP-MS technique.

The analytical instrumentation engaged in this study consists of a New Wave UP-213 nm laser ablation system coupled with an Agilent 7700s Quadrupole ICP-MS. The methodology is described in detail by Large et al. (2009) and briefly introduced here.

Depending on the sulfides size, analyses were performed by laser ablating spot diameters of 15-43  $\mu\text{m}$  and at a repetition rate of 5 Hz. The laser beam energy used was 90 mJ and the fluence was maintained between 2.7 and 5.0  $\text{J cm}^{-2}$ . The analysis time for each sample was 90 s, which includes 30 s of background measurement with laser off and 60 s of analysis with laser on. Acquisition time for all masses was set to 0.02 s, with a total sweep time of  $\sim 0.6$  s.

Data reduction was performed according to standard methods (Longerich et al., 1996), with Fe as the internal standard. Calibration was performed using the in-house standard (STDGL2b-2), comprising powdered sulfides doped with certified element solutions and fused to a lithium borate glass disk (Danyushevsky et al., 2011). The standard was analyzed twice every 1.5 h with a 100- $\mu\text{m}$  beam size at 10 Hz to correct for instrument drift. Accuracy is expected to be better than 20% for most elements (Danyushevsky et al., 2011). A set of 35 elements was chosen for spot analyses ( $\text{Na}^{23}$ ,  $\text{Mg}^{24}$ ,  $\text{Al}^{27}$ ,  $\text{Si}^{29}$ ,  $\text{Ca}^{43}$ ,  $\text{Ti}^{49}$ ,  $\text{V}^{51}$ ,  $\text{Cr}^{53}$ ,  $\text{Mn}^{55}$ ,  $\text{Fe}^{57}$ ,  $\text{Co}^{59}$ ,  $\text{Ni}^{60}$ ,  $\text{Cu}^{65}$ ,  $\text{Zn}^{66}$ ,  $\text{As}^{75}$ ,  $\text{Se}^{77}$ ,  $\text{Zr}^{90}$ ,  $\text{Mo}^{95}$ ,  $\text{Ag}^{107}$ ,  $\text{Cd}^{111}$ ,  $\text{Sn}^{118}$ ,  $\text{Sb}^{121}$ ,  $\text{Te}^{125}$ ,  $\text{Gd}^{157}$ ,  $\text{Hf}^{178}$ ,  $\text{Ta}^{181}$ ,  $\text{W}^{182}$ ,  $\text{Pt}^{195}$ ,  $\text{Au}^{197}$ ,  $\text{Hg}^{202}$ ,  $\text{Tl}^{205}$ ,  $\text{Pb}^{206, 207, 208}$ ,  $\text{Bi}^{209}$ ,  $\text{Th}^{232}$  and  $\text{U}^{238}$ ).

### **3.6 Turbidites of the Córrego do Sítio lineament**

The Rio das Velhas Orogenic Event (Carneiro, 1992), reworking of Archean sialic crust, intrusion of tonalitic bodies and felsic volcanism of the Rio das Velhas greenstone belt (Baltazar and

Zucchetti, 2007). The clastic sedimentary rocks of the upper unit of the greenstone belt are dominated by graywacke–argillite sequences, with evidence of significant contribution in the turbidites from both the felsic volcanic rocks of the greenstone belt and the reworked ancient Archean crust.

The clastic association is distributed in the Cuadrilátero Ferrífero, it includes three different sequences of graywacke-argillite, two metamorphosed in the greenschist facies in the northern and eastern sectors (they are composed mainly of graywackes, quartz graywackes, sandstones and siltstones, with cyclic layers and abrupt basal contacts between cycles) and one in the amphibolite facies in the south. In the eastern and northern sectors (Baltazar and Zucchetti, 2007; Roncato et al., 2015).

### **3.6.1 Petrographic studies**

In the eastern sector, graywackes in all deposits are gray to light-green (Fig. 3.4A), fine- to coarse-grained rocks, where the original clasts are angular and reach 2 mm. Quartz can make up 70-80% of the rock volume, with several shapes, and commonly recrystallized; white mica (10%) and incipiently saussuritized, coarse-grained plagioclase (5-10%) are also present (Fig. 3.4C). Epidote, zircon, rutile and sulfides are common accessory minerals, which may be in part hydrothermal. Oriented white mica imprints the main foliation planes between quartz grains.

Pelites are very fine-grained dark gray rocks, with a well defined bedding plane. They exhibit a lepidoblastic texture, and contain white mica (60-70%), quartz (15-25%) and oriented occurrence of carbonaceous matter (10-40%), along the foliation. Plagioclase, epidote and rutile are also common. Hydrothermal phases such as carbonate, chlorite and sulfide minerals may occur.

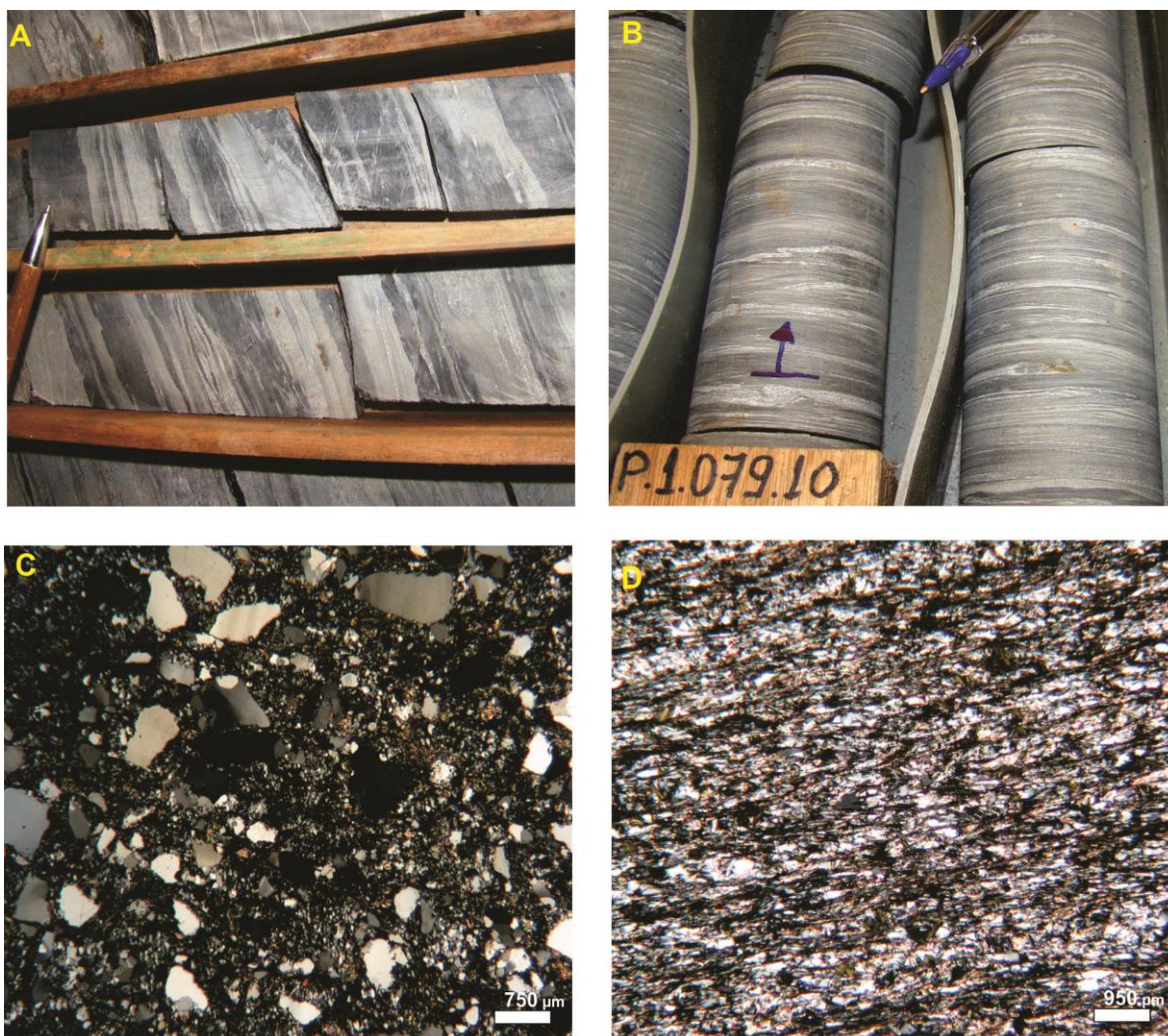


Figure 3.4. Rocks of the clastic sedimentary association from the eastern (A) and northern (B) sectors of the Quadrilátero Ferrífero district, showing alternating pelitic (dark) and psamitic (clear) bands. Photomicrographs of graywacke (C, eastern) and pelite (D, northern); transmitted light, crossed polars, 25X.

### 3.6.2 Hydrothermal alteration in gold deposits of the Córrego do Sítio lineament

Gold mineralization at the Córrego do Sítio turbidite sequence is characterized mainly spatially associated with silification zones, represented by the development of quartz veins and veinlets, carbonate, sericite and sulfide minerals (Lima, 2012; Ribeiro et al., 2015; Roncato et al., 2015; Fig. 3.5), which results from hydrothermal alteration (e.g. replacement) of the previous rock. Mineralogical and textural transformations accompanying wall-rock alteration are observed surrounding the main mineralized vein systems. A review of the generations of quartz veins is found in Sequetto Pereira et al. (2014) and (Ribeiro et al., 2015), with the latter having detailed their fluid inclusions.

Although the limits between the alteration zones are not always sharp and regular at Córrego do Sítio, they have a somewhat parallel distribution in relation to the veins, and their characterization is made possible particularly where the host rock is graywacke. In the case of pelites in general, the hydrothermal alteration halos are often narrow, discrete or apparently absent. Locally, alteration halos can be observed with carbonate and sericite plus quartz, where rocks have been bleached mainly in the original carbonaceous and-or graywacke portions.

There are two main distinct hydrothermal alteration assemblages of the host sedimentary rocks, which depend on the proximity to mafic dikes. The Cachorro Bravo deposit (Fig. 3.1) is closely limited on both sides by mafic dikes and sills, but these igneous intrusions are located farther away in the Laranjeiras and Carvoaria deposits. In Cachorro Bravo, chlorite and pyrrhotite (not pyrite) dominate, whereas at Laranjeiras and Carvoaria, berthierite, stibnite and pyrite are part of the distinct mineral assemblage (*e.g.*, Roncato et al., 2015).

Gold is mainly present as free particles and disseminated in quartz-carbonate veins mainly in Laranjeiras deposit. In Cachorro Bravo deposit, the substitution is the main form of hydrothermal alteration. It also forms inclusions in disseminated arsenopyrite, pyrite or pyrrhotite, as well as in other silicates and berthierite.

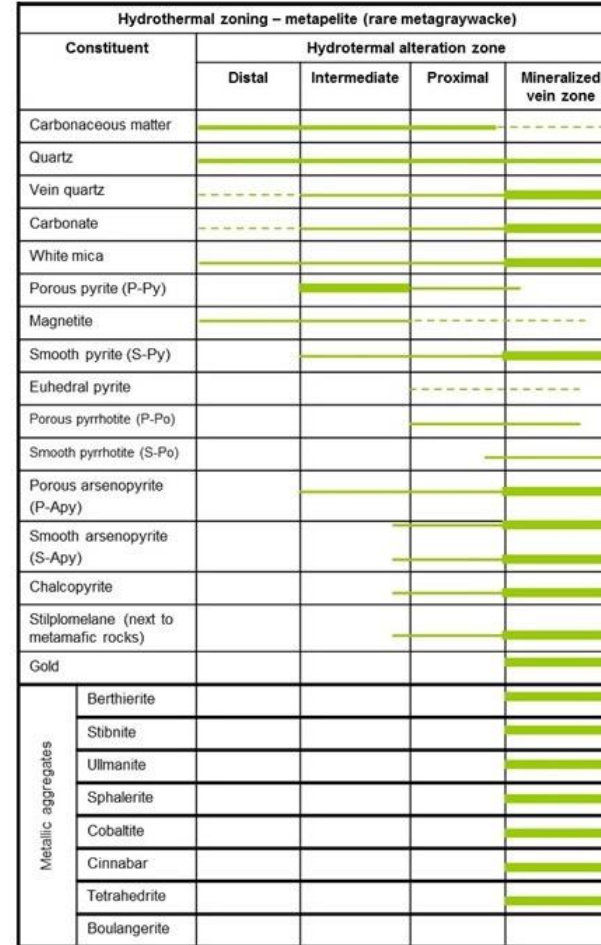
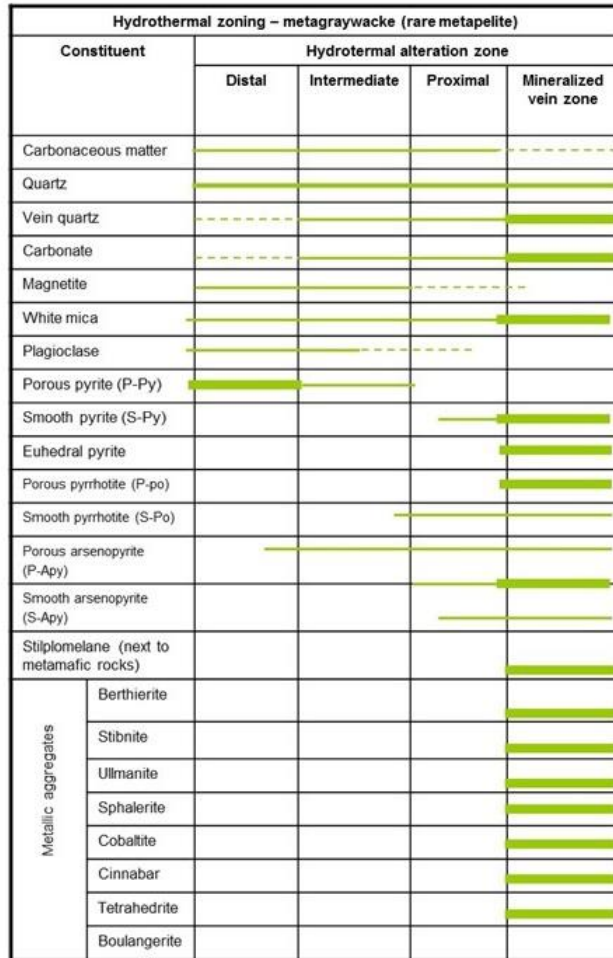


Figure 3.5. Hydrothermal Spatial zoning of hydrothermal minerals, including main sulfide minerals associated with gold in (A) greywackes (B) pelite, Córrego do Sítio auriferous lineament. Line thicknesses represent schematically the relative quantities of each mineral (after Roncato et al., 2015).



### 3.6.3 Textural features and paragenetic sequence of ore minerals

Ore minerals at the Córrego do Sítio lineament have been described mainly by Canale (1999), Porto (2008), Lima (2012), Ribeiro et al. (2015), and Roncato et al. (2015). The latter three publications structured them in paragenetic sequences, which are summarized in Figure 3.6. Sulfide minerals are present mainly along the edges of veins, with pyrite being the most common. In the hydrothermal zones, arsenopyrite forms after pyrite or pyrrhotite, both locally seen to originate from the consumption of magnetite. Near the metamafic dikes, especially in the Cachorro Bravo deposit, arsenopyrite develops after pyrrhotite in mineralized veins and veinlets. The pyrrhotite/arsenopyrite association along dike zones may reflect local conditions of relatively higher temperature (Ribeiro et al., 2015; Roncato et al., 2015).

Arsenopyrite after pyrite is typical of alteration zones far from metamafic dikes, where veins are dominated by smoky quartz-carbonate veins with berthierite, stibnite and pyrite, and gold. In the Sb-Au-quartz veins, berthierite and stibnite are the most abundant Sb-bearing minerals. This mineralization style is mainly observed in carbonaceous pelites, and has a gold-dominated association with porous arsenopyrite, which is the predominant gold-associated sulfide mineral in the Córrego do Sítio lineament.

Opaque minerals in trace amounts include chalcopyrite, galena, sphalerite, berthierite and tetrahedrite. Other hydrothermal minerals are quartz, carbonate, white mica, chlorite and accessory rutile, titanite, apatite, ilmenite and sphalerite. Some of these minerals are also present in the unaltered metasedimentary rocks to varying degrees.

Four pyrite generations have long been recognized, and are here designated porous pyrite (P-Py), smooth pyrite (S-Py), porous pyrrhotite (P-Po), smooth pyrrhotite (S-Po), porous arsenopyrite (P-Apy), and smooth arsenopyrite (S-Apy): i) isolated and disseminated Primary rounded pyrite in non-altered carbonaceous layers that commonly form subrounded aggregates (Fig. 3.7A); ii) ± P-Py, which may contain gold, associated with a myriad of other sulfide minerals, and that may be

replaced by arsenopyrite (Fig. 3.7B); iii) S-Py overgrowths forming irregular contours around P-Py (Fig. 3.7B); and iv) late-stage, euhedral pyrite in isolated and randomly distributed grains (Fig. 3.7C) apparently resulting from the detachment of smooth pyrite.

PARAGENETIC SEQUENCE OF ORE MINERALS					
Minerals	Sedimentation	Deformation/Metamorphism/Hydrothermalism			Characteristics
Primary rounded pyrite*	████████████████████				Microeuhedral, rounded
Porous pyrrhotite (P-Po)		██			Coarse-grained, anhedral
Smooth pyrrhotite (S-Po)			██		Coarse-grained, euhedral, clear
Porous pyrite (P-Py)		██			Coarse-grained, anhedral
Smooth pyrite (S-Py)			██		Coarse-grained, euhedral, clear
Porous arsenopyrite (P-Apy)		██			Coarse-grained, anhedral to subhedral
Smooth arsenopyrite (S-Apy)			██		Anhedral and subhedral, smooth in prisms or needles
Gold	██				See text
*Berthierite			██		Associated with the main sulfide minerals
*Chalcopyrite		██			Coarse-grained, anhedral to subhedral
*Euhedral Pyrite				██	Isolated crystals from borders of the porous pyrite

\*Not analyzed by LA-ICP-MS

**Figure 3.6. Paragenetic sequence of ore minerals and their characteristics with the advance of hydrothermal alteration – Córrego do Sítio lineament (modified after Roncato et al., 2015).**

Early-stage, P-Po may be replaced by S-Po (Fig. 3.7D), and P-Po was formed before, but is in equilibrium with S-Po. P-Po is marked as stable during all mineralization stage (Fig. 3.6). Two generations of arsenopyrite are identified: i) P-Apy in anhedral to subhedral crystals (Fig. 3.7F) associated with pyrite or pyrrhotite, preserving the original habit and porosity of the latter sulfides, and (ii) S-Apy in subhedral, very fine-grained crystals, in prisms or needles (Fig. 3.7E).

Berthierite is commonly associated with the main sulfide minerals in the mineralized sedimentary rocks (Fig. 3.7G), mainly in quartz (smoky)-carbonate-sulfide-berthierite veins. Both porous pyrrhotite and pyrite occur in the core of sulfide crystal aggregates (Fig. 3.7H), with berthierite, chalcopyrite and gold.

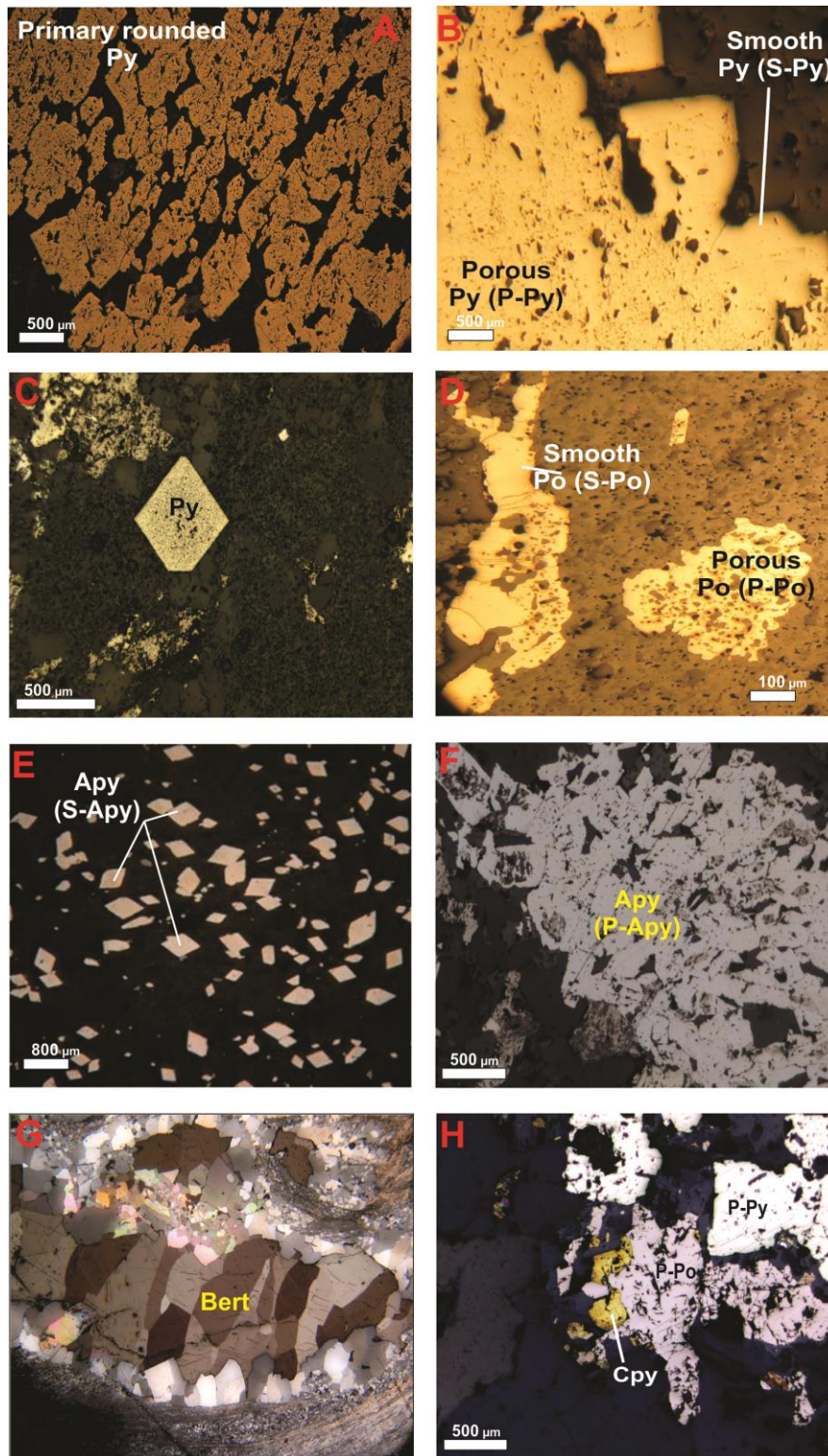


Figure 3.7. Photomicrographs of generations of ore minerals associated with Laranjeiras gold deposit of the Córrego do Sítio lineament. (A) Primary rounded pyrite (reflected light-RL, crossed nicols- CN; not analyzed in the LA-ICP-MS study). (B): ± Porous replaced by smooth pyrite – P-Py / S-Py (RL, CN). (C): Euhedral pyrite (RL, CN; not analyzed in this study). (D): Porous pyrrhotite replaced by smooth pyrrhotite – P-Po / S-Po (RL, CN). (E): Smooth euhedral, acicular arsenopyrite – S-Apy (RL, CN), (F): Porous anhedral to subhedral arsenopyrite – P-Apy (RL, CN). (G): Subhedral to euhedral berthierite in vugs (RL, CN, 50X). (H): Sulfide crystal aggregates (RL, CN, 50X). Apy: arsenopyrite; Bert: berthierite; Cpy: chalcopyrite; Py: pyrite; Po: pyrrhotite.

### **3.6.4 In-situ LA-ICP-MS in Trace elements of eastern sector**

The low detection limit and simultaneous capture of data for up to 20 trace elements make the LA-ICP-MS a powerful analytical tool for understanding hydrothermal mineral genesis and evolution. The sulfide minerals commonly contain a wide range of enriched trace elements (Fig. 3.8), which are described for each mineral. The trace element abundance (Fig. 3.8) and the data obtained are presented in Table 3.3.

The P-Py and S-Py from the Laranjeiras and the S-Py from the Cachorro Bravo deposits are consistently enriched in As, Ni, Cu, Co, Cr, Se, Pb, Sb, Zn, Ag, Sn, Te, W and Au, following this order of elements (Fig. 3.8A). Many of them are generally within the structure of sulfide grains, or may be distributed as nanoinclusions.

For S-Po (Fig. 3.8B) of the Laranjeiras deposit shows an enrichment similar to the generations of previously described pyrites, with the exception of As, which occurs with less abundance than Ni and Cu. The difference between analyses of P-Apy and S-Apy from Laranjeiras and the sulfides previously described is the elements are As, Co, Te, Ni, Sb, Bi, Se, Pb, Cu, Cd, Ag, Zn and Au, in order of abundance (Fig. 3.8C).

Cobalt correlates moderately well with Ni and Te in the majority of analyzed sulfide grains. Similarly to Ni, Co tends to be incorporated into the structure of pyrite and other sulfide minerals, or to be evenly distributed as nanoinclusions.

### **3.6.5 Composition of pyrites, pyrrhotites and arsenopyrites**

The present study analyzed P-Py, S-Py, S-Po, P-Apy and S-Apy from the Laranjeiras deposit (Table 3). Smooth pyrites from the Cachorro Bravo deposit were analyzed to compare the early hydrothermal stage of both deposits (Fig. 3.9). Sedimentary, primary rounded pyrite has not been investigated, but rather pyrites similar to those classified by Large et al. (2009) as porous Py-3 and euhedral Py-4.

#### 3.6.5.1 Porous pyrite (P-Py) composition

The P-Py from the Laranjeiras deposit (Table 3; Fig. 3.9) contains a wide range of trace elements, the most abundant of which are Ni (46-1332 ppm), Cu (0.11-41 ppm), Co (11-228 ppm), Cr (0.10-34 ppm), Se (31-41 ppm), Pb (0.37-45 ppm), Sb (0.54-55 ppm), Zn (0.22-7.30 ppm), Ag (0.01-0.84 ppm), Sn (0.1-1.0 ppm), Te (0.27-25 ppm) and W (0.01-0.18 ppm). The invisible gold content varies from 0.00032 to 0.73 ppm, whereas arsenic varies from 248 to 2998 ppm.

#### 3.6.5.2 Laranjeiras smooth pyrite (S-Py) composition

The gold content (Table 3; Fig. 3.9) of S-Py from the Laranjeiras deposit varies from 0.00047 to 0.023 ppm and arsenic varies from 436 to 777 ppm. The Ni (2.9-32 ppm), Cu (0.17-0.61 ppm), Co (0.27-52 ppm), Cr (0.01-21 ppm), Se (4.33-4.87 ppm), Pb (undetected to 3.84 ppm), Sb (2.92-3.52 ppm), Zn (0.48-13 ppm), Ag (0.33-1.7 ppm), Sn (0.13-0.18 ppm), and W (undetected to 1.24 ppm) are representative of the most abundant elements.

#### 3.6.5.3 Smooth pyrrhotite (S-Po) composition

The S-Po from the Laranjeiras deposit contains Ni (236-543 ppm), Cu (123-747 ppm), Co (38-67 ppm), Cr (13-458 ppm), Se (6.35-7.72 ppm), Pb (0.28-11 ppm), Sb (1.43-17 ppm), Zn (0.43-34 ppm), Ag (0.19-3.57 ppm), Sn (0.42-4.42 ppm), Te (0.16-0.52 ppm), W (undetected to 0.92 ppm), and Mo (0.04 ppm). The gold content varies from 0.004 to 0.052 ppm, and arsenic is 358 ppm (Table 3.3; Fig. 3.9).

#### 3.6.5.4 Porous arsenopyrite (P-Apy) composition

The Laranjeiras P-Apy contains (Table 3.3; Fig. 9) As (445007 ppm), Co (24-618 ppm), Te (1.38-2305 ppm), Ni (54-435 ppm), Sb (0.05-263 ppm), Se (6.40 ppm), Pb (11.67 ppm), Cu (2.0-10 ppm), Cd (0.03-5.63 ppm), Ag (0.42-7.61 ppm), Zn (1.18-1.69 ppm) and Au (0.01-135 ppm).

#### 3.6.5.5 Smooth arsenopyrite (S-Apy) composition

The Laranjeiras P-Apy (Table 3; Fig. 3.9) contains As (438266-442244 ppm), Co (392-1725 ppm), Te (6.38-746 ppm), Ni (166-390 ppm), Sb (0.03-646 ppm), Se (5.40 ppm), Pb (undetected to 74 ppm), Cu (1.02-2.11 ppm), Cd (0.01-3.76 ppm), Ag (0.44-1.31 ppm), Zn (0.20-0.28 ppm) and Au (0.01-1.17 ppm).

#### 3.6.5.6 Cachorro Bravo smooth pyrite (S-Py) composition

For the S-Py of the Cachorro Bravo deposit, the invisible gold content varies from 0.032 to 0.10 ppm and arsenic varies from 924 to 1595 ppm (Table 3; Fig. 3.9). The most abundant trace elements range as follow: Ni (29-101 ppm), Cu (0.06-0.71 ppm), Co (0.1-1.4 ppm), Cr (0.2-2.0 ppm), Se (43-63 ppm), Pb (0.3-3.0 ppm), Sb (0.2-1.8 ppm), Zn (0.3-0.6 ppm), Ag (0.024-0.03 ppm), Sn (0.09-0.15 ppm), and Te (0.10-0.16 ppm).

#### 3.6.5.7 Correlating sulfide textures and composition

Box and whisker plots (Fig. 3.9) show that for 11 (eleven) elements examined there is relevant element enrichment or depletion depending on texture, generation and type of mineral. The diagrams are constructed following the paragenetic sequence of Figure 3.6, and the elements under consideration are: Co, Ni, Se, Te, Cu, Pb, Au, Ag, Sb, Pt and As. Following removal of extreme outliers, box plots for each of the elements analyzed (Fig. 3.9) are used to evaluate the trends and variability of the data.

Gold, As, Pb, Te, Co, Ni and Sb are highly correlated (Fig. 3.9), recording very similar behavior for different sulfide minerals, even though statistically some of these elements display the same range. These concentrations are together in the same interval, and except for Ni they are highest in P-Apy and S-Apy. Gold, As and Sb are best concentrated in the S-Apy.

For the Laranjeiras gold deposit, from P-Py relatively to S-Py, our data show that Co, Ni, Se, Te, Cu and Pb are commonly enriched, Ag and Sb are depleted, whereas Au, Pt and As remain unchanged, considering the average values, although these can be seen as statistically the same; Au,

Co, Sb and Pb are enriched in S-Apy in relation to P-Apy. These latter elements have lower concentration in the S-Py of the Cachorro Bravo deposit.

In Laranjeiras (Fig. 3.9), some trace elements (Co, Ni, Se, Te, Cu, Pb, Pt) have statistically similar, high values, recorded mainly in P-Py; Ag and Sb are more enriched in the S-Py. Tellurium, Cu and Ag are enriched in P-Apy, whereas the S-Apy records the highest Co, Pb, Au and Sb. In P-Py and S-Py, As levels are in the range 0.25 to 3.0 ppm; Ni from 2.9 to 1332,00 ppm, and Co from 0.1 to 1725,00 ppm. In Laranjeiras, Sb has a tenfold enrichment in P-Py and S-Py, and S-Po; in P-Apy and S-Apy it is a hundredfold higher. Arsenic varies from 438,00 to 445,00 ppm in P-Apy and S-Apy.

These pyrites and pyrrhotites record similar contents, in ppm, of Au enrichment when compared to analyzed arsenopyrites (Fig. 3.9). The P-Apy and S-Apy exhibit a large interval of Au content, between 0.00032 to 135 ppm, with the highest value in a sample of S-Apy.

At the Cachorro Bravo deposit, the S-Py becomes progressively richer in As and Au in comparison to Laranjeiras, containing the gold richest pyrite, although they are statistically the same. On the other hand, the Laranjeiras S-Py contains the richest contents in Sb, Co, Ni, Pb and Te.

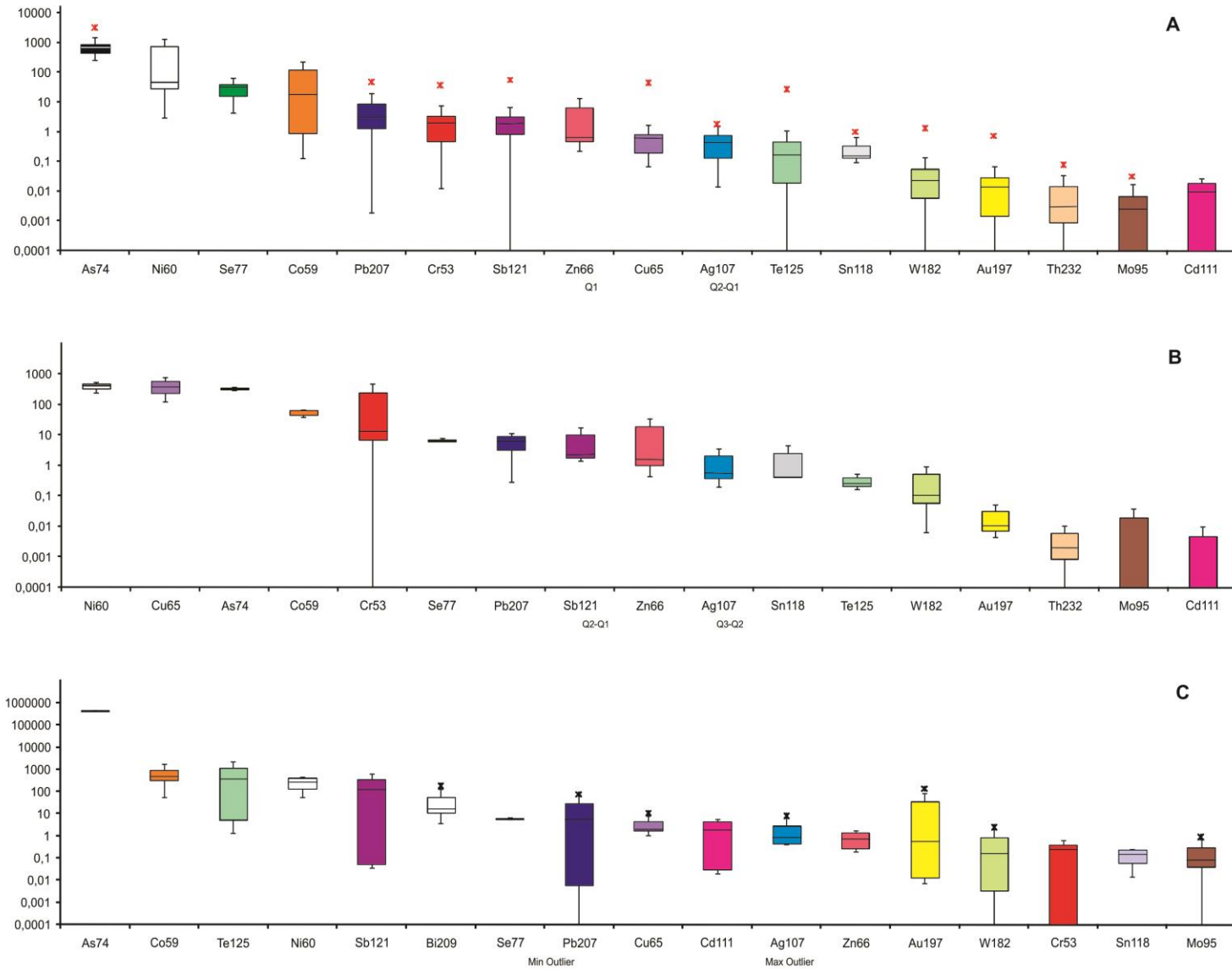


**Figure 3.8. Box plot of trace metal content in descending order of elemental abundance of (A) P-Py and S-Py; (B) S-Po; (C) P-Apy and S-Apy. Py: pyrite; Po: pyrrhotite; Apy: arsenopyrite of Laranjeiras Deposit – Eastern Sector.**



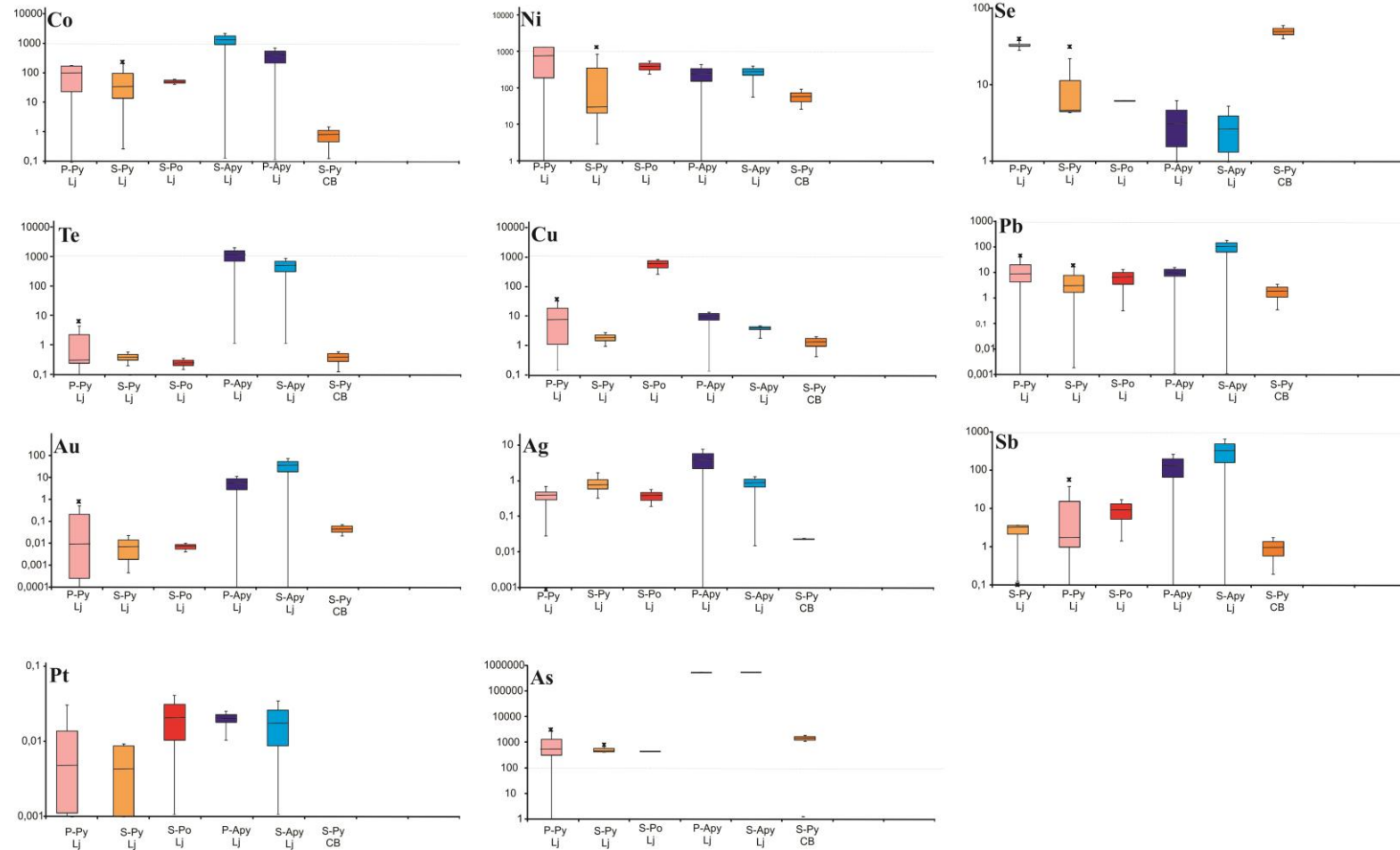


**Figure 3.9.** Trace element contents (ppm) of sulfide minerals (P-Py and S-Py; S-Po; P-Apy and S-Apy. Py: pyrite; Po: pyrrhotite; Apy: arsenopyrite ), Laranjeiras (Lj) and Cachorro Bravo (CB) deposits, for Co, Ni, Se, Te, Cu, Pb, Au, Ag, Sb, Pt and As. The bar = median; box = 25 to 75<sup>th</sup> percentile of data (interquartile range); asterisk = outliers.

### **3.7 Cuiabá-Lamego gold deposit area**

The sedimentary samples from the Córrego do Sítio lineament and Cuiabá-Lamego gold deposit area have very similar petrographic composition, texture and macroscopic characteristics (Figs. 3.3A and B, respectively). Graywackes of the northern sector are light-gray, medium- to coarse-grained rocks, with granoblastic and granolepidoblastic textures. They are composed of quartz (70%), white mica (10-15%) and plagioclase (5%). Epidote, zircon, magnetite, rutile and sulfides occur as accessory minerals. The carbonaceous pelite is composed mainly of carbonaceous matter (20-40%), quartz (10-20%), chlorite (5%) and carbonate (1%), whereas the micaceous pelite (Fig. 3.3D) has quartz (30-40%), white mica (10-20%), and carbonate (10%).

### **3.8 Whole-rock geochemistry**

As pointed out by Hayashi et al. (1997), the mineralogical and geochemical composition of clastic sedimentary rocks is controlled by various factors, including the: (1) composition of their source rocks; (2) environmental parameters influencing the weathering of source rocks (*e.g.*, atmospheric chemistry, temperature, rainfall and topography); (3) duration of weathering; (4) transportation mechanisms of clastic material from the source region to the depocenter; (5) depositional environment; and (6) post-depositional processes (*e.g.*, diagenesis, metamorphism, hydrothermal alteration).

Turbidites of the eastern and northern sectors have been subjected to geochemical studies in order not only investigate their composition, but also to help constrain their tectonic setting and provenance.

#### **3.8.1 Major elements analyses**

The distribution of major and trace elements is shown in Table 1, Figures 3.10A and 3.10B, respectively, normalized to the NASC (Groumet et al., 1983). All seventeen samples from both sectors display a similar general pattern, and suggest that hydrothermal alteration did not impose considerable geochemical changes. Several important differences may be highlighted. For instance,

rocks from the eastern sector have higher contents of MnO, K<sub>2</sub>O, Rb, Cs and Sb, and wider variation of CaO, Na<sub>2</sub>O, P<sub>2</sub>O<sub>5</sub> and As. The northern metagraywackes show higher contents of MgO and Ni and lower Th and U contents.

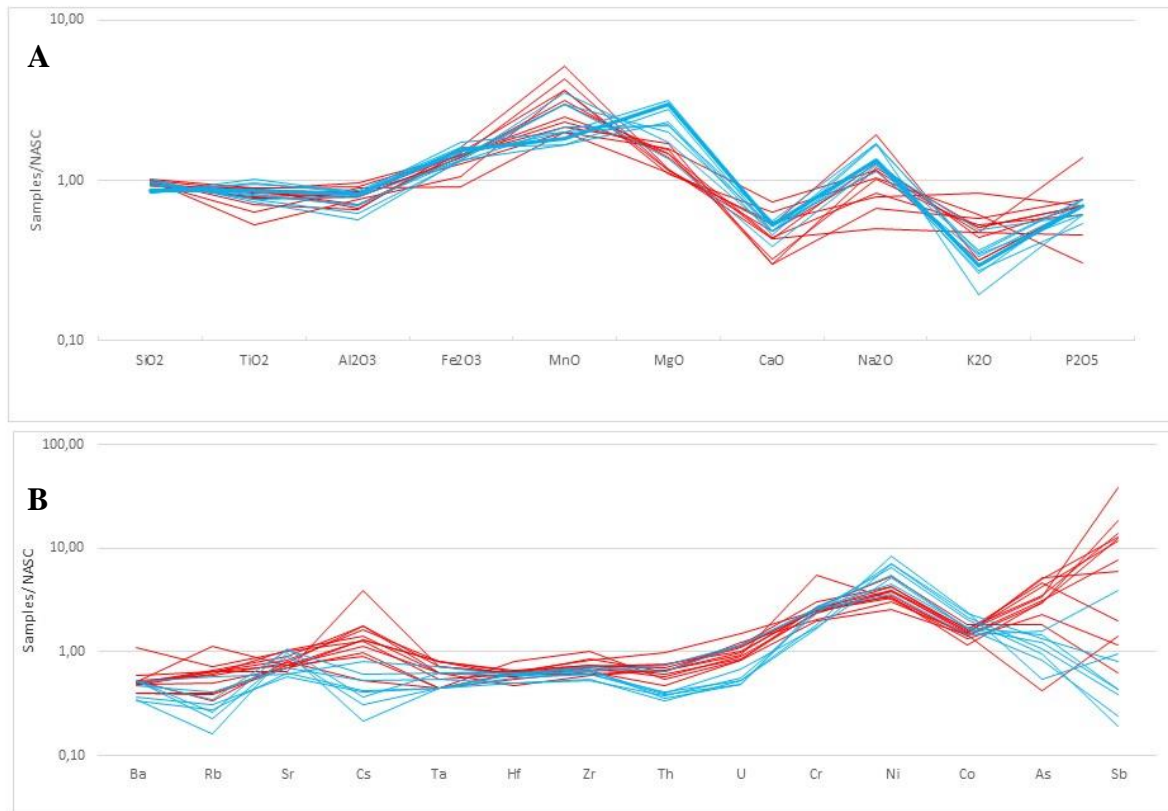


**Figure 3.10. Spider diagrams normalized to the NASC of major (A) and trace elements (B) of the eastern (red) and northern (blue) sectors, Quadrilátero Ferrífero district.**

The concentration of major elements in graywackes varies within a relatively narrow range (Table 1). Silica varies between 56.01 to 66.61 wt.%, and Al<sub>2</sub>O<sub>3</sub> from 10.59 to 16.28 wt.%, with its concentration being highest where pelite levels dominate; TiO<sub>2</sub>: 0.50 to 0.74 wt.%; Fe<sub>2</sub>O<sub>3</sub>: 5.14 to 9.13 wt.%; MnO: 0.01 to 0.31 wt. %; CaO: 1.1 to 2.69 wt.%; MgO: 3.21 to 8.03 wt.%; Na<sub>2</sub>O: 0.57 to 2.19 wt.%; K<sub>2</sub>O: 0.77 to 3.33 wt.%, and P<sub>2</sub>O<sub>5</sub>: 0.06 to 0.18 wt.%. Total iron is expressed as Fe<sub>2</sub>O<sub>3</sub>.

Pelites consist of 53.66 to 66.61 wt.% SiO<sub>2</sub>; 9.57 to 14.20 wt.% Al<sub>2</sub>O<sub>3</sub>; 0.41 to 0.79 wt.% TiO<sub>2</sub>; 5.96 to 9.73 wt.% Fe<sub>2</sub>O<sub>3</sub>; 3.15 to 9.06 wt.% MgO; 1.40 to 2.31 wt.% CaO; 1.18 to 1.90 wt.% Na<sub>2</sub>O (Table 1).

The 3K/Al ratios that reflect the muscovite amount in a rock (*e.g.*, Kishida and Kerrich, 1986) average 0.33 in the eastern and 0.48 in the north sectors, respectively. In general, graywackes and pelites are classified variously based on their chemical composition (*e.g.*, Crook, 1974; PettiJohn, 1975; Herron, 1988). In the present study these rocks are classified according to the bivariate  $\log(\text{Fe}_2\text{O}_3/\text{K}_2\text{O})$  versus  $\log(\text{SiO}_2/\text{Al}_2\text{O}_3)$  diagram after Herron (1988), where the samples plot in different fields (Fig. 3.11), being concentrated in the Fe-shale, shale and Fe-sand fields. Some samples show enrichment in Al, due to the presence of pelitic levels. One sample in particular (4506, Cachorro Bravo deposit, eastern sector) is the richest of all in K<sub>2</sub>O, denoting its micaceous nature (Fig. 3.11).

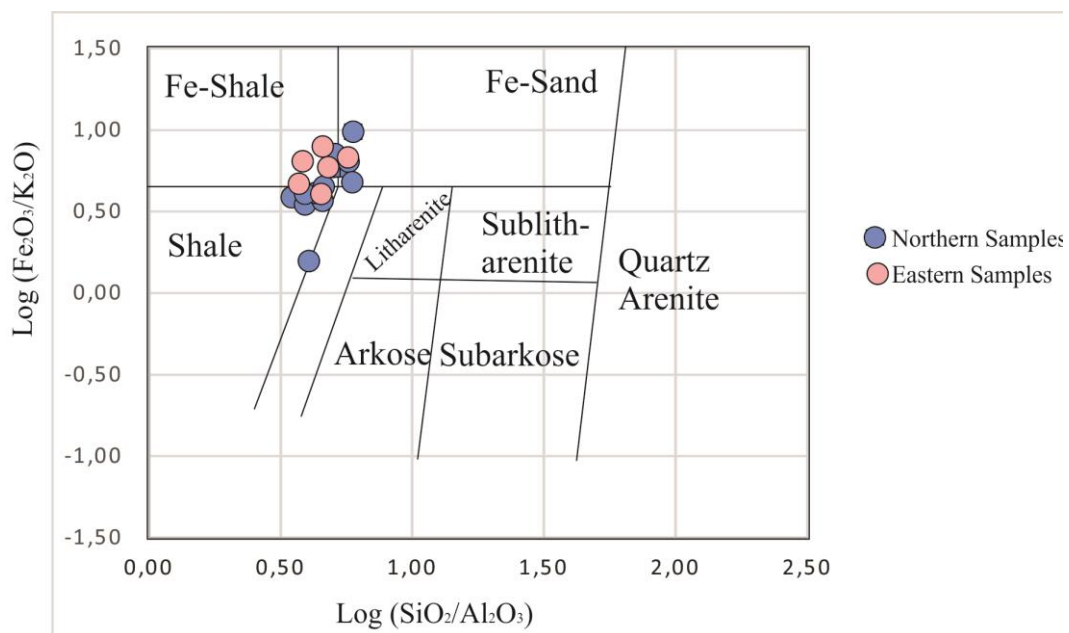


**Figure 3.11. Geochemical classification of graywackes and pelites of eastern and northern sectors.  $\log(\text{Fe}_2\text{O}_3/\text{K}_2\text{O})$  versus  $\log(\text{SiO}_2/\text{Al}_2\text{O}_3)$  bivariate diagram (after Herron, 1988).**

### 3.8.2 Trace and rare earth element geochemistry

The northern sector samples have higher Rb, lower Ba and equivalent Sr contents when compared to values of Archean mafic volcanic rocks (Taylor and McLennan, 1985). In the majority of analyses (Table 1) for this sector, Th, U, Zr and Hf are higher than in the eastern sector, but all of these elements have comparable abundances with samples from the Yellowknife (Taylor and McLennan, 1985).

The trace elements Rb and Th are relatively depleted, whereas Ni and Cr are enriched. Cesium, As and Sb show an irregular pattern, and are depleted in the northern and enriched in the eastern sectors, respectively. The clastic metasedimentary rocks are also characterized by high concentration of the transition metals, including V, Sc, and Co (Table 1) in the both sectors.

In all samples, Cr and Ni contents fluctuate with MgO, with Cr > 290 ppm in the northern and > 340 ppm to the eastern sectors; Ni is higher in the Cuiabá-Lamego area than in the Córrego do Sítio lineament (Table 1). All samples have indistinguishable V contents, which are correlated with Al<sub>2</sub>O<sub>3</sub> and TiO<sub>2</sub> (Table 1). Cobalt is slightly more abundant in samples of the northern sector.

Arsenic and Sb are high, ranging from 248 to 445,000 ppm and 0.03 to 646 ppm, respectively. Gold has the highest content in the eastern sector (average 20 ppb), with samples in the northern sector averaging 5 ppb. These elements May be attributed to hydrothermal processes.

The REE patterns are distinct. The eastern sector samples have higher LREE contents and more accentuated fractionation between LREE and HREE. In eastern graywackes values of Eu/Eu\* seem to be higher. For the eastern sector, the La/Ybn ratios ranging from 2.60 to 3.43, and Eu/Eu\* from 0.96 to 1.12. In the northern sector, the values of La/Ybn ratios ranging from 1.76 to 2.58, and Eu/Eu\* from 0.94 to 0.96. The latter is characterized by lower La/Yb<sub>n</sub> ratios (< 4.1). The rocks show light rare earth element (LREE) enriched and flat heavy rare earth element (HREE) patterns.; a weak or absent Eu anomaly is characteristic.

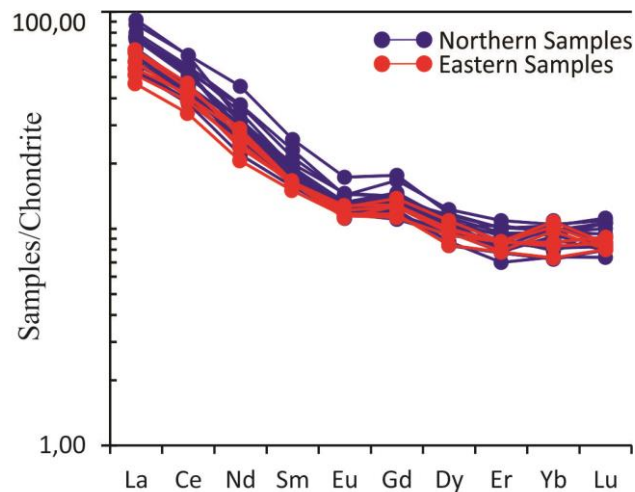


**Figure 3.12. Chondrite-normalized REE patterns for the clastic sedimentary association in the eastern (red) and northern (blue) sectors (data in Table 2).**

### 3.9 Zircon radiogenic isotope results

From the 1054 U-Th-Pb spot analyses investigated, 689 zircons are from the eastern (Cachorro Bravo, Carvoaria and Laranjeiras deposits) and 365 from the northern (Cuiabá and Lamego deposits) sectors (Fig. 3.1). Subsequently, Lu-Hf isotope analyses were carried out on 378 spot analyses, with 329 and 49 samples analyzed from the eastern and northern sectors, respectively. The 378 in-situ zircon Lu-Hf analyses were performed within the same spots chosen for U-Pb dating.

The SEM images suggest that all zircon grains under study are probably detrital in origin. Detrital zircons are rounded, euhedral to subhedral, with several grains as broken fragments; most show oscillatory zoning and some grains are either unzoned or exhibit sector zoning. Only zircon analyses with a level of concordance between 95% and 101% are used for the interpretation of age spectra and depositional ages. Chosen images of representative types of zircon grains are shown in Figure 3.13.

#### 3.9.1 U-Pb geochronology

The U-Pb isotope studies were performed (Table 5) on samples of individual deposits, including Cachorro Bravo, Laranjeiras and Carvoaria (eastern sector) and Cuiabá, Lamego (northern sector). Metagraywackes are referred to as MG and pelites as Pl.

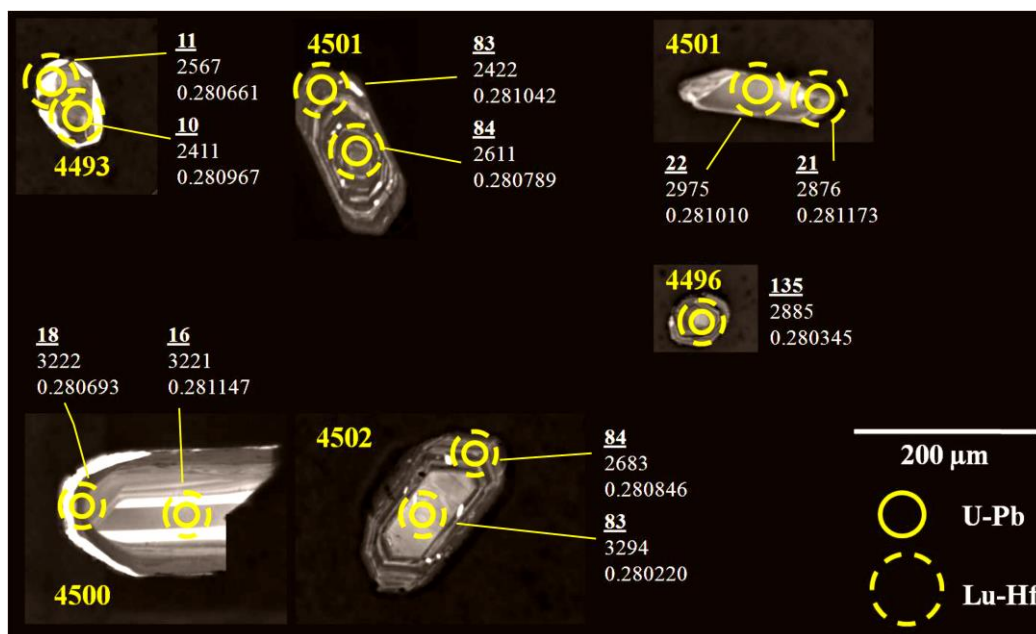


**Figure 3.13. SEM representative images of zircon grains from the graywackes and pelites of clastic sedimentary association, with U-Pb and Lu-Hf measurement spots indicated.**

### 3.9.1.1 Cachorro Bravo deposit

The samples were extracted from the FCS0756 (48.65 – 91.57 m) and FCS1053 (209.00 – 260.10 m) drill cores. The zircons range from 20 to 200 micrometers, are translucent and pinkish.

In the **pelite** of the FCS0756 drill hole, some percentage of the analyzed spots, 30 out of 106, are concordant; these data show a polymodal distribution pattern (Fig. 3.14A). The concordant spots yield ages from  $2.02 \pm 0.018$  to  $3.65 \pm 0.025$  Ga. The highest peak between 2.80 Ma and 2.99 Ga corresponds to 48 zircons ages, and the secondary peak comprises ages between 3.11 Ga and 3.49 Ga, which contains 36 zircons. There are relevant subordinate peaks at 2.60 Ga and 3.24 Ga (Fig. 3.14A).

In the **metagraywacke** of the FCS1053 drill hole, 36 concordant spots out of 128 produced ages from  $2.43 \pm 0.015$  to  $3.49 \pm 0.020$  Ga. The polymodal age (Fig. 3.14B) distribution records highest peak between ages of 2.80 Ga and 2.88 Ga, corresponding to 12 zircon ages. The secondary peak comprises ages between 2.88 Ga and 3.10 Ga, which contain 10 zircons. There are relevant subordinate peaks at 2.60 and 3.25 Ga.

### 3.9.1.2 Laranjeiras deposit

Zircons of the **metagraywacke** FCS0831 (267.20 – 296.44 m) have concordant spots with ages ranging from  $1.93\pm 0.015$  to  $3.38\pm 0.020$  Ma (Fig. 3.14C). The highest peak, in polimodal age distribution (Fig. 3.14C), is between 3.03 Ga and 3.38 Ga, corresponding to 17 zircon ages; the secondary peak is represented by ages from 2.69 Ga to 2.96 Ga. There are relevant subordinate peaks at 2.60 Ga, 1.93 Ga and 1.988 Ga.

The **pelite** FCS0929 (191.50 – 257.15 m) has 46 out of 91 concordant zircon analyses, where the spots yielded ages ranging from  $2.43\pm 0.022$  to  $3.55\pm 0.032$  Ga. The polimodal age distribution records (Fig. 3.14D) highest peaks between 2.69 Ga and 2.87 Ga, corresponding to 24 zircon ages; the secondary peak comprises ages between 2.90 Ga and 3.16 Ga, which contains 11 zircons. There are relevant subordinate peaks at 3.27 and 2.54 Ga.

### 3.9.1.3 Carvoaria deposit

Detrital zircon grains from **graywackes** in the FCS1196 (279.15 – 312.20 m) and FCS1261 (247.75 – 252.65 / 258.80 – 283.95 m) drill cores have sizes ranging from 10 to 180 micrometers; they are translucent and pinkish.

The analyzed concordant zircons (Fig. 3.14E) of sample FCS1196 (68 out of 126) were dated, and produced ages ranging from  $1.80\pm 0.022$  Ma to  $350\pm 0.021$  Ga ( $n = 20$  and  $n = 7$ , respectively). The highest peak, in polimodal age distribution, is between 1.80 and 2.03 Ga.

**Graywacke** sample FCS1261 has concordant spots (59 out of 122) with ages from  $1.58\pm 0.011$  to  $3.38\pm 0.021$  Ga. The polimodal age distribution records the highest peak between ages of 2.57 and 3.03 Ga ( $n = 40$ ; Fig. 3.14F), with the secondary peak between 3.21 Ga and 3.33 Ga, which is represented by 10 zircons. There are relevant subordinate peaks at 1.94, 3.16 and 3.38 Ga (Fig. 3.14F).



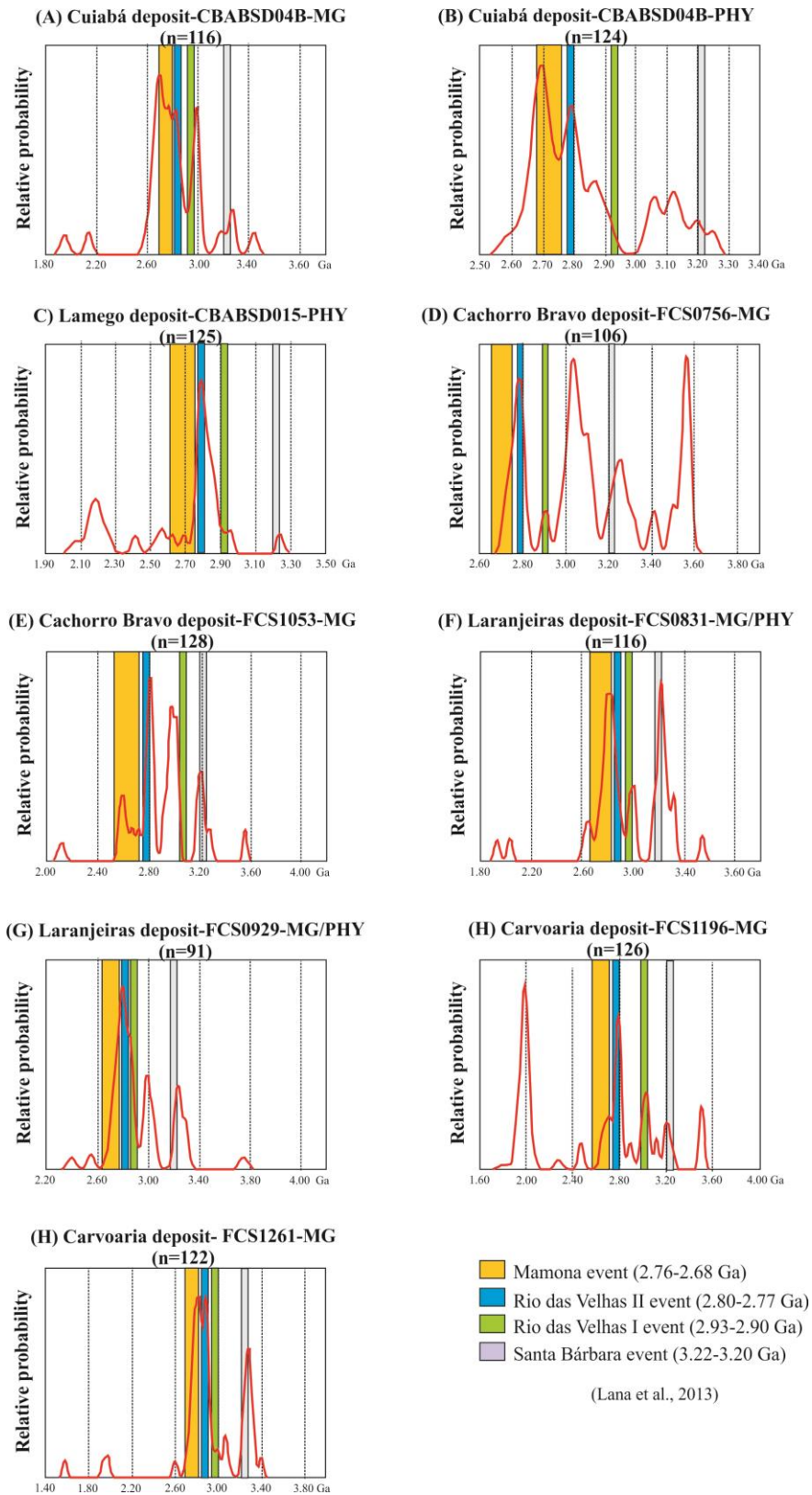


Figure 3.14. Probability density diagrams showing  $^{207}\text{Pb}/^{206}\text{Pb}$  age spectra of zircon grains from graywackes and pelites of the Nova Lima Group clastic sedimentary association of the eastern (A-F) and northern (G-I) sectors. Cachorro Bravo (A, B), Laranjeiras (C, D), Carvoaria (E, F), Cuiabá (G, H), and Lamego (I) deposits. The events indicated are from Lana et al. (2013).

#### 3.9.1.4 Cuiabá deposit

Sample CBABSD04B-MG was extracted between 1.274,10 - 1.310,35 m, and CBABSD04B-PI between 1.274,05 - 1.279,01 m in a graywacke-pelite intercalation. The zircons (n = 240) have sizes ranging from 50 to 200 micrometers, are translucent, pinkish to brownish. The relative percentage of analyzed zircon spots is 81 out of 240.

The age distribution pattern is polimodal for both rocks (Fig. 3.14G and H). The concordant spots yield ages ranging from  $1.93\pm 0.018$  to  $3.42\pm 0.030$  Ma for **graywacke** intercalations (Fig. 3.14G). The highest Cuiabá peak is between 2.57 Ga and 3.09 Ga (Fig. 3.14G), with the secondary peak comprising ages between 2.57 Ga and 2.73 Ga (Fig. 3.14G), represented by 14 zircons. There are relevant, subordinate peaks at 3.22 Ga and 3.42 Ga (Fig. 3.14G).

**Pelite** intercalations yield ages ranging from  $2.57\pm 0.016$  to  $3.27\pm 0.020$  Ga based on concordant spots (Fig. 3.14H). The highest peak is between  $2.57\pm 0.016$  to  $2.76\pm 0.018$  Ma (Fig. 3.14H), corresponding to n = 25 zircons ages; the secondary peak comprises 3.03 Ga and 3.09 Ga (Fig. 3.14H), which contains n = 9 zircons.

#### 3.9.1.5 Lamego deposit

In the sampled interval of the **micaceous pelite** CARBSD15-PI, between 125.62 and 157.75 m, zircons ranging from 30 to 220 micrometers are translucent, pinkish to brownish, and the relative percentage of the analyzed zircon spots is 35 out of 125.

The polimodal pattern (Fig. 3.14I) has concordant spots and yields ages ranging from  $2.05\pm 0.019$  to  $3.24\pm 0.021$  Ga. The highest peak at Lamego between 2.71 Ga and 2.98 Ga corresponds to 17 zircon ages, whereas the secondary peak comprises ages between 2.05 Ga and 2.17 Ga, with 8 zircons. There are relevant, subordinate peaks at 2.39 Ga, 2.57 and 2.66 Ga (Fig. 3.14I).

### 3.10 Lu-Hf analyses

#### 3.10.1 Eastern sector

Zircon grains from samples of the Córrego do Sítio lineament, only in concordant U-Pb ages belong to the major age population ranging between ca. 2.60 and 2.90 Ga, and have  $\epsilon\text{Hf}_t$  between 0 and –6.0. There is a high spread of ages between ca.1.90 and 3.40 Ga (Fig. 3.15A).

The initial  $^{176}\text{Hf}/^{177}\text{Hf}$  ratios vary from 0.280444 to 0.282506 calculated on the concordant ages of 329 concordant zircons, such that the ratio increases from older to younger grains (Fig. 3.16A). The zircons have a large spread of ages, varying from sub-chondritic to near *chondritic* and *superchondritic*  $\epsilon\text{Hf}$ . The Hf isotopic composition has  $\epsilon\text{Hf}$  values between +2.0 and –6.0. The typical increase in the dispersion of  $\epsilon\text{Hf}$  values, becoming increasingly negative as the zircons become younger, is indicated in Figure 3.15A.

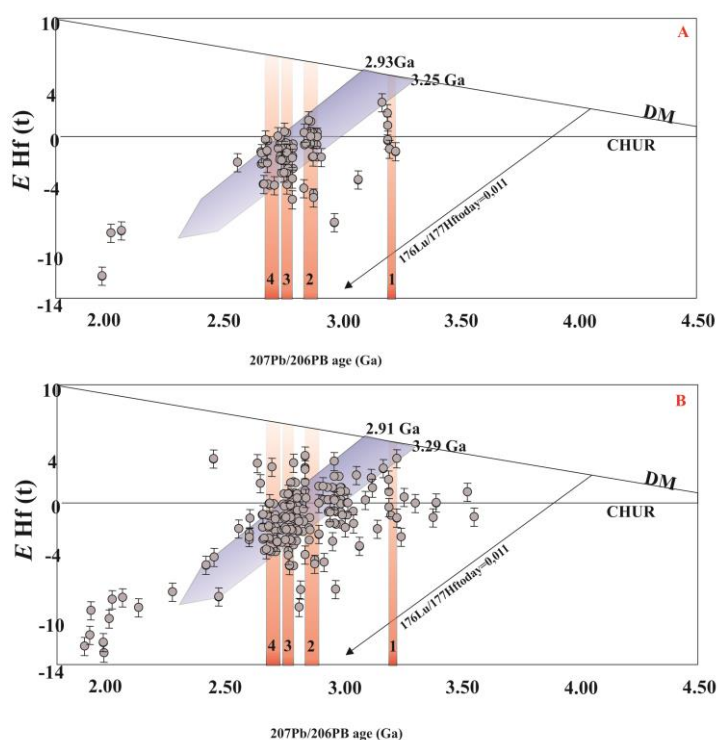


Figure 3.15. Epsilon Hf versus  $^{207}\text{Pb}/^{206}\text{Pb}$  age diagram showing the data obtained from zircon grains for the Cachorro Bravo, Laranjeiras and Carvoaria (Córrego do Sítio lineament) (A); Cuiabá and Lamego (B) deposits. CHUR = chondritic uniform reservoir, DM = depleted mantle. (1) Santa Bárbara, (2) Rio das Velhas I, (3) Rio das Velhas II, (4) Mamona events after Lana et al. (2013).

### 3.10.2 Northern sector

The zircon grains from samples of the Cuiabá and Lamego deposit area (Fig. 3.15B), with only concordant U-Pb ages of the major age population between ca.2.6 and 2.85 Ga, have  $\epsilon_{\text{Hf}}$  between 0 and  $-6.0$ . Zircon grains with ages between ca.2.86 and 3.20 Ga generally scatter between  $\epsilon_{\text{Hf}}$  of 0 and  $-5$ .

The initial  $^{176}\text{Hf}/^{177}\text{Hf}$  ratios range from 0.280678 to 0.281563, calculated based on 49 concordant zircon ages, and these increase from older to younger grains (Fig. 3.16B). Zircons older than 2.90 Ga display mainly *superchondritic* to near *chondritic*  $\epsilon_{\text{Hf}}$ , between  $-0.5$  and  $+4.0$ , with a variation in the Hf model age ( $T_{\text{DM}}$ ) between 2.90 Ga and 3.20 Ga. The Hf isotopic composition has  $\epsilon_{\text{Hf}}$  values between  $-0.5$  and  $-16.0$ . The typical increase in the dispersion of  $\epsilon_{\text{Hf}}$  values, becoming increasingly negative as zircons become younger, may be verified in Figure 3.15B.

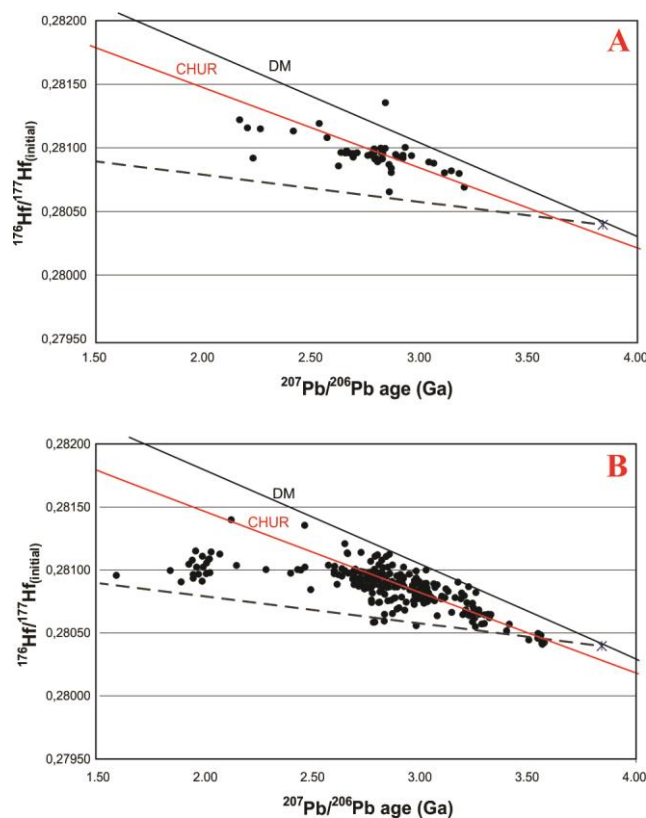


Figure 3.16. Initial  $^{176}\text{Hf}/^{177}\text{Hf}$  versus  $^{207}\text{Pb}$ - $^{206}\text{Pb}$  age diagram showing the results of combined U-Pb and Lu-Hf isotope analyses on zircons for the Cachorro Bravo, Laranjeiras and Carvoaria (Córrego do Sítio lineament) (A); Cuiabá and Lamego (B) deposits. CHUR = chondritic uniform reservoir; DM = depleted mantle.

### 3.11 Discussion

#### 3.11.1 Geochemical features, provenance and tectonic setting of the clastic sedimentary association of the eastern and northern sectors

Remnants of Archean rocks are exposed on all continents, with sedimentary rocks preserved in two major settings: as volcanoclastic and chemical sediments interbedded with volcanic rocks and as clastic sedimentary sequence (*e.g.*, Taylor and McLennan, 1985; Helmstaedt, H. and Padgham, 1986; Anhaeusser, 2014). In Archean greenstone belts, these sequences are typically about 1000-5000 m thick (Taylor and McLennan, 1985); calculations by Martins et al. (2016) for the Rio das Velhas greenstone belt of the QF district are compatible with this range, an approximate thickness of 5,550 m of clastic, clastic-chemical and volcanoclastic sedimentary rocks. The turbidite sequences found in the eastern and northern sectors of the QF are representative of other Archean greenstone belts (*e.g.*, Condie, 1981; Helmstaedt, H. and Padgham, 1986), where volcanic sequences overlain by laterally persistent BIF-shale units have thick, terrigenous clastic turbidite deposits overlying them. As previously discussed, Archean metaturbidites are similar to the QF especially the Slave province of Canada, where deposits of the Quetico metasedimentary belt (Sawyer, 1986) and the world-class Roberto deposit (Fontaine et al., 2015) are examples.

The supracrustal rocks of the Nova Lima Group are an important component of the Rio das Velhas greenstone belt, similarly to those of other Archean terrains. This is the case for example of the Yellowknife Supergroup, where sedimentary rocks dominate (*e.g.*, Condie, 1981; Helmstaedt and Padgham, 1986), and are composed of widespread turbidites (Burwash-Wash Formations) derived from granite-gneiss and felsic and mafic volcanic rocks. (Taylor and McLennan, 1985).

Most Archean sedimentary rocks are generally characterized by high mineralogical and geochemical immaturity, high concentration of transition metals, low REE abundance and absence of Eu anomaly (Taylor and McLennan, 1985; Condie and Wronkiewicz, 1990).

According to Zucchetti and Baltazar (2000) and Baltazar and Zucchetti (2007), at least two different sources, mixed and felsic, contributed to the clastic rocks of the clastic sedimentary association of the Rio das Velhas greenstone belt. The relation of source rocks to the composition of these turbidites can help deduce the origin and composition of the clastic precursors of low-grade metamorphosed sedimentary rocks. In the present study, primary textures are well preserved, and there is no petrographic evidence for large-scale hydrothermal alteration effects, which could potentially have changed bulk geochemical compositions.

The results obtained for major elements (Fig. 3.10A), of all seventeen samples normalized to the NASC (Groumet et al., 1983), show that these lack major geochemical modifications due to hydrothermal alteration. The high  $\text{Fe}_2\text{O}_3$  content (average 7.92 wt.%) is similar that of Archean metaturbidite deposits elsewhere (Taylor and McLennan, 1985; Naqvi et al., 1988; Devaraju et al., 2010; Koti et al., 2011). The average 3K/Al ratios in the eastern and northern sectors of 0.48 and 0.33, respectively, may be interpreted as a reflection of the percentage of muscovite in the rocks (48% and 33%). The rocks sampled in the eastern sector recorded hydrothermal minerals than the northern sector, confirming the data of Figure 3.10, which several important differences may be highlighted in hydrothermal alteration, where rocks from the eastern sector have higher contents of MnO, K<sub>2</sub>O, Rb, Cs and Sb, and wider variation of CaO, Na<sub>2</sub>O, P<sub>2</sub>O<sub>5</sub> and As. The northern metagraywackes show higher contents of MgO and Ni and lower Th and U contents.

Graywacke and pelite show remarkable similarities in trace element abundances, particularly REE. They are also comparable to the geochemistry of many Archean sedimentary rocks (Taylor and McLennan, 1985; Condie and Wronkiewicz, 1990) in having high LREE content, steep chondrite-normalized patterns, and a slight or absent Eu anomaly; such is the case with analogous Archean metasedimentary rocks from Quetico (Sawyer, 1986), Superior Province, and from the Abitibi (Feng and Kerrich, 1990), both in Canada.

High abundances of As and Sb are registered (Table 2). The analyzed samples are adjacent to orogenic gold deposits in the respective sectors, where gold association with Pb, Te, Se, As, and Sb has in fact been demonstrated (Vial et al., 2007; Porto, 2008; Lima, 2012; Roncato et al., 2015; Martins et al., 2016). Gold has the highest content in the eastern sector (average 20 ppb), with samples in the northern sector having an average of 5 ppb.

The provenance diagram presented in Figures 3.17 uses the discriminant functions calculated based on a set of major elements (Roser and Korsch, 1988), indicating that recycled sources represent quartzose sediments of mature continental provenance, where the sediments could derive from granite-gneissic terrain (Figs. 3.17). The selected samples plot in the field of the quartzose sedimentary provenance, trending towards the mafic igneous provenance.

The provenance diagrams (Figs. 3.17) point to a mixture of source areas, predominantly sedimentary quartzose, although a mafic igneous source must also be considered, indicating subdivision of the source area. Provenance diagrams for tectonic environments indicate a passive margin (Figs. 3.18 A and B).

The most noticeable differences between the eastern and northern sectors for trace elements (Fig. 3.10B) are depicted by Ba, Rb, Cs, Cr, Co, and Ni abundances, suggesting that these clastic sediments were derived from source regions of contrasting overall composition. Opposite to figure 3.17, the northern sector, with higher MgO, Fe<sub>2</sub>O<sub>3</sub>, Cr, Ni, and Co, requires a percentage of mafic and ultramafic source rocks reaffirming its bimodal character. Whereas the eastern samples require some proportion of felsic rocks. Larger amounts of Au, Sb, As, K, Al, Rb, and Ba, and correspondingly less of Sr and Ca (Table 3, anexo 2, Figs. 3.10A and B), are characteristic of both sectors.

Compared to other Archean greenstone belt sedimentary rocks (*e.g.* Kalgoorlie, Yellowknife; Taylor and McLennan, 1985; Feng and Kerrich, 1990), our samples show equivalent REE distribution, but lower La<sub>N</sub>/Yb<sub>N</sub> values. The Archean sedimentary rocks are characterized by

$\text{Eu}/\text{Eu}^* \approx 1.00$  (Taylor and McLennan, 1985), which is similar to that of the present study (Table 2, Fig. 3.12). Many workers (Taylor and McLennan, 1985; Feng and Kerrich, 1990; Baltazar et al., 1998; Baltazar and Zucchetti, 2007) have shown that the compositions of Archean clastic sedimentary rocks may be modeled as bimodal mixtures of mafic-ultramafic and felsic volcanic rocks (a very steep HREE-depleted pattern; Taylor and McLennan, 1985). The major and trace element geochemical data obtained in the present study do not support a high contrasting provenance between the eastern and northern sectors, but the REE patterns are distinct. The eastern sector samples have higher LREE contents and more accentuated fractionation between LREE and HREE. In eastern graywackes values of  $\text{Eu}/\text{Eu}^*$  seem to be higher. Suggesting different sources for the rocks which involve a mixture of felsic and mafic rock.

The lack of an Eu anomaly in both graywackes and pelites is indicative of a passive margin origin associated with intermediate graywackes, whereas Eu negative anomalies confirm the passive margin provenance, environments characteristic of absence of plagioclásios (Taylor and McLennan, 1985), which is the case of the samples under investigation (Figs. 3.12). The data are comparable with the Kalgoorlie Group I sedimentary rocks, having  $\text{La}_N/\text{Yb}_N \leq 6.00$ ,  $\text{Eu}/\text{Eu}^* \geq 1.00$  (Taylor and McLennan, 1985). The authors specify that Group I is closely associated with mafic volcanic rocks, derived from calc-alkaline island arc volcanic, or a mixture of mafic and felsic rocks.

Based on these geochemical data, the provenance of the eastern and northern sectors turbidites must have had a contribution from both felsic and mafic/ultramafic sources, with the eastern sector having had a higher proportion of mafic/ultramafic inheritance (Lima, 2012; Ribeiro et al., 2015; Roncato et al., 2015). Based on a smaller number of samples, Baltazar and Zucchetti (2007) concluded that the northern sector is derived from a felsic source.



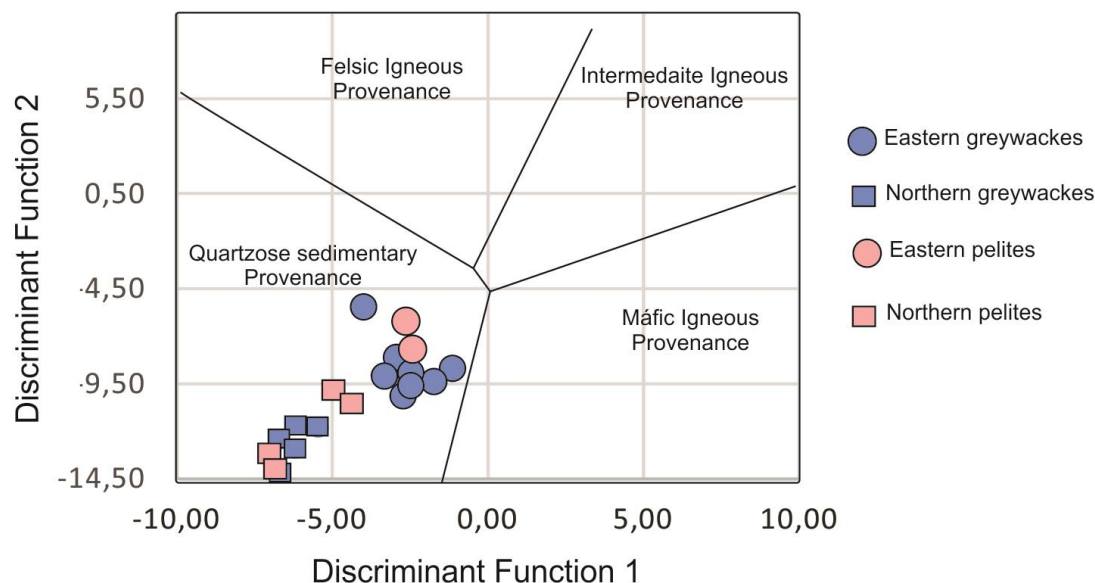


**Figure 3.17. Provenance discrimination diagram (after Roser and Korsch, 1988). Discriminant Function 1 =  $(-1.773 \times \text{TiO}_2\%) + (0.607 \times \text{Al}_2\text{O}_3\%) + (0.76 \times \text{Fe}_2\text{O}_{3T}\%) + (-1.5 \times \text{MgO}\%) + (0.616 \times \text{CaO}\%) + (0.509 \times \text{Na}_2\text{O}\%) + (-1.22 \times \text{K}_2\text{O}\%) + (-9.09)$ . Discriminant Function 2 =  $(0.445 \times \text{TiO}_2\%) + (0.07 \times \text{Al}_2\text{O}_3\%) + (-0.25 \times \text{Fe}_2\text{O}_{3T}\%) + (-1.142 \times \text{MgO}\%) + (0.432 \times \text{Na}_2\text{O}\%) + (1.426 \times \text{K}_2\text{O}\%) + (-6.861)$ .**

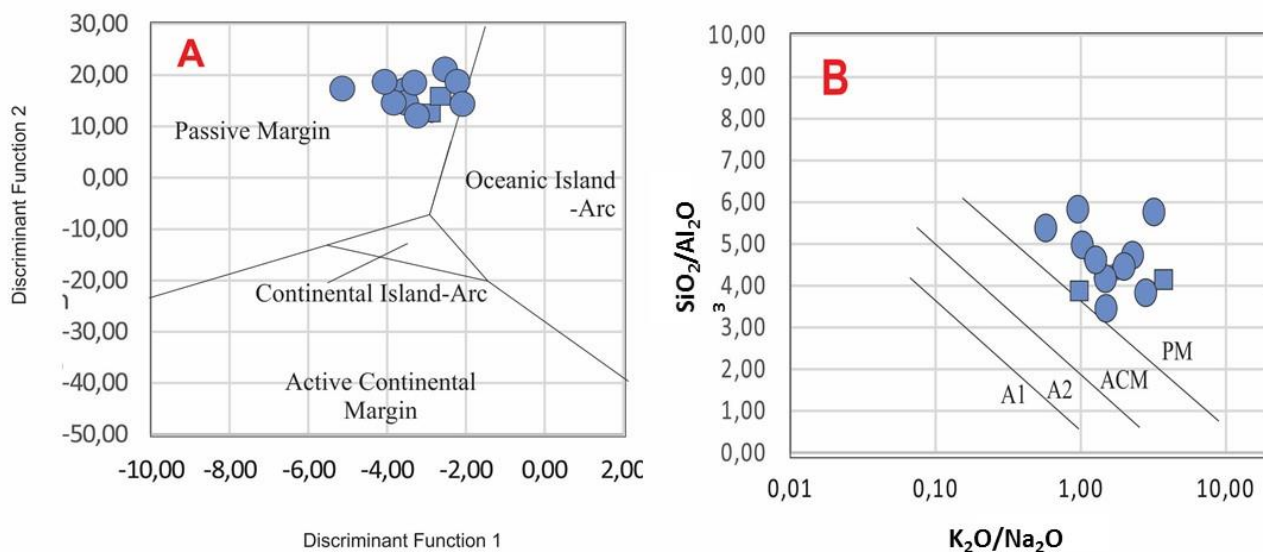


**Figure 3.18. Tectonic setting discrimination diagrams based on major element composition. (A) Bivariate discriminant function diagrams (from Bhatia, 1983). Discriminant Function 1 =  $(-0.0447 \times \text{SiO}_2\%) + (-0.972 \times \text{TiO}_2\%) + (0.008 \times \text{Al}_2\text{O}_3\%) + (-0.267 \times \text{Fe}_2\text{O}_3\%) + (0.208 \times \text{FeO}\%) + (-3.082 \times \text{MnO}\%) + (0.140 \times \text{MgO}\%) + (0.195 \times \text{CaO}\%) + (0.719 \times \text{Na}_2\text{O}\%) + (-0.032 \times \text{K}_2\text{O}\%) + (7.510 \times \text{P}_2\text{O}_5\%)$ . Discriminant Function 2 =  $(-0.421 \times \text{SiO}_2\%) + (1.988 \times \text{TiO}_2\%) + (-0.526 \times \text{Al}_2\text{O}_3\%) + (-0.551 \times \text{Fe}_2\text{O}_3\%) + (-1.610 \times \text{FeO}\%) + (2.720 \times \text{MnO}\%) + (0.881 \times \text{MgO}\%) + (-0.907 \times \text{CaO}\%) + (-0.117 \times \text{Na}_2\text{O}\%) + (-1.840 \times \text{K}_2\text{O}\%) + (7.244 \times \text{P}_2\text{O}_5\%)$ . (B)  $\text{SiO}_2/\text{Al}_2\text{O}_3$  versus  $\text{K}_2\text{O}/\text{Na}_2\text{O}$  diagram (Maynard et al., 1982). A1 = arc setting, basaltic and andesitic detritus, A2 = evolved arc setting, felsic-plutonic detritus.**

### 3.11.2 U-Pb geochronology and Lu-Hf signature

The U-Pb data for detrital zircons of the Rio das Velhas greenstone belt clastic sedimentary association are given in the cumulative probability diagrams of the  $^{207}\text{Pb}/^{206}\text{Pb}$  ages (Fig. 3.14). The detrital zircons in the study areas help establish the maximum ages relevant to the source rocks of the Archean gold-hosted deposits of the QF district. The age of deposition of sedimentary rocks based on detrital zircons presents some problems arising from an uncorrected common Pb; Pb loss is caused by metamorphic, tectonic or magmatic events; systematic analytical errors, to mention a few. Spots with high common Pb was not be considered in this results.

Dickinson and Gehrels (2009) calculate the maximum deposition age for sedimentary rocks with the weighted peak age probability of the youngest cluster. Based on this study, the average between the main relative mean ages of the eastern and northern sectors are 2.72 and 2.61 Ga, respectively. The average of the maximum depositional age of both sectors is coherent with published data for the QF (Machado et al., 1996; Noce et al., 2005).

These ages (2.72 and 2.61 Ga) are close to the range of the Rio das Velhas (2.78-2.76 Ga) magmatic event of Baltazar and Zucchetti (2007), and also the Rio das Velhas II (2.80-2.77 Ga) and mainly Mamona (2.76-2.68 Ga) magmatic events of Lana et al. (2013). Also, rocks of the 2.72-2.61 Ga time bracket may be considered to be significant sources of zircons for both sectors. In the eastern sector, where the Santa Bárbara (3.22-3.20 Ga) event of Lana et al. (2013) perseveres (Fig. 3.14), the older ages are more persistent than in the northern sector. This maximum depositional age is similar in many greenstone belts such as in the Superior Province (*e.g.*, Kerrich et al., 1998), Yilgarn Craton (*e.g.*, Pidgeon and Wilde, 1990) and Zimbabwe Craton (*e.g.*, Bolhar et al., 2003).

The Paleoproterozoic record is present in all samples analyzed (Fig. 3.14), with ages ranging from 1.8 to 2.45 Ga, and are best recorded for the Carvoaria deposit, eastern sector. These data are obviously not considered in the calculation of the maximum deposition age of the Nova Lima Group.

The youngest Paleoproterozoic ages (Fig. 3.14) obtained in the present study are compatible with those of detrital zircons from the Sabará Group graywackes, dated at  $2.12 \pm 0.04$  Ma by U-Pb (Machado et al., 1996), marking the end of deposition of the ca. 2.6-2.1 Ga Minas Supergroup (Machado et al., 1996; Hartman et al., 2006). The younger proterozoic ages were not used for maximum deposition age calculations of the Nova Lima Group. They were presented separately only to record the occurrence of possible associations between rocks of different ages.

Reis et al. (2002) and Alkmim and Martins Neto (2012) point out that the Sabará Group diamictites and conglomerates carry lithic fragments of supracrustal sequences (Rio das Velhas and Minas Supergroups, and Mineiro belt) and uplifted basement rocks. The authors also show that these units were tectonically superimposed during the Transamazonian (2.1-1.9 Ga) orogeny (*e.g.*, Alkmim and Marshak, 1998). The geological maps by Dorr (1957) and Renger et al. (2005) also indicate the close contact between rocks of the Nova Lima and Sabará groups near both the eastern and northern sectors. This most likely reveals the tectonic imbrication of the Nova Lima Group and Paleoproterozoic turbidites, explaining the presence of detrital zircons of older and younger ages together, a feature that is expressed in Figure 3.14.

The  $\epsilon_{\text{Hf}}$  values from  $-6$  to  $0$ , with crustal residence times from 3.00 to 2.60 Ga, are derived from the reworking of Archean crust. The juvenile zircons have  $\epsilon_{\text{Hf}}$  values from 1 to 6, and cover long crustal residence times (from 3.40 to 2.80 Ga), derived from the Archean to Paleoproterozoic (Fig. 3.15A and B). These isotopic data point to a provenance predominantly from rocks crystallized in the Archean (3.0–2.6 Ga), from either mantle or crustal sources.

Proterozoic zircon grains have exclusively crustal signature, with very negative  $\epsilon_{\text{Hf}}$  values (from  $-20$  to  $-12$ ), and relative crustal residence times (from 2100 to 1800 Ma). The zircon grains from the eastern sector samples record mainly reworked crustal  $\epsilon_{\text{Hf}}$  values with minor juvenile  $\epsilon_{\text{Hf}}$  values. Similarly, the northern sector has negative  $\epsilon_{\text{Hf}}$  values in a consistent derivation from reworked crustal source (Fig. 3.15A).

The turbidites preserved in the clastic sedimentary association were recycled from a prior sedimentary source, supplied by either juvenile or reworked terrains between 3.2 and 2.6 Ga. The Proterozoic age zircons may have been associated with the Sabará Group provenance, which are mainly represented by turbidites of Rhyacian age, where these units were tectonically superimposed during the Transamazonian (2.1-1.9 Ga) orogeny (*e.g.*, Alkmin and Marshak, 1998).

### **3.11.3 LA-ICP-MS and the host rock signature**

The LA-ICP-MS data help indicate the host rock contribution for the genesis of the analyzed sulfide minerals. For example, the presence of both Sb phases, berthierite and stibnite (Ribeiro et al., 2013) in the Córrego do Sítio lineament gold deposits, seems to result from the pronounced availability of this metal in the clastic sedimentary rocks as also verified by Morales et al. (2015).

The in situ LA-ICP-MS data show systematic trace element variations between different sulfide minerals of the Laranjeiras (porous and smooth pyrite - P-Py and S-Py; smooth pyrrhotite - S-Po; porous and smooth arsenopyrite - P-Apy and S-Apy) and Cachorro Bravo (smooth pyrite - S-Py) gold deposits.

#### **3.11.3.1 Sulfide trace element evolution in carbonaceous pelite**

The richest average trace element values of the sulfide minerals analyzed by in situ LA-ICP-MS are highlighted. They help establish the hydrothermal stages in carbonaceous pelite, the main host to gold at the Córrego do Sítio lineament.

1- Early hydrothermal (early-ore) stage: It is marked by the development of porous pyrite (P-Py) and arsenopyrite (P-Apy; Figs. 3.7B, D and F). Nickel, Se, Te, Cu, Pb, Ag (in P-Apy) and Pt correspond to the highest trace elements in the early-ore hydrothermal stage (Fig. 3.9) locked in the structures of both P-Py and P-Apy.

2- Main to late hydrothermal stage: It is characterized by the formation of smooth sulfides S-Py, S-Po and S-Apy (Fig. 3.7B, D and E), which develop after the porous sulfides. Cobalt is the highest trace element in S-Py, S-Po and S-Apy, whereas Au, Pb, Sb and As are enriched only in S-Apy.

These phases define the late ore stage typified by enrichment of most elements. Gold increases from stages 1 to 2, and correlates with Pb, Sb and As. The Au-As-Sb association (Fig. 3.9) also increases from 1 to 2.

In summary, Au increases according to a sequence of sulfide development (Figs. 3.7 B, D, E and F): P-Py ~ S-Po ~ S-Py (Laranjeiras deposit) → S-Py (Cachorro Bravo deposit) → P-Apy → S-Apy, suggesting that Au precipitation dominated in the main to late hydrothermal stage.

This may be a potential mechanism for the migration of gold from the early to late hydrothermal stages in the sedimentary rocks of Rio das Velhas greenstone belt sequence, involving newly formed sulfide minerals in greenschist facies conditions, precipitated together with Sb and As.

As pointed out by Large et al. (2011), pyrrhotite does not hold Au and As in its structure. This mineral is particularly more abundant in the Cachorro Bravo deposit, where mafic dikes and sills are closely associated with the host rocks. The presence of these mafic rocks seems to have been responsible for the higher pyrrhotite percentage (*e.g.*, Lima 2012; Roncato et al., 2015). It is thus possible that the conversion of pyrite to pyrrhotite, mainly at Cachorro Bravo, may have been responsible for releasing both Au and As to the hydrothermal fluid.

### 3.11.3.2 Evolution of sulfide minerals and related host rocks

In comparison to other Archean sedimentary deposits of the Rio das Velhas greenstone belt, those of the turbidite-hosted eastern sector contain a larger variety of ore minerals other than pyrite, arsenopyrite and pyrrhotite. These include sulfide and sulfosalt minerals that contain Sb, Pb, Hg, As, Zn, Cu, as well as Ni, Co and Pt (Fig. 3.5; Lima, 2012; Ribeiro et al., 2015; Roncato et al., 2015). This has been interpreted as a reflection of the variety in sources to the sediments, including mixed and felsic rocks.

Based on rock and isotope geochemistry, a mixed contribution of source rocks has also been demonstrated for the clastic sedimentary association of the eastern sector.

The LA-ICP-MS data on pyrite, pyrrhotite and arsenopyrite reinforce this notion. For instance, gold correlates to Se, As, Sb and Te of sedimentary affiliation, as well as to the mafic-ultramafic elements Co, Ni, and Pt.

The trace elements commonly concentrated in carbonaceous black shales of orogenic gold deposits include As, Cu, Zn, Cr, W, Ni, V, Pb, Sb, Bi, Te, and Mo (Boyle, 1986; Perring et al., 1991; Large et al., 2011); most of them are also concentrated in the sulfide minerals analyzed by LA-ICP-MS in the present study. Several workers (Reich et al., 2005; Large et al., 2009; 2011) have shown that these elements are released by the source rocks, and also concentrated by hydrothermal processes.

Large et al. (2011) pointed out that the Au-As-S association is typical of sedimentary-hosted ores, and inherited from the carbonaceous pelites. This sedimentary record has recently been indicated by LA-ICP-MS analyses on fluid inclusions from the Carvoaria deposit (Morales et al., 2016), where Sb-rich inclusions were detected suggesting leaching of this element from carbonaceous-dominated host rocks. Phillips and Powell (2010), Large et al. (2011), and Pitcairn et al. (2015) also show that gold must have been incorporated into the hydrothermal fluids during metamorphic devolatilization of carbonaceous pelites.

As pointed out by Ribeiro et al. (2015), a metamorphic fluid was responsible for mineralization at the deposits of the Córrego do Sítio lineament. Considering the data presented here, it is possible that the carbonaceous pelite was in part the source for Au, As, S and Sb during hydrothermal interaction, however, this a discuss. Goldfarb and Groves (2015) explain that a sedimentary rock source for gold-bearing metamorphic fluids is plausible for Phanerozoic orogenic gold provinces, where world-class to giant deposits are hosted in thick turbidite sequences, it cannot be a valid option for Archean provinces and it is also unlikely for many Paleoproterozoic provinces. These same authors argued that are impossible the carbonaceous pelite as the source of gold in the sedimentary deposits, because there is no evidence to support their required hypothesis that

significant volumes of pyrite-rich sedimentary rock underlie many of the productive greenstone areas.

Arsenic is the most abundant trace element in Au-bearing P-Py and S-Py, and P-Apy and S-Apy, of the Laranjeiras and Cachorro Bravo deposits, followed by Ni and Co. Fluid-rock interaction involving metamorphic-hydrothermal fluids and mafic-ultramafic rocks may also explain the Ni-Co contents in sulfides.

### **3.12 Implications for gold exploration**

Gold mineralization in the clastic sedimentary association is structurally controlled by a system of veins and veinlets, characterized by quartz-carbonate-sericite and sulfidation of the turbidite host rocks (Vial et al., 2007; Roncato et al., 2015; Beleque, 2016). The present studies introduce insights on the geological characteristics and ore-forming processes associated with turbidite-hosted gold deposits in the Rio das Velhas greenstone sequence, based mainly on rock and isotope geochemistry. The in situ LA-ICP-MS analyses of sulfide minerals suggest a possible genetic model for their evolution. The features summarized below can be used as gold exploration tools in this region:

- 1) Gold shows a positive correlation with As, Co, Ni, Te, Pb and Sb. Anomaly of these elements in soil or stream sediments may be used as an indicator for exploration of new turbidite-hosted gold orebodies.
- 2) Carbonaceous pelite has pyrite (P-Py and S-Py) and pyrrhotite (P-Po and S-Po) that are devoid of economic gold, and increase with the intensity of hydrothermal alteration, where this metal is best concentrated in porous arsenopyrite (P-Apy) and mainly in smooth arsenopyrite (S-Apy). The recognition of areas where sulfide-rich, carbonaceous pelite displays arsenopyrite in the proximity of turbidite sequences and-or silicification zones can help identify economic blind orebodies.

- 3) The U-Pb and Lu-Hf isotope signatures point to a provenance predominantly from rocks crystallized in the Archean (3.0–2.6 Ga), from either mantle or crustal sources. The mantle contribution may have been important to generate a larger diversity of sulfide minerals in the eastern sector. This suggests that sulfur, which complexed with gold, was buffered more efficiently along fluid path. Regions with these isotope data may be used in exploration to indicate favorable turbidite sequences as host to gold.
- 4) Gold exploration in rocks of the Archean resedimented greenstone belt must take into consideration that younger, Proterozoic turbidites, known to be devoid of gold, are imbricated with them.

### 3.13 Conclusions

The present synthesis (Table 4, Anexo 4) on the clastic sedimentary association of the Rio das Velhas greenstone belt, and other associated rocks in the QF (Fig. 3.1), highlights the variation of lithological, sedimentological, volcanic, hydrothermal and other evolutionary aspects of the geology of this Archean terrain. The study is particularly relevant bearing in mind that the greenstone belt is dominated by sedimentary rocks (*e.g.*, Baars, 1997).

Focus is given to the age and sedimentary source of the turbidites (greywacke, carbonaceous and micaceous pelite) in the Córrego do Sítio lineament, eastern sector, where these rocks are host to gold, and in the Cuiabá-Lamego gold deposit area, northern sector, where gold diggings are located. The results have been constrained with the use of U-Pb zircon analyses, rock geochemistry, Lu-Hf determinations on zircons of both areas, as well as elemental data with EPMA and quantitative in situ LA-ICP-MS analyses on sulfide minerals from the eastern sector.

The integration of these data with the proposed evolution put forward by Baltazar and Zucchetti (2007) results in the sketch model of Figure 3.19. These authors indicate that the clastic sedimentary associations of the eastern and northern sectors developed during different stages of tectonic evolution of the Rio das Velhas greenstone belt, with the Córrego do Sítio sediments



having been associated with the progression of an island-arc advance, and the Cuiabá-Lamego sediments with a continental arc. The scheme of Figure 3.19 accommodates much of the data obtained in the present contribution, which are summarized below:

- 1) The turbidite-hosted gold deposits of the eastern sector Córrego do Sítio lineament carries a large variety of ore minerals, other than pyrite, arsenopyrite and pyrrhotite, including sulfide and sulfosalt minerals that contain Sb, Pb, Hg, Cu, Zn, as well as Co and Ni. This has been interpreted as a reflection of the variety in sources to the sediments, including quartzose sources, mixed and felsic rocks (Lima, 2012; Ribeiro et al., 2015; Roncato et al., 2015).
- 2) Major (Fig. 3.10A) and trace (Fig. 3.10B) elements vary within a narrow range, with the
- 3) The eastern sector samples geochemistry is comparable to that of many Archean sedimentary rocks in having high LREE content, steep chondrite normalized patterns, and a slight or absent Eu anomaly.
- 4) Geochemical data for major (Fig. 3.10A), trace (Fig. 3.10B) and REE (Fig. 3.12) elements show that the provenance of the eastern and northern sectors turbidites must have had a contribution from both felsic and mafic sources, with the eastern sector having had a higher proportion of mafic inheritance and the northern sector having had a concentration of important trace elements as Ni and Co.
- 5) Tectonic setting discrimination diagrams (Fig. 3.18A and B) indicate that the rocks were supplied from a passive margin-type environment, with an orogenic source area having  $LaN/YbN \leq 6.00$ ,  $Eu/Eu^* \geq 1.00$ , similar to Taylor and McLennan (1985), which specify that this group closely associated with mafic volcanic rocks, derived from calc-alkaline island arc volcanic, or a mixture of mafic and felsic rocks.
- 6) Rocks formed during the Rio das Velhas (2.78-2.76 Ga) event of Baltazar and Zucchetti (2007), and also the Rio das Velhas II (2.80-2.77 Ga) and mainly Mamona (2.76-2.68 Ga)

magmatic events of Lana et al. (2013; Figs. 3.14 and 3.19), are the most significant source of zircons in both sectors. The ancient Santa Barbara (3.22- 3.20 Ga) magmatic event is best registered in zircons of the Córrego do Sítio sedimentary rocks.

- 7) Zircons of the clastic sedimentary association turbidites of both sectors are sourced in Paleoproterozoic to Archean rocks (Fig. 3.14). These Paleoproterozoic data probably reflect the presence of lithic fragments and zircons of the Sabará Group age graywackes in the Archean clastic sedimentary association turbidites. This most likely reveals the tectonic imbrication of the Nova Lima Group and Paleoproterozoic turbidites, explaining the presence of detrital zircons of older and younger ages clearly together.
- 8) The  $\epsilon_{\text{Hf}}$  values point to a provenance predominantly from rocks crystallized in the Archean (3.0–2.6 Ga), from either mantle or crustal sources (Fig. 3.15A and B). The eastern sector samples record mainly reworked crust  $\epsilon_{\text{Hf}}$  values with minor juvenile  $\epsilon_{\text{Hf}}$  values (Fig. 3.15A). The Lu-Hf results support the assumption that magmas were partially juvenile and incorporated a significant amount of reworked material, for both sectors.
- 9) In situ LA-ICP-MS analyses are compared in three sulfide minerals of carbonaceous pelites from the Córrego do Sítio lineament. In the Laranjeiras deposit these encompass porous (P-Py) and smooth (S-Py) pyrites, smooth (S-Po) pyrrhotite, porous (P-Apy) and smooth (S-Apy) arsenopyrite. Smooth (S-Py) pyrite of the Cachorro Bravo deposit is also included (Figs. 3.7 and 3.9). Box and whisker plots (Fig. 3.9) show that for 11 (eleven) elements examined there is relevant enrichment or depletion depending on texture, generation and type of mineral.
- 10) The typical trace elements commonly concentrated in carbonaceous shales around the world (Large et al., 2011), Mo, V, Ni, Cr, Zn, As, Sb, Hg, Cu, Se, Te, Bi, and W, are also found in the sulfide minerals of the analyzed samples (Figs. 3.8 and 3.9).

- 11) Two hydrothermal stages of evolution for carbonaceous pelites are recognized: (1) Early hydrothermal, marked by the development of porous sulfides (P-Py and P-Apy), during which some gold precipitation took place. (2) Main to late hydrothermal, recognized by the development of smooth sulfides (S-Py, S-Po and S-Apy), with gold peaking its values. This stage is dominated by recrystallization of the porous sulfide phases from (1) to produce smooth sulfides in (2) (Fig. 3.7).
- 12) The As, Co, Ni, Te, Pb and Sb concentration in arsenopyrite from the main stages of gold mineralization has important implications for the genesis of the deposits. Arsenopyrite and pyrite, which have the highest Au content, also record high As and Co.
- 13) Cobalt, Sb and Pb are enriched in P-Apy and S-Apy (Fig. 3.9). Gold, As and Sb are best concentrated in the S-Apy; gold precipitation dominates in the main to late hydrothermal stages together with Sb and As.
- 14) Smooth pyrite (S-Py) at the Cachorro Bravo deposit displays the highest As and Au concentration in comparison to the Laranjeiras deposit. At Cachorro Bravo, where pyrrhotite devoid of gold is more abundant, there is an important association with mafic dikes and sills, and this sulfide seems to have evolved from the metamorphic upgrade of pyrite. This could have been responsible for releasing Au to the hydrothermal fluid.
- 15) The carbonaceous pelite may have been in part the source for Au, As, S during hydrothermal interaction at the Córrego do Sítio lineament deposits, since these metals are relatively enriched in the original sediment, although it is a questionable by several authors (*e.g.* Goldfarb and Groves, 2015), which support that there is no evidence to significant volumes of pyrite-rich sedimentary rock underlie many of the productive greenstone areas.
- 16) The mixed source for the host rocks may explain why gold correlates to Se, As, Sb and Te of sedimentary affiliation, as well as to the mafic-ultramafic elements Co, Ni, and Pt.

17) The interaction of the hydrothermal fluid with the host rocks has determined the incorporation and depletion of certain elements in the remaining fluid, detected by in situ LA-ICP-MS analyses on sulfide minerals. Arsenic is the most abundant trace element in Au-bearing porous and smooth pyrite (P-Py and S-Py) and porous and smooth arsenopyrite (P-Apy and S-Apy), of the Laranjeiras and Cachorro Bravo deposits (S-Py), followed by Ni and Co. These elements were probably leached during hydrothermal alteration indicating a local metal and fluid source during gold mineralization.

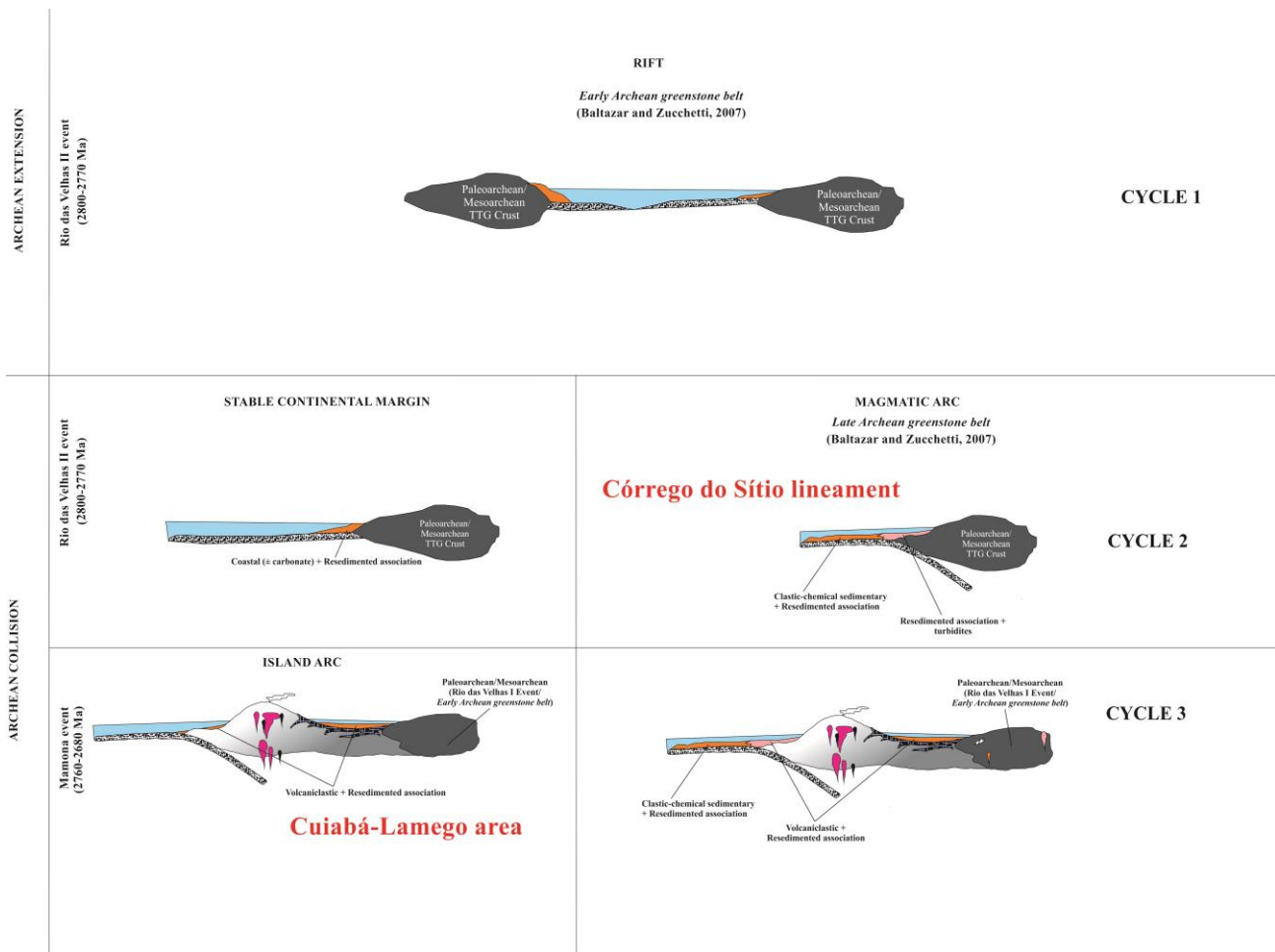


**Figure 3.19.** Sketch of Archean tectonic environments portrayed for the Cuiabá-Lamego area (northern sector) and Córrego do Sítio lineament (eastern sector), contextualized in the Rio das Velhas greenstone belt evolution and its associated sedimentary cycles, as suggested by Baltazar and Zucchetti (2007), as well as in the magmatic evolution events of Lana et al. (2013).

### 3.14 Acknowledgments

This research is the result of the on-going Ph. D. thesis by the first author at the Federal University of Minas Gerais-UFMG, fully financed by Conselho Nacional de Desenvolvimento Científico e Tecnológico (CNPq), Vale and AngloGold Ashanti Córrego do Sítio S/A-AGABM. We acknowledge the support of Universidade Federal de Minas Gerais (UFMG), Coordenação de Aperfeiçoamento de Pessoal de Nível Superior (CAPES), Fundação de Amparo à Pesquisa do Estado de Minas Gerais (FAPEMIG) and Fundação de Desenvolvimento da Pesquisa (FUNDEP).

We thank all members of AGABM for their help, logistic and financial support, especially Rodrigo<sup>20</sup> Martins and Juliano Maciel, who have maintained their commitment to our research group. We are particularly indebted to the team at the Córrego do Sítio office. We also thank João Orestes dos Santos (University of Western Australia - UWA); Sarah Gilbert from the Centre of Excellence in Ore Deposits-CODES, Hobart, who helped us with the LA-ICP-MS analyses and final quantification of the chemical elements; colleagues at the Applied Isotope Research Group, Universidade Federal de Ouro Preto (UFOP), for the support in the isotopic data; and M.A. da Costa for providing additional information on gold occurrences. We also thank the editor and reviewers for their support and comments.

#### **PARTE IV - INTEGRAÇÃO E CONCLUSÕES DO TRABALHO**

#### **4 CONSIDERAÇÕES FINAIS**

As investigações realizadas nas rochas da associação ressedimentada forneceram informações adicionais para um melhor entendimento destas sequências clásticas na região do Quadrilátero Ferrífero, assim como uma melhor avaliação do potencial econômico de depósitos auríferos hospedados em rochas turbidíticas arqueanas. De grande extensão regional, essa associação se destaca pela variação litológica, sedimentológica, vulcânica e hidrotermal, além de outros aspectos evolutivos. O presente estudo é particularmente relevante pelo fato deste *greenstone belt* ser dominado por rochas sedimentares (e.g., Baars, 1997).

Os trabalhos de detalhamento no setor leste representam importante passo na compreensão da mineralização aurífera e da paragênese mineral, fornecendo semelhanças genéticas entre as rochas dessa associação nas jazidas de Cachorro Bravo, Laranjeiras e Carvoaria, balizados por levantamentos geológicos, petrográficos, litoquímicos, geocronológicos (Porto, 2008; Lima, 2012;

Sequetto-Pereira et al., 2015; Roncato et al., 2015; Ribeiro et al., 2015) e por análises de ablação a *laser in situ* ICP-MS em sulfetos. O entendimento da associação ressedimentada é proposto através da comparação das rochas turbidíticas dos setores leste e norte (Figs. 2.1, 3.1, 3.2 e 3.3), que contribuíram na construção do modelo de evolução geodinâmica apresentado na Figura 3.20, através de estudos petrográficos, litoquímicos e geocronológicos, resumidamente apresentados a seguir:

1. Os depósitos de ouro hospedados em sequência turbidítica do lineamento Córrego do Sítio contém variedade de minerais-minério, tais quais pirita, arsenopirita e pirrotita, incluindo sulfetos e sulfossais que contêm Sb, Pb, Hg, Cu, Zn, além de Co e Ni. Do ponto de vista da ambiência geológica, o setor leste tem relação, com as associações de litofácies (Baltazar e Zucchetti, 2007) vulcanoplutônica máfica-ultramáfica, vulcanossedimentar química, sedimentar química-pelítica e, principalmente, sedimentar clástica marinha e sedimentar clástica não-marinha, o que favorece a variedade nas fontes sedimentares.
2. Duas galerias mapeadas nas rochas mineralizadas do depósito Cachorro Bravo (Figs. 2.5 e 2.6), setor leste, mostraram que o aumento da intensidade da alteração hidrotermal com a proximidade dos veios de quartzo torna-se evidente pelo clareamento das rochas hospedeiras e aumento na quantidade de sulfetos disseminados (Fig. 2.8).
3. Os elementos maiores (Fig. 3.11) das rochas clásticas estudadas, normalizados pelo NASC, não apresentam significativas modificações geoquímicas devido à alteração hidrotermal, tanto nos setores leste e norte, onde as rochas foram amostradas na parte distal dos depósitos, distante da mineralização.
4. Elementos maiores (Fig. 3.11A) e tracos (Fig. 3.11B) apresentaram uma pequena variação geoquímica nas amostras dos setores leste e norte. Já os ETR são muito semelhantes para a maioria das amostras, especialmente dentro do mesmo grupo de rochas (Fig. 3.13A e B), evidenciando grande similaridade geoquímica nas rochas clásticas da associação

ressedimentada. Os resultados geoquímicos são comparáveis ao de rochas sedimentares arqueanas, registrando alto conteúdo de ETR pesados, padrões normalizados ao condrito abrupto, e uma incipiente ou ausente anomalia de Eu.

5. Dados geoquímicos para elementos maiores (Fig. 3.11A), traços (Fig. 3.11B) e ETR (Figs. 3.13A e B) mostram que a proveniência das sequências turbidíticas dos setores leste e norte receberam contribuição de fontes félsicas e máficas, tendo o setor leste maior proporção de herança máfica, mais abundante naquele setor do Quadrilátero Ferrífero;
6. O evento Rio das Velhas (2780-2760 Ma) de Baltazar e Zucchetti (2007), e também os eventos Rio das Velhas II (2800-2770 Ma) e, principalmente, Mamona (2760-2680 Ma) de Lana et al. (2013; Figs. 3.15) são os mais significativos períodos-fonte de zircões em ambos os sectores. O evento Santa Barbara (3220 - 3200 Ma), mais antigo, é melhor registrado nos zircões das rochas clásticas do lineamento Córrego do Sítio, cujas estruturas regionais colocam em contato rochas do complexo granito-gnáissico e com as da associação ressedimentada.
7. Zircões provenientes dos turbiditos da associação ressedimentada, de ambos os setores, registram idades desde o Paleoarqueano até o Proterozoico (Fig. 3.15). Os dados (Fig. 3.15, Tabelas anexo 3) paleoproterozoicos provavelmente refletem a presença de fragmentos líticos e zircões das grauvacas com idades semelhantes ao Grupo Sabará nos turbiditos arqueanos.
8. A presença desses fragmentos líticos indica o imbricamento tectônico do Grupo Nova Lima com turbiditos paleoproterozoicos, possivelmente do Grupo Sabará, explicando a presença de zircões detríticos de idades mais avançadas e mais jovens claramente juntos (Reis et al., 2002; Alkmim e Martins-Neto, 2012). Este fato pode ser evidenciado pela grande quantidade de falhas encontradas nos dois setores, mas notadamente estudadas no setor leste, onde quatro eventos deformacionais principais são reconhecidos (Figs. 2.5 e 2.6). O



evento  $D_1$  é caracterizado por uma foliação progressiva  $S_{1-2}$ .  $D_2$  é caracterizado por uma clivagem crenulação;  $D_3$  é representado dobras abertas de grande escala que arqueam  $S_0$ ,  $S_{1-2}$  e  $S_3$ ;  $D_4$  é representado por fraturas paralelas e espaçadas.

9. Os valores de  $\epsilon_{Hf}$  apontam para uma proveniência predominantemente de rochas cristalizadas no Arqueano (3,0-2,6 Ga), a partir de fontes mantélicas ou crustais retrabalhadas (Figs. 3.16A e B). As amostras do setor leste registram principalmente valores de  $\epsilon_{Hf}$  para crosta retrabalhada e valores secundários de origem juvenil (Fig. 3.16A). Os resultados isotópicos Lu-Hf suportam a hipótese de que os magmas eram parcialmente juvenis com significativa incorporação de material crustal retrabalhado, para ambos os setores.

O detalhamento do setor leste incluiu análises por ablação a *laser in situ* ICP-MS em sulfetos nos depósitos de Laranjeiras e Cachorro Bravo, cujas conclusões estão discriminadas abaixo:

1. Próximo aos diques metamáficos encaixados na associação ressedimentada, especialmente no depósito de Cachorro Bravo, as arsenopiritas porosa (P-Apy) e lisa (S-Apy) se desenvolvem nos veios mineralizados a partir do consumo de pirrotitas (S-Po, P-Po). Arsenopirita formada a partir das piritas porosa (P-Py) e lisa (S-Py) é típica de zonas de alteração hidrotermal distante das rochas metamáficas, onde os veios são dominados por quartzo fumê e carbonato, associados a bertierita, estibnita e ouro.
2. Dois estágios hidrotermais de evolução para os pelitos carbonosos são reconhecidos: (1) estágio cedo hidrotermal, marcado pelo desenvolvimento de sulfetos porosos (P-Py e P-Apy), durante o qual alguma precipitação do ouro ocorreu; (2) Estágio hidrotermal principal a tardio, reconhecido pelo desenvolvimento de sulfetos lisos (S-Py, S-Po e S-Apy), registrando o pico de ouro entre seus valores. Esta fase é dominada por recristalização a partir das fases de sulfetos porosos (1) para produzir sulfetos lisos (2) (Fig. 3.7).
- 3.

4. As análises *in situ* de LA-ICP-MS são comparadas em três tipos de sulfetos amostrados em pelitos carbonosos da associação ressedimentada, no lineamento Córrego do Sítio. No depósito Laranjeiras foram analisadas pirita porosa (P-Py) e lisa (S-Py), pirrotita lisa (S-Po), arsenopirita porosa (P-Apy) e lisa (S-Apy). Cristais de pirita lisa (S-Py) do depósito Cachorro Bravo foram também analisadas (Figs. 3.6, 3.7 e 3.8). *Box-whisker* (Fig. 3.9) mostram que para 11 (onze) elementos analisados existe enriquecimento ou empobrecimento relevantes dependendo da textura, geração e tipo de sulfeto.
5. Os elementos traço típicos comumente concentrados em xistos carbonosos em todo o mundo (Large et al., 2011), Mo, V, Ni, Cr, Zn, As, Sb, Hg, Cu, Se, Te, Bi, e W, também foram encontrados nas amostras analisadas (Figs. 3.9 e 3.10).
6. A concentração de As, Co, Ni, Te, Pb e Sb em arsenopirita nas principais fases de mineralização de ouro tem implicações importantes para a gênese dos depósitos do lineamento Córrego do Sítio. Arsenopirita e pirita, sulfetos com maior teor de Au, também registram alto As e Co.
7. Cobalto, Sb e Pb são enriquecidos em P-Apy e S-Apy (Fig. 3.10). Ouro, As e Sb são mais concentrados em S-Apy; precipitação do ouro ocorre principalmente nos estágios hidrotermais tardios juntamente com Sb e As.
8. Pirita lisa (S-Py) do depósito Cachorro Bravo mostra concentração mais elevada de Au e As em comparação com o depósito Laranjeiras. Em Cachorro Bravo, onde a pirrotita carente de ouro é mais abundante, há importante associação do depósito com os diques e *sills* máficos. Este sulfeto parece ter evoluído a partir do sobrecrescimento da P-Py, transformação que pode ser responsável pela liberação de Au para o fluido hidrotermal.
9. O fluido hidrotermal foi provavelmente modificado desde a sua gênese, durante sua ascensão, e consequente interação com as rochas hospedeiras da associação ressedimentada (*e.g.*, Goldfarb et al., 1988; 1991; Goldfarb e Groves, 2015). O pelito carbonoso pode ter

sido, ao menos em parte, fonte para Au, As e S durante a alteração hidrotermal nos depósitos do lineamento Córrego do Sítio, uma vez que estes metais são relativamente enriquecidos nos sedimentos originais. Esse ponto é questionado por outros autores (*e.g.* Goldfarb e Groves, 2015), que afirmam não ter evidências para significantes quantidades de sulfetos nessas rochas sedimentares.

10. A fonte mista para as rochas da associação ressedimentada no setor leste pode ser evidenciada no fato do ouro possuir boa correlação com Se, As, Sb e Te de filiação sedimentar, assim como elementos de afinidade máfica-ultramáfica como Co, Ni e Pt.
11. A interação do fluido hidrotermal com rochas hospedeiras permitiu a incorporação e a depleção de certos elementos no fluido remanescente, detectada por meio de análises *in situ* LA-ICP-MS nos sulfetos. Arsênio é o elemento traço mais abundante, seguido de Ni and Co, nas piritas (P-Py e S-Py), e também nas arsenopiritas (P-Apy e S-Apy). Estes elementos foram provavelmente assimilados durante a alteração hidrotermal indicando fonte local desses elementos durante a mineralização de ouro.

## 5 BIBLIOGRAFIA

- Alkmim, F.F., Marshak, S., 1998. Transamazonian orogeny in the Southern São Francisco Craton region, Minas Gerais, Brazil: evidence for Paleoproterozoic collision and collapse in Quadrilátero Ferrífero. *Precambrian Research*, 90, 29-58.
- Alkmim, FF; Martins-Neto, MA. 2012. Proterozoic first-order sedimentary sequences of the São Francisco craton, eastern Brazil. *Marine and Petroleum Geology*, 33 (1), 127-139.
- Almeida F.F.M. 1976. Estruturas do Pré-Cambriano Inferior Brasileiro. In: 29º Congresso Brasileiro de Geologia, 1976. Ouro Preto, Resumos SBG, p. 201-202.
- Almeida, F.F.M. 1977. O Cráton do São Francisco. *Revista Brasileira de Geociências*, 7: 349-364.
- Anhaeusser, C.R., 2014. Archaean greenstone belts and associated granitic rocks – A review. *Journal of African Earth Sciences*, 100, 684–732.
- Arehart G.B., Chryssoulis S.L., Kesler S.E. 1993. Gold and arsenic in iron sulfides from sediment-hosted disseminated gold deposits: implications for depositional processes. *Economic Geology*, 88: 171-185.
- Ávila, C.A., Teixeira, W., Cordani, U.G., Moura, C.A.V., Pereira, R.M., 2010. Rhyacian (2.23-2.20) juvenile accretion in the southern São Francisco craton, Brazil: Geochemical and isotopic evidence from the Serrinha magmatic suite, Mineiro belt. *Journal of South American Earth Sciences* 29, 143-159.
- Baars, F.J., 1997. The São Francisco Craton. In: M.J. de Wit; L. D Ashwal. (eds.). *Greenstone Belts*. Oxford, England. Clarendon Press, 529-557 (Oxford Monographs on Geology and Geophysics 35).
- Babinsky, M.; Chemale Junior, F.; Schmus, W. R. V. The Pb/Pb age of the minas supergroup carbonate rocks quadrilátero ferrífero, Brazil. *Precambrian Research*, v. 72, n. 3-4, p. 235-245, 1995.
- Baltazar, O.F., Silva, S.L., 1996. Projeto Rio das Velhas: Mapa Geológico Integrado do Supergrupo Rio das Velhas, escala 1:100.000. Departamento Nacional de Produção Mineral/CPRM–Serviço Geológico do Brasil, Belo Horizonte.
- Baltazar O.F. & Silva S.L. 1998a. Mapa geológico integrado do supergrupo Rio das Velhas, escala 1: 100.000. Brasília, Departamento Nacional de Produção Mineral, CPRM.
- Baltazar O.F. & Silva S.L. 1998b. Projeto Rio das Velhas - texto explicativo do mapa geológico integrado, escala 1: 100.000. Belo Horizonte, Departamento Nacional de Produção Mineral. 126 p.
- Baltazar O.F. & Zucchetti M. 2007. Lithofacies associations and structural evolution of the Archean Rio das Velhas greenstone belt, Quadrilátero Ferrífero, Brazil: a review of the setting of gold deposits. *Ore Geology Reviews*, 32(3-4):471-499.
- Beauchamp, A -M; Dubé, B; Malo, M; McNicoll, V J; Brisson, T; Archer, P; Lavoie, J; Chartrand, F; Geology, mineralization and alteration of the turbidite-hosted Mustang Au showing, Lower Eastmain greenstone belt, Superior Province, Quebec; in, Targeted Geoscience Initiative 4: Contributions to the understanding of Precambrian lode gold deposits and implications for exploration; Dubé, B (ed.); Mercier-Langevin, P (ed.). Geological Survey of Canada, Open File 7852, 2015,; p. 227-243.

- Bhatia, M.R., 1983. Plate tectonics and geochemical composition of sandstones. *Jour.Geol.* 91(4), 611-626.
- Bierlein F.P., Fuller T., Stuwel K., Arne D.C., Keays R.R. 1998. Wallrock alteration associated with turbidite-hosted gold deposits examples from Central. Victoria. *Ore Geology Reviews*, 13(1-5):345-380.
- Bierlein, FP, Arne, DC, Foster, DA, Reynolds, P.2001. A geochronological framework for orogenic gold mineralisation in central Victoria, Australia. *Mineral Deposit* 36: 741–767.
- Bolhar, R., Woodhead J.D., Hergt J.M. 2003, Continental setting inferred for emplacement of the 2.9–2.7 Ga Belingwe Greenstone Belt, Zimbabwe: *Geology*, v.31, p. 295– 298.
- Bouma, Arnold H. 1962. *Sedimentology of some Flysch deposits: A graphic approach to facies interpretation*, Elsevier, Amsterdam, 168 p.
- Bouma A.H. 1983. Intraslope basins in northwest Gulf of Mexico: a key to ancient submarine canyons and fans. *American Association of Petroleum Geologists Special. Publication*, 32:567-581.
- Boyle, R.W. 1986. Gold deposits in turbidite sequences: Their geology, geochemistry and history of theories of their origin, in Keppie J.D., Boyle R.W., Haynes S.J. *Turbidite-hosted Gold Deposits, Volume Special. Paper*, 32:1-13.
- Brito Neves, B. B. The Paleoproterozoic in the South American Continent: Diversity in the Geological time. *Journal of South American Earth Sciences*, v. 32, p. 1-20, 2011.
- Canale A.L. 1999. *Geologia do depósito Córrego do Sítio, Quadrilátero Ferrífero (MG), e caracterização mineralógica do minério sulfetado*. MS Dissertation, Universidade Federal do Rio Grande do Sul, Porto Alegre, 142 p.
- Chu, N.C., Taylor, R.N., Chavagnac, V., Nesbitt, R.W., Boella, R.M., Milton, J.A., German, C.R., Bayon, G., Burton, K., 2002. Hf isotope ratio analysis using multi-collector inductively coupled plasma mass spectrometry: an evaluation of isobaric interference corrections. *Journal of Analytical Atomic Spectrometry*. 17, 1567-1574.
- Condie K.C. 1981. *Archean greenstone belts*. Amsterdam, Elsevier, 433 p.
- Cook N.J. & Chryssoulis S.L. 1990. Concentrations of “invisible” gold in the common sulfides. *Canadian Mineralogist*, 28:1-16.
- Cox S.F., Sun S.S., Etheridge M.A., Wall V.J., Potter T.F. 1995. Structural and geochemical controls on the development of turbidite-hosted gold quartz vein deposits, Wattle Gully mine, central. Victoria, Australia. *Economic Geology*, 90:1722-1746.
- Cox S.F., Wall V.J., Etheridge M.A., Potter T.F. 1991. Deformational. and metamorphic processes in the formation of mesothermal vein-hosted gold deposits - examples from the Lachlan Fold Belt in Central. Victoria, Australia. *Ore Geology Reviews*, 6(5):391-423.
- Crook, K. A. W., 1974. Lithogenesis and geotectonics: the significance of compositional variation in flysch arenites and graywackes. In : R.H. Dott and R.H. Shaver (Ed.), *Modern and ancient geosynclinal sedimentation*. Soc. Econ. Paleontol Mineral, Spec. Pub.19, 304-310.
- Danyushevsky, L., Robinson, P., Gilbert, S., Norman, M., Large, R., McGoldrick, P., Shelley, M., 2011. Routine quantitative multi-element analysis of sulphide minerals by laser ablation ICP-MS: Standard development and consideration of matrix effects. *Geochem., Explor. Environ. Anal.* 11, 51–60.

- David M.E.V. 2006. Composição isotópica de Pb, Sr e Nd da mineralização de ouro do depósito Córrego do Sítio, Quadrilátero Ferrífero (MG): implicações na modelagem conceitual, MS Dissertation, Instituto de Geociências, Universidade de São Paulo, São Paulo, 76 p.
- Devajaru, T. C., Sudhakar, T.L., Kaukonen, R. J., Viljoen, R.P., Alapieti, T. T., Ahmed, S.A. and Sivakumar, S. (2010) Petrology and geochemistry of graywackes from Goa-Dharwar sector, western Dharwar craton: implications for volcanoclastic origin. *Jour. Geol. Soc. India*, v.75, pp.465–487.
- Dickin, A. P. 2005. *Radiogenic Isotope Geology*, 2nd Ed. Cambridge University Press, 492 pp.
- Dickinson, W.R., Lawton, T.F., and Gehrels, G.E., 2009, Recycling detrital zircons: A case study from the Cretaceous Bisbee Group of southern Arizona: *Geology*, v. 37, p. 503–506.
- Dorr II J.V.N. 1969. Physiographic, stratigraphic and structural development of the Quadrilátero Ferrífero, Minas Gerais, Brazil. U.S. Geological. Survey Professional. Paper, 614(A):1-110.
- Dorr II J.V.N., Gair J.E., Pomerene J.G., Rynearson G.A. 1957. Revisão da estratigrafia pré-cambriana do Quadrilátero Ferrífero. v. 81. Brasília, Divisão de Fomento da Produção Mineral.
- Emsbo P., Hofstra A.H., Lauha E.A., Griffin G.L., Hutchinson R.W. 2003. Origin of high-grade gold ore, source of ore fluid components, and genesis of the Meikle and neighboring Carlin-type deposits, northern Carlin trend, Nevada. *Economic Geology*, 98:1069-1100.
- Eschewege, W.L. von. 1822. *Geognostisches Gemälde von Brasilien und wahrscheinliches Muttergestein der Diamanten*. Landes-Industrie-Comptoir, Weimar, 44 pp.
- Dubé, B., and Gosselin, P., 2007, Greenstone-hosted quartz-carbonate vein deposits, in Goodfellow, W.D., ed., *Mineral. Deposits of Canada: A Synthesis of Major Deposit-Types, District Metallogeny, the Evolution of Geological. Provinces, and Exploration Methods: Geological. Association of Canada, Mineral. Deposits Division, Special. Publication No. 5*, p. 49-73.
- Farina, F., Albert, C., Lana, C., 2015. The Neoproterozoic transition between medium- and high-K granitoids: Clues from the Southern São Francisco Craton (Brazil). *Precambrian Research* 266, 375–394.
- Fedo, C.M., Sircombe, K.N., Rainbird, R.H., 2003. Detrital zircon analysis of the sedimentary record. In: Hanchar, J.M., Hoskin, P.W.O. (Eds.), *Zircon, Reviews in Mineralogy and Geochemistry*. 53, 277 – 303.
- Feng, R., Kerrich, R., 1990. Geochemistry of fine-grained clastic sediments in the Archean Abitibi greenstone belt, Canada: implications for provenance and tectonic setting. *Geochem. Cosmochim. Acta* 54, 1061-1081.
- Fleet, M.E., Chrysoulis, S.L., Maclean, P.J., Davidson, R., and Weisener, G.G., 1993, Arsenian pyrite from gold deposits—Au and As distribution investigated by SIMS and EMP, and color staining and surface oxidation by XPS and LIMS: *Canadian Mineralogist*, v. 31, p. 1–17.
- Fontaine, A; Dubé, B; Malo, M; McNicoll, V J; Brisson, T; Doucet, D; Goutier, J; Geology of the metamorphosed Roberto gold deposit (Éléonore Mine), James Bay region, Quebec: diversity of mineralization styles in a polyphase tectonometamorphic setting; in, Targeted Geoscience Initiative 4: Contributions to the understanding of Precambrian lode gold deposits and implications for exploration; Dubé, B (ed.); Mercier-Langevin, P (ed.). Geological. Survey of Canada, Open File 7852, 2015,; p. 209-225.

- Friedl J., Wagner F.E., Wang N. 1995. On the chemical state of combined gold in sulfidic ores: conclusions from Mössbauer source experiments. *Neues Jahrbuch für Mineralogie*, 169:279-290.
- Gao Z.L. & Kwat T.A.P. 1995. Turbidite-hosted gold deposits in the Bendigo-Ballarat and Melbourne zones, Australia. 1. Geology, mineralisation, stable isotopes, and implications for exploration. *International Geology Review*, 37:910-944.
- Gaboury, D., 2013. Does gold in orogenic deposits come from pyrite in deeply buried carbon-rich sediments? : Insight from volatiles in fluid inclusions. *Geology* 41, 1207– 1210.
- Gair, J.E., 1962. Geology and ore deposit of the Nova Lima and Rio Acima quadrangles, Minas Gerais, Brazil. United States Geological Survey Professional Paper 341-A. 67 pp.
- Goldfarb, R.J. and Groves, D.I. Orogenic gold: common or evolving fluid and metal sources through time. *Lithos* 233 (2015) 2–26.
- Leach D.L., Pickthorn W.J., Paterson C.J. 1988. Origin of lode-gold deposits of the Juneau gold belt, southeastern Alaska. *Geology*, 16:440-443.
- Goldfarb R.J., Newberry R.J., Pickthorn W.J., Gent C.A. 1991. Oxygen, hydrogen, and sulfur isotope studies in the Juneau gold belt, southeastern Alaska: constraints on the origin of the hydrothermal fluids. *Economic Geology*, 86:66-80.
- Goldfarb, R.J., Baker, T., Dube, B., Groves, D.I., Hart, C.J.R., and Gosselin, P., 2005. Distribution, character, and genesis of gold deposits in metamorphic terranes. In Hedenquist, J. W., Thompson, J. F. H., Goldfarb, R. J., and Richards, J. P., eds., *Economic Geology. 100th Anniversary Volume 1905–2005*: Littleton, Colorado, Society of Economic Geologists, p. 407–450.
- Golding, S. D., McNaughton, N.J., Barley, M.E., Groves, D.I., Ho, S.E., Rock, N.M.S. and Turner, J.V., 1989. Archaean Carbon and Oxygen Reservoirs: Their Significance for Fluid Sources and Circulation Paths for Archaean Mesothermal. Gold Deposits of the Norseman-Wiluna Belt, Western Australia. In: *The Geology of Gold Deposits: The Perspective in 1988* (ed. Keays, R. R., Ramsay, W.R.H. and Groves, D.I.) *Economic Geology Monograph #6*, The Economic Geology Publishing Company, New Haven CT.
- Gregory, D.D. The Trace Element Composition of Sedimentary Pyrite: Factors Effecting Uptake and Uses of the Data for Determining Paleo-Ocean Conditions [PhD]. Hobart, Tasmania: University of Tasmania; 2014.
- Gregory, D D, Large, R R, Halpin, J A, Lounejeva Baturina, E, Lyons, T W, Wu, S, Sack, P J, Chappaz, A, Maslennikov, V V and Bull, S W, in review (2015). Trace element content of background sedimentary pyrite in black shales, *Economic Geology*
- Gromet, L. P., Dymek, R. F., Haskin, L. A. and Korotev, R. L. (1983) The 'North American Shale Composite': its compilation, major and trace element characteristics. *Geochim. Cosmochim. Acta* 48, 2469– 2482.
- Gross, G.A., 1980, A classification of iron formations based on depositional environments: *Canadian Mineralogist*, v. 18, p. 215-222.
- Groves, D.I., Foster, R.P.; 1993. Archean lode gold deposits. In: R.P. Foster (ed.) *Gold Metallogeny and Exploration*. New York, Chapman & Hall, 63-103 p.

- Groves D.I., Goldfarb R.J., Gebre-Marian M., Hagemann S.G., Robert F. 1998. Orogenic gold deposits: a proposed classification in the context of their distribution and relationship to other gold deposit types. *Ore Geology Reviews*, 13:7-27.
- Groves, D.I., Goldfarb, R.J., Santosh, 2015. The conjunction of factors that lead to the formation of giant gold provinces and deposits in non-arc settings. *Geoscience Frontiers*. 7 (2016) 409-417.
- Hayashi, K.I., Fujisawa, H., Holland, H.D., Ohomoto, H., 1997. Geochemistry of ~ 1.9 Ga sedimentary rocks from northern Labrador, Canada. *Geochim. Cosmochim. Acta*. 61(19), 4115-4137.
- Helmstaedt, H. and Padgham W. A., 1986. A new look at the stratigraphy of the Yellowknife Supergroup at Yellowknife, N.W.T. — implications for the age of gold-bearing shear zones and Archean basin evolution. *Canadian Journal of Earth Sciences*, 1986, 23:454-475, 10.1139/e86-049
- Herron, M.M., 1988. Geochemical. Classification of terrigenous sands and shales from core or log data. *Jour. Sed. Pet.* 58, 820-829.
- Herz N. 1970. Gneissic and igneous rocks of the Quadrilátero Ferrífero, Minas Gerais, Brazil. U.S. Geological. Survey Professional. Paper, 641(B):1-58.
- Hoskin, P. W. O. & Schaltegger, U. (2003). The composition of zircon and igneous and metamorphic petrogenesis. In: Hanchar, J. M. & Hoskin, P.W.O. (eds) *Zircon. Reviews in Mineralogy and Geochemistry* 53, 27–62.
- Huston, D.; Blewett, R.; Mernaugh, T.; Sun, S-S.; Kamprad, J. (2001). Gold deposits of the Pilbara Craton: results of AGSO Research, 1998–2000, vol 10, p 32
- Jackson S.L., Fyona A.J., Corfub F. 1994. Review of Archean supracrustal assemblages of the southern Abitibi greenstone belt in Ontario, Canada: products of microplate interaction within a large-scale plate-tectonic setting. *Precambrian Research*, 65:183-205.
- Jackson, S.E., Pearson, N.J., Griffin, W.L., Belousova, E.A., 2004. The application of laser ablation-inductively coupled plasma-mass spectrometry to in situ U–Pb zircon geochronology. *Chem. Geol.* 211, 47–69.
- Krapez B. 1993. Sequence stratigraphy of the Archaean supracrustal belts of the Pilbara Block, Western Australia. *Precambrian Research*, 60:1-45.
- Kerrick, R., Wyman, D., Fan, J., and Bleeker, W., 1998, Boninite series: Low Ti-tholeiite associations from the 2.7 Ga Abitibi greenstone belt: *Earth and Planetary Science Letters*, v. 164, p. 303–316.
- Ketris, M.P., and Yudovitch, Y.E., 2009, Estimations of Clarkes for Carbonaceous bioliths: World averages for trace element contents in black shales and coals: *International. Journal of Coal. Geology*, v. 78, p. 135–148.
- Kinny, P.D., Maas, R., 2003. Lu–Hf and Sm–Nd isotope systems in zircon. In: Hanchar J.M., Hoskin P.W.O.(eds.) *Zircon. Reviews in Mineralogy and Geochemistry*. Mineralogical Society of America 53, Washington, DC,327-341.
- Kishida, A. and Kerrich, R., 1986. Hydrothermal alteration zoning and gold concentration at the Kerr-Addison Archean lode gold deposit, Kirkland Lake, Ontario. *Econ. Geol.*, 82: 649-690.



- Klein, C., Ladeira, E.A. Geochemistry and petrology of some Proterozoic banded iron-formations of the Quadrilátero Ferrífero, Minas Gerais, Brazil. *Economic Geology*, 95, p. 405-428, 2000.
- Kohler, E., Anhaeusser, C.R., 2002. Geology and geodynamic setting of Archean silicic metavolcaniclastic rocks of the Bien Venue Formation, Fig Tree Group, northeast Barberton greenstone belt, South Africa. *Precambrian Research* 116,199–235.
- Koti, B.K.; Hegde, V.S.; Shalini., G; Krishna-Prasad, P.A. 2011. Geochemistry of Late Archean Greywacke - Argillite Suite of Rocks from Kittur Khanapur Area, Karnataka: Implications on their Provenance. *International Journal of Earth Sciences and Engineering*, vol. 04, pp. 84-95.
- Ladeira, E. A. 1980. Metallogenesis of gold at the Morro Velho Mina and in the Nova Lima District , Quadrilátero Ferrífero , Minas Gerais , Brazil. 1980. 272 f. Tese de Doutorado. University of Western Ontario.
- Ladeira, E.A. 1991. Genesis of gold in Quadrilátero Ferrífero: a remarkable case of permanency, recycling and inheritance - a tribute to Djalma Guimaraes, Pierre Routhier and Hans Ramberg. In: E.A. Ladeira (ed.) *Proceedings of GOLD'91, the Economics, Geology, Geochemistry and Genesis of Gold Deposits*. Rotterdam, A.A. Balkema, 11- 30p.
- Lana, C., Alkmim, F.F., Armstrong, R., Scholz, R., Romano, R., Nalini Jr., H.A., 2013. The ancestry and magmatic evolution of Archean TTG rocks of the Quadrilátero Ferrífero province, southeast Brazil. *Precambrian Research* 231, 157– 173.
- Large, R.R., Maslennikov, V., Robert, F., Danyushevsky, L.V., and Chang, Z., 2007, Multistage sedimentary and metamorphic origin of pyrite and gold in the giant Sukhoi Log deposit, Lena gold province, Russia: *ECONOMIC GEOLOGY*, v. 102, p.
- Large, R.R., Danyushevsky, L.V., Hollit, C., Maslennikov, V., Meffre, S., Gilbert, S., Bull, S., Scott, R., Emsbo, P., Thomas, H., and Foster, J., 2009, Gold and trace element zonation in pyrite using a laser imaging technique: Implications for the timing of gold in orogenic and Carlin-style sedimenthosted deposits: *ECONOMIC GEOLOGY*, v. 104, p. 635–668.
- Large, R.R., Bull, S.W., Maslennikov, V.V.A., 2011. Carbonaceous sedimentary source-rock model for Carlin-type and orogenic gold deposits. *Economic Geology*. 106, 331–358.
- Li X, Kwak T A P, Brown R W. 1998. Wallrock alteration in the Bendigo gold ore field, Victoria, Australia: Uses in exploration. *Ore Geol Rev*, 13: 381-406.
- Lima, L.C. 2012. Depósito LODE Au-As-Sb Laranjeiras, em metaturbitos do Grupo Nova Lima, Quadrilátero Ferrífero, Minas Gerais. MS Dissertation, Instituto de Geociências, Universidade Federal. de Minas Gerais, Belo Horizonte, 306 p.
- Lobato, L.M., Ribeiro-Rodrigues, L.C., Vieira, F.W.R., 2001a. Brazil's premier gold province: Part II. Geology and genesis of gold deposits in the Archean Rio das Velhas greenstone belt, Quadrilátero Ferrífero. *Mineralium Deposita* 36, 249–277.
- Lobato, L.M., Ribeiro-Rodrigues, L.C., Zucchetti, M., Noce, C.M., Baltazar, O.F., Silva, L.C., Pinto, C.P., 2001b. Brazil's premier gold province: Part I. The tectonic, magmatic, and structural setting of the Archean Rio das Velhas greenstone belt, Quadrilátero Ferrífero. *Mineralium Deposita* 36, 228–248.
- Lobato L.M., Baltazar O.F., Reis L.B., Achtschin A.B., Baars F.J., Timbó M.A., Berni G.V., Mendonça B.R.V., Ferreira D.V. 2005. Projeto Geologia do Quadrilátero Ferrífero -

integração e correção cartográfica em SIG com nota explicativa. Belo Horizonte, CODEMIG. 1 CD-ROM.

- Longerich, H.P., Jackson, S.E. and Günther D. 1996. Laser ablation inductively coupled plasma mass spectrometric transient signal data acquisition and analyte concentration calculation, *Journal of Analytical. Atomic Spectrometry*, 11: 899-904.
- Ludwig, K.R., 2012. Isoplot 3.75, A geochronological toolkit for Microsoft Excel; Berkeley Geochronology Center Special. Publication no.5.
- Machado, N., Schrank, A.; Abreu, F.R.; Knauer, L.G.; Abreu, P.A. 1989. Resultados preliminares da geocronologia U/Pb na Serra do Espinhaço Meridional. In: 5º Simpósio de Geologia de Minas Gerais. Belo Horizonte. SBG, Bol., v. 10, p. 171-174.
- Machado, N. and Carneiro, M.A., 1992. U-Pb evidence of Late Archean tectonothermal activity in southern São Francisco shield, Brazil. *Canadian Journal of Earth Sciences* 29, 2341–2346.
- Machado, N., Carneiro, M.A., 1992. U–Pb evidence of late Archean tectono-thermal activity in the southern São Francisco shield, Brazil. *Canadian Journal of Earth Science* 29, 2341–2346.
- Machado, N., Schrank, A., Noce, C.M., Gauthier, G., 1996. Ages of detrital zircon from Archean-Paleoproterozoic sequences: Implications for Green-stone Belt setting evolution of a Transamazonian foreland basin in Quadrilátero Ferrífero, southeast Brazil. *Earth and Planetary Science Letters* 141,259–276.
- Martins, B.S. 2011. Controle da mineralização aurífera de Lamego, Sabará, Quadrilátero Ferrífero, MG. M.Sc. thesis, Universidade Federal de Minas Gerais, Belo Horizonte, Brazil, 250 pp.
- Martins, Pereira, S.L, Lobato, L.M., Ferreira, J.E., Jardim, E.C., 2007. Nature and origin of the BIF-hosted São Bento gold deposit, Quadrilátero Ferrífero, Brazil, with special emphasis on structural controls. *Ore Geology Reviews* 32, 571-595.
- Martins, BS, Lobato, LM, Rosière, CA, Hagemann, SG, Figueiredo e Silva, RC, Villanova, FLSP, Lemos, LHA (2016). The Archean BIF-hosted Lamego gold deposit, Rio das Velhas greenstone belt, Quadrilátero Ferrífero: Evidence for Cambrian structural modification of an Archean orogenic gold deposit. *Ore Geology Reviews*, 72: 963-988.
- Maynard, J.B., Valloni, R., Yu, H.S., 1982. Composition of modern deep-sea sands from arc-related basins. *Geolo. Soc. London, Spec. Publ.* 10, 551-561.
- Matteini, M., Dantas, E.L., Pimentel, M.M., Bühn, B., 2010. Combined U-Pb and Lu-Hf isotope analyses by laser ablation MC-ICP-MS: methodology and applications. *Annals Brazil. Acad. Scienc.* 82, 479-491.
- Mendes, M. ; Lobato, L. ; Suckau, V. ; Lana, C. . In situ LA-ICPMS U-Pb dating of detrital zircons from the Cercadinho Formation, Minas Supergroup. *Geologia USP. Série Científica* , v. 14, p. 55-68, 2014.
- Morales, M. J.; SILVA, Rosaline Cristina Figueiredo e; Lobato, Lydia M. ; Gomes, S. D. ; Gomes, C. C. C. O. ; BAanks, David . Metal source and fluid-rock interaction in the Archean BIF-hosted Lamego gold mineralization: microthermometric and LA-ICP-MS analysis of fluid inclusions in quartz veins, Rio das Velhas greenstone belt, Brazil. *Ore Geology Reviews*, v. 72 (1), p. 510-531, 2016
- Naqvi, S.M., 1986. Geochemical characters and tectonic evolution of the Chitradurga Schist Belt: an Archean suture (?) of the Dharwar Craton, India. In: deWitt, M.J., Ashwal, L.D. (Eds.), *Workshop on Tectonic Evolution of Greenstone Belts*. Lunar and Planetary Institute Technical. Report, vol. 86–10, pp. 160–161.

- Noce, C.M., 2000. Geochronology of the Quadrilátero Ferrífero: a review. *Geonomos* 8 (1), 15–23.
- Noce, C.M., Machado, N., Teixeira, W., 1998. U–Pb geochronology of gneisses and granitoids in the Quadrilátero Ferrífero (southern São Francisco craton): age constraints for Archean and Paleoproterozoic magmatism and metamorphism. *Revista Brasileira de Geociências* 28, 95–102.
- Noce, C.M., Zucchetti, M., Baltazar, O.F., Armstrong, R., Dantas, E.L., Renger, F.E., Lobato, L.M., 2005. Age of felsic volcanism and the role of ancient continental crust in the evolution of the Neoproterozoic Rio das Velhas greenstone belt (Quadrilátero Ferrífero, Brazil): U–Pb zircon dating of volcanoclastic graywackes. *Precambrian Research* 141, 67–82.
- Noce, C.M., Tassinari, C.G., Lobato, L.M., 2007. Geochronological framework of the Quadrilátero Ferrífero, with emphasis on the age of gold mineralization hosted in Archean greenstone belts. *Ore Geology Reviews* 32, 500–510.
- Ootes L., Morelli R.M., Creaser R.A. Lentz D.R., Davis H.W.J. 2011. The timing of Yellowknife gold mineralization: a temporal relationship with crustal anatexis? *Economic Geology*, 106:713-720.
- O'Rourke, J.E., 1957. The stratigraphy of metamorphic rocks of the Rio de Pedras and Gandarela quadrangles, Minas Gerais, Brazil. PhD thesis, University of Wiscosin. Wiscosin, 106 pp.
- Padgham W.A. 1992. Mineral deposits in the Archean Slave Structural Province: lithological and tectonic setting. *Precambrian Research*, 58:1-24.
- Palenik C.S., Utsunomiya S., Reich M., Kesler S.E., Wang L.M., Ewing R.C. 2004. “Invisible” Au revealed: direct imaging of Au nanoparticles in a Carlin-type deposit. *American Mineralogist*, 89:1359-1366.
- Pettijohn, F.J., 1975. Sedimentary rocks. Harper and Row, New York, 3rd ed., 628p.
- Perring, C.S., Groves, D.I., and Shellabear, J.N., 1991, The geochemistry of Archean gold ores from the Yilgarn block of Western Australia: Implications for gold metallogeny: Minerals and Energy Research Institute of Western Australia Report 82, 15 p.
- Phillips, G.N. & Groves, D.I. 1984. Fluid access and fluid wall-rock interaction in the genesis of the Archean gold-quartz vein deposit at Hunt Mine, Kambalda, Western Australia. In: Foster R.P. (ed.) *Gold '82: the Geology, Geochemistry and Genesis of Gold Deposits* (Geological Society of Zimbabwe special publications). Oxfordshire, Taylor & Francis, p. 389-416.
- Phillips, G.N., Powell, R., 2010. Formation of gold deposits: a metamorphic devolatilization model. *Journal of Metamorphic Geology* 28, 689–718.
- Pidgeon, R. T., Wilde, S. A., Compston, W. & Shield, M. W. 1990. Archean evolution of the Wongan Hills Greenstone Belt, Yilgarn Craton, Western Australia. *Australian Journal of Earth Science* 37, 279-92.
- Pitcairn, I.K., Craw, D., Teagle, D.A.H., 2015. Metabasalts as sources of metals in orogenic gold deposits. *Mineralium Deposita* 50, 373–390.
- Porto, C.G. 2008. A mineralização aurífera do depósito Córrego do Sítio e sua relação com o enxame de diques metamórficos no corpo Cachorro Bravo - Quadrilátero Ferrífero - Minas Gerais. MS Dissertation, Universidade Federal de Minas Gerais, Belo Horizonte, 117 p.
- Porto C.G., Lobato L.M., Massucatto A.J. 2006. Caracterização da mineralização aurífera de Córrego do Sítio. Sessão Pôster. In: II Simpósio Brasileiro de Exploração Mineral. - SIMEXMIN. Ouro Preto, ADIMB, CD-ROM.

- Poulsen, K.H., Robert, F., and Dubé, B., 2000, Geological. Classification of Canadian Gold Deposits: Geological. Survey of Canada, Bulletin 540, 106 p.
- Reich, M., Kesler, S.E., Utsunomiya, S., Palenik, C.S., Chryssoulis, S.L., and Ewing, R., 2005, Solubility of gold in arsenian pyrite: *Geochimica et Cosmochimica Acta*, v. 69, p. 2781–2796.
- Reis, L.A., Martins-Neto, M.A., Gomes, N.S., Endo, I., 2002. A bacia de antepaís paleoproterozóica Sabará, Quadrilátero Ferrífero, MG. *Revista Brasileira de Geociências* 32, 43-58.
- Renger, F.E., Noce, C.M., Romano, A.W., Machado, N., 1995. Evolução sedimentar do Supergrupo Minas: 500 Ma. de registro geológico no Quadrilátero Ferrífero, Minas Gerais, Brasil. *Geonomos* 2 (1), 1-11.
- Ribeiro-Rodrigues L.C. 1998. Gold in Archean banded iron-formation of the Quadrilátero Ferrífero, Minas Gerais, Brazil. The Cuiabá Mine. PhD Thesis, Aachen University, Aachen, 264 p.
- Ribeiro-Rodrigues, L.C., Oliveira, C.G., Friedrich, G., 2007 The Archean BIF-hosted Cuiabá Gold deposit, Quadrilátero Ferrífero, Minas Gerais, Brazil. *Ore Geology Reviews* 32, 543–570.
- Ribeiro Y., Silva R.C.F., Lobato L.M., Lima L.C., Hagemann S.G., Cliff J. 2013. Estudo de inclusões fluidas em veios de quartzo e carbonato ( $\pm$  sulfetos e sulfossais) do depósito Carvoaria Velha, Lineamento Aurífero Córrego do Sítio, Santa Bárbara, Quadrilátero Ferrífero, MG. *Geonomos*, 21:7-28.
- Robert, F., Poulsen K.H., Cassidy, K.F., and Hodgson, C.J., 2005, Gold Metallogeny of the Superior and Yilgarn Cratons, in *Economic Geology 100th Anniversary Volume*, 1001-1034.
- Romano, R., Lana, C., Alkmim, F.F., Stevens, G.S., Armstrong, R., 2013. Stabilization of the southern portion of the São Francisco Craton, SE Brazil, through a long-lived period of potassic magmatism. *Precambrian Research* 224, 143–159.
- Romano, A.W., 1989. Evolution tectonique de la région NW du Quadrilatère Ferrifère – Minas Gerais, Brésil. Unpublished PhD Thesis. University of Nancy, France, 259 p.
- Roncato, J.G., Lobato, L.M., Lima, L.C., Porto, C.G., Figueiredo e Silva, R.C., 2015. Metaturbidite-hosted gold deposits, Córrego do Sítio Lineament, Quadrilátero Ferrífero, Brazil. *Brazilian Journal of Geology* 45: 5-2.
- Roser, B.P., Korsch, R.J., 1988. Provenance signatures of sandstone-mudstone suites determined using discriminant function analysis of major-element data. *Chem. Geol.* 67, 119-139.
- Sandeman H.A., Rafuse H., Copeland D. 2010. The setting of orogenic auriferous quartz veins at the Golden Promise prospect, central Newfoundland, and observations on veining and wall-rock alteration. St. John's, Newfoundland Department of Natural Resources, Geological Survey, 16 p.
- Schorscher H.D., Carbonari F.S., Polonia J.C., Moreira J.M.P. 1982. Quadrilatero Ferrífero - Minas Gerais State: Rio das Velhas Greenstone Belt and Proterozoic Rocks. In: *International Symposium on Archean and Early Proterozoic Crustal Evolution and Metallogenesis*. Salvador, 46 p.
- Sawyer, E.W. 1986. The influence of source rock type, chemical weathering and sorting on the geochemistry of clastic sediments from the Quetico Metasedimentary Belt, Superior Province. *Chemical Geology* 55, 77-95.

- Sequetto-Pereira, M.A., Lobato, L.M., Rosière C.A., Silva, R.C.F. 2013. Classificação dos veios quartzo-carbonáticos de depósitos auríferos no Lineamento Córrego do Sítio, QF, MG. *Geonomos*, 21:53-71.
- Sibson, R. H.; Robert, F.; Poulsen, K. H. 1988. High angle reverse faults, fluid-pressure cycling, and mesothermal gold-quartz deposits. *Geology*, v. 16, p. 551-555.
- Simon G., Kesler S.E., Chryssoulis S. 1999. Geochemistry and textures of gold-bearing Arsenian pyrite, Twin Creeks, Nevada: implications for deposition of gold in Carlin-type deposits. *Economic Geology*, 94:405-422.
- Schorscher, H.D., 1978. Komatiitos na estrutura “Greenstone Belt” Série Rio das Velhas, Quadrilátero Ferrífero, Minas Gerais, Brasil. 30th Congresso Brasileiro de Geologia. Sociedade Brasileira de Geologia, Recife, pp. 292–293.
- Stacey, J. S. and Kramers, J. D. (1975). Approximation of terrestrial lead isotope evolution by a two-stage model. *Earth Planet. Sci. Lett.* 26, 207-211.
- Taylor, S.R., McLennan, S.M., 1985. *The Continental Crust: its Composition and Evolution*. Blackwell Scientific Publications, Oxford. 312 pp.
- Teixeira, W. & Figueiredo, M.C.H. 1991. An outline of early Proterozoic crustal evolution in the São Francisco craton, Brazil. *Precamb. Res.*, 53:1-22.
- Teixeira, W., Carneiro, M.A., Noce, C.M., Machado, N., Sato, K., Taylor, P.N. 1996. Pb, Sr and Nd isotope constrains on the Archaean evolution of gneissic -granitoid complexes in São Francisco Craton, Brazil. *Precambrian Research*, 78:151-164.
- Teixeira, W., Ávila C.A., Dussin, I.A., Corrêa Neto, A.V., Bongioiolo, E.M., Santos, J.O., Barbosa, N.S., A juvenile accretion episode (2.35–2.32Ga) in the Mineiro belt and its role to the Minas accretionary orogeny: Zircon U–Pb–Hf and geochemical evidences, *Precambrian Research*, 2015, 256, 148.
- Toledo C.L.B. 1997. Controle estrutural da mineralização aurífera na mina de Cuiabá, setor noroeste do Greenstone Belt Rio das Velhas, Quadrilátero Ferrífero. Universidade Estadual de Campinas, M.Sc. Thesis, 166p.
- Van Achterbergh, E., Ryan, C.G., Jackson, S.E., Griffin, W., 2001. Data reduction soft-ware for LA-ICP-MS. In: Sylvester, P. (Ed.), *Laser Ablation ICPMS in the Earth Science*, 29. Mineralogical Association of Canada, pp. 239–243.
- Vial, D.S. Mapeamento Geológico do Nível 3 da Mina de Cuiabá. Relatório interno da Mineração Morro Velho S.A. 1980. 21p.
- Vial, D.S., DeWitt, E., Lobato, L.M., Thorman, C.H., 2007. The geology of the Morro Velho gold deposit in the Archean Rio das Velhas greenstone belt, Quadrilátero Ferrífero, Brazil. *Ore Geology Reviews* 32, 511–542.
- Woodhead, J.D., and Hergt, J.M.(2005). A preliminary appraisal of seven natural zircon reference materials for In Situ Hf isotope determination. *Geostandards and Geoanalytic Res.* 29, 183–195.
- Wronkiewicz, D. J. and Condie, K. C. (1990) Geochemistry and mineralogy of sediments from the Ventersdorp and Transvaal. Supergroups, South Africa: cratonic evolution during the early Proterozoic. *Geochim. Cosmochim. Acta* 54, 343–354.
- Zucchetti, M., Baltazar, O.F., Raposo, F.O., 1998. Estratigrafia. In: M. Zucchetti, O.F. Baltazar (Eds.), *Projeto Rio das Velhas—Texto explicativo do mapa geológico integrado, escala*

1:100.000. 2nd ed. Departamento Nacional de Produção Mineral/CPRM–Serviço Geológico do Brasil, Belo Horizonte, p. 13–42.

- Zucchetti, M., Lobato, L.M., Baltazar, O.F., 2000a. Volcanic and volcanoclastic features in Archean rocks and their tectonic environment, Rio das Velhas Greenstone Belt, Quadrilátero Ferrífero, MG. Brazil. *Revista Brasileira de Geociências* 30, 388–392.
- Zucchetti, M., Lobato, L.M., Baars, F.J., 2000b. Genetically diverse basalt geochemical signatures developed in the Rio das Velhas Greenstone Belt, Quadrilátero Ferrífero, Minas Gerais, Brazil. *Revista Brasileira de Geociências* 30, 397–402.
- Ye Z., Kesler S.E., Essene E.J., Zohar P.B., Borhauer J.L. 2001. Relation of Carlin-type gold mineralization to lithology, structure and alteration: Screamer zone, Betze-Post deposit, Nevada. *Mineralium Deposita*, 38:22-38.
- Zucchetti M. & Baltazar O.F. 2000. Rio das Velhas Greenstone Belt lithofacies associations, Quadrilátero Ferrífero, Minas Gerais, Brazil. In: 31th International. Geological. Congress, Rio de Janeiro. CD-ROM.

# **ANEXO 1**

DADOS MAPEAMENTO SUBTERRÂNEO  
DADOS FUROS DE SONDAGEM

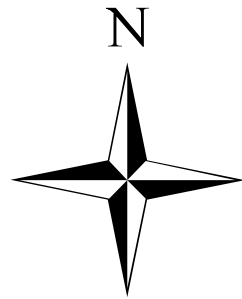
# AngloGold Ashanti

## Mapa Geológico

### Mina de Córrego do Sítio - Nível 658

### Depósito Cachorro Bravo


### Corpos - 200 / 211 Sul



#### Legenda

#### PROTEROZÓICO

#### Rochas Ígneas de Idade Incerta

 Rocha Intrusiva Metamorfisada (anfibiólio-plagioclásio-carbonato-epidoto-clorita Xisto)


#### ARQUEANO


#### Supergrupo Rio das Velhas


#### NEOARQUEANO


#### Grupo Nova Lima


#### Unidade Córrego do Sítio - Intermediária


 Venulações mili-centimétricas de quartzo e carbonato

 Veios de quartzo fumê com sulfetos e sulfossais de espessuras variável de milímetros a metros.

 Veios de quartzo branco com sulfetos e sulfossais de espessuras variável de milímetros a metros.

 Zona hidrotermal mineralizada rica em venulações

 Plagioclásio-clorita-mica-quartzo Filito Carbonoso, clorita-quartzo-mica Xisto carbonoso, metapelito carbonoso intercalados com subordinadas lentes de metagrauvaca e metapsamito carbonoso Indivisos


 Metagrauvaca e metapsamito carbonoso Indivisos


#### Geologia Estrutural

 Foliação

 Foliacao Milonitica

 Lineacao

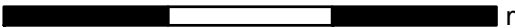
 Clivagem Crenulacao

 Falhas e Fraturas

 Acamamento

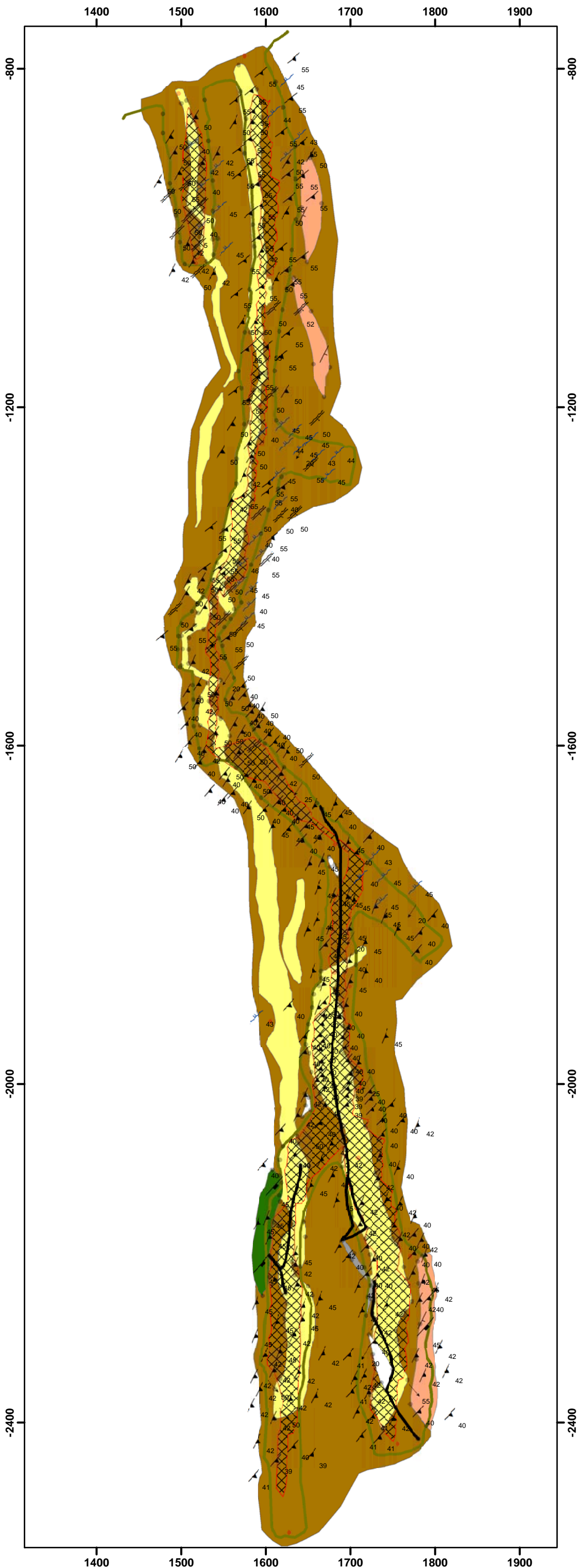
 Limite Galeria 658

 Mergulho Dique

0 100 200 300  
 m

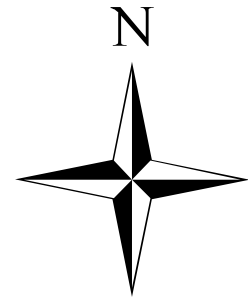
#### Sistema de Coordenadas Local

**Autor: Jorge G. Roncato Jr.**  
**Orientador: Profa. Dra. Lydia Maria Lobato**  
**Apoio: Vale S/A., AngloGold Ashanti Brasil**  
**Mineração Ltda., Capes**





**AngloGold Ashanti**  
**Mapa Geológico**  
**Mina de Córrego do Sítio - Nível 711**  
**Depósito Cachorro Bravo**  
**Corpos - 200 / 211 Norte**



**Legenda**






**ARQUEANO**

**Supergrupo Rio das Velhas**

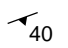
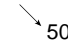

**NEOARQUEANO**

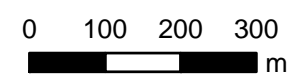
**Grupo Nova Lima**

**Unidade Córrego do Sítio - Intermediária**

-  Venulações mili-centimétricas de quartzo e carbonato
-  Veios de quartzo fumê com sulfetos e sulfossais de espessuras variável de milímetros a metros.
-  Veios de quartzo branco com sulfetos e sulfossais de espessuras variável de milímetros a metros.
-  Zona hidrotermal mineralizada rica em venulações
-  Plagioclásio-clorita-mica-quartzo Filito Carbonoso, clorita-quartzo-mica Xisto carbonoso, metapelite carbonoso intercalados com subordinadas lentes de metagrauvaca e metapsamito carbonoso Indivisos

**Geologia Estrutural**

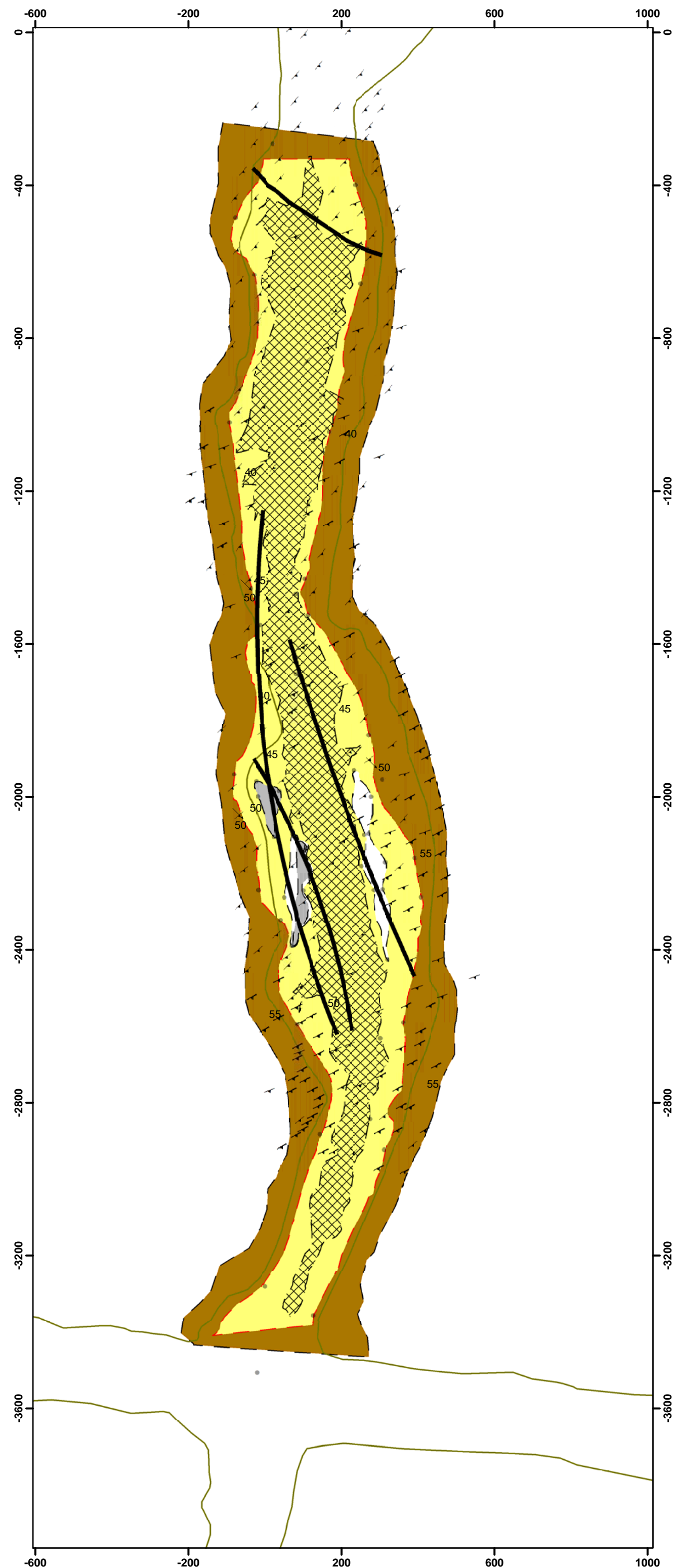
-  Foliação
-  Lineacao
-  Falhas e Fraturas



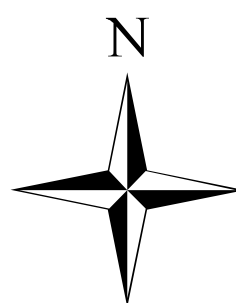
1:10,000

**Sistema de Coordenadas Local**

**Autor: Jorge G. Roncato Jr.**  
**Orientador: Profa. Dra. Lydia Maria Lobato**  
**Apoio: Vale S/A., AngloGold Ashanti Brasil**  
**Mineração Ltda., Capes**











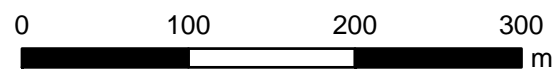
**AngloGold Ashanti**  
**Mapa Geológico**  
**Mina de Córrego do Sítio - Nível 658**  
**Depósito Cachorro Bravo**  
**Corpos - 200 / 211 Sul**



**Legenda**

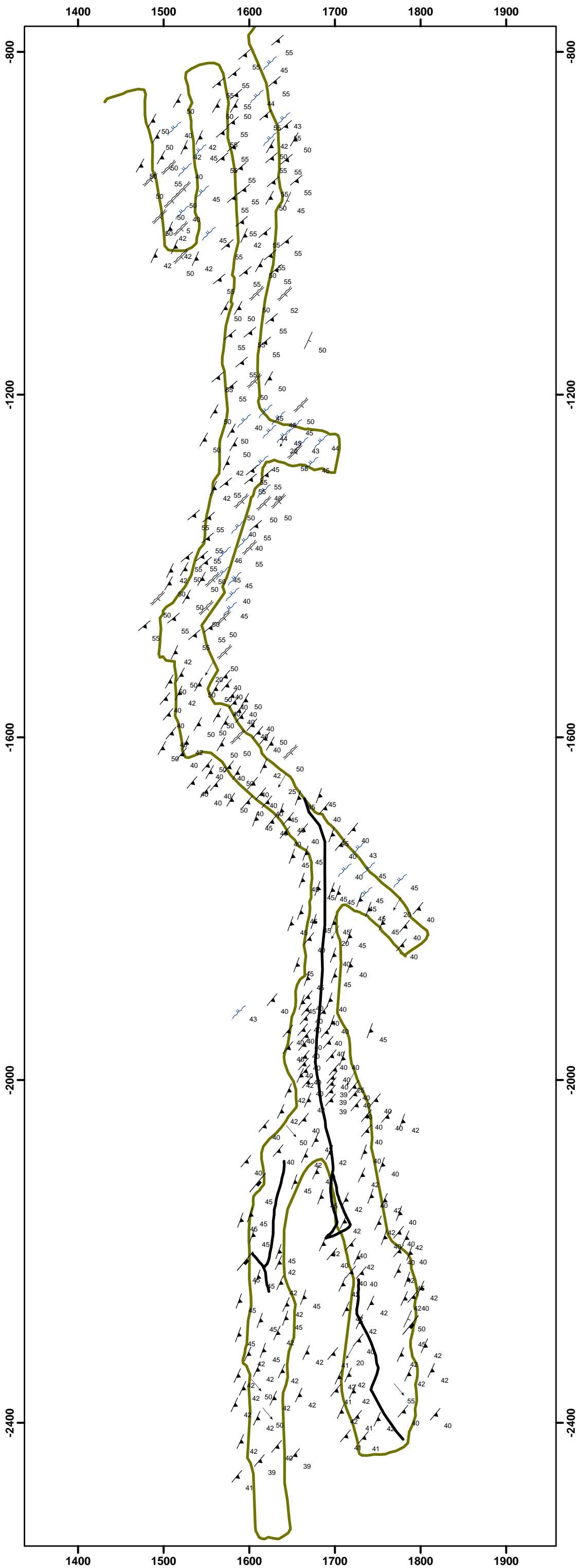
**Geologia Estrutural**

- |  |   |
|--|---|
|  Foliação             |  Foliacao Milonitica |
|  Lineacao             |  Clivagem Crenulacao |
|  Falhas e Fraturas   |  Acamamento          |
|  Limite Galeria 658 |  Mergulho Dique    |

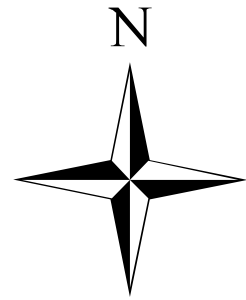


**Sistema de Coordenadas Local**

**Autor: Jorge G. Roncato Jr.**  
**Orientador: Profa. Dra. Lydia Maria Lobato**  
**Apoio: Vale S/A., AngloGold Ashanti Brasil**  
**Mineração Ltda., Capes**

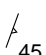
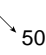



**AngloGold Ashanti**  
**Mapa Estrutural**  
**Mina de Córrego do Sítio - Nível 711**  
**Depósito Cachorro Bravo**  
**Corpos - 200 / 211 Norte**



**Legenda**

**Geologia Estrutural**

-  Foliação 45
-  Lineação 50
-  Falhas e Fraturas

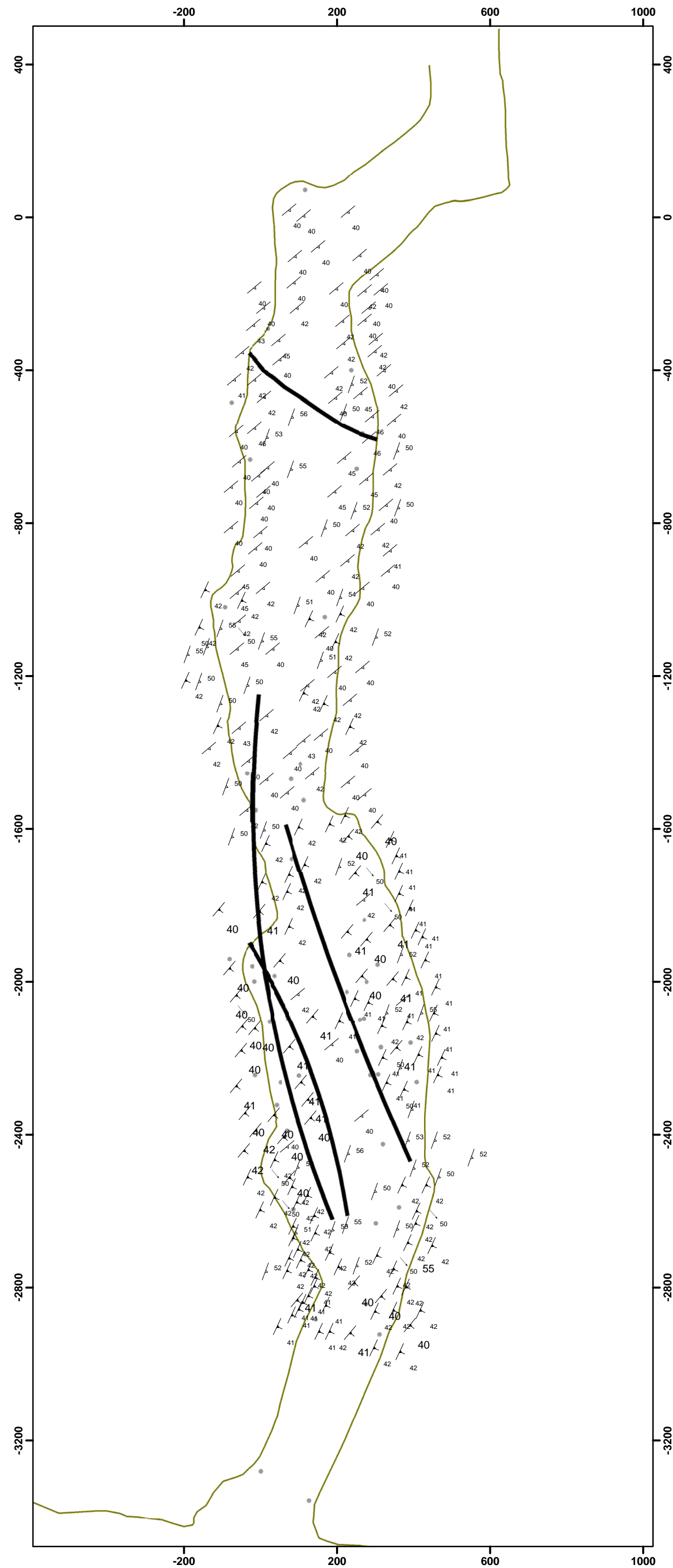
 40

0 100 200 300  
m

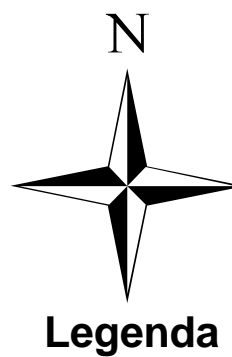
1:10,000

**Sistema de Coordenadas Local**

**Autor: Jorge G. Roncato Jr.**  
**Orientador: Profa. Dra. Lydia Maria Lobato**  
**Apoio: Vale S/A., AngloGold Ashanti Brasil**  
**Mineração Ltda., Capes**



**AngloGold Ashanti**  
**Mapa Geológico**  
**Mina de Córrego do Sítio - Nível 658**  
**Depósito Cachorro Bravo**  
**Corpos - 200 / 211 Sul**

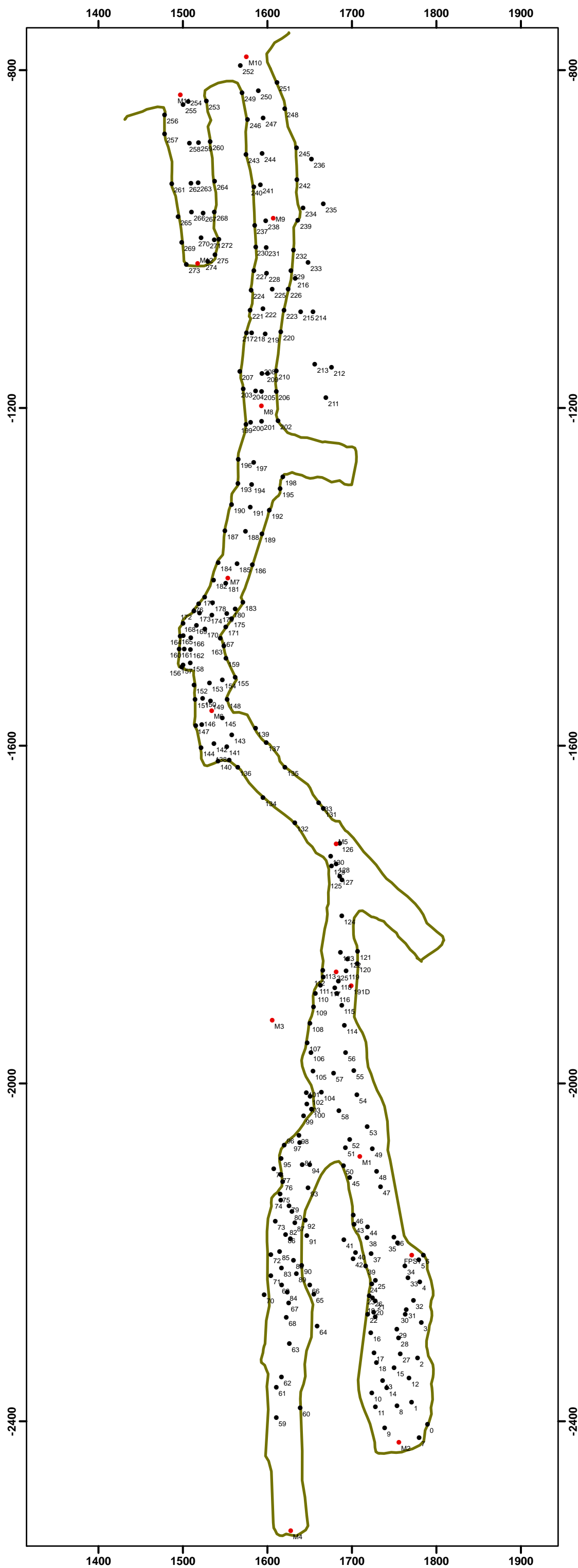


- Pontos Topográficos
- Estação de Campo

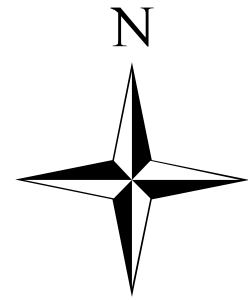


Sistema de Coordenadas Local

**Autor: Jorge G. Roncato Jr.**  
**Orientador: Profa. Dra. Lydia Maria Lobato**  
**Apoio: Vale S/A., AngloGold Ashanti Brasil**  
**Mineração Ltda., Capes**

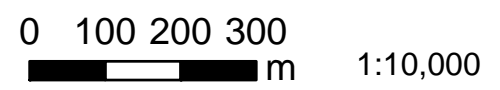


**AngloGold Ashanti**  
**Mapa de Pontos**  
**Mina de Córrego do Sítio - Nível 711**  
**Depósito Cachorro Bravo**  
**Corpos - 200 / 211 Norte**



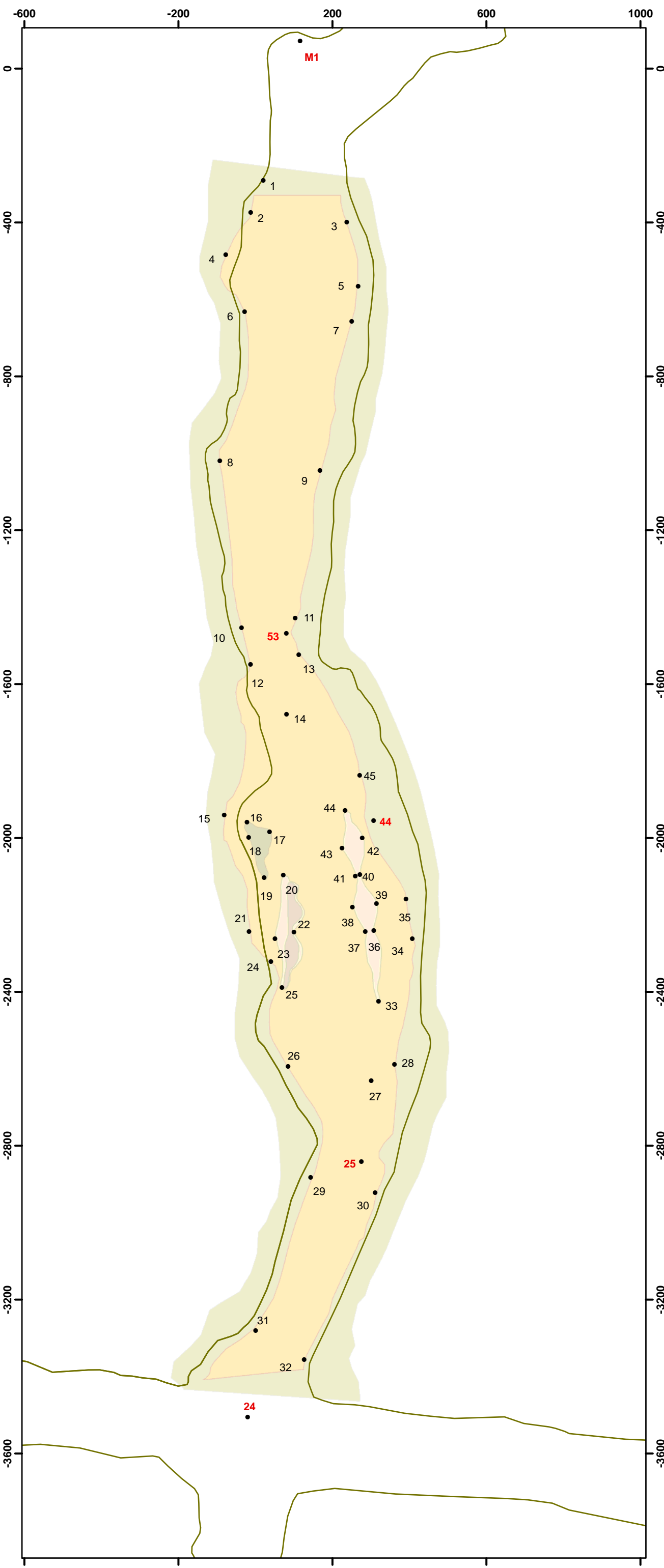
**Legenda**

- 1 Estação de campo
- 44** Ponto Topográfico



Sistema de Coordenadas Local

**Autor: Jorge G. Roncato Jr.**  
**Orientador: Profa. Dra. Lydia Maria Lobato**  
**Apoio: Vale S/A., AngloGold Ashanti Brasil**  
**Mineração Ltda., Capes**



# **ANEXO 2**

TABELAS ANÁLISES QUÍMICA DE ROCHA  
TABELAS ANÁLISES LA-ICP-MS EM  
SULFETOS

**Table 1 - Major, trace and REE values of the selected greywackes and pelites samples of eastern and northern sectors of Quadrilátero Ferrífero.**

Origin	Borehole	Sampling Interval (m)	Major Elements										
			SiO <sub>2</sub>	TiO <sub>2</sub>	Al <sub>2</sub> O <sub>3</sub>	Fe <sub>2</sub> O <sub>3</sub>	MnO	MgO	CaO	Na <sub>2</sub> O	K <sub>2</sub> O	P <sub>2</sub> O <sub>5</sub>	LOI
			%	%	%	%	%	%	%	%	%	%	%
<b>CDS* - Cachorro Bravo Deposit</b>	FCS0756 (MG**+PL***)	48,65 - 91,57	56,09	0,69	16,28	8,23	0,13	4,84	1,10	1,37	2,03	0,09	8,8
<b>CDS - Cachorro Bravo Deposit</b>	FCS1053 (MG)	209,00 - 260,10	62,96	0,50	15,27	5,14	0,12	3,21	2,01	0,90	3,33	0,09	6,1
<b>CDS - Cachorro Bravo Deposit</b>	FCS1273 (MG)	248,00 - 274,55	61,44	0,61	13,42	7,89	0,18	4,21	1,61	0,95	2,09	0,08	7,2
<b>CDS - Cachorro Bravo Deposit</b>	FCS1273 (MG)	283,55 - 316,90	60,28	0,70	15,38	8,15	0,14	4,44	1,10	0,77	2,30	0,10	6,3
<b>CDS - Carvoaria Deposit</b>	FCS1196 (MG)	279,15 - 312,20	65,67	0,70	11,26	8,42	0,22	3,29	1,77	1,33	1,25	0,09	5,7
<b>CDS - Carvoaria Deposit</b>	FCS1261 (MG)	247,75 - 252,65	64,96	0,67	12,08	8,00	0,26	3,30	1,93	2,19	1,27	0,09	5,0
<b>CDS - Carvoaria Deposit</b>	FCS1261 (MG)	258,80 - 283,95	62,37	0,65	13,38	7,81	0,19	3,96	1,56	1,48	1,75	0,09	6,5
<b>CDS - Laranjeiras Deposit</b>	FCS0831 (MG + PL)	267,20 - 296,44	60,31	0,67	14,44	7,19	0,12	4,56	2,69	1,33	1,87	0,18	6,4
<b>CDS - Laranjeiras Deposit</b>	FCS0886 ( PL)	331,50 - 361,55	65,37	0,41	12,77	5,96	0,22	3,15	2,31	1,18	2,43	0,04	5,9
<b>CDS - Laranjeiras Deposit</b>	FCS0929 (MG + PL)	191,50 - 257,15	60,55	0,62	14,01	8,20	0,15	4,19	1,18	1,17	2,04	0,09	7,5
<b>CDS - Laranjeiras Deposit</b>	FCS0932 (MG)	127,75 - 175,75	65,43	0,55	11,19	9,13	0,31	3,36	1,57	0,57	1,88	0,06	5,7
<b>Cuiabá Mine</b>	CBABSD00004B (MG)	1,274,10 - 1,310,35	61,72	0,64	11,82	8,01	0,18	5,76	1,90	1,30	1,37	0,08	6,9
<b>Cuiabá Mine</b>	CBABSD00004B (PL)	1,274,05 - 1,279,01	66,61	0,57	9,57	7,65	0,21	4,93	1,75	1,44	1,09	0,07	5,8
<b>Cuiabá Mine</b>	CBABSD00005 (MG)	1,462,40 - 1,520,67	63,71	0,59	10,59	7,41	0,13	6,27	2,03	1,94	0,77	0,08	6,1
<b>Cuiabá Mine</b>	CBABSD00005 ( Black PL)	312,32 - 319,94	63,29	0,60	13,47	7,62	0,18	3,94	1,40	1,43	1,94	0,08	5,8
<b>Cuiabá Mine</b>	CBABSD00005 (MG)	1,462,40 - 1,520,67	60,42	0,63	12,04	7,53	0,10	6,62	1,74	1,93	1,34	0,09	7,2
<b>Lamego Mine</b>	CARBSD12A (PL)	471,40 - 548,60	56,19	0,67	13,93	8,81	0,11	8,59	1,93	1,53	1,17	0,09	6,6
<b>Lamego Mine</b>	CARBSD15 (PL)	125,62 - 157,75	54,35	0,79	14,20	8,35	0,12	6,41	1,66	1,90	1,41	0,10	10,3
<b>Lamego Mine</b>	CARBSD17 (MG+PL)	485,29 - 554,82	56,01	0,74	14,53	9,08	0,10	8,03	1,75	1,52	1,47	0,10	6,2
<b>Lamego Mine</b>	CARBSD17 (PL)	586,78 - 598,84	53,66	0,75	14,10	9,73	0,12	9,06	1,95	1,51	1,05	0,10	7,5

\* Córrego do Sítio auriferous lineament (Roncato et al., 2015)

\*\* MG - Greywackes intercalations

\*\*\* PL - Pelites intercalations

**Table 1 - Major, trace and REE values of the selected grey**

Origin	Borehole	Trace Elements														
		Ba	Rb	Sr	Cs	Ga	Tl	Ta	Nb	Hf	Zr	Y	Th	U	Sc	Cr
		PPM	PPM	PPM	PPM	PPM	PPM	PPM	PPM	PPM	PPM	PPM	PPM	PPM	PPM	PPM
<b>CDS* - Cachorro Bravo Deposit</b>	FCS0756 (MG**+PL***)	321	83,8	126,6	9,2	18,4	0,1	0,8	8,9	3,9	145,2	25,1	9,4	2,7	21	323
<b>CDS - Cachorro Bravo Deposit</b>	FCS1053 (MG)	695	91,0	142,9	6,5	18,2	0,1	0,6	7,6	3,8	121,5	15,6	8,2	2,5	15	697
<b>CDS - Cachorro Bravo Deposit</b>	FCS1273 (MG)	337	74,5	111,6	9,2	15,7	0,1	0,7	6,7	3,0	117,9	18,0	8,1	2,6	17	339
<b>CDS - Cachorro Bravo Deposit</b>	FCS1273 (MG)	381	81,2	90,6	20,0	17,1	0,1	0,8	8,0	3,9	134,0	20,5	7,9	3,1	20	383
<b>CDS - Carvoaria Deposit</b>	FCS1196 (MG)	251	48,8	100,6	5,0	13,0	0,1	0,5	6,7	5,1	202,3	20,8	6,7	2,2	14	253
<b>CDS - Carvoaria Deposit</b>	FCS1261 (MG)	256	49,2	105,2	4,7	13,7	0,1	0,5	7,5	3,9	171,6	21,8	8,0	3,3	15	258
<b>CDS - Carvoaria Deposit</b>	FCS1261 (MG)	307	62,5	100,5	6,8	14,1	0,1	0,9	7,8	4,1	148,6	20,5	7,4	2,3	17	309
<b>CDS - Laranjeiras Deposit</b>	FCS0831 (MG + PL)	316	76,6	146,2	7,3	15,4	0,1	0,7	9,2	4,0	165,6	22,0	12,0	4,0	16	318
<b>CDS - Laranjeiras Deposit</b>	FCS0886 ( PL)	331	140,4	105,3	6,7	14,9	0,1	0,9	8,2	4,2	149,1	17,3	8,7	2,9	11	333
<b>CDS - Laranjeiras Deposit</b>	FCS0929 (MG + PL)	315	79,9	117,5	8,5	14,9	0,1	0,9	8,5	3,7	142,2	22,5	9,2	3,0	17	317
<b>CDS - Laranjeiras Deposit</b>	FCS0932 (MG)	298	79,8	104,5	5,9	12,9	0,1	0,7	7,7	3,6	140,2	23,6	7,1	2,4	16	300
<b>Cuiabá Mine</b>	CBABSD00004B (MG)	340	41,8	115,1	2,7	13,2	0,1	0,5	5,7	3,4	130,1	18,3	5,8	2,2	18	342
<b>Cuiabá Mine</b>	CBABSD00004B (PL)	332	28,7	127,8	1,6	11,2	0,1	0,5	6,4	3,8	143,1	19,2	7,9	3,1	13	334
<b>Cuiabá Mine</b>	CBABSD00005 (MG)	220	20,1	141,3	1,1	11,1	0,1	0,5	6,0	3,8	128,2	17,8	4,9	1,8	15	222
<b>Cuiabá Mine</b>	CBABSD00005 ( Black PL)	327	72,7	86,5	4,2	15,7	0,1	0,8	7,6	3,7	133,6	18,9	9,2	3,1	16	329
<b>Cuiabá Mine</b>	CBABSD00005 (MG)	338	33,0	150,8	1,9	12,9	0,1	0,7	5,9	3,9	135,0	18,6	4,4	1,3	17	340
<b>Lamego Mine</b>	CARBSD12A (PL)	211	34,8	89,8	2,2	14,0	0,1	0,5	5,7	3,1	107,6	18,2	4,1	1,4	23	213
<b>Lamego Mine</b>	CARBSD15 (PL)	322	43,8	146,8	3,1	16,7	0,1	0,7	5,9	3,7	122,8	18,1	4,7	1,3	23	324
<b>Lamego Mine</b>	CARBSD17 (MG+PL)	300	50,5	98,4	2,7	16,4	0,1	0,6	5,5	3,1	106,7	19,0	4,6	1,5	24	302
<b>Lamego Mine</b>	CARBSD17 (PL)	232	38,5	82,7	2,1	16,2	0,1	0,5	5,5	3,5	120,4	20,5	5,0	1,4	25	234

\* Córrego do Sítio auriferous lineament (Roncato et al., 2015)

\*\* MG - Greywackes intercalations

\*\*\* PL - Pelites intercalations



**Table 1 - Major, trace and REE values of the selected grey**

Origin	Borehole	Trace Elements														
		Pb	Ni	V	Zn	Co	Cu	Bi	Cd	Sn	W	Mo	Be	Ag	Au	Hg
		PPM	PPM	PPM	PPM	PPM	PPM	PPM	PPM	PPM	PPM	PPM	PPM	PPM	PPB	PPM
<b>CDS* - Cachorro Bravo Deposit</b>	FCS0756 (MG**+PL***)	5,7	248,8	153	104	40,2	70,2	0,1	0,1	2	4,8	2,4	2	0,4	37,3	0,67
<b>CDS - Cachorro Bravo Deposit</b>	FCS1053 (MG)	71,1	184,1	101	741	34,3	102,2	0,6	1,5	3	2,0	2,9	3	0,3	1,5	0,12
<b>CDS - Cachorro Bravo Deposit</b>	FCS1273 (MG)	14,9	228,2	123	78	38,9	83,6	0,3	0,2	2	4,2	3,4	1	0,1	2,6	0,20
<b>CDS - Cachorro Bravo Deposit</b>	FCS1273 (MG)	7,1	249,2	148	90	41,5	80,7	0,2	0,1	2	5,4	2,9	3	0,1	1,7	0,09
<b>CDS - Carvoaria Deposit</b>	FCS1196 (MG)	6,6	148,3	118	103	38,0	103,6	0,1	0,2	1	1,7	3,4	2	0,1	0,5	0,12
<b>CDS - Carvoaria Deposit</b>	FCS1261 (MG)	14,4	177,7	120	115	38,7	80,8	0,2	0,5	1	3,7	4,4	1	0,1	95,4	0,26
<b>CDS - Carvoaria Deposit</b>	FCS1261 (MG)	12,2	205,1	123	80	36,4	61,1	0,2	0,2	2	3,4	3,7	1	0,1	11,1	0,18
<b>CDS - Laranjeiras Deposit</b>	FCS0831 (MG + PL)	6,7	193,8	127	98	37,3	52,1	0,1	0,3	2	3,3	2,3	2	0,1	7,7	0,15
<b>CDS - Laranjeiras Deposit</b>	FCS0886 ( PL)	19,4	194,6	74	293	29,7	56,5	0,2	0,9	3	4,1	3,5	1	0,2	2,1	0,87
<b>CDS - Laranjeiras Deposit</b>	FCS0929 (MG + PL)	8,0	221,9	125	69	41,0	57,5	0,2	0,2	2	3,1	2,4	2	0,1	11,0	0,12
<b>CDS - Laranjeiras Deposit</b>	FCS0932 (MG)	36,5	225,9	117	94	43,1	73,3	0,2	0,2	2	3,9	4,3	1	0,1	43,7	0,14
<b>Cuiabá Mine</b>	CBABSD00004B (MG)	11,6	308,5	130	111	47,5	66,8	0,2	0,2	1	1,9	2,7	3	0,1	17,9	0,01
<b>Cuiabá Mine</b>	CBABSD00004B (PL)	14,3	260,3	99	104	43,9	57,7	0,2	0,2	1	1,1	3,3	1	0,1	8,3	0,01
<b>Cuiabá Mine</b>	CBABSD00005 (MG)	31,2	301,8	108	136	42,6	64,3	0,3	0,5	1	0,8	1,7	1	0,1	0,5	0,01
<b>Cuiabá Mine</b>	CBABSD00005 ( Black PL)	12,3	208,5	118	85	37,2	77,4	0,2	0,1	2	2,8	4,1	1	0,1	15,0	0,16
<b>Cuiabá Mine</b>	CBABSD00005 (MG)	13,6	318,0	125	121	42,6	60,4	0,2	0,5	2	1,1	1,5	2	0,1	1,8	0,01
<b>Lamego Mine</b>	CARBSD12A (PL)	13,3	411,6	152	111	59,8	65,6	0,2	0,2	2	1,2	1,3	1	0,1	0,9	0,01
<b>Lamego Mine</b>	CARBSD15 (PL)	16,6	377,3	165	127	52,1	67,5	0,1	0,2	2	1,6	1,6	1	0,1	0,5	0,01
<b>Lamego Mine</b>	CARBSD17 (MG+PL)	9,1	413,0	168	118	55,4	75,3	0,2	0,2	1	1,6	1,4	2	0,1	0,7	0,01
<b>Lamego Mine</b>	CARBSD17 (PL)	16,6	491,5	165	121	62,5	76,7	0,2	0,3	1	1,4	1,4	2	0,1	2,6	0,01

\* Córrego do Sítio auriferous lineament (Roncato et al., 2015)

\*\* MG - Greywackes intercalations

\*\*\* PL - Pelites intercalations

**Table 1 - Major, trace and REE values of the selected grey**

Origin	Borehole	Trace Elements				Th/Sc	La/Sc	K2O/Na2O
		As	Se	Sb	La			
		PPM	PPM	PPM	PPM			
<b>CDS* - Cachorro Bravo Deposit</b>	FCS0756 (MG**+PL***)	121,5	0,5	24,9	26,4	0,45	1,26	1,48
<b>CDS - Cachorro Bravo Deposit</b>	FCS1053 (MG)	64,3	0,5	2,4	25,5	0,55	1,70	3,70
<b>CDS - Cachorro Bravo Deposit</b>	FCS1273 (MG)	148,4	0,5	12,5	24,7	0,48	1,45	2,20
<b>CDS - Cachorro Bravo Deposit</b>	FCS1273 (MG)	132,0	0,5	4,2	30,3	0,40	1,52	2,99
<b>CDS - Carvoaria Deposit</b>	FCS1196 (MG)	12,0	0,5	3,0	24,9	0,48	1,78	0,94
<b>CDS - Carvoaria Deposit</b>	FCS1261 (MG)	141,7	0,8	26,7	25,2	0,53	1,68	0,58
<b>CDS - Carvoaria Deposit</b>	FCS1261 (MG)	83,9	0,5	38,3	25,2	0,44	1,48	1,18
<b>CDS - Laranjeiras Deposit</b>	FCS0831 (MG + PL)	88,2	0,5	16,3	20,1	0,75	1,26	1,41
<b>CDS - Laranjeiras Deposit</b>	FCS0886 ( PL)	86,3	0,5	25,7	28,8	0,79	2,62	2,06
<b>CDS - Laranjeiras Deposit</b>	FCS0929 (MG + PL)	95,7	0,5	79,9	24,5	0,54	1,44	1,74
<b>CDS - Laranjeiras Deposit</b>	FCS0932 (MG)	99,9	0,5	29,1	24,8	0,44	1,55	3,30
<b>Cuiabá Mine</b>	CBABSD00004B (MG)	51,7	0,5	1,3	18,1	0,32	1,01	1,05
<b>Cuiabá Mine</b>	CBABSD00004B (PL)	41,6	0,5	0,9	17,9	0,61	1,38	0,76
<b>Cuiabá Mine</b>	CBABSD00005 (MG)	23,4	0,5	0,5	20,3	0,33	1,35	0,40
<b>Cuiabá Mine</b>	CBABSD00005 ( Black PL)	44,7	0,5	8,2	22,3	0,58	1,39	1,36
<b>Cuiabá Mine</b>	CBABSD00005 (MG)	34,9	0,5	0,9	21,3	0,26	1,25	0,69
<b>Lamego Mine</b>	CARBSD12A (PL)	38,0	0,5	1,7	18,8	0,18	0,82	0,76
<b>Lamego Mine</b>	CARBSD15 (PL)	27,4	0,5	0,4	20,6	0,20	0,90	0,74
<b>Lamego Mine</b>	CARBSD17 (MG+PL)	30,2	0,5	0,8	19,2	0,19	0,80	0,97
<b>Lamego Mine</b>	CARBSD17 (PL)	15,6	0,5	2,0	17,4	0,20	0,70	0,70

\* Córrego do Sítio auriferous lineament (Roncato et al., 2015)

\*\* MG - Greywackes intercalations

\*\*\* PL - Pelites intercalations

Table 2 - REE values of the selected greywackes samples of eastern and northern sectors of Quadrilátero Ferrífero with their normalized data.

SAMPLES	La	Ce	Nd	Sm	Eu	Gd	Dy	Er	Yb	Lu	La/YbN
	PPM	PPM	PPM	PPM	PPM	PPM	PPM	PPM	PPM	PPM	
Cuiabá depósit	18,10	32,70	16,40	3,46	0,90	3,21	3,33	2,02	1,74	0,31	2,29
Cuiabá depósit	17,90	33,80	15,80	3,30	0,90	3,05	3,22	1,94	1,79	0,28	2,20
Cuiabá depósit	20,30	37,10	16,40	3,23	0,88	3,50	3,46	1,76	2,03	0,29	2,20
Lamego deposit	18,80	37,10	15,80	3,36	0,98	3,63	3,64	1,85	2,23	0,29	1,85
CDS* lower Laranjeiras	20,10	38,10	18,10	3,73	0,86	3,73	3,97	2,26	2,27	0,38	1,95
CDS Intermediate Laranjeiras	28,80	54,60	28,60	5,24	1,33	4,86	4,03	2,27	2,17	0,36	2,92
CDS Intermediate Laranjeiras	24,50	43,30	20,10	3,89	0,93	3,92	3,85	2,16	2,05	0,36	2,63
CDS Intermediate Carvoaria	24,90	45,30	23,30	4,32	1,11	3,89	3,48	2,14	2,10	0,36	2,61
CDS Intermediate Carvoaria	25,20	47,20	21,70	3,89	1,02	4,04	3,72	2,08	2,14	0,32	2,59
CDS Intermediate Carvoaria	25,20	44,00	19,80	4,04	1,12	3,90	3,42	1,95	1,89	0,31	2,93
CDS Intermediate Cachorro Bravo	26,40	48,60	23,50	4,69	1,10	4,61	4,20	2,45	2,30	0,37	2,53
CDS Intermediate Cachorro Bravo	25,50	45,40	17,50	3,49	1,00	3,49	3,28	1,84	1,96	0,27	2,86
CDS Intermediate Cachorro Bravo	24,70	45,80	18,30	3,65	1,02	3,74	3,53	2,32	2,11	0,34	2,58
CDS Upper Cachoro Bravo	30,30	54,20	19,90	3,75	0,96	3,36	2,99	1,57	1,63	0,25	4,09
Média de Valores	23,62	43,37	19,66	3,86	1,01	3,78	3,58	2,04	2,03	0,32	2,59
Max	30,30	54,60	28,60	5,24	1,33	4,86	4,20	2,45	2,30	0,38	4,09
Min	17,90	32,70	15,80	3,23	0,86	3,05	2,99	1,57	1,63	0,25	1,85
<b>Nakamura (1974)</b>	<b>0,33</b>	<b>0,87</b>	<b>0,63</b>	<b>0,20</b>	<b>0,08</b>	<b>0,28</b>	<b>0,34</b>	<b>0,23</b>	<b>0,22</b>	<b>0,03</b>	

\* Córrego do Sítio lineament deposits

AMOSTRAS / Chondrite	La	Ce	Nd	Sm	Eu	Gd	Dy	Er	Yb	Lu	(Ce/Yb) <sub>N</sub>	(Gd/Yb) <sub>n</sub>	(La/Sm) <sub>n</sub>	Eu/Eu*
Cuiabá depósit	55,02	37,80	26,03	17,04	11,69	11,63	9,71	8,98	7,91	9,14	26,83	8,56	12,41	0,96
Cuiabá depósit	54,41	39,08	25,08	16,26	11,69	11,05	9,39	8,62	8,14	8,26	30,70	9,17	12,27	0,95
Cuiabá depósit	61,70	42,89	26,03	15,91	11,43	12,68	10,09	7,82	9,23	8,55	32,54	9,51	14,23	0,91
Lamego deposit	57,14	42,89	25,08	16,55	12,73	13,15	10,61	8,22	10,14	8,55	32,54	10,00	11,84	0,91
CDS lower Laranjeiras	61,09	44,05	28,73	18,37	11,17	13,51	11,57	10,04	10,32	11,21	25,50	8,33	14,42	1,10
CDS Intermediate Laranjeiras	87,54	63,12	45,40	25,81	17,27	17,61	11,75	10,09	9,86	10,62	38,57	8,92	13,36	0,89
CDS Intermediate Laranjeiras	74,47	50,06	31,90	19,16	12,08	14,20	11,22	9,60	9,32	10,62	30,59	8,52	16,25	0,98
CDS Intermediate Carvoaria	75,68	52,37	36,98	21,28	14,42	14,09	10,15	9,51	9,55	10,62	32,00	7,71	13,84	1,01
CDS Intermediate Carvoaria	76,60	54,57	34,44	19,16	13,25	14,64	10,85	9,24	9,73	9,44	37,51	9,27	15,24	1,03
CDS Intermediate Carvoaria	76,60	50,87	31,43	19,90	14,55	14,13	9,97	8,67	8,59	9,14	36,10	8,79	13,88	1,00
CDS Intermediate Cachorro Bravo	80,24	56,18	37,30	23,10	14,29	16,70	12,24	10,89	10,45	10,91	33,41	9,05	14,81	0,99
CDS Intermediate Cachorro Bravo	77,51	52,49	27,78	17,19	12,99	12,64	9,56	8,18	8,91	7,96	42,77	9,68	15,73	0,96
CDS Intermediate Cachorro Bravo	75,08	52,95	29,05	17,98	13,25	13,55	10,29	10,31	9,59	10,03	34,26	8,28	14,94	0,96
CDS Upper Cachoro Bravo	92,10	62,66	31,59	18,47	12,47	12,17	8,72	6,98	7,41	7,37	55,14	9,53	19,47	0,95

Table 2 - REE values of the selected pelites samples of eastern and northern sectors of Quadrilátero Ferrífero with their normalized data.

AMOSTRAS	La	Ce	Nd	Sm	Eu	Gd	Dy	Er	Yb	Lu	La/Yb			
	PPM	PPM	PPM	PPM	PPM	PPM	PPM	PPM	PPM	PPM				
Cuiabá	22,30	39,40	19,20	3,46	0,88	3,61	3,41	1,94	1,90	0,31	2,58			
Lamego Carruagem	20,60	40,50	16,00	3,49	1,01	3,65	3,46	1,94	2,27	0,28	2,00			
Lamego Carruagem	19,20	37,50	16,90	3,41	0,99	3,93	3,79	1,96	2,40	0,29	1,76			
Lamego Carruagem / MAN	17,40	32,60	13,80	3,17	0,90	3,17	3,21	1,95	1,82	0,29	2,10			
CDS Inter Laranjeiras	24,80	43,50	19,90	3,54	0,92	3,28	2,87	1,74	1,59	0,27	3,43			
CDS Sup Cachoro Bravo	25,50	45,80	18,20	3,51	0,96	3,57	3,30	1,76	2,16	0,27	2,60			
Média de Valores	21,63	39,88	17,33	3,43	0,94	3,54	3,34	1,88	2,02	0,29	2,41			
Max	25,50	45,80	19,90	3,54	1,01	3,93	3,79	1,96	2,40	0,31	3,43			
Min	17,40	32,60	13,80	3,17	0,88	3,17	2,87	1,74	1,59	0,27	1,76			
<b>Nakamura (1974)</b>	<b>0,33</b>	<b>0,87</b>	<b>0,63</b>	<b>0,20</b>	<b>0,08</b>	<b>0,28</b>	<b>0,34</b>	<b>0,23</b>	<b>0,22</b>	<b>0,03</b>				
AMOSTRAS/Nasc	La	Ce	Nd	Sm	Eu	Gd	Dy	Er	Yb	Lu	(Ce/Yb) <sub>N</sub>	(Gd/Yb) <sub>n</sub>	(La/Sm) <sub>n</sub>	Eu/Eu*
Cuiabá	67,78	45,55	30,48	17,04	11,43	13,08	9,94	8,62	8,64	9,14	32,33	8,77	15,64	0.94
Lamego Carruagem	62,61	46,82	25,40	17,19	13,12	13,22	10,09	8,62	10,32	8,26	36,79	9,85	12,58	0.96
Lamego Carruagem	58,36	43,35	26,83	16,80	12,86	14,24	11,05	8,71	10,91	8,55	32,89	10,42	11,97	0.96
Lamego Carruagem / MAN	52,89	37,69	21,90	15,62	11,69	11,49	9,36	8,67	8,27	8,55	28,59	8,82	11,93	1.12
CDS Inter Laranjeiras	75,38	50,29	31,59	17,44	11,95	11,88	8,37	7,73	7,23	7,96	40,98	8,47	16,63	1.02
CDS Sup Cachoro Bravo	77,51	52,95	28,89	17,29	12,47	12,93	9,62	7,82	9,82	7,96	43,14	9,74	16,39	0.98

**Table 3: Trace Element Contents (ppm) of sulfide minerals.**

SampleName	Borehole	Cr53	Co59	Ni60	Cu65	Zn66	Se77	Mo95
<b>Arsenopyrite (P-Apy) - Lj</b>	F871-306,70 m	0,23128	54,55754	54,83191	2,00320	1,69305	6,40120	0,05162
<b>Arsenopyrite (S-Apy) - Lj</b>	F871-306,70 m	0,09870	392,19244	166,76888	1,02670	0,28141	5,40229	0,11517
<b>Arsenopyrite (S-Apy) - Lj</b>	FCS910-319,15 m	0,57488	1725,89827	390,37383	2,11481	0,20118		0,85720
<b>Arsenopyrite (P-Apy) - Lj</b>	FCS910-319,15 m		618,18977	435,30031	10,94470	1,18361		
<b>Pyrrhotite (S-Po) - Lj</b>	F871-306,70 m		55,27824	543,73319	123,22245	0,43154	6,38392	0,00000
<b>Pyrrhotite (S-Po) - Lj</b>	F865-287,30 m	13,75892	67,14215	421,81924	364,48359	1,61479	7,72867	0,00000
<b>Pyrrhotite (S-Po) - Lj</b>	FCS910-319,15 m	458,06000	38,41472	236,83731	747,10640	34,29838	6,35772	0,03877
<b>Pyrite (S-Py) - CB</b>	FCS718 - 201,50 m	0,25346	1,49099	101,24349	0,06646	0,29163	63,52575	0,00667
<b>Pyrite (S-Py) - CB</b>	FCS718 - 201,50 m	2,05761	0,12657	29,00994	0,71868	0,58799	43,10545	
<b>Pyrite (S-Py) - Lj</b>	F871-306,70 m	3,12682	52,45165	32,81163	0,40962	0,63944	4,50713	
<b>Pyrite (S-Py) - Lj</b>	FCS910-319,15 m	21,04244	18,38449	2,97705	0,61323	13,44873	4,87110	0,00232
<b>Pyrite (S-Py) - Lj</b>	F871-306,69 m	0,01285	0,27532	27,17935	0,17301	0,48220	4,33160	0,00449
<b>Pyrite (P-Py) - Lj</b>	F871-306,70 m	0,10383	30,42898	227,84496	0,23069	0,22798	33,73303	0,00000
<b>Pyrite (P-Py) - Lj</b>	FCS910-319,15 m	34,64129	11,71321	46,18610	7,17779	7,30885	41,00810	0,03187
<b>Pyrite (P-Py) - Lj</b>	FCS910-319,16 m	3,42648	228,85069	1332,82336	0,90203	5,98445	31,30654	0,00709
<b>Pyrite (P-Py) - Lj</b>	F865-287,30 m	1,48708	187,29538	1278,84156	0,11762	6,47281	34,03794	0,00000
<b>Pyrite (P-Py) - Lj</b>	F865-287,31 m	0,70189	193,86282	1261,40693	41,40828	1,29196	31,83072	0,03033

CB - Cachorro Bravo Deposit

Lj - Laranjeiras Deposit

\*(As) data are from micropobe (EPMA)

**Table 3: Trace Element Contents (ppm)**

SampleName	Borehole	Ag107	Cd111	Sn118	Sb121	Te125	Gd157	W182
<b>Arsenopyrite (P-Apy) - Lj</b>	F871-306,70 m	0,42764	0,03558	0,23223	263,86294	1,38431		2,27392
<b>Arsenopyrite (S-Apy) - Lj</b>	F871-306,70 m	0,44772	0,01989	0,24197	646,28538	6,38785	0,00000	0,32852
<b>Arsenopyrite (S-Apy) - Lj</b>	FCS910-319,15 m	1,31249	3,76185	0,07245	0,03485	746,38932	31,49381	0,00536
<b>Arsenopyrite (P-Apy) - Lj</b>	FCS910-319,15 m	7,61095	5,63439	0,01379	0,05976	2305,28471	102,85847	
<b>Pyrrhotite (S-Po) - Lj</b>	F871-306,70 m	0,19274	0,00000	0,43845	1,43147	0,16261	0,00000	0,00651
<b>Pyrrhotite (S-Po) - Lj</b>	F865-287,30 m	3,57529	0,00000	0,42294	2,24380	0,25964	0,04690	0,10638
<b>Pyrrhotite (S-Po) - Lj</b>	FCS910-319,15 m	0,56670	0,00963	4,42691	17,24268	0,52134	0,00000	0,92353
<b>Pyrite (S-Py) - CB</b>	FCS718 - 201,50 m	0,02492		0,09219	0,20219	0,16005	0,00000	0,00000
<b>Pyrite (S-Py) - CB</b>	FCS718 - 201,50 m	0,02650	0,00000	0,15481	1,84797	0,10900	0,00605	0,00953
<b>Pyrite (S-Py) - Lj</b>	F871-306,70 m	0,33024	0,01128	0,15533	2,92633		1,55425	1,24788
<b>Pyrite (S-Py) - Lj</b>	FCS910-319,15 m	0,67070	0,01380	0,18203	3,52615		1,17178	0,07350
<b>Pyrite (S-Py) - Lj</b>	F871-306,69 m	1,70230		0,13959			0,00000	0,00253
<b>Pyrite (P-Py) - Lj</b>	F871-306,70 m	0,01455		0,13523	0,54724	0,27064	0,00000	
<b>Pyrite (P-Py) - Lj</b>	FCS910-319,15 m	0,46552		1,01474	55,54733	25,11136	0,05665	0,18030
<b>Pyrite (P-Py) - Lj</b>	FCS910-319,16 m	0,84953	0,01407	0,39355	3,70912	0,66863	0,00000	0,02377
<b>Pyrite (P-Py) - Lj</b>	F865-287,30 m	0,79038		0,37638	2,40866	0,53962		0,01428
<b>Pyrite (P-Py) - Lj</b>	F865-287,31 m	0,44987		0,29884	1,14122	0,34025	0,05372	0,04148

CB - Cachorro Bravo Deposit

Lj - Laranjeiras Deposit

\*(As) data are from micropobe (EPMA)

**Table 3: Trace Element Contents (ppm)**

<b>SampleName</b>	<b>Borehole</b>	<b>Pt195</b>	<b>Au197</b>	<b>Pb207</b>	<b>*As74</b>
<b>Arsenopyrite (P-Apy) - Lj</b>	F871-306,70 m	0,01444	135,37091	11,67265	445007,00
<b>Arsenopyrite (S-Apy) - Lj</b>	F871-306,70 m		1,17394	74,51976	438266,00
<b>Arsenopyrite (S-Apy) - Lj</b>	FCS910-319,15 m	0,03278	0,00746	0,00868	442244,00
<b>Arsenopyrite (P-Apy) - Lj</b>	FCS910-319,15 m	0,02376	0,01471		
<b>Pyrrhotite (S-Po) - Lj</b>	F871-306,70 m	0,03886	0,00431	0,28953	358,24
<b>Pyrrhotite (S-Po) - Lj</b>	F865-287,30 m		0,05283	6,36755	
<b>Pyrrhotite (S-Po) - Lj</b>	FCS910-319,15 m		0,01061	11,45622	
<b>Pyrite (S-Py) - CB</b>	FCS718 - 201,50 m		0,10814	0,30366	1595,58
<b>Pyrite (S-Py) - CB</b>	FCS718 - 201,50 m		0,03216	3,05585	924,33
<b>Pyrite (S-Py) - Lj</b>	F871-306,70 m	0,00863	0,00241	2,27123	462,43
<b>Pyrite (S-Py) - Lj</b>	FCS910-319,15 m		0,02301	3,84221	777,22
<b>Pyrite (S-Py) - Lj</b>	F871-306,69 m	0,00939	0,00047	0,00186	436,51
<b>Pyrite (P-Py) - Lj</b>	F871-306,70 m	0,00827	0,01807	0,37118	516,72
<b>Pyrite (P-Py) - Lj</b>	FCS910-319,15 m	0,03055	0,73553	45,65042	738,82
<b>Pyrite (P-Py) - Lj</b>	FCS910-319,16 m		0,01219	19,13189	2998,29
<b>Pyrite (P-Py) - Lj</b>	F865-287,30 m	0,00148	0,00032	11,61138	334,11
<b>Pyrite (P-Py) - Lj</b>	F865-287,31 m			5,88459	248,84

CB - Cachorro Bravo Deposit

Lj - Laranjeiras Deposit

\*(As) data are from micropobe (EPMA)

# **ANEXO 3**

**DADOS ANÁLISES GEOCRONOLÓGICAS**















FILE NAME	CORRECTED 0																			RHO	Disc.			
	Pb206*	Pb207*	Th/U	207/206	1s	206/238	1s	207/235	1s	206/207	206/238	207/235	208/232	Conc	207/235	206/238								
4.sSMPABC029	186032,8581	27077,94	0,315772	0,14726	0,00156	0,13212	0,00099	2,68145	0,0214	2314,35	18,1	799,9	5,64	1323,4	5,9	702,5	10,61	34,55432	2,68145	0,0214	0,13212	0,00099	0,938907	-39,5572
4.sSMPABC166	158255	30727	1,849568	0,19241	0,00288	0,18167	0,00157	4,81517	0,06178	2762,87	24,39	1076,1	8,59	1787,6	10,79	255,8	15,74	33,88161	4,81517	0,06178	0,18167	0,00157	0,673566	-39,802
4.sSMPABC105	383678,1716	54569,97	0,390826	0,1428	0,00207	0,12312	0,00102	2,42113	0,02937	2261,44	24,82	748,5	5,83	1248,9	8,72	539,7	32,26	33,14629	2,42113	0,02937	0,12312	0,00102	0,682945	-40,0673
4.sSMPABC144	101116	15788	3,101118	0,15565	0,00214	0,13782	0,00115	2,95543	0,03357	2408,94	23,21	832,3	6,51	1396,2	8,62	125,2	6,05	32,24799	2,95543	0,03357	0,13782	0,00115	0,734607	-40,3882
4.sSMPABC049	123887	23812	0,360715	0,19405	0,00233	0,17346	0,00144	4,6382	0,0445	2776,79	19,59	1031,1	7,92	1755,2	8,01	1072,8	28,74	29,67704	4,6382	0,0445	0,17346	0,00144	0,865272	-41,288
4.sSMPABC152	188224,9948	30181,68	1,012239	0,16339	0,00179	0,14044	0,00113	3,16236	0,02817	2491,05	18,37	847,1	6,4	1448	6,87	381,6	9,54	29,06386	3,16236	0,02817	0,14044	0,00113	0,903259	-41,4986
4.sSMPABC142	210592,4381	38374,58	2,659405	0,18368	0,00198	0,15596	0,00123	3,94785	0,03378	2686,38	17,69	934,3	6,86	1623,5	6,93	157,4	3,65	26,23354	3,94785	0,03378	0,15596	0,00123	0,921707	-42,4515
4.sSMPABC095	151679	29169	2,450296	0,19292	0,00205	0,15651	0,00121	4,16159	0,03426	2767,22	17,35	937,4	6,75	1666,5	6,74	115,2	2,14	22,22104	4,16159	0,03426	0,15651	0,00121	0,939107	-43,7504
4.sSMPABC157	184849,9184	27727,98	0,791526	0,15433	0,00171	0,10756	0,00085	2,28762	0,0203	2394,47	18,72	658,6	4,96	1208,5	6,27	378	10,17	16,50471	2,28762	0,0203	0,10756	0,00085	0,890545	-45,5027
4.sSMPABC096	86431	16105	2,066427	0,18677	0,00278	0,13375	0,00117	3,44125	0,042	2713,93	24,38	809,2	6,67	1513,9	9,6	127,1	6,45	12,91399	3,44125	0,042	0,13375	0,00117	0,716736	-46,5486
4.sSMPABC149	108240,5745	19677,02	2,481072	0,1835	0,00202	0,12991	0,00104	3,28514	0,02894	2684,76	18,04	787,3	5,94	1477,5	6,86	167,7	4,08	12,33329	3,28514	0,02894	0,12991	0,00104	0,908754	-46,714
4.sSMPABC159	229500,3032	36745,62	0,731927	0,16504	0,00187	0,10279	0,00083	2,33793	0,02164	2507,96	18,98	630,7	4,84	1223,9	6,58	497	14,98	5,945775	2,33793	0,02164	0,10279	0,00083	0,872372	-48,468
4.sSMPABC160	218320,5178	38720,32	1,212967	0,18036	0,00205	0,11001	0,0009	2,73456	0,02556	2656,18	18,69	672,8	5,23	1337,9	6,95	311,8	9,18	1,144471	2,73456	0,02556	0,11001	0,0009	0,87526	-49,7122
4.sSMPABC158	204386,0705	40516,02	0,640491	0,20134	0,00248	0,12426	0,00102	3,44762	0,03509	2837,09	19,95	755,1	5,86	1515,3	8,01	862,5	33,87	-0,67541	3,44762	0,03509	0,12426	0,00102	0,806501	-50,1683
4.sSMPABC147	71822,19616	12473,26	1,852005	0,17624	0,00243	0,0669	0,00056	1,62431	0,01835	2617,8	22,74	417,5	3,4	979,7	7,1	145,8	6,98	-34,6587	1,62431	0,01835	0,0669	0,00056	0,74096	-57,3849







FILE NAME	CORRECT			0																				
	Pb206*	Pb207*	Th/U	207/206	1s	206/238	1s	207/235	1s	206/207	206/238	207/235	208/232	Conc	207/235	206/238	RHO	Disc.						
4.sSMPABC093	306927,3	92284,11	0,526492	0,29223	0,00478	0,14125	0,00131	5,68786	0,08138	3429,515	25,21	851,7	7,41	1929,5	12,36	1108,7	80,06	-26,5469	5,68786	0,08138	0,14125	0,00131	0,648208	-55,859
4.sSMPABC104	144200,3	28236,02	0,369657	0,19408	0,00259	0,08108	0,00073	2,16803	0,02477	2777,048	21,68	502,6	4,37	1170,8	7,94	434,1	21,84	-32,9487	2,16803	0,02477	0,08108	0,00073	0,78804	-57,0721
4.sSMPABC114	132394,5	28813	0,178657	0,21298	0,0029	0,09217	0,00083	2,70352	0,03144	2928,358	21,82	568,4	4,93	1329,4	8,62	1487,6	80,37	-33,8846	2,70352	0,03144	0,09217	0,00083	0,774347	-57,2439
4.sSMPABC052	129496	25547	0,265455	0,19827	0,0029	0,07397	0,00066	2,0195	0,02432	2812,008	23,67	460	3,99	1122,1	8,18	615,1	32,72	-43,9348	2,0195	0,02432	0,07397	0,00066	0,740915	-59,0054
4.sSMPABC042	135508,9	35224,09	0,234373	0,25351	0,00267	0,09157	0,00071	3,19918	0,02589	3206,82	16,53	564,8	4,19	1457	6,26	1870,2	38,65	-57,9674	3,19918	0,02589	0,09157	0,00071	0,958102	-61,2354
4.sSMPABC089	171186,5	35846,34	0,138991	0,20752	0,00263	0,06202	0,00053	1,77337	0,01866	2886,276	20,43	387,9	3,19	1035,8	6,83	1479,4	67,29	-67,0276	1,77337	0,01866	0,06202	0,00053	0,812142	-62,5507
4.sSMPABC092	117009	25049	0,21233	0,21458	0,00323	0,05932	0,00054	1,75203	0,02228	2940,457	24,15	371,5	3,29	1027,9	8,22	1188,6	66,45	-76,6891	1,75203	0,02228	0,05932	0,00054	0,715845	-63,8584
4.sSMPABC091	121187,8	28931,1	0,210522	0,23595	0,00325	0,06648	0,00058	2,16063	0,02481	3092,854	21,81	414,9	3,49	1168,5	7,97	1442,6	72	-81,6341	2,16063	0,02481	0,06648	0,00058	0,759785	-64,4929
4.sSMPABC054	166459,6	46850,62	0,166756	0,27171	0,00366	0,07219	0,00066	2,70058	0,03061	3315,921	20,96	449,3	3,97	1328,6	8,4	2156,4	101	-95,7044	2,70058	0,03061	0,07219	0,00066	0,806604	-66,1824
4.sSMPABC036	6772,146	2674,771	0,332056	0,30802	0,00827	0,06476	0,0012	2,74751	0,05856	3511,029	40,86	404,5	7,24	1341,4	15,87	1139,9	61,78	-131,619	2,74751	0,05856	0,06476	0,0012	0,869386	-69,8449







FILE NAME	CORRECT			0																				
	Pb206*	Pb207*	Th/U	207/206	1s	206/238	1s	207/235	1s	206/207	206/238	207/235	208/232	Conc	207/235	206/238	RHO	Disc.						
4.sSMPABC079	121810	25076	0,376838	0,20644	0,00263	0,54643	0,00451	15,53867	0,16192	2877,802	20,52	2810,3	18,78	2848,9	9,94	1903,8	109,81	98,62648	15,53867	0,16192	0,54643	0,00451	0,792055	-1,35491
4.sSMPABC034	147497	39487	0,320715	0,26717	0,00342	0,64656	0,0058	23,77074	0,25649	3289,491	19,97	3214,7	22,71	3259	10,51	3015,8	265,83	98,62196	23,77074	0,25649	0,64656	0,0058	0,831364	-1,35931
4.sSMPABC092	91257	17870	0,58023	0,20009	0,00298	0,5336	0,0047	14,68571	0,18522	2826,931	24,1	2756,6	19,77	2795,1	11,99	3892	649,35	98,60335	14,68571	0,18522	0,5336	0,0047	0,698376	-1,37741
4.sSMPABC058	96956	21927	0,290035	0,23624	0,00432	0,59592	0,00639	19,34031	0,31224	3094,813	28,86	3013,4	25,82	3058,9	15,59	2765,7	447,24	98,49008	19,34031	0,31224	0,59592	0,00639	0,664183	-1,48746
4.sSMPABC061	137008	27011	0,7079	0,19752	0,00223	0,52731	0,0042	14,34796	0,12901	2805,813	18,32	2730,1	17,72	2773	8,54	1522,4	49,22	98,42863	14,34796	0,12901	0,52731	0,0042	0,885829	-1,54706
4.sSMPABC048	113316,8	28933,88	0,383993	0,26781	0,00337	0,64215	0,00524	23,64362	0,23821	3293,247	19,63	3197,5	20,59	3253,8	9,81	2285,4	116,69	98,23925	23,64362	0,23821	0,64215	0,00524	0,809932	-1,73028
4.sSMPABC078	119468	25389	0,324934	0,21026	0,00256	0,54932	0,00448	15,92288	0,15754	2907,55	19,58	2822,4	18,64	2872,2	9,45	1987,6	97,23	98,23554	15,92288	0,15754	0,54932	0,00448	0,824296	-1,73386
4.sSMPABC031	131807	25261,11	0,6674	0,20029	0,00265	0,52709	0,00455	14,49237	0,15825	2828,561	21,45	2729,2	19,19	2782,5	10,37	2600,1	181,12	98,04705	14,49237	0,15825	0,52709	0,00455	0,790537	-1,91554
4.sSMPABC047	218073	46260	0,388799	0,20713	0,00225	0,53818	0,00464	15,36738	0,14152	2883,222	17,5	2775,8	19,43	2838,3	8,78	1247,3	32,49	97,7484	15,36738	0,14152	0,53818	0,00464	0,936208	-2,20202
4.sSMPABC043	270094	52274	0,327628	0,19015	0,00262	0,50518	0,00483	13,22101	0,16057	2743,459	22,49	2636	20,67	2695,6	11,46	1846,7	126,68	97,739	13,22101	0,16057	0,50518	0,00483	0,787229	-2,21101



FILE NAME	CORRECT			0																				
	Pb206*	Pb207*	Th/U	207/206	1s	206/238	1s	207/235	1s	206/207	206/238	207/235	208/232	Conc	207/235	206/238	RHO	Disc.						
4.sSMPABC045	473434,2	85608,68	0,182575	0,18295	0,00195	0,23376	0,00182	5,88858	0,04937	2679,796	17,57	1354,2	9,48	1959,6	7,28	645,2	16,3	55,29464	5,88858	0,04937	0,23376	0,00182	0,928643	-30,8941
4.sSMPABC113	240515,5	46013,43	0,084971	0,19492	0,00284	0,23881	0,00199	6,41452	0,07904	2784,126	23,7	1380,5	10,33	2034,3	10,82	1258	103,19	52,64035	6,41452	0,07904	0,23881	0,00199	0,676266	-32,1388
4.sSMPABC111	179042	33426	0,003707	0,18224	0,00313	0,21641	0,00198	5,43075	0,08162	2673,362	28,12	1262,9	10,49	1889,7	12,89	*****	2916,02	50,3682	5,43075	0,08162	0,21641	0,00198	0,608767	-33,1693
4.sSMPABC069	394820,5	63284,93	0,018222	0,15895	0,00168	0,18449	0,00146	4,04049	0,03425	2444,522	17,82	1091,5	7,95	1642,4	6,9	844,9	22,89	49,52817	4,04049	0,03425	0,18449	0,00146	0,933584	-33,5424
4.sSMPABC086	286097,2	55387,44	0,287105	0,19159	0,00223	0,22304	0,00171	5,8874	0,05428	2755,859	18,98	1297,9	8,99	1959,4	8	1057,5	51,19	49,03305	5,8874	0,05428	0,22304	0,00171	0,831567	-33,7603
4.sSMPABC134	286218	59854	0,400852	0,20334	0,00347	0,22111	0,00198	6,19504	0,09312	2853,195	27,53	1287,8	10,48	2003,7	13,14	2525,8	829,84	44,40907	6,19504	0,09312	0,22111	0,00198	0,595742	-35,7289
4.sSMPABC018	85633	13051	0,28375	0,1622	0,00229	0,16798	0,00139	3,73801	0,04207	2478,724	23,63	1001	7,65	1579,5	9,02	1109,4	102,57	42,20779	3,73801	0,04207	0,16798	0,00139	0,735233	-36,6255



FILE NAME	CORRECT		0															
Pb206*	Pb207*	Th/U	207/206	1s	206/238	1s	207/235	1s	206/207	206/238	207/235	208/232	Conc	207/235	206/238	RHO	Disc.	

- a - Corrigido para o background, dentro do fracionamento analítico do Pb/U (no caso do  $^{206}\text{Pb}/^{238}\text{U}$ ) e correção de Pb comum usando a metodologia de Takenada et al. (2015) e subsequente normalização a GJ-1 (valor ID-TIMS/valor medido);  $^{207}\text{Pb}/^{235}\text{U}$  calculado usando  $^{207}\text{Pb}/^{206}\text{Pb}/(^{238}\text{U}/^{206}\text{Pb} * 1/137,88)$
- b - Conteúdo de U e Pb e razão  $^{232}\text{Th}/^{238}\text{U}$  foram calculadas em relação ao zircão de referência GJ-1
- c - Rho é o coeficiente de correlação do erro da razão  $^{207}\text{Pb}/^{235}\text{U}/^{206}\text{Pb}/^{238}\text{U}$
- d - Grau de discordância:  $100 * ((^{206}\text{Pb}/^{238}\text{U} - ^{207}\text{Pb}/^{235}\text{U}) / ^{207}\text{Pb}/^{235}\text{U})$





FILE NAME	CORRECTED 0																			RHO	Disc.			
	Pb206*	Pb207*	Th/U	207/206	1s	206/238	1s	207/235	1s	206/207	206/238	207/235	208/232	Conc	207/235	206/238								
4.sSMPABC120	122985,8114	19030,08	0,140171	0,15398	0,00179	0,20604	0,00169	4,37364	0,04196	2390,6	19,69	1207,7	9,05	1707,4	7,93	1190,1	54,53	58,62383	4,37364	0,04196	0,20604	0,00169	0,854954	-29,2667
4.sSMPABC143	201303	36982	0,348592	0,18322	0,00262	0,24571	0,0021	6,20626	0,07632	2682,23	23,45	1416,3	10,85	2005,3	10,75	1171,5	81,77	58,41277	6,20626	0,07632	0,24571	0,0021	0,695005	-29,3722
4.sSMPABC149	52086,9874	12368,79	0,428175	0,23612	0,00416	0,29448	0,00303	9,58396	0,15005	3094	27,81	1663,9	15,07	2395,6	14,39	1409,2	132,6	56,025	9,58396	0,15005	0,29448	0,00303	0,657197	-30,5435
4.sSMPABC147	203817,3123	36771,1	0,408978	0,17909	0,00232	0,22819	0,00188	5,63372	0,0616	2644,46	21,37	1325	9,86	1921,3	9,43	967,8	58,73	54,99623	5,63372	0,0616	0,22819	0,00188	0,753487	-31,0363
4.sSMPABC073	498294,4729	99357,7	0,137144	0,19869	0,00273	0,24286	0,00222	6,64461	0,07977	2815,47	22,26	1401,6	11,53	2065,3	10,6	4342,6	313,23	52,64697	6,64461	0,07977	0,24286	0,00222	0,761425	-32,1358
4.sSMPABC020	563421	117133	0,161631	0,20639	0,00214	0,25124	0,002	7,14717	0,05907	2877,41	16,76	1444,9	10,3	2129,9	7,36	3699,1	93,21	52,59187	7,14717	0,05907	0,25124	0,002	0,963182	-32,1611
4.sSMPABC138	347826,239	68996,54	0,285891	0,19896	0,00342	0,23269	0,00214	6,38319	0,09813	2817,68	27,76	1348,6	11,19	2030	13,5	3434,1	496,27	49,47353	6,38319	0,09813	0,23269	0,00214	0,598235	-33,5665
4.sSMPABC048	315997	64809	0,425938	0,20305	0,00215	0,23211	0,00191	6,49593	0,05641	2850,87	17,14	1345,6	10,01	2045,3	7,64	1580,5	45,08	48,00089	6,49593	0,05641	0,23211	0,00191	0,947599	-34,2101
4.sSMPABC113	417228,5255	77370,18	0,022115	0,18375	0,00236	0,20913	0,0019	5,29297	0,05973	2687,01	21,04	1224,2	10,13	1867,7	9,64	3262,3	193,05	47,43506	5,29297	0,05973	0,20913	0,0019	0,80509	-34,4541
4.sSMPABC074	342798,463	56189,87	0,143252	0,16339	0,0018	0,15692	0,00128	3,53397	0,03173	2491,05	18,42	939,7	7,11	1534,9	7,11	1280,7	51,19	36,66064	3,53397	0,03173	0,15692	0,00128	0,908499	-38,7778
4.sSMPABC134	272997	47981	0,155846	0,17404	0,00207	0,15492	0,00134	3,7152	0,03794	2596,88	19,73	928,5	7,47	1574,6	8,17	1059,2	57,76	30,41465	3,7152	0,03794	0,15492	0,00134	0,846998	-41,0326
4.sSMPABC133	213345,193	43110,11	0,203845	0,20009	0,00236	0,17559	0,00143	4,84356	0,04724	2826,93	19,16	1042,9	7,85	1792,5	8,21	1396,2	67,65	28,1235	4,84356	0,04724	0,17559	0,00143	0,835009	-41,8187
4.sSMPABC119	83820,79044	15529,36	0,074982	0,18408	0,00219	0,1259	0,00102	3,19494	0,0308	2689,98	19,49	764,5	5,85	1455,9	7,45	2676,2	125,07	9,561805	3,19494	0,0308	0,1259	0,00102	0,840401	-47,4895
4.sSMPABC083	103740,7865	25272,64	0,259698	0,23891	0,00255	0,07254	0,00058	2,38897	0,02037	3112,72	16,9	451,4	3,5	1239,3	6,1	1182,3	37,58	-74,5459	2,38897	0,02037	0,07254	0,00058	0,937713	-63,5762
4.sSMPABC082	133002	32763	0,150028	0,2437	0,00565	0,06749	0,00084	2,26718	0,04668	3144,29	36,37	421	5,09	1202,1	14,51	3190,3	532,42	-85,5344	2,26718	0,04668	0,06749	0,00084	0,604498	-64,978





FILE NAME	CORRECTED			0																				
	Pb206*	Pb207*	Th/U	207/206	1s	206/238	1s	207/235	1s	206/207	206/238	207/235	208/232	Conc	207/235	206/238	RHO	Disc.						
4.sMPABC093	212988,628	35956,38	1,368256	0,16949	0,00181	0,12972	0,00105	3,0302	0,02609	2552,613	17,8	786,3	5,97	1415,3	6,57	220,7	5,5	20,00509	3,0302	0,02609	0,12972	0,00105	0,940112	-44,4429
4.sMPABC146	183568,1806	27883,77	1,465748	0,15244	0,00176	0,09931	0,00083	2,08642	0,02001	2373,478	19,51	610,4	4,87	1144,3	6,58	223,3	7,89	12,53277	2,08642	0,02001	0,09931	0,00083	0,871445	-46,6573
4.sMPABC106	118815	19772	2,057582	0,16265	0,00198	0,1009	0,0008	2,26183	0,02186	2483,396	20,36	619,7	4,7	1200,5	6,8	198,2	7,88	6,277231	2,26183	0,02186	0,1009	0,0008	0,820368	-48,3798
4.sMPABC107	223941,0026	43118,31	1,323254	0,19168	0,00203	0,10857	0,00085	2,86799	0,02376	2756,63	17,28	664,4	4,92	1373,5	6,24	172,9	4,34	-6,72787	2,86799	0,02376	0,10857	0,00085	0,945018	-51,6272
4.sMPABC042	112411,594	19874,72	2,283096	0,17971	0,00194	0,09521	0,00073	2,35803	0,01924	2650,196	17,76	586,3	4,27	1230	5,82	179,4	3,78	-9,79021	2,35803	0,01924	0,09521	0,00073	0,93969	-52,3333
4.sMPABC128	111508	23113	3,09972	0,20183	0,00285	0,1089	0,00093	3,02645	0,03524	2841,052	22,8	666,3	5,39	1414,3	8,89	126,2	7,4	-12,2617	3,02645	0,03524	0,1089	0,00093	0,73342	-52,8884
4.sMPABC043	116511	21011	2,251576	0,17978	0,00218	0,08821	0,00071	2,18499	0,02066	2650,842	19,99	544,9	4,19	1176,3	6,59	188,8	6,27	-15,8745	2,18499	0,02066	0,08821	0,00071	0,851255	-53,6768
4.sMPABC047	124888	23407	2,738137	0,186	0,00216	0,08727	0,00069	2,23676	0,02008	2707,111	19,01	539,4	4,08	1192,6	6,3	131,7	4,01	-21,0975	2,23676	0,02008	0,08727	0,00069	0,880724	-54,7711
4.sMPABC060	808276	172804	0,13261	0,2102	0,00279	0,10049	0,00092	2,90787	0,03359	2907,088	21,35	617,3	5,37	1384	8,73	561,3	31,3	-24,2022	2,90787	0,03359	0,10049	0,00092	0,792556	-55,3974
4.sMPABC133	90235,52684	18502,97	3,714579	0,20096	0,0023	0,06154	0,00048	1,70435	0,01525	2834,009	18,58	385	2,89	1010,2	5,73	79	2,96	-62,3896	1,70435	0,01525	0,06154	0,00048	0,871711	-61,8887
4.sMPABC131	62556,06654	11710,34	1,542466	0,18714	0,00284	0,0417	0,00037	1,07511	0,0136	2717,189	24,84	263,4	2,29	741,2	6,66	98,6	5,6	-81,3971	1,07511	0,0136	0,0417	0,00037	0,701422	-64,463
4.sMPABC096	75110,653	13989,98	0,274482	0,18482	0,00209	0,03711	0,00029	0,94515	0,00836	2696,605	18,52	234,9	1,83	675,6	4,36	518,2	14,78	-87,6117	0,94515	0,00836	0,03711	0,00029	0,88349	-65,2309
4.sMPABC095	94359,53889	20649,2	0,268097	0,21583	0,00269	0,04835	0,00039	1,43819	0,01428	2949,838	20,02	304,4	2,42	905	5,95	890,2	35,72	-97,3062	1,43819	0,01428	0,04835	0,00039	0,812374	-66,3646
4.sMPABC132	64994,30924	13745,37	1,891264	0,20695	0,00283	0,04153	0,00035	1,18411	0,01318	2881,81	22,03	262,3	2,16	793,2	6,13	95,6	4,78	-102,402	1,18411	0,01318	0,04153	0,00035	0,757151	-66,9314
4.sMPABC150	93743,74751	21481,22	0,154818	0,22186	0,00309	0,03612	0,00033	1,10443	0,01299	2994,239	22,23	228,8	2,02	755,5	6,27	879,5	50,9	-130,201	1,10443	0,01299	0,03612	0,00033	0,776775	-69,7154
4.sMPABC149	144571	41754	0,101789	0,28072	0,00372	0,04542	0,0004	1,75724	0,01959	3366,94	20,51	286,4	2,46	1029,8	7,22	2539,4	129,43	-159,567	1,75724	0,01959	0,04542	0,0004	0,789968	-72,1888
4.sMPABC147	119735,744	35024,85	0,209094	0,28502	0,00458	0,02685	0,00027	1,05387	0,01475	3390,647	24,8	170,8	1,71	730,8	7,29	691,4	45,52	-227,869	1,05387	0,01475	0,02685	0,00027	0,71848	-76,6284





FILE NAME	CORRECTED		0																		RHO	Disc.		
	Pb206*	Pb207*	Th/U	207/206	1s	206/238	1s	207/235	1s	206/207	206/238	207/235	208/232	Conc	207/235	206/238								
4.sMPABC047	763840.6113	175770.1	0.044632	0.23223	0.00277	0.34936	0.00308	11,18112	0.11589	3067.48	18,91	1931.6	14.72	2538.3	9.66	8542.9	318.95	68,59081	11,18112	0.11589	0.34936	0.00308	0.850583	-23.90182406
4.sMPABC058	709803.6355	96690.97	0.353263	0.13853	0.00175	0.21102	0.00165	4,02449	0.04102	2208.91	21.7	1234.2	8.76	1639.2	8.29	1130	90.56	67,18522	4,02449	0.04102	0.13853	0.00165	0.767142	-24.70717423
4.sMPABC022	176548.2498	34669.18	0.567778	0.1943	0.00223	0.29494	0.00228	7,88972	0.07043	2778.91	18.69	1666.2	11.37	2218.5	8.04	1378	56.81	66,85272	7,88972	0.07043	0.29494	0.00228	0.865974	-24.89519946
4.sMPABC050	836104.4059	150917.9	0.072971	0.18186	0.00205	0.27477	0.00226	6,88312	0.06412	2669.91	18.53	1565	11.44	2096.5	8.26	1188.5	49.83	66,03834	6,88312	0.06412	0.27477	0.00226	0.868294	-25.35177677
4.sMPABC108	15838	3198	0.167347	0.20392	0.0048	0.30063	0.00436	8,4391	0.17622	2857.83	37.83	1694.4	21.61	2279.4	18.96	3583	344.04	65,4745	8,4391	0.17622	0.30063	0.00436	0.694537	-25.66464859
4.sMPABC072	650548.6084	137327.9	0.401154	0.21221	0.00245	0.30816	0.00254	9,00709	0.08626	2922.5	18.57	1731.7	12.51	2338.7	8.75	1438.8	64.41	64,94774	9,00709	0.08626	0.30816	0.00254	0.860662	-25.95459016
4.sMPABC079	431036.4504	99508.5	0.315727	0.23394	0.0028	0.32946	0.00284	10,61204	0.10867	3079.2	18.97	1835.8	13.78	2489.8	9.5	2077	84.04	64,3752	10,61204	0.10867	0.32946	0.00284	0.841792	-26.26717005
4.sMPABC080	337866.0112	54832.68	1.156341	0.15938	0.002	0.23439	0.00189	5,13738	0.05294	2449.09	21.06	1357.5	9.85	1842.3	8.76	1306.1	104.5	64,28729	5,13738	0.05294	0.23439	0.00189	0.782493	-26.31493242
4.sMPABC064	170087.1124	25314.28	0.141966	0.14875	0.00171	0.21432	0.0017	4,38802	0.04027	2331.61	19.53	1251.8	9.03	1710.1	7.59	1391.8	69.68	63,38872	4,38802	0.04027	0.21432	0.0017	0.864317	-26.79960236
4.sMPABC031	253317.2101	60430.08	0.401345	0.24398	0.00338	0.32836	0.00275	11,03962	0.12577	3146.12	21.81	1830.4	13.34	2526.5	10.61	2380	245.66	61,97006	11,03962	0.12577	0.32836	0.00275	0.735122	-27.55194934
4.sMPABC032	461347	108143	0.176939	0.23551	0.00292	0.31606	0.00286	10,25502	0.11057	3089.88	19.62	1770.4	14.03	2458.1	9.98	1604.4	78.85	61,15567	10,25502	0.11057	0.31606	0.00286	0.839258	-27.97689272
4.sMPABC088	257057.0173	53857.84	0.142294	0.20033	0.00335	0.27573	0.00288	7,62021	0.11543	2828.89	27.04	1569.8	14.54	2187.2	13.6	1584.3	105.3	60,67015	7,62021	0.11543	0.27573	0.00288	0.689536	-28.22787125
4.sMPABC010	316715.23	58534.84	0.734784	0.18707	0.00205	0.25763	0.00198	6,64074	0.05629	2716.57	17.94	1477.7	10.15	2064.8	7.48	1606.8	76.03	60,26934	6,64074	0.05629	0.25763	0.00198	0.90668	-28.43374661
4.sMPABC050	642225.6037	107062.2	0.049702	0.16903	0.00197	0.22983	0.00185	5,34938	0.05063	2548.06	19.35	1333.6	9.7	1876.8	8.1	3927	174.93	59,26815	5,34938	0.05063	0.22983	0.00185	0.850473	-28.9428815
4.sMPABC066	682132.849	114431.1	0.069431	0.16983	0.002	0.23089	0.00199	5,39912	0.05466	2555.97	19.61	1339.2	10.44	1884.7	8.67	1194.5	49.37	59,26673	5,39912	0.05466	0.23089	0.00199	0.851337	-28.94359845
4.sMPABC049	336391.7619	90335.6	0.19434	0.25555	0.00422	0.3248	0.00347	11,44728	0.17072	3219.48	25.84	1813.1	16.9	2560.3	13.93	1744.5	49.37	59,26673	11,44728	0.17072	0.3248	0.00347	0.711636	-29.18407999
4.sMPABC036	474274.0911	90040.57	0.260086	0.19214	0.00218	0.25525	0.00221	6,75706	0.06545	2760.57	18.5	1465.5	11.33	2080.1	8.57	1205.4	43.04	58,06209	6,75706	0.06545	0.25525	0.00221	0.893871	-29.54665641
4.sMPABC009	306013.5334	48299.59	0.425346	0.15962	0.00204	0.2107	0.00167	4,63313	0.04762	2451.64	21.48	1232.5	8.91	1755.6	8.58	1308.1	94.2	57,58215	4,63313	0.04762	0.2107	0.00167	0.771147	-29.78408249
4.sMPABC084	476793.6047	121524	0.126271	0.25163	0.00272	0.31293	0.00251	10,83552	0.0948	3195.05	16.97	1755.1	12.34	2509.1	8.13	1971.1	67.45	57,03948	10,83552	0.0948	0.31293	0.00251	0.916786	-30.05061576
4.sMPABC005	506604	126463	0.055061	0.24281	0.00383	0.30287	0.00303	10,13726	0.14519	3138.48	24.82	1705.1	15.02	2447.4	13.24	1328.5	88.6	56,49956	10,13726	0.14519	0.30287	0.00303	0.698506	-30.3138024
4.sMPABC107	263128.4465	59922.05	0.050911	0.21735	0.00381	0.27238	0.00255	8,12988	0.12498	2961.16	27.96	1552.9	12.9	2245.6	13.9	1566.3	183.92	55,39314	8,12988	0.12498	0.27238	0.00255	0.608988	-30.84698967
4.sMPABC021	272410.0847	48532.67	0.522247	0.1748	0.00212	0.22234	0.00173	5,34583	0.0514	2604.14	20.1	1294.2	9.12	1876.2	8.22	1004.7	48.42	55,03013	5,34583	0.0514	0.22234	0.00173	0.809246	-31.02014711
4.sMPABC082	519010.3605	87665.16	0.145251	0.16663	0.00204	0.2086	0.00165	4,78335	0.04769	2524.07	20.41	1221.4	8.79	1782	8.37	2187.7	161.49	54,10185	4,78335	0.04769	0.2086	0.00165	0.793368	-31.45903079
4.sMPABC071	382082	79242	0.198729	0.20858	0.00259	0.25844	0.00224	7,42338	0.07885	2894.54	20.03	1481.9	11.46	2163.8	9.51	1255.4	64.73	53,98475	7,42338	0.07885	0.25844	0.00224	0.815996	-31.54104314
4.sMPABC078	699305.2867	169818.1	0.063933	0.24629	0.0035	0.29277	0.00274	9,93008	0.1269	3161.07	22.39	1655.4	13.66	2428.3	11.79	3044.1	645.25	53,31038	9,93008	0.1269	0.29277	0.00274	0.732344	-31.82885146
4.sMPABC030	675043.2366	133045.9	0.035176	0.20125	0.00246	0.24772	0.00209	6,86632	0.07027	2836.36	19.76	1426.7	10.82	2094.3	9.07	3044.1	150.76	53,2067	6,86632	0.07027	0.24772	0.00209	0.824403	-31.87699947
4.sMPABC042	212731.8858	53662.83	0.820759	0.24979	0.0028	0.29369	0.00236	10,10131	0.09063	3183.44	17.65	1660	11.77	2444.1	8.29	2223.9	91.82	52,76506	10,10131	0.09063	0.29369	0.00236	0.895613	-32.08133873
4.sMPABC029	748913.7323	151013.7	0.045052	0.20579	0.00237	0.25101	0.00217	7,11747	0.07028	2872.68	18.63	1443.7	11.18	2126.2	8.79	1498.6	65.55	52,72564	7,11747	0.07028	0.25101	0.00217	0.875513	-32.09952027
4.sMPABC053	486813	100677	0.032962	0.20955	0.00246	0.25433	0.0022	7,33959	0.07366	2902.07	18.88	1460.8	11.32	2153.6	8.97	2099.2	89.61	52,57393	7,33959	0.07366	0.25433	0.0022	0.861916	-32.16939079
4.sMPABC065	215203.537	31603.6	0.159191	0.14445	0.00188	0.17012	0.0014	3,37413	0.03621	2281.24	22.23	1012.8	7.69	1498.4	8.41	1430.9	133.06	52,05371	3,37413	0.03621	0.17012	0.0014	0.766842	-32.40790176
4.sMPABC068	537808.7796	88642.16	0.074493	0.16743	0.002	0.20314	0.00174	4,6815	0.04778	2532.11	19.92	1192.2	9.34	1763.9	8.54	1282	54.01	52,04664	4,6815	0.04778	0.20314	0.00174	0.839253	-32.41113442
4.sMPABC043	247482.181	78821.37	0.468837	0.31778	0.00444	0.34251	0.00303	14,96284	0.17509	3559.12	21.33	1898.7	14.53	2812.9	11.14	4896.4	423.61	51,85127	14,96284	0.17509	0.34251	0.00303	0.756	-32.50026663
4.sMPABC039	577489	115094	0.031636	0.20145	0.00237	0.23667	0.00195	6,56661	0.06363	2837.98	19.04	1369.3	10.17	2054.9	8.54	1648	81.46	49,93062	6,56661	0.06363	0.23667	0.00195	0.850297	-33.36415397
4.sMPABC013	602097.1534	122452	0.072494	0.20805	0.00233	0.24123	0.002	6,91358	0.06369	2890.42	18.06	1393.1	10.38	2100.8	8.2	2815	97.44	49,22834	6,91358	0.06369	0.24123	0.002	0.897017	-33.67453818
4.sMPABC063	188306.6529	21993.9	0.139711	0.11911	0.00155	0.15974	0.00099	1,93078	0.02099	1942.92	23.14	717.6	5.7	1091.8	7.27	1356.5	92.79	47,85396	1,93078	0.02099	0.11911	0.00099	0.773383	-34.2736765
4.sMPABC051	756862.3146	108417.1	0.578809	0.14584	0.00189	0.15994	0.00126	3,21176	0.03388	2297.71	22.05	956.5	6.99	1460	8.17	575.9	49.79	47,36017	3,21176	0.03388	0.15994	0.00126	0.746815	-34.48630137
4.sMPABC018	534079.5096	99139.3	0.224723	0.18764	0.00204	0.2058	0.00164	5,31936	0.04631	2721.59	17.8	1206.4	8.79	1872	7.44	818.9	28.48	44,82759	5,31936	0.04631	0.			





Sample	Sys#	Sys#_Abv	<sup>187</sup> Pu/Py App. Ma	Δt	Δz	<sup>137</sup> Ba/ <sup>135</sup> Ba	<sup>137</sup> La/ <sup>135</sup> La	<sup>137</sup> La/ <sup>139</sup> La	<sup>137</sup> La/ <sup>139</sup> La	<sup>137</sup> La/ <sup>139</sup> La	<sup>137</sup> La/ <sup>139</sup> La	<sup>137</sup> La/ <sup>139</sup> La	TDM Ma (Δ)	TDM Ma_Ma (Δ)	TDM Ma_Ma (Δ)	<sup>137</sup> La/ <sup>139</sup> La <sub>orig</sub>	<sup>137</sup> La/ <sup>139</sup> La <sub>orig</sub>
Franco C: Niguan Dior Pegmatite Dield La IR 24099a1_20107010_1027725a2c1p.cpx.dta	287148060	6	26	0.26807	6	0.2680353	0.2680757	0.2681152	7	-0.0448315	0.17671						
Franco C: Niguan Dior Pegmatite Dield La IR 24099a2_20107010_1027725a2c1p.cpx.dta	585131305	6	17	0.26844	6	0.26844	0.2684342	0.2684342	6	-0.2715789	0.17656						
Franco C: Niguan Dior Pegmatite Dield La IR 24099a3_20107010_1027725a2c1p.cpx.dta	328049540	18	37	0.268752	6	0.268752	0.268751	0.268751	6	-0.0448315	0.17671						
Franco C: Niguan Dior Pegmatite Dield La IR 24099a4_20107010_1027725a2c1p.cpx.dta	251740471	11	23	0.268979	6	0.268979	0.2689871	0.2689794	6	-0.0447994	0.17653						
Franco C: Niguan Dior Pegmatite Dield La IR 24099a5_20107010_1027725a2c1p.cpx.dta	728331451	10	20	0.268953	6	0.268953	0.2689736	0.2689736	6	-0.0448958	0.17655						
Franco C: Niguan Dior Pegmatite Dield La IR 24099a6_20107010_1027725a2c1p.cpx.dta	239743492	10	20	0.268923	6	0.268923	0.2689267	0.2689267	6	-0.1310910	0.17639						
Franco C: Niguan Dior Pegmatite Dield La IR 24099a7_20107010_1027725a2c1p.cpx.dta	272241471	19	37	0.268951	7	0.268951	0.2689532	0.2689532	7	-0.0419145	0.17654						
Franco C: Niguan Dior Pegmatite Dield La IR 24099a8_20107010_1027725a2c1p.cpx.dta	358320794	6	17	0.268957	8	0.268957	0.2689574	0.2689574	8	-0.2788426	0.17654						
Franco C: Niguan Dior Pegmatite Dield La IR 24099a9_20107010_1027725a2c1p.cpx.dta	375149910	19	37	0.268971	7	0.268971	0.2689684	0.2689684	7	-0.2788426	0.17654						
Franco C: Niguan Dior Pegmatite Dield La IR 24099a10_20107010_1027725a2c1p.cpx.dta	351144134	6	17	0.268445	7	0.268445	0.2684454	0.2684454	7	-0.0823229	0.17658						
Franco C: Niguan Dior Pegmatite Dield La IR 24099a11_20107010_1027725a2c1p.cpx.dta	362410713	6	17	0.268484	7	0.268484	0.2684844	0.2684844	7	-0.0823229	0.17658						
Franco C: Niguan Dior Pegmatite Dield La IR 24099a12_20107010_1027725a2c1p.cpx.dta	307217091	13	25	0.268718	7	0.268718	0.2687256	0.2687256	7	-0.0803182	0.17650						
Franco C: Niguan Dior Pegmatite Dield La IR 24099a13_20107010_1027725a2c1p.cpx.dta	366344044	6	17	0.268961	7	0.268961	0.2689612	0.2689612	7	-0.0823229	0.17658						
Franco C: Niguan Dior Pegmatite Dield La IR 24099a14_20107010_1027725a2c1p.cpx.dta	302748009	6	17	0.268984	6	0.268984	0.2689894	0.2689894	6	-0.0823229	0.17658						
Franco C: Niguan Dior Pegmatite Dield La IR 24099a15_20107010_1027725a2c1p.cpx.dta	278119166	10	20	0.268956	6	0.268956	0.268956	0.268956	6	-0.0448315	0.17671						
Franco C: Niguan Dior Pegmatite Dield La IR 24099a16_20107010_1027725a2c1p.cpx.dta	279240408	11	23	0.269160	7	0.269160	0.2691641	0.2691641	7	-0.0788846	0.17658						
Franco C: Niguan Dior Pegmatite Dield La IR 24099a17_20107010_1027725a2c1p.cpx.dta	346619946	6	17	0.268979	6	0.268979	0.268979	0.268979	6	-0.1707196	0.17671						
Franco C: Niguan Dior Pegmatite Dield La IR 24099a18_20107010_1027725a2c1p.cpx.dta	449120974	9	19	0.268968	6	0.268968	0.2689781	0.2689781	6	-0.3389824	0.17658						
Franco C: Niguan Dior Pegmatite Dield La IR 24099a19_20107010_1027725a2c1p.cpx.dta	321140717	10	14	0.268969	7	0.268969	0.268969	0.268969	7	-0.0448315	0.17671						
Franco C: Niguan Dior Pegmatite Dield La IR 24099a20_20107010_1027725a2c1p.cpx.dta	304215211	20	20	0.268925	6	0.268925	0.2689359	0.2689359	6	-0.1657407	0.17674						
Franco C: Niguan Dior Pegmatite Dield La IR 24099a21_20107010_1027725a2c1p.cpx.dta	304215211	10	22	0.268940	7	0.268940	0.268940	0.268940	7	-0.0448315	0.17671						
Franco C: Niguan Dior Pegmatite Dield La IR 24099a22_20107010_1027725a2c1p.cpx.dta	321140718	11	22	0.268960	6	0.268960	0.268960	0.268960	6	-0.2208646	0.17646						
Franco C: Niguan Dior Pegmatite Dield La IR 24099a23_20107010_1027725a2c1p.cpx.dta	311414248	11	21	0.268963	5	0.268963	0.2689635	0.2689635	5	-0.0623678	0.17654						
Franco C: Niguan Dior Pegmatite Dield La IR 24099a24_20107010_1027725a2c1p.cpx.dta	26114961	10	20	0.268951	6	0.268951	0.2689516	0.2689516	6	-0.2208646	0.17646						
Franco C: Niguan Dior Pegmatite Dield La IR 24099a25_20107010_1027725a2c1p.cpx.dta	300211538	10	19	0.268975	7	0.268975	0.2689963	0.2689963	7	-0.0467473	0.17678						
Franco C: Niguan Dior Pegmatite Dield La IR 24099a26_20107010_1027725a2c1p.cpx.dta	278119166	12	24	0.268968	7	0.268968	0.2689687	0.2689687	7	-0.0991471	0.17651						
Franco C: Niguan Dior Pegmatite Dield La IR 24099a27_20107010_1027725a2c1p.cpx.dta	278119166	12	24	0.268959	6	0.268959	0.2689593	0.2689593	6	-0.2705845	0.17651						

Table with columns: Sample, Spot, Spot size, 210Pb/210Pb Age Ma ±1σ ±2σ, 137Ba/137Ba ±1σ ±2σ, 147Sm/147Sm ±1σ ±2σ, 232Th/232Th ±1σ ±2σ, 230Th/230Th ±1σ ±2σ, T(DM) (Ma), T(DM) (Ma), T(DM) (Ma), 106Hf/106Hf, 107Hf/107Hf, 108Hf/108Hf. Includes sample names like 'C:\Neptune\User\Neptune\Data\La-Hf 2406\test2\_20150702-133853\test11xyz.dat' and numerical data for each.

# **ANEXO 4**

TABELA EVOLUÇÃO QUADRILÁTERO  
FERRÍFRO

Table 4: Summary table indicating the main characteristics of the eastern and northern sectors. These reflect the tectonic environment of their formation portrayed in Figure 19.

Cycles (Baltazar and Zucchetti, 2007)	Environment	Sediment source				Sediment timing		Implications to gold mineralization
		Associated minerals	Geochemistry	Lu-Hf	LA-ICP-MS on sulfide minerals	Archean U-Pb geochronology	Proterozoic U-Pb geochronology	
<b>C</b> Córrego do Sítio lineament	Clastic-chemical-sedimentary association+turbidites	Quartz-ankerite-arsenopyrite-pyrite-pyrrhotite, free gold, berthierite, stibnite, sphalerite, cobaltite, cinnabar, tetrahedrite, boulangerite-group minerals and ullmanite.	Major and trace elements suggest mixture of felsic and mafic rock sources, with a higher proportion of mafic inheritance.	Zircon grains record mainly reworked crustal $\epsilon_{Hf}$ values with minor juvenile $\epsilon_{Hf}$ values.	Large variety of ore minerals including sulfides and sulfosalts that contain Sb, Pb, Hg, As, Zn, Cu, as well as Ni and Co Pt. This seems to reflect a variety in the source to the sediments - mixed and felsic rocks.	Rocks of Rio das Velhas II (2800-2770 Ma) and mainly Mamona (2760-2680 Ma) events considered to be significant sources of zircons. Santa Bárbara (3200-3200 Ma) event perseveres and is more persistent than in northern sector.	Paleoproterozoic record is present in all deposits and are best recorded for the Carvoaria deposit.	Mixed source of host rocks may have facilitated sulfidation reactions, and consequently enhanced gold precipitation, since sediments in eastern sector were probably more prone to form sulfide minerals.
<b>E</b> Cuiabá-Lamego area	Volcaniclastic association Resedimented association	Gold-rich zones are related to iron-rich bands of BIF and silicification zones with pyrite, As-pyrite, and arsenopyrite.	Major and trace elements suggest mixture of felsic and mafic rock sources, with a smaller proportion of mafic inheritance.	Zircon grains have negative $\epsilon_{Hf}$ values indicating consistent derivation from reworked crustal sources.	-	Rocks of the Rio das Velhas II (2800-2770 Ma) and mainly Mamona (2760-2680 Ma) events considered to be significant sources of zircons.	Paleoproterozoic record is present and more important than the eastern sector; best recorded at the Lamego deposit.	Gold in carbonaceous pelite pyrite displays excellent affinity with crustal elements such as Bi, Pb and Sb; good correlation is also observed with Ni, Co, Cu, Ag and Te.